A STUDY OF STRAY LOAD LOSSES IN CORE CLAMP PLATES OF SALIENT POLE SYNCHRONOUS MACHINES.

A thesis submitted for the Degree of Master of Science in the Faculty of Engineering of the University of Aston in Birmingham.

Philip Harold Conceicao

Department of Electrical Engineering

Electrical Machines Centre

1966 - 1969.

August 1969.

THE UNIVERSITY
O
R
-3 DEC 1969
124442
621·3/332
CO A

Abstract.

The importance of stray loss evaluation in machines is discussed, and the literature on clamp plate loss in particular is extensively reviewed. The design of two models having their core lengths in the ratio 3 : 1 is presented, and from tests on the models, the loss in clamp plates of various materials is evaluated at various excitation currents and power frequencies.

The flux densities at the clamp plate surfaces are extensively examined using Hall probes. Hall probe instrumentation and date handling by computer, is presented. The clamp plate surface flux densities are obtained with both a.c. and d.c. excitation. The waveforms of the surface flux densities are presented in detail, and indicate the complex nature of the problem.

The use of the Hall probe equipment on actual machines in industry is illustrated, and further evidence of the intricate nature of the end-field problem is given.

The flux density and loss investigations on the models show that even with a moderate degree of saturation in the laminated cores, the end region flux density patterns are materially affected. The clamp plate loss can then be considered as having two components, one due to winding overhang m.m.f., and the other due to flux passing from core to clamp plate at the interface.

Within the limitation of the method used, a technique is presented for evaluating clamp plate losses in machines from the test results obtained on the models.

<u>Contents.</u>

List of Illustrations.

Page.

Figure

Figure		Page.

Figure		Page
5.1 - 4	Air gap flux density pattern with four consecutive coils excited	113
5.1 - 5	Air gap flux density pattern with all coils in one phase excited	113
5.1 - 6	Air gap flux density pattern for 1, 2 and 3 phases excited	116
5.2 - 1	Test positioning for probe	119
5.2 - 2	Core Surface density plot, single short pitched coil excited with d.c.	119
5.2 - 3	Core Surface density plot, four consecutive coils excited with d.c. ..	120
5.2 - 4	Core Surface density plot, all coils in one phase excited with d.c.	120
5.2 - 5	Flux density plots showing effect of grouping of conductors	122
5.2 - 6	Photograph showing the various jigs used for mounting the Hall probes	123
5.2 - 7	Relative probe numbering on jigs shown in Fig. 5.2 - 6	124
5.2 - 8	Slot numbering with relative phase dispositions	124
5.3 - 1	Radial surface density traces with varying stator excitation. Stator connected series - parallel with d.c. excitations. Aluminium and mild steel clamp plates	127
5.3 - 2	Radial surface density traces with varying stator excitation stator connected with two phases in series with d.c. excitation, aluminium and mild steel clamp plates	128
5.3 - 3	Radial surface density traces with varying stator excitation. Stator excited three phase, 50 Hz. aluminium and mild steel clamp plates	129
6.1 - 1	Calculation of correction factor K_i for short core loss	138
6.1 - 2 to 6.1 - 9	Tabulation of total losses corrected for copper loss, for various condition of test	140 to 147
6.2 - 1	Summary of test exponents of A and 'f' for clamp plate losses	149

Figure		page

Figure | Page

Figure		Page

List of Tabulations.

List of Symbols.

Unless referred to directly in the text, all other symbols follow this listing.

B	Flux density; general symbol Wb/m^2.
Bg	Air gap flux density Wb/m^2.
B_θ , B_{1c}	Leakage path flux density (from core) Wb/m^2.
d_e	Effective overhang distance, mm.
D_e	Effective clamp plate diameter, mm.
f	Frequency, Hz.
H	Magnetising Force; general symbol A/m.
H_m	Peak magnetising force A/m.
H_{cn}	Core magnetising force A/m.
I	Magnetising current; general symbol. A.
k	General constant of proportionality.
K_i	Iron loss correction factor.
K_p	Winding chording factor $\ngtr$ 1.0
Kd	Winding distribution factor $\ngtr$ 1.0
n	Order of harmonics, 1, 2, 3 etc.,
N	Turns per coil.
s	Slot opening.
t	Time in seconds.

T	Effective turns per pole.
w	Tooth width.
W	Total series conductors per phase.
W_c	Total clamp plate losses, kilowatts.
W_i	Iron loss, kilowatts.
W_1	Short core loss, kilowatts.
W_2	Long core loss, kilowatts.
Xd	Synchronous reactance per unit.
Xl	Leakage reactance per unit.
ρ	Resistivity ohmn - metre.
δ	Skin depth or depth of penetration - metres.
Φ	Total flux per pole; general symbols, Wb.
τ	Pole pitch; general symbol.

<u>Chapter I</u>

1.0 Introduction

Early in the history of the development of the alternating current (A.C.) generator, it was recognised that there might be losses present under load conditions in addition to the no-load losses and the armature copper loss due to load current. Initially, as there was no means of measuring this loss, it was not included in the evaluation of machine efficiency. As competition increased and as economic pressures demanded a more precise evaluation of efficiency, a method of testing was evolved to segregate this extra loss, which was eventually known as stray load loss.

The definition of this loss gives a good understanding of the problem that had to be faced. Stray load losses in rotating A.C. machines are defined as "the additional losses caused by the load current due to changes in flux distribution and eddy currents." These losses are partly due to the eddy currents in armature conductors, solid copper, end windings, clamping rings, and are also partly due to hysteresis and eddy currents in portions of the main magnetic circuit as well as in the stationary structural metal parts of machines.

Initially, the determination of total stray load losses was governed by the pressure of competition and a search for high efficiencies, but by now the problem has resolved into a search for more accurate prediction of the various components of stray load loss. Consider the way in which the specific outputs of rotating A.C. machines have increased in recent years.

The induction motor is now being regularly manufactured in outputs up to 25 MW. The turbo generator is being manufactured in sizes of 1200 MW, with single sets at 2000 MW being investigated. The salient pole waterwheel generator has reached the 500 MW level, and sets of 1200 MW are proposed. By direct water cooling the rotor conductors, the outputs of both types of synchronous machines could well become equal. Considering Fig. 1.0 - 1a., and 1.0 - 1b., it will be seen that the total stray losses, while a small percentage of the output, nevertheless represent a large amount of loss that has to be removed either directly by water cooling, or indirectly by radiation and gas cooling. It is not surprising therefore to find that with greater usage and the associated larger outputs, the determination of losses has reached a stage where greater accuracy than ever is necessary.

This thesis considers specifically the determination of stray load losses in the stator core clamping plates. The subject of end region losses in general, and clamp plates in particular has been studied by a number of authors over the past forty five years, generally based on observations on built machines (Fig. 1.0 - 2), theoretical considerations alone, analogue models, and a combination of all three aspects. This thesis presents curves for clamp plate losses obtained from tests on experimental models for various clamp plate materials and at various commercial power frequencies; factors affecting these losses are investigated in detail in an attempt to achieve a better understanding of the problem.

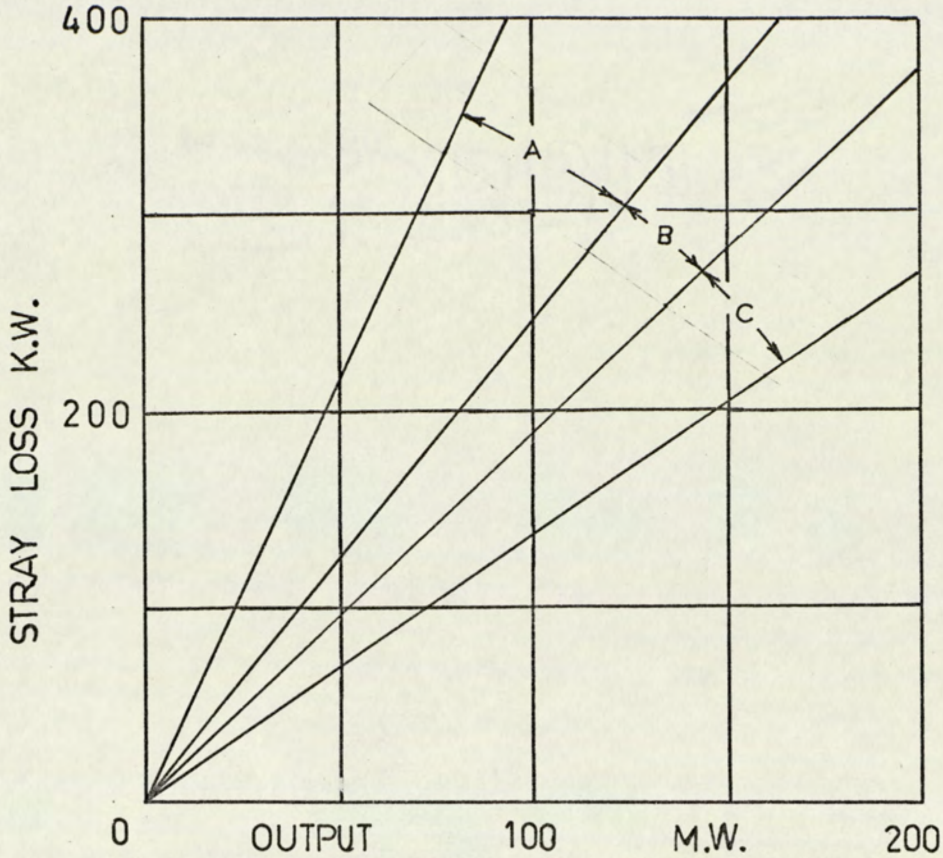

FIG
1·0-1a

Stray Losses in Salient Pole Machines.

A Nose transposed, magnetic clamps, guards and duct spacers.

B Roebel transposition, magnetic clamps, guards and duct spacers.

C Roebel transposition, glass fibre guards and fan guides, non-magnetic clamp and duct spacers.

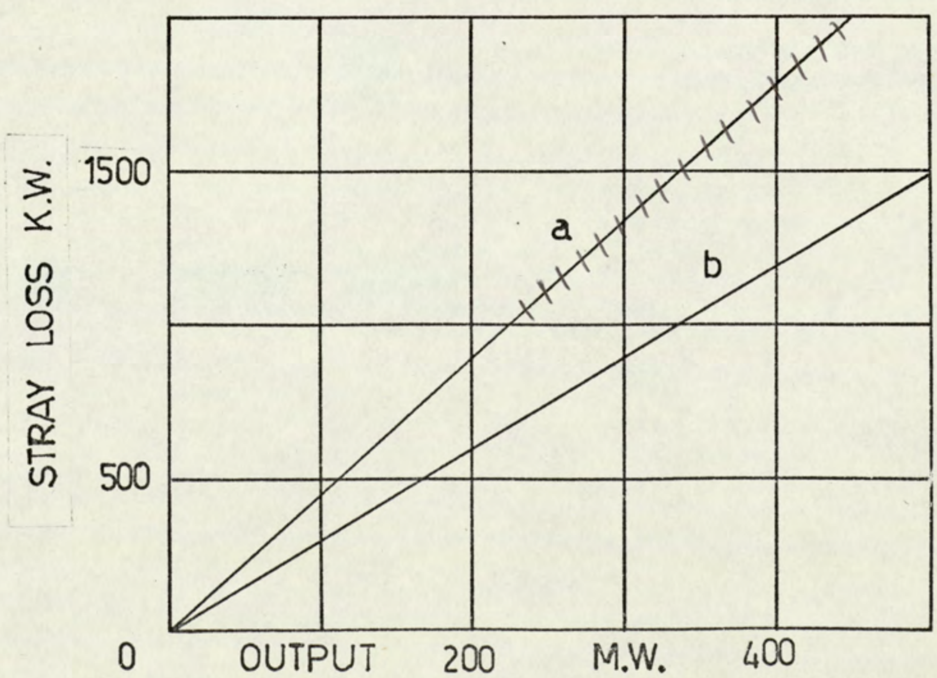

FIG
1·0-1b

Caution—
Curves show
trends only

Stray Losses in Turbo-Type Machines.

a Nose transposed, magnetic end bells and clamps.

b Roebel transposition non-magnetic or shielded clamps, non-magnetic end bells.

FIG

1·0-2

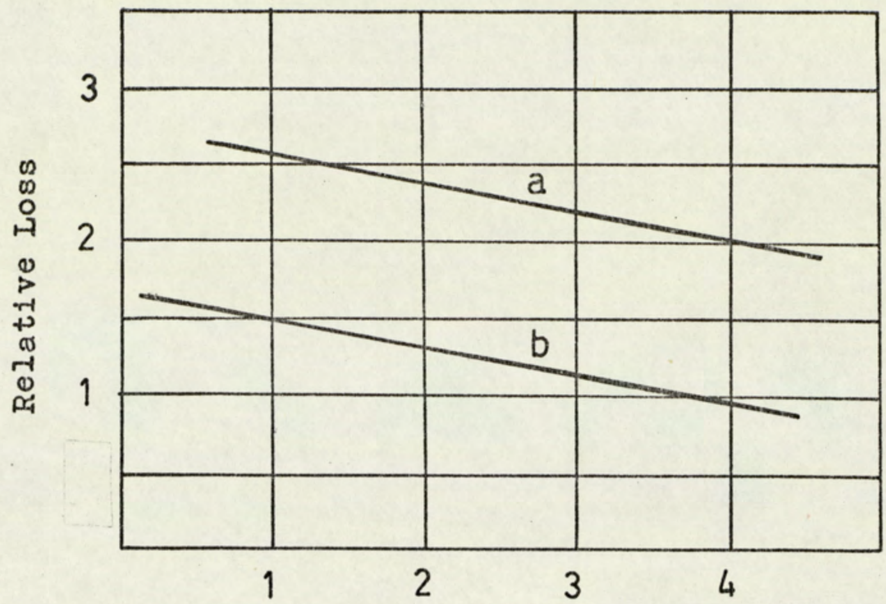

With acknowledgement to C.A. PARSONS & Co. Ltd

Air Gap Length in inches.

Typical variation of end region loss with air gap length for turbo machines above 30 M.W.

a) Magnetic end bells.

b) Non-magnetic end bells.

1.1 The Problem.

In rotating machine structures, the design engineer is confronted with the problem of eddy current losses in conducting solids due to nearby alternating currents. Where ever possible, the machine parts exposed to alternating or pulsating magnetic fields are laminated to break up the eddy current paths and reduce the losses. However, in certain parts of the machine, solid metallic structures occur which are exposed to alternating fields and which are impossible to laminate or replace by non-metallic materials such as glass-fibre mouldings. Amongst these parts are core end clamp plates of rotors and stators which are in the magnetic field of the end windings. Similarly, within the machine frame, heavy current leads may cause eddy currents in the end winding guards and frame. Where possible, end guards are constructed from non-magnetic materials such as brass and cast aluminium or glass-fibre mouldings. The author recalls a vertical water wheel generator on which the mild steel plates immediately above the windings had to be replaced by cast brass plates to reduce heating and losses: unfortunately, as this trouble had to be remedied on site, an accurate measurement of the loss was not obtained. The temperature was certainly reduced by 20°C.

On each machine, the designer has to make a decision regarding the materials to be used, and on the spacing or clearances of conductors from nearby metal in excess of normal clearances required to prevent flashovers. Any resulting reductions in losses must be evaluated on the basis of capitilised costs and efficiency bonus or penalty charges.

It may prove cheaper to redesign the machine in a larger frame, using conventional materials or techniques.

For example, two "No-du-mag" clamp plates costing £1,000 on a 25 MW generator give a reduction of 20 kW of stray loss capitalised at £150 per kW. It is quite reasonable in this instance to use this method of reducing stray losses, rather than redesigning the machine, unless of course redesign gives an even greater loss reduction.

To assess loss reduction, the designer must therefore know what advantages result from varying the various parameters affecting the design of synchronous machines. A study of tests on a larger number of turbo type machines built in the author's organization gave the following relationships.

<u>End Bell Material</u> There is a definite reduction in stray losses due to the use of non-magnetic end bells. This is reflected in the curves of Fig. 1.0 - 1b.

<u>Air Gap Length</u> As seen in Fig. 1.0 - 2 there is a reduction in end region losses in turbo generators, as the airgap length is increased. Tests on a 1.5 MW salient pole generator showed a 10 percent reduction in total stray load losses when the air gap was increased 28.5 percent.

<u>Chording of Windings</u> In general, chording has a strong effect, with a marked minimum loss occurring in the region of 80 - 90 percent pitched windings. There is a tendency to higher than normal stray load losses on salient pole machines with less than 1.5 slots per pole per phase where it is not possible to pitch the coils less than 90 percent.

Stator Ampere-conductor loading Stray losses are roughly proportional to the square of the current. In general the loss varies as I^x where x lies between 2.0 and 2.25, for both turbo-type and salient pole synchronous machines.

Frequency Stray losses vary as $(\text{Frequency})^y$

$$\text{where } y = 1.2 \text{ to } 1.56$$

Stator Stamping Material The use of hot and cold rolled stampings of equal silicon content show no difference in end stray losses. Tests on salient pole machines however, where the silicon content had been changed from 3 to 4 percent showed a 5 percent increase in total stray losses which, when considering the accuracy of commercial testing, can be ignored and the stray losses regarded as being virtually unchanged.

End Winding Guards and Fan Guides The use of non-metallic guards and guides reduces the total stray losses, a reduction of 40 KW in a total of 770 KW stray loss being typical on a large turbo-generator. A similar study on a 5 MW geared salient pole turbo-generator showed a 5 KW reduction in a total of 23 KW when cast iron end guards were replaced with glass-fibre guards.

From this brief survey, it becomes obvious that the problem of stray load losses, and particularly the end region losses is very complex and is subject to a large number of variables.

1.2 A Historical Review.

Although it was as early as 1913 when the existence of stray load losses was acknowledged in an amendment to the A.I.E.E. rules, it was only in 1921 that the first serious study of the problem was published. In 1921, Miles Walker (33) published the results of experimental investigations on end plate losses carried out by the British Westinghouse Company and the Manchester College of Technology. The machines considered in that investigation were turbo-generators having magnetic core clamp plates and concentric (hairpin) windings. These results are summarised in Fig. 1.2 - 1. No mention is made of the rotor end bell material, but considering machine design techniques in 1921, it is reasonably safe to assume that magnetic steel was used.

In the report it is observed that the clamp plates losses varied with the end winding configuration, the minimum losses being obtained with a barrel type winding. The formulation is extremely elegant in its presentation, taking into account most of the physical parameters which should affect clamp plate losses. It has some weakness in that there is no difference shown between two-tier and three-tier windings. It does not appear that the rotor effects, if any, have been considered, and that the number of poles is not considered as influencing the pitch of the winding and losses. With this qualification, and bearing in mind that the experimental results were based on turbo generators, this formulation could be applied to all forms of A.C. machines.

In 1927 Rockwood (51) published his paper on stray load losses in which he divided the losses into a number

FIG 1·2-1

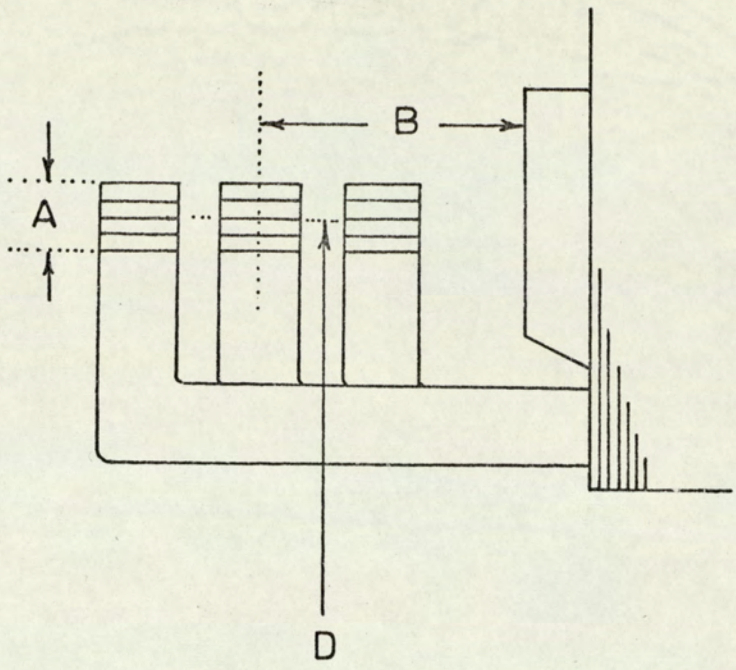

The loss in watts in each clamp plate is given by:-

$$W = (0.008\ D^{2.1}\ \frac{A}{B} + 0.32\ D^{0.45})\ f^{\ 1.4}\ (A.T.)^{\ 2} \times 10^{-8}$$

Where; all dimensions are in inches.

A.T. = Series Conductor/tier x 2 x Amps/Cond.

f = frequency.

B = Mean distance from clamp plates.

D = Mean diameter of bent up portion or mean diameter of clamp plates.

CLAMP PLATE LOSS FORMULA AS GIVEN BY MILES WALKER (33) of components, one of which was the "end" loss. Rockwood developed a dimensionally correct expression for end losses which contained some familiar relations as seen below.

$$W_{end} = K_3 \, D \, V \, f^{\,0.5} \, (A\,R)^2 \times \text{Coil Pitch} \times 10^{-11}$$

where K_3 is a constant, D the bore diameter in inches, V the peripheral velocity in thousands of feet per minute, f the frequency hertz, (A R) the ampere turns of armature reaction per pole.

If we replace V by a function of diameter, frequency and poles, then:

$$V = \pi \times D \times \frac{120\,f}{\text{poles}}$$

$$W_{end} = K_x \, D^2 \, f^{\,1.5} \, \frac{\text{Coil Pitch}}{\text{Poles}} \times (AR)^2$$

Rockwood does not give any value for the constant in his formula. On comparison with the earlier expression, both coil pitch and the number of poles are introduced. This is not surprising since Rockwood is considering Salient Pole synchronous machines with two layer windings which can be short pitched. Compared with the earlier work it is noticed that the actual physical configuration of the end winding is not considered, neither are the clamp plates nor end guards. It can only be assumed that the usefulness of Rockwood's work is limited to a specific range of machines with a similar mechanical construction.

Shortly afterwards, in 1929 Richter (34) published his now classical book 'Elektrische Maschinen.' We see for the first time a rigorous approach to the problems in the end regions, again however treating turbo machines with hairpin windings exclusively. With the aid of flux plots (Fig. 1.2 - 2.) the distribution of field strength is shown for a variety of conditions, with magnetic and non-magnetic end bells, with rotor removed and with the machine on short circuit with the rotor in position. From the various plots, it is seen that boundary conditions play an important part in the field distributions, this being particularly noticeable when magnetic end bells are used, the maximum densities as seen from Fig. 1.2 - 3a, occurring near the clamp plates, thus accentuating losses. However, apart from giving a very good physical concept of the problem, no practical or theoretical solutions are put forward.

In 1934 Liwschitz (35) enlarges on Richter's work, again by means of field plots. In Fig. 1.2 - 2, we see the effect of changing from a hairpin to a diamond type winding but unfortunately it is difficult to draw any positive conclusions, as the boundary conditions are not identical. It would appear that the diamond winding produces a weaker field concentration at the clamp plate surface resulting in a correspondingly lower loss. Liwschitz (Fig. 1.2 - 3b,) also sets down what appears to be a semi-empirical solution in graphical form for the approximate losses in overhangs of salient pole synchronous machines. Three conditions are considered,

FIG 1·2-2

Ref: Richter (34)

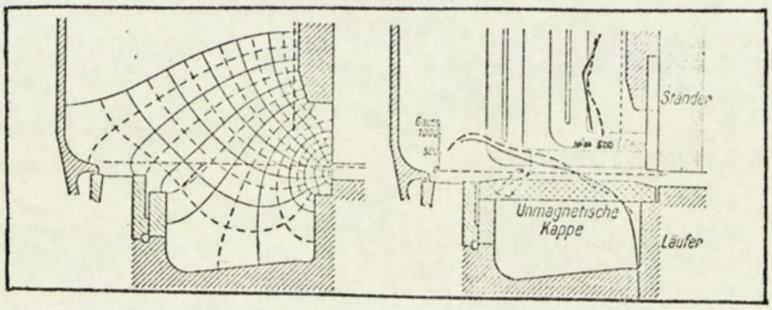

20 MVA machine with non magnetic end bells
(on short circuit)

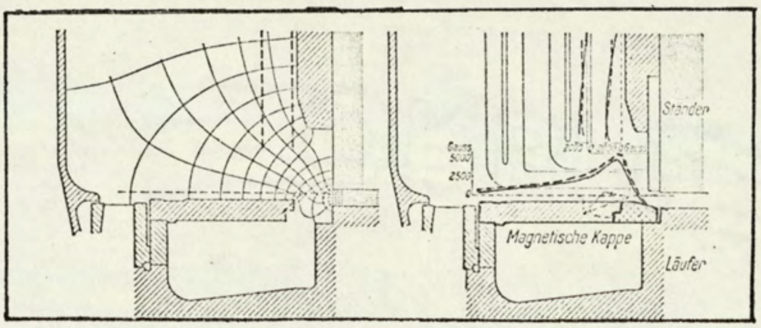

---------- calculated

—— measured

20 MVA machine with magnetic end bells
(on short circuit)

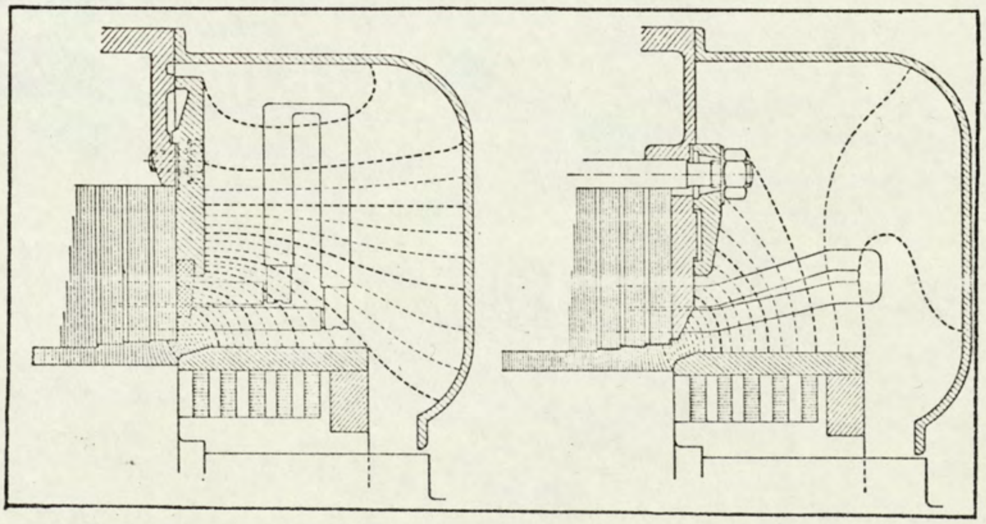

Ref: Liwschitz (35)

influence of type of connection on field distribution

END REGION FLUX PLOTS AS GIVEN BY RICHTER AND LIWSCHITZ

FIG 1.2-3 a

Ref: Richter, Liwschitz
(34) (35)

radial and axial surface flux density traces

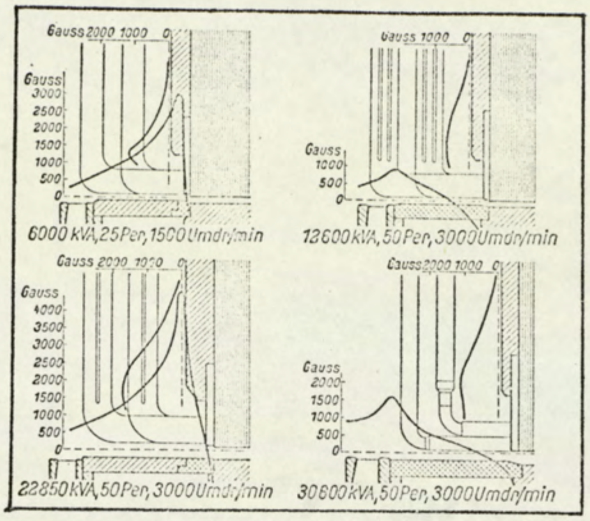

magnetic end bells ↑ non magnetic end bells ↑

FIG 1.2-3b

REF: Liwschitz, (35)
Klamt (36)

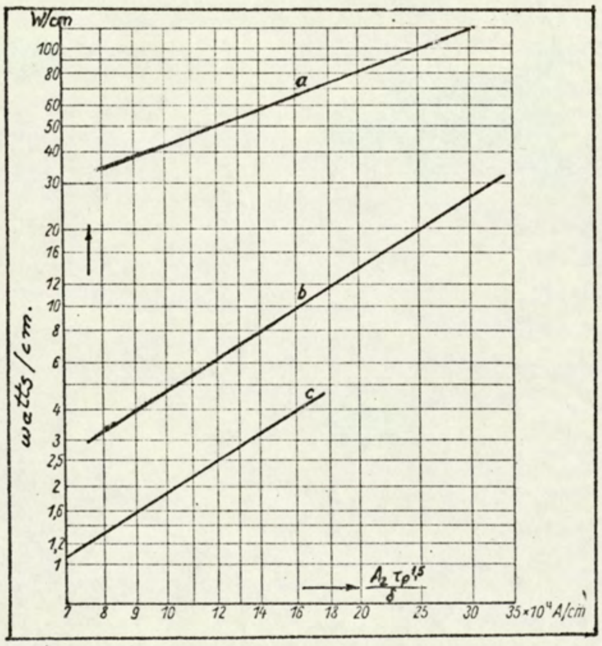

A_2 = AC/cm

τ_p = pole pitch, cm

δ = single gap cm

D = bore dia. cm

$W_{END} = \pi$ D × watts/cm

a = large b = medium c = small machines
(see text)

METHOD OF CALCULATING END REGION LOSS AS GIVEN BY LIWSCHITZ AND KLAMT

a) Large machine with pressure plates and heavy short circuited bracing rings.

b) Medium machines with pressure fingers and light bracing.

c) Small machines with welded end stampings and no bracing.

Since frequency does not appear in the results, it must be assumed that the curves apply only to 50 c/s machines. Although bore diameter and pole pitch dimensions are used, the physical shape and dimensions of the end winding appear to be completely ignored. In an attempt to check these it was found that the definition of machine size based on manufacturing records circa 1934 gives the following,

Curve a) 20 MVA and above

Curve b) 2 MVA to 20 MVA

Curve c) below 2 MVA

However in 1962 we find that Klamt (36) repeats Liwschitz's work, and in a worked example indicates that a 4 MW 250 r.p.m. motor with a bore of 4500 mm. can be considered as a medium sized machine.

When checked on some large modern water wheel generators, curve (a) gives an end loss value that appears reasonable in magnitude.

It is strange to find from Fig. 1.2 - 3b, that the air gap has such a significant influence on the loss calculation. (e.g., a decrease in gap by a factor of two increases the predicted loss by a factor nearly three to one.) When applied to induction machines with their significantly smaller air gaps, the method gives

FIG 1·2-4

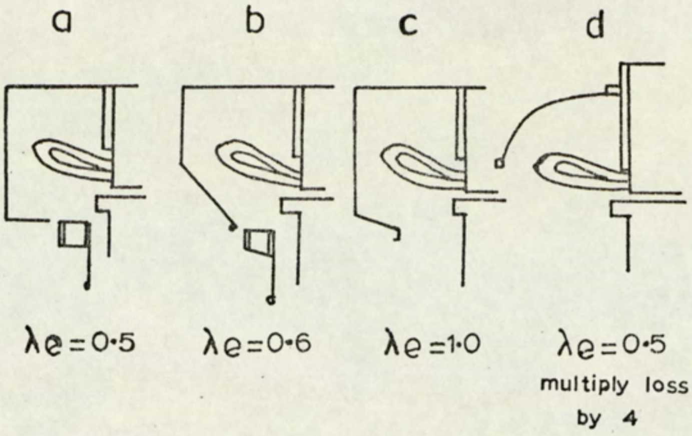

Totaleffective end bell area = 3·5 τ_r x bore dia(sq.ins.)

λe = 0·25 for end plate loss (evaluated separately)

τ_r = pole pitch, inches.

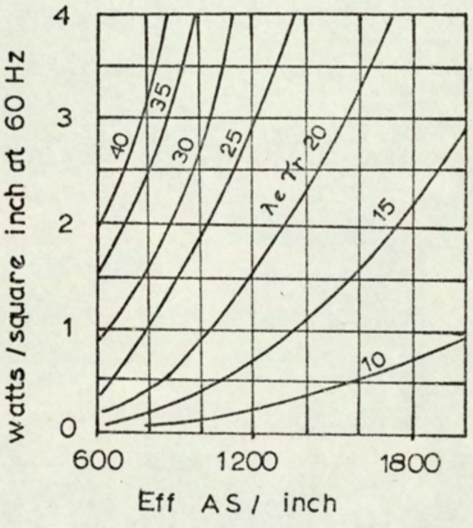

method of calculating
end losses in salient pole synchronous machines
as given by Pollard (52)

unacceptably high values of end zone losses.

Pollard's (52) paper on load losses in salient pole synchronous machines in 1935 presents a semi-empirical solution (Fig. 1.2 - 4) to what is described as end zone loss. Curves are given to enable end region losses to be calculated in terms of pole pitch and bore diameter for various shapes of ferrous end guards. From a machine design engineer's viewpoint this presentation is attractive as it appears to cover nearly all the parameters connected with variations in stator winding. As the curves are for 60 c/s machines, use can be made of the variation with frequency given in the two earlier formulations, i.e. loss varies as $f^{1.5}$. There is no reason why the work cannot be applied directly to Induction as well as Synchronous machines.

Despite its attractiveness, this work is also of limited interest in so far that it does not allow for variations in materials for the various boundaries shown. For non-metallic guards we could assume $\lambda_e = 0$ but for non-magnetic metallic materials, there is no allowance. Some useful points emerge, e.g., (1) end losses are noticeably greater with large pole pitches, (2) shrouded fans near the rotor divert flux away from the end guards thus reducing stray losses, this explaining a two-to-one reduction between configurations (a) and (c) in Fig. 1.2 - 4. This paper can still be considered among the best published on the subject of load losses.

Another attractive paper is that by Richardson (53) in 1945. The author indicates that magnetic end-bells on the rotor windings of turbo generators can increase the clamp

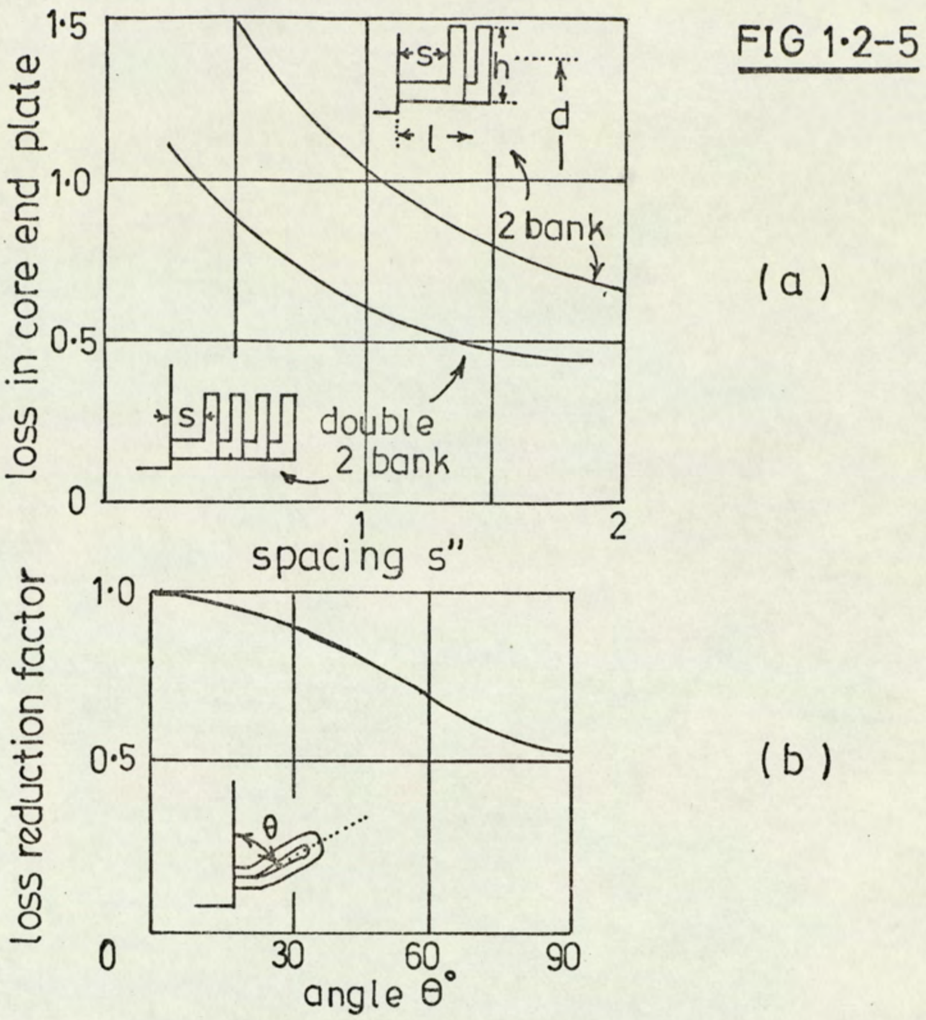

$$\text{Loss}/_{\text{end}} = K \times d\ (h + l)\ \left(\frac{at}{l}\right)^{1.6} \times 10^{-8}\ \text{KW.}$$

Where d = mean diameter (in) of the winding bank.

h = Height (in) of winding bank

l = mean distance (in) of windings from the core end plate or end shield.

at = stator ampere-turns per pole pair.

K = 1.2 for a "skeleton" type core end plate of cast iron or mild steel.

= 3.3 for a solid core end plate or end shield.

Where non-magnetic iron is used, the above constants should be reduced to one third of their value.

METHOD OF CALCULATING CLAMP PLATE LOSS AS GIVEN BY RICHARDSON (53) plate losses by as much as 15% due to flux crowding in near the stator core. With end bells, it appears that losses are noticeably affected by air gap variations. From his field plots for involute and diamond windings a shift in the end field distribution is seen which would indicate lower losses as the winding approaches a cylindrical or barrel form. (Fig. 1.2 - 5). From Figure (a) it will be seen that a double 2-bank winding gives lower clamp plate losses. This can be explained by the fact that the centre of gravity of the end winding mass is further away from the clamp plate. In Figure (b) the effect of cone angle is seen. This substantiates Miles Walker's claim that the losses decrease as the cone flattens. Richardson gives the loss per end clamp plate or end shield at 50 c/s by a simple formula. (Fig. 1.2 - 5).

The effect of using copper end shielding on the core end plates is studied. Richardson notes that losses decrease as the thickness of the shield is increased up to $\frac{1}{4}$ inch, after which no significant improvements were obtained. As the depth of penetration of copper is approximately $\frac{3}{8}$ inch, at $20^{\circ}C$ and 5/16 inch at $100^{\circ}C$ this gives adequate justification for the belief that there is no appreciable increase in eddy losses beyond this thickness if a clamp plate has a thickness greater than the depth of penetration.

In 1955 Winchester (54) considered the problem of stray losses in the end packet of stampings in the armature. Only two dimensions are considered since there is symmetry in the axial direction. The analytical solution to the loss equation contains the flux density term B_o which is obtained from an electrolytic tank analogue. It is noted that the end packet losses can be reduced by splitting the end teeth and chamfering the core end.

Data is presented which shows a reduction in end plate loss if copper shields are used. It is odd to see that Winchester considers using non magnetic clamp plates when shields are used. As discussed earlier, with shields, magnetic material could be used. It is indicated that loss decreases as the resistivity of the non magnetic shield is lowered. Apart from this reference to the clamp plates, this paper does not contribute a solution to clamp plate losses.

Another paper of general interest is that by Staats (55) in 1957. The end winding (copper) eddy current losses are treated by reducing the complex three dimensional field problem into sub-divisions due to the various portions of the current-carrying conductors and the fringing of the main air gap field, the circumferential and radial components of the sub-divisions being considered. The stator end winding is treated as lying on the frustum of two cones. This is in turn reduced to two concentric cylinders. The problem is finally resolved into two parallel planes and current sheets, the cylindrical co-ordinates being transformed to Cartesian. It must be appreciated that there will be a pair of cylinders for each point that is considered on the end winding. Staats finally develops an expression for power loss per cubic centimetre of end winding copper.

In his study on the end components of leakage reactance Smith (56) in 1958 resolves a turbo generator end winding into a cylinder the radius of which is arbitrarily taken to be:-

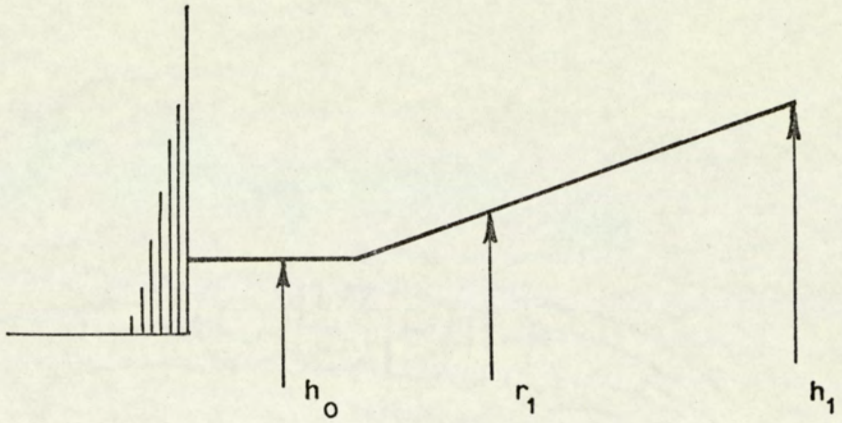

$$r_1 = h_o + \frac{1}{3}(h_1 - h_o)$$

Smith states that this value of r_1 is not critical and that in a typical example, a 10% variation in r_1 gave a 1.5% difference in the end result. This however does not necessarily mean that the selection of r_1 for the cylinder is the correct equivalent representation for the cone. The end winding is then replaced by a current sheet at radius r_1. This paper is of interest because it presents yet another way of expressing an end winding as a simple geometrical model.

In the joint paper by Alger, Angst and Davies (57) in 1959, a simple formulation for end loss in Induction machines is given,

$$W_e = 0.3\ m\ I^2 \left[\frac{1.6\ f.m.\ N^2\ D_1}{P^2 \times 10^7} \quad \log\left(1 + \frac{A^2}{4Y_1\ Y_2}\right)\right]$$

where I is the current, m the number of phases, f the frequency, P the number of poles, and all dimensions are as shown below.

The formula is dimensionally correct and it can be easily seen from a substitution of terms that the formulation reduces to the same structure as in Rockwood's paper with the exception that frequency is not raised to any power.

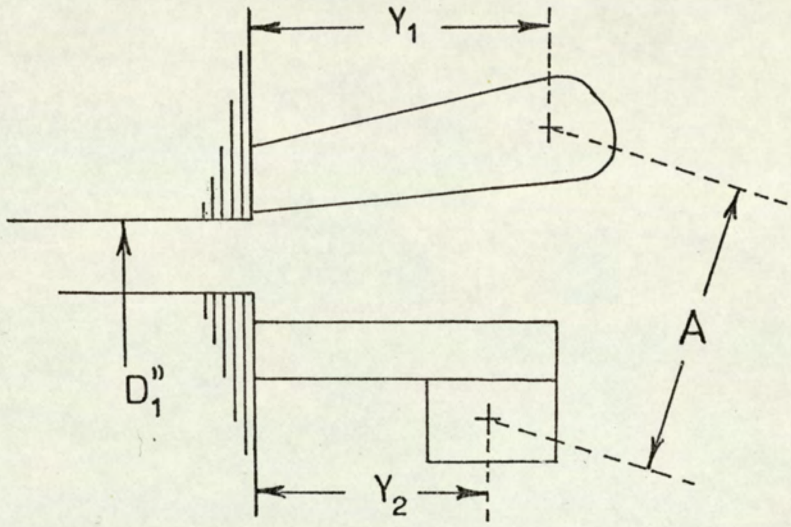

Further the term $\log\left(1 + \frac{A^2}{4Y_1\ Y_2}\right)$

can be replaced by a constant varying with the poles in salient pole synchronous machines, on the basis that

$$A \simeq Y_1 \simeq k\ Y_2$$

From the range of machines that have been considered, both random wire and former wound coils are considered in the end loss formulation which must therefore include all components such as clamp plates, end guards, bracing rings and copper losses.

In the same year, Honsinger (58) in treating the problem of end winding leakage reactance for induction motors considers the effect of different shapes of coils. Three in particular are examined.

a) Rectangular

b) Elliptical

c) V - Shaped.

As can be expected, Honsinger shows that the V - shaped winding has the lowest influence factor when considering the iron boundaries and the coil cross-sections. The rectangular configuration produces the highest leakage reactance being approximately 40% higher than the V - shaped configuration.

In considering the iron boundaries such as formed by clamp plates and end brackets, Honsinger assumes that all flux is perpendicular to the surfaces because it appears that eddy currents induced in the iron are not sufficient to reduce substantially the normal components, thus implying that the radial and tangential components are zero.

In 1961 there appeared the first of a set of five papers on the calculation of the magnetic field of rotating machines by Hammond (60) in association with various other authors. In the first part, treating the field of a tubular current, the ground work is laid for an explanation of current sheets. Consider the three examples:-

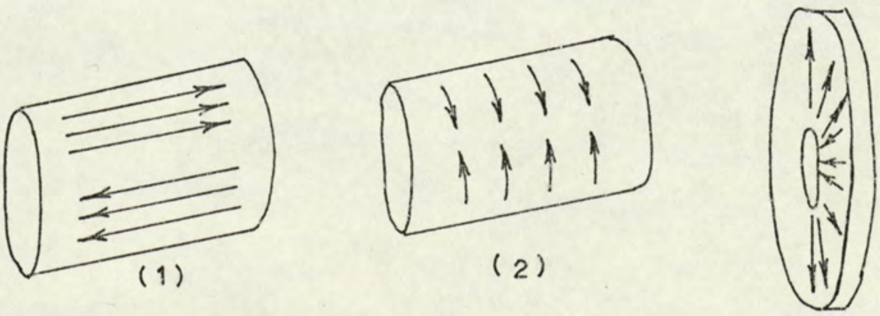

(1) (2) (3)

It is now easily appreciated that the first case can be described as a sheet of Axial current, the second as circumferential and the third as radial. It is clear therefore that any current distribution can be built up by the superposition of appropriate current elements, for example the case of an induction motor cage winding with its end rings, which is illustrated below.

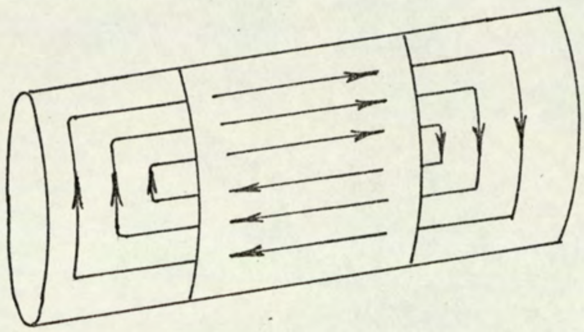

Further, Hammond lays down three basic assumptions.

a) Actual conductor currents are replaced by current sheets.

b) Current Sheets are of simple geometrical shape.

c) No iron is considered in the vicinity of the current sheets.

With an infinite distribution of conductors the first assumption can be considered reasonable. When considering the second assumption the degree of approximation will be governed by the complexity of the end winding considered. The third assumption is corrected at a later date. The paper is of further interest as Hammond develops a means of evaluating the cylindrical co-ordinates for the basic problem of tubular current.

In 1960, Hammond (4) shows how Searl's (1) method of images can be applied to the end winding of electrical machines. A distinction is made between images in magnetic surfaces and in conducting surfaces, the two types being of opposing sign. The point being stressed is that in treating the field of a machine end winding, it is necessary to decide whether the eddy currents in the core end plates make the surface of these plates into a conducting sheet, or whether they are sufficiently inhibited to allow the end plate to act as a magnetic sheet.

In closing, Hammond warns that the method of images often requires measurements rather than calculation, and theorises that in problems involving low frequency currents near iron boundaries, the method is difficult to apply. It is also suggested that the method of images be confined to problems involving infinitely conducting boundaries. It is well to remember these warnings when studying the treatment of end winding by various other authors.

In the second part of the series of papers on the magnetic field of rotating machines, Hammond and Ashworth (60) in 1961 consider the end winding of turbo-generators. The actual conductors of the stator and rotor windings are replaced by current sheets, and the effect of iron in the vicinity of the windings is generally ignored.

The authors find that a turbo-generator end winding with its large cone angle of 30° to 45° and having a slant portion which is markedly spiral in shape cannot be described analytically without simplification.

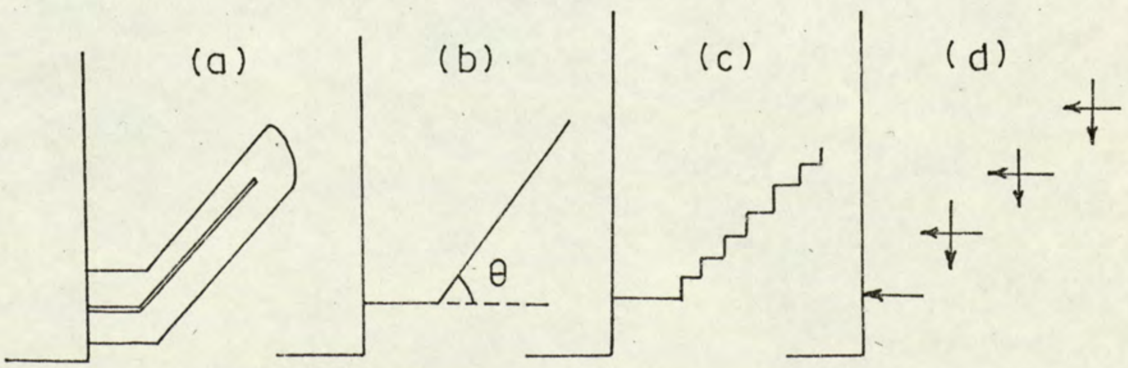

It will be seen from the above diagrams that the end winding has been simplified in stages until finally it can be considered as a number of finite cylinders and discs. The authors indicated that the number of components into which the winding is broken up is not critical, and that three should suffice. With six sections considered there is only a 2% difference between the results of the calculations. Further, in the final representation (d) it can be seen that the end winding has been broken up into a series of cylinders and discs which can in turn be replaced by a series of circumferential, axial and radial current sheets.

From curves of Hr and Hz, the radial and tangential components of field strength are shown to increase with increasing cone angle. This is consistent with the findings of earlier authors. However, we immediately find inconsistencies in the authors' findings on the influence of chording of the stator winding, and with the value Z (see below). Contrary to the authors' statement that Z increases with low cone angles, Z does not vary in practice for a given insulation level.

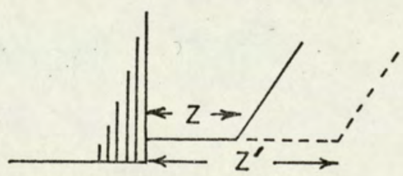

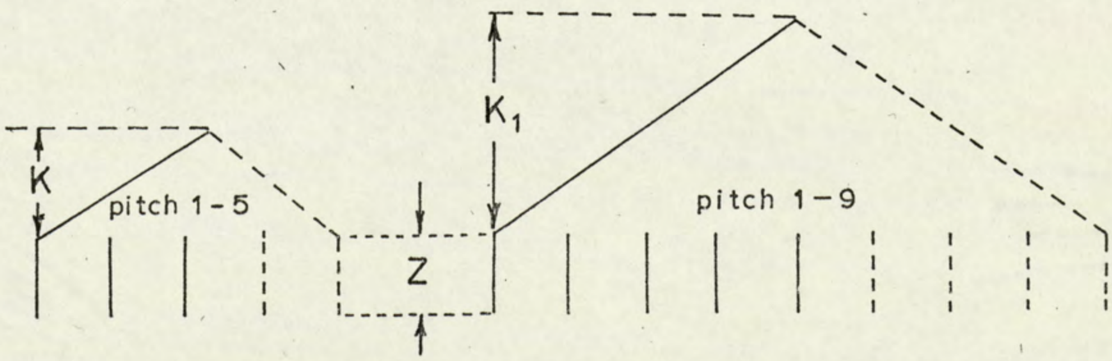

It is interesting to note that the effects of short pitching can be neglected, although this produces a reduction in overhang mass, as seen from the diagram. It is true, however, that if Z is increased then losses decrease as the winding slant portion moves further away from the stator core.

Lawrenson's (59) treatment of the end winding fields was published simultaneously with Hammond and Ashworth's. In his paper Lawrenson considers the magnetic field being set up by a number of finely divided current filaments consisting of small straight elements. The advantage of this approach is that the field at any point is found as the vector-sum of all the field components due to all the elements of the filament. These components are expressed simply in terms of the co-ordinates of each element and the co-ordinates of the point considered. It will be seen that all shapes of filament can be considered because any calculation requires only co-ordinates of a series of points on a filament.

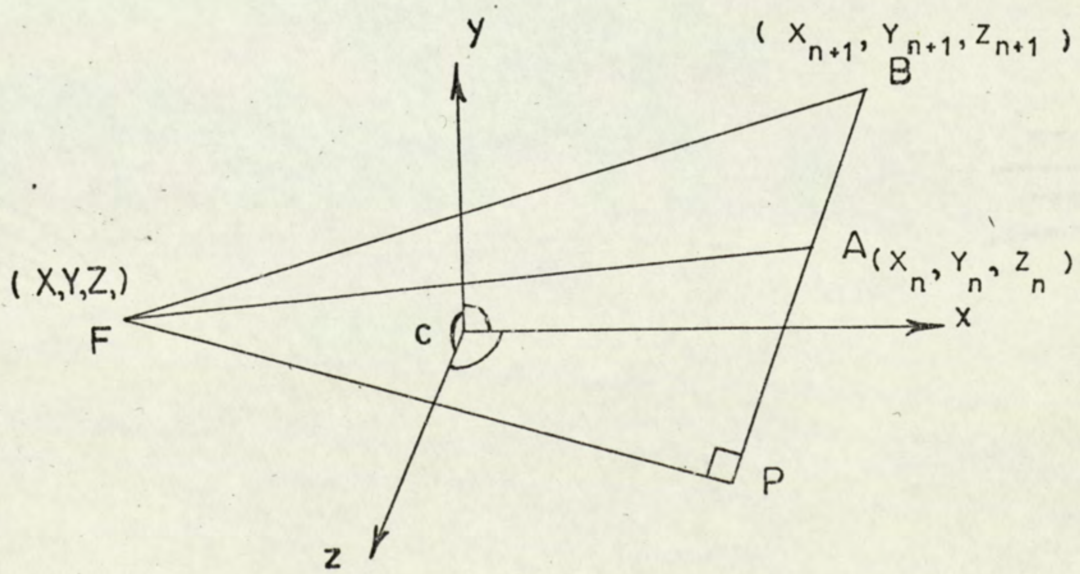

The figure shows a typical element A B (of some filament) with end co-ordinates $(X, Y, Z)_n$ and $(X, Y, Z)_{n+1}$ and a point F with co-ordinates (X, Y, Z). The field strength at any point F is given by using the Biot-Savat law and integrating between A and B. It has a magnitude given by:-

$$H = \frac{1}{4\pi} \times \frac{i}{FP} (\sin\theta_{n+1} - \sin\theta_n) \text{ at/m}$$

where F P is the normal from F on the element or its projection, and i is the filament current.

Lawrenson makes three boundary assumptions which are not strictly true, as his experimental work was based on a 6.5 MW air-cooled turbo-generator whose scaling bears no real relation to large modern hydrogen-cooled turbo-generators.

The first assumption is that end castings are thin and in regions of weak fields and can thus be ignored. There is at least one known instance of a 350 MW set where severe burning and damage was encountered in the shaft seal region. What appears to be forgotten is that many manufacturers use magnetic end discs with non-magnetic end bells. Thus, there can be strong end-field effects in the castings, which are usually made of 2-3 inches thick structural steel.

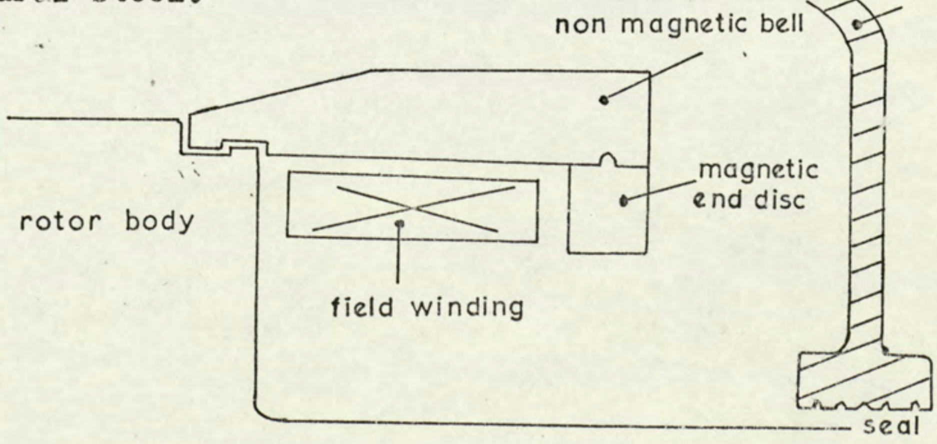

The second assumption considers the shaft as being small and far from the stator end winding, so that it also can be ignored. This is not true since often the magnetic end disc acts as a flux bridge between windings and shaft. Incidentally, field plots by various authors show that the shaft does have an influence on the resultant plot. The third assumption is that the clamp plate extends radially to infinity and that all other iron boundaries can be ignored. A quick examination of modern machines shows this to be untrue. In fact, at points, the end casing is sometimes closer to the endwinding than is the clamp plate, and must be shielded. Whilst Lawrenson presents a series of theoretical curves indicating expected variations in the three components of the field, there is no test or analogue evidence to substantiate these curves. However, the paper is of interest for the resolution of the problem into a series of current filaments which can follow the coil shapes more closely than any other method presented by earlier authors. It is believed that the filament representation is possibly acceptable for evaluating fields reasonably distant from the windings. If however the study is to include eddy copper losses, then due to the bulk of the coil sides, three filaments or more may be necessary for each coil, (see below).

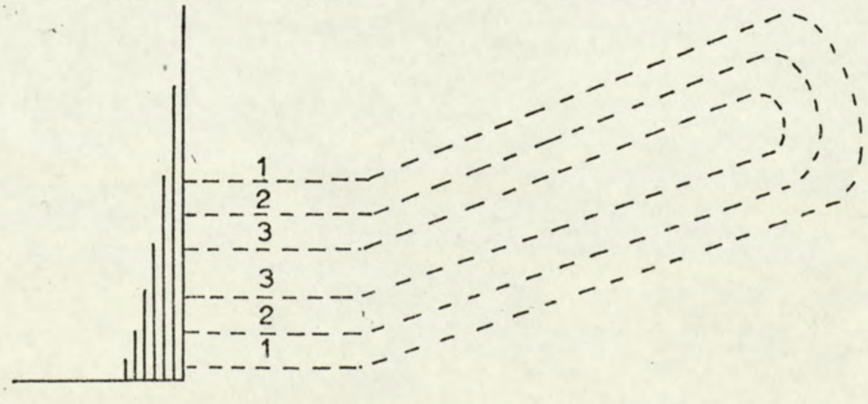

Early 1963 saw the first of a series of papers by Tegopoulos (61, 62, 64, 67) which, over the next five years covered the end zone of turbo-generators thoroughly. The first paper is devoted entirely to the mathematical representation of the stator and rotor end windings in the form of sinusoidal current sheets. These sheets are assumed to lie on cylindrical surfaces of radius P_i and P_m

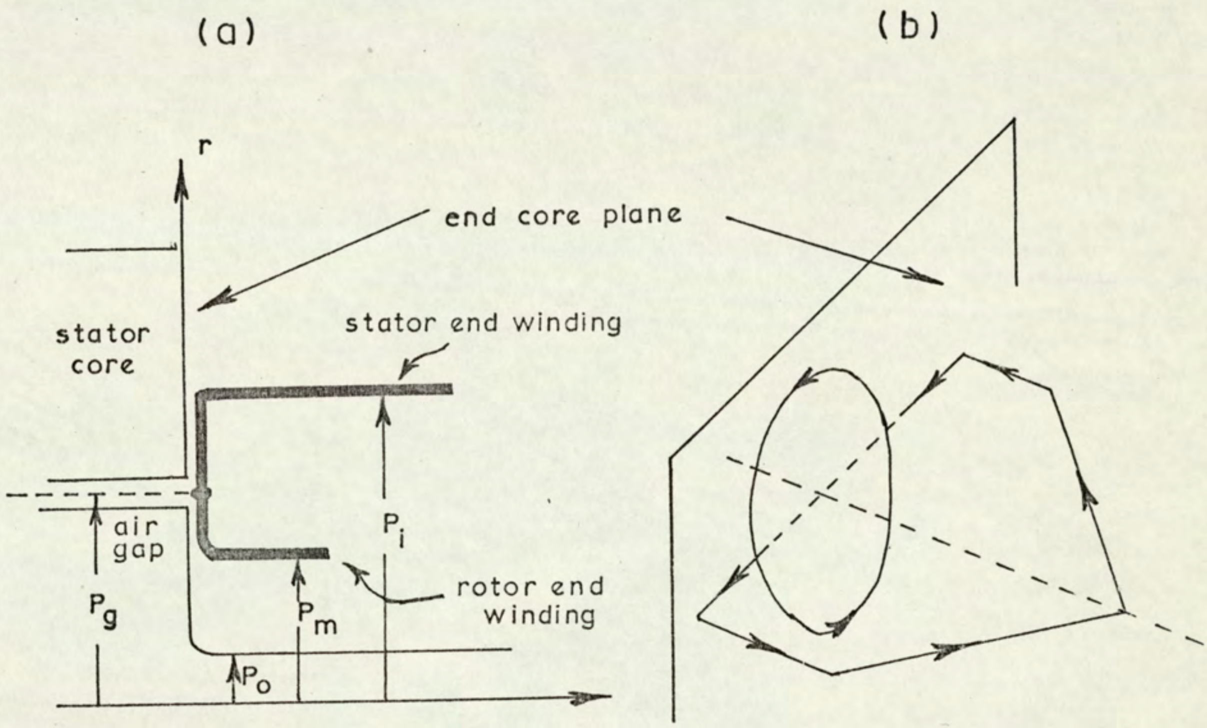

For P_i Tegopoulos follows Smith (56) in his arbitrary choice of magnitude. From a field point of view Tegopoulos feels that these approximations are justified for points reasonably far from the conductors.

The effect of the air gap is considered by assuming a return of the current in the end winding of the stator and rotor in the centre of the gap, or at a radius P_g. According to this assumption the end coils of the stator and rotor are considered to be closed circuits. In fig. (b) above, a stator end winding coil is shown schematically, as well as its fictitious return in the centre of the air gap and on the end core plane. Tegopoulos derives expressions for the stator and rotor current sheets for the four components listed below,

a) Radial current sheet.

b) Peripheral current sheet.

c) Axial current sheet.

d) A return current.

The derived equations are applicable to the fundamental components. Harmonics could be included by similar derivations, but Tegopoulos feels that this should not be necessary.

In considering the stator and rotor current sheets separately it must be remembered that both are rotating synchronously but that there is a phase difference between them depending on the power factor of the load. The paper is pleasing in that for the first time we see a fully developed theory put forward that appears simple in its presentation.

The second paper by Tegopoulos deals with flux impinging on the end plate of turbine generators only. It is assumed that there are no iron boundaries other than the end-core plates, which are also eliminated by considering the mirror images of the current sheet components as developed in his first paper. The conclusions are of particular interest, as Tegopoulos shows a very close agreement between calculated and test values of normal flux density on the core end plates for an Induction Motor. (Fig. 1.2 - 6). Bearing in mind that the author considers turbo-generators only, it is possible that the machine considered is a large two pole motor with a turbo-type

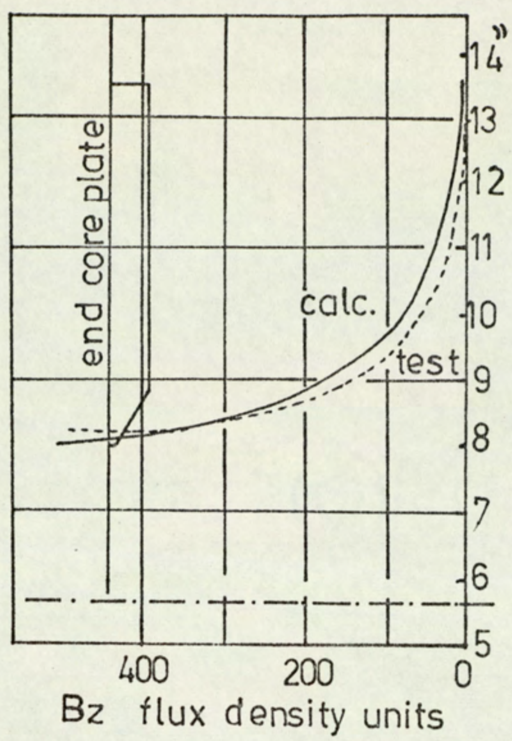

FIG 1·2–6

Ref : Tegopoulos (62)
normal flux density on end core plate of an induction motor, stator effect, no load condition

end winding. In passing it may be said that the assumptions of the end plate having infinite permeability and being non-conducting are probably justified for the machines considered by the author, as the machines had clamp plate shields (flux traps) made up of thin silicon iron stampings.

A third paper by Tegopoulos is devoted entirely to the analytical determination of the magnetic field in the end zone of turbo-generators.

It will be remembered that in his second paper the same field was determined only on the end core plate ignoring iron boundaries. As before the assumptions on which this paper is based ties the work to turbo-generators with non-magnetic end bells. When examining the field plots, illustrated in Fig. 1.2 - 7, it is apparent that the author has allowed for the presence of magnetic end discs as discussed when considering Lawrenson's work. It must be mentioned that Tegopoulos checks his analytical studies against two-dimensional flux maps by using resistive paper analogues. This is justified only because the author considers that there is axial symmetry. It is also indicated that the calculated flux densities for points in the neighbourhood of the actual conductors are not accurate and Tegopoulos attributes this to his use of a cylinder to replace the end winding. If this is true, then Smith's work on end copper losses must suffer from the same degree of error. It is suggested that this error can be reduced by replacing the end winding with a staircase Fig. 1.2 - 8a, made up of zones of partial axial and circumferential current sheets. This approach is similar to Hammond's and Tegopoulos actually uses it in his next two papers in 1966. At this point it appears opportune to refer to these papers,

FIG 1·2-7

TWO DIMENSIONAL FLUX PLOTS AS GIVEN BY TEGOPOULOS(64)

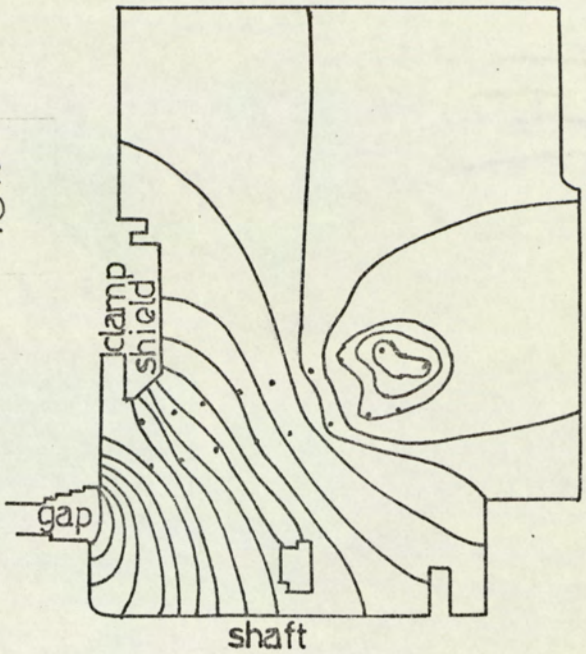

a) Stator Excitation only

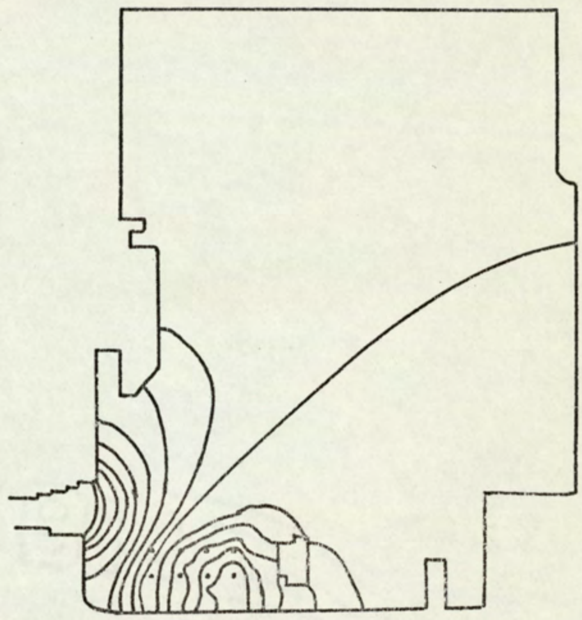

b) Rotor Excitation only

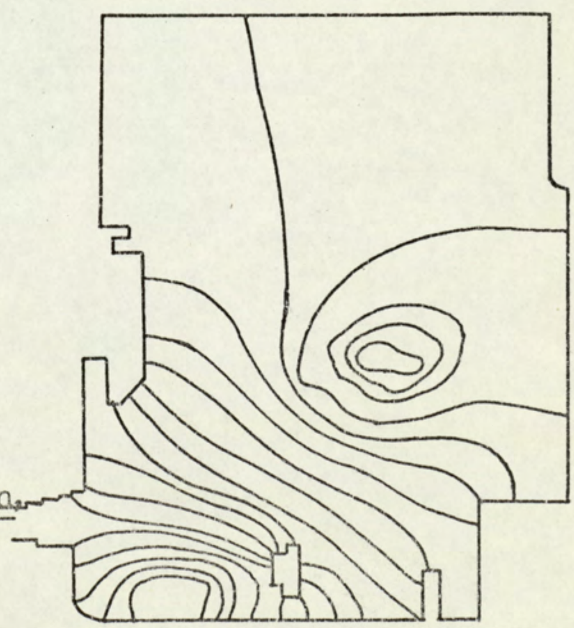

c) Stator and Rotor Excitation, Short Circuit condition.

FIG

1·2-8a

Ref: Tegopoulos.(67)

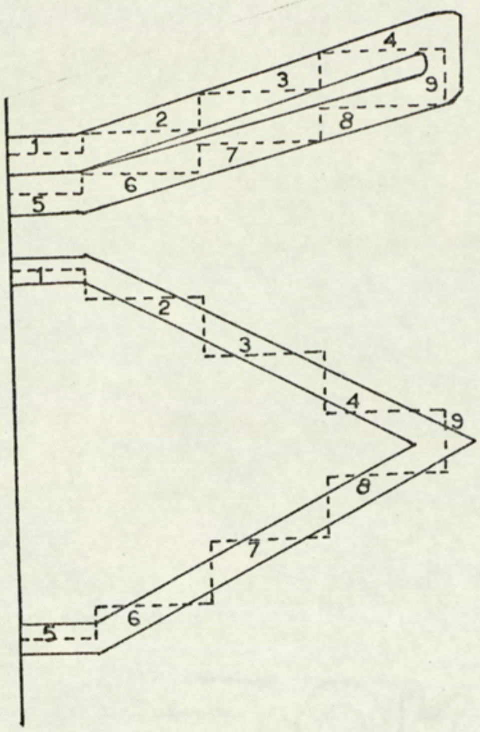

equivalent representation of coil overhang as given by Tegopoulos

FIG

1·2-8b

Ref: Oberretl.(63)

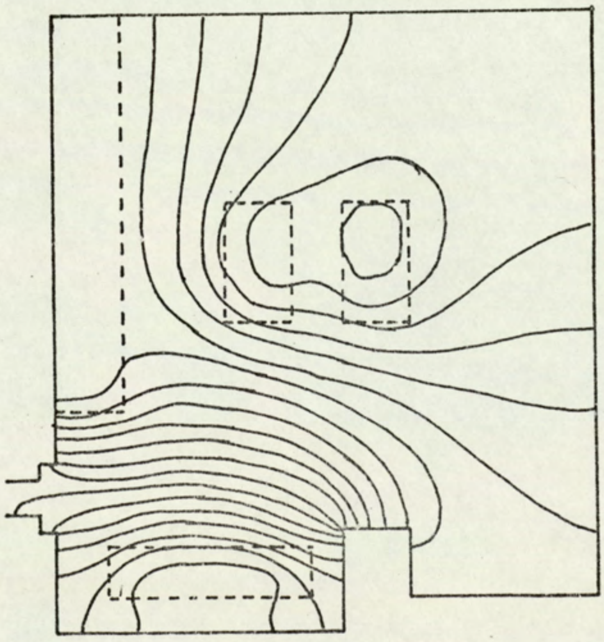

field plot determined on the lattice model for a machine on short circuit. bronze clamp plates.

which are on forces in the end winding, even though they were not published until 1966.

The electromagnetic forces exerted on conductors of the end winding can be determined on the basis of:-

$$F = I\,L\,B$$

where F is the concentrated force exerted at a certain point, lying on the centre line of a coil end, B is the flux density at the same point, L is the length of a coil segment in the middle of which the point lies and I is the current flowing in the coil. It will be seen that these papers are extensions of earlier work by Tegopoulos and as stated, he seeks greater accuracy when evaluating flux density on the conductors by turning to his step representation of the end winding. The present writer wonders whether Staat's method would not have been a better approach.

Up to now, we have considered the use of electrolytic analogues (Smith), resistive paper analogues (Tegopoulos) and actual end windings (Hammond). We find that Oberretl (63) in 1963 makes use of a lattice model made up of 5000 resistances and condensers. The treatment is restricted entirely to non-magnetic boundaries and leads to an expression and curves, Fig. 1.2 - 9, for losses in the clamp plates, axial and radial planes of the end guard. The use of different non-magnetic materials is allowed for by the introduction of electrical conductance into the loss equation. The winding cone-angles considered are 0°, 30° and 90°. Richardson's semi-empirical ratios of losses for varying cone-angles compare favourably with this work.

FIG 1·2-9

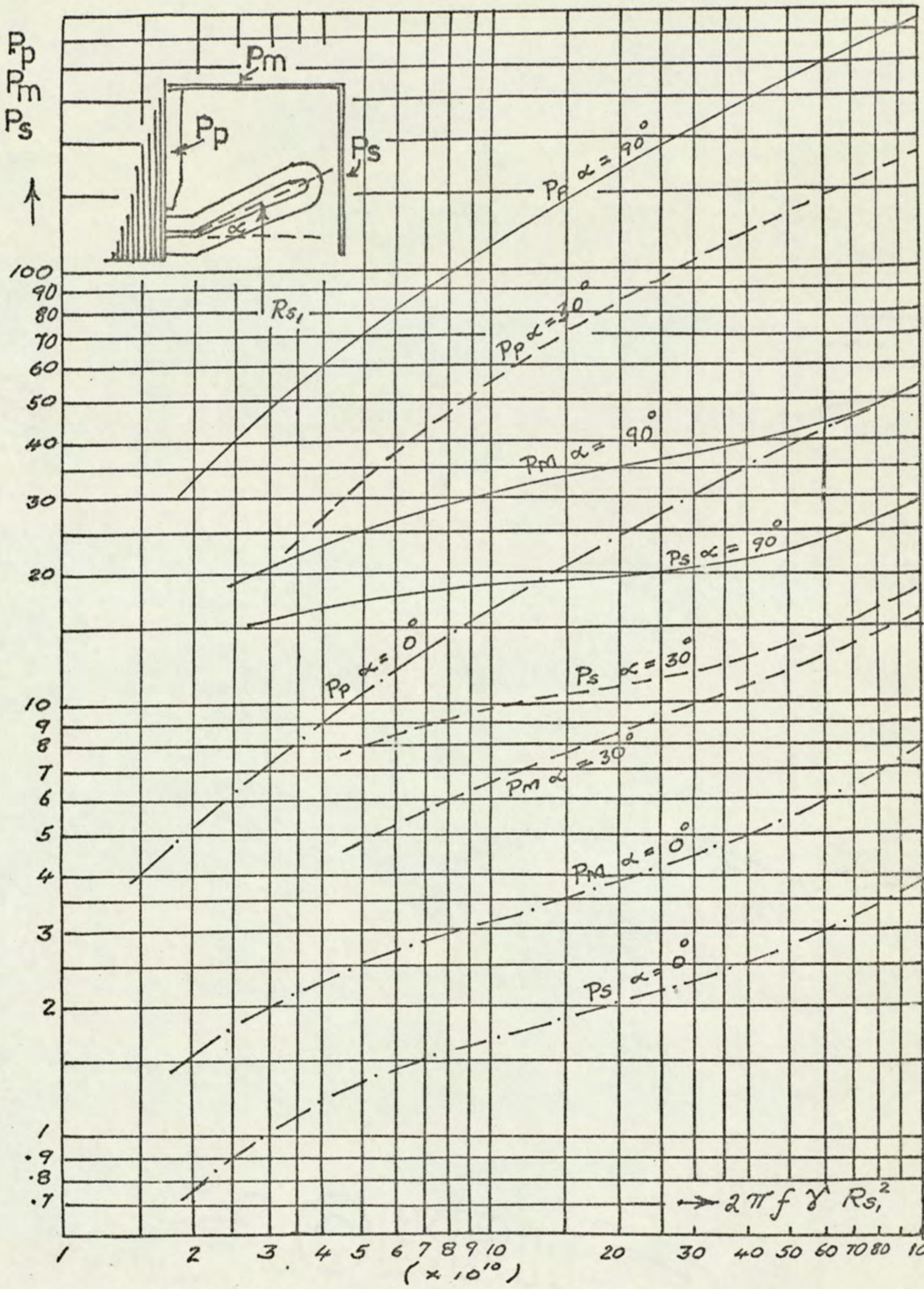

METHOD OF CALCULATING END REGION LOSS AS GIVEN BY OBERRETL (63)

Loss for both ends of machine, all boundaries non-magnetic,

$$W_{atts} = \frac{1}{R_{s_1}\gamma} (A_{max})^2 \{ P_p + P_m + P_s \}$$

f = frequency c/s. R_{s_1} = mean radius (cms)

A_{max} refer to page 219 . γ = electrical conductivity mho/cm

Oberretl takes Maxwell's equations for electromagnetic fields neglecting displacement currents. With the introduction of the magnetic vector potential and working in Cartesian co-ordinates in two dimensions, a partial differential equation is obtained, leading to the setting up of a lattice model for its solution, Fig. 1.2 - 8b. The presentation of results of this paper is such that the approach is similar to Liwschitz's work, no elaborate computation being required. When checked on typical salient pole machines the calculated values appear reasonable in magnitude. At this time of writing however, test values are not available for comparision.

In his article on magnetic fields, Althammer, 1963, uses the method of current sheet representation of windings as detailed by Hammond and Tegopoulos. The end-winding slant portion is treated as lying on a truncated cone, but each coil being considered as part of a helix before transformation. In general this paper offers nothing new and appears to be a repetition of earlier work, slightly modified.

Hammond's fourth paper is published jointly with Stoll in 1965. The main purpose of this paper is to investigate the relationship between magnetic fields and eddy currents. The authors consider a current sheet parallel to a conducting slab and modify their solution to cover the case of a semi-infinite slab. The equation for eddy-current loss is used for calculating stator clamp-plates loss. In the application to turbo generators and salient pole machines they find the following loss ratios:

	Loss Ratio	
Material	Turbo Type	Salient Pole
Magnetic	1.0	0.131
Non-Magnetic	0.404	0.164
Copper	0.045	0.0407

It seems odd to find that on the salient pole machine, the non-magnetic clamp plate has higher apparent loss than the magnetic clamp plate and it can only be assumed that the authors' methods are not truly applicable. Comparing magnetic end-plate loss in salient pole machines with turbo generators, a reduction from 1.00 to 0.131 is indicated. This again appears very large and judging from the fact that the salient pole machine has been attributed with a pole pitch of 20 cms. no other dimensions stated, the ratios given are of doubtful value.

In their fifth paper 1966, Stoll and Hammond specifically treat the problem of eddy current loss in the end plates. The authors are particularly interested in the effect of the field on a magnetic end-bell, which is treated as a tubular region of definite permeability. Earlier work considers the magnetic end bell as being infinitely permeable. The authors assign a linear magnetisation characteristic to all magnetic materials, i.e., $B = k H$. The writer feels that the authors should consider the magnetisation curves for magnetic materials as a smooth continuous function. (FIG. A.)

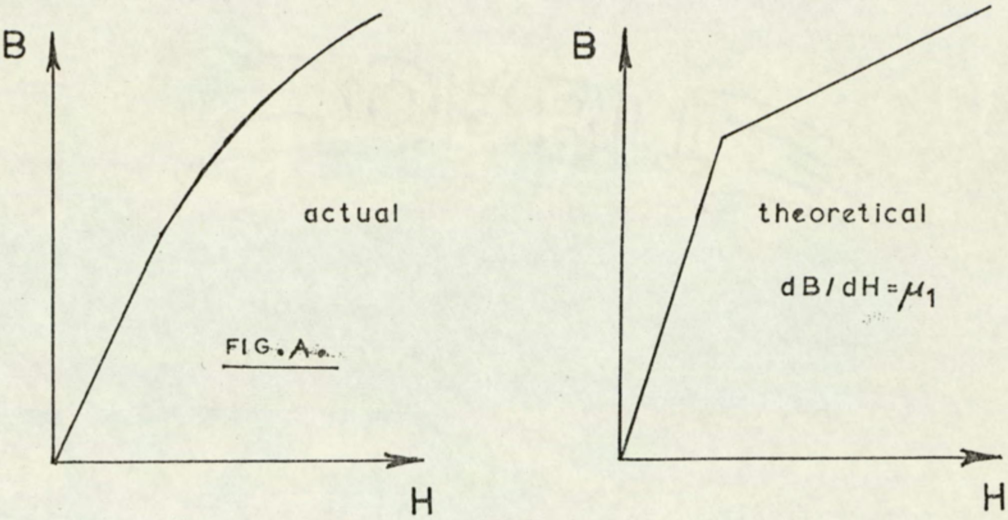

FIG. A.

If this is inconvenient at least a continuous function such as $B = m\,H^n$ should be used, as suggested by Davies (8) and Subba Rao (18).

However, if we accept the assumption of linearity, the problem is resolved into a series of cylindrical permeable boundaries. as shown below.

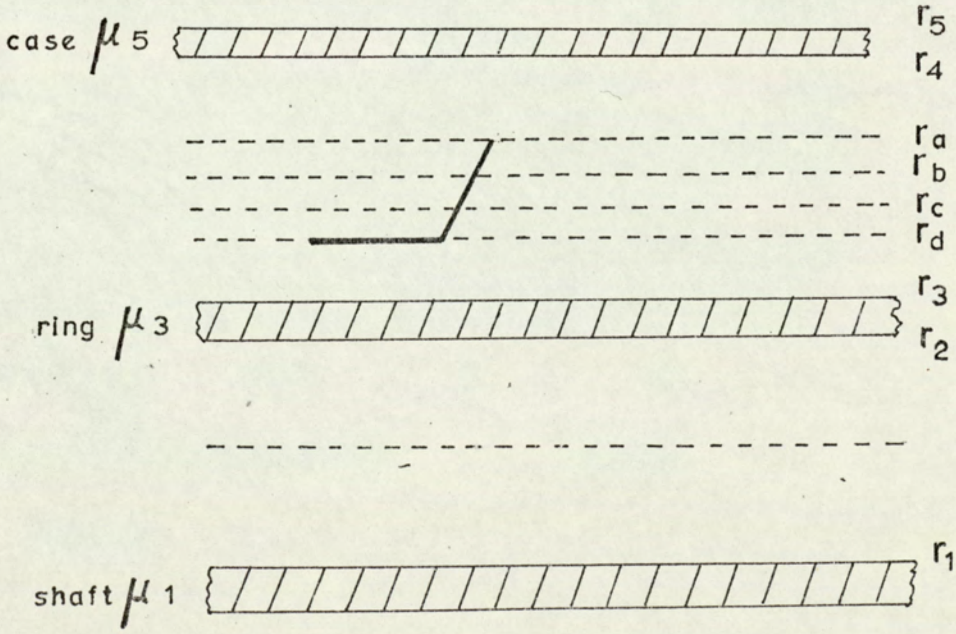

From their mathematical resolution of the above problem the authors obtain an expression for the clamp plate surface loss density in terms of the radial and circumferential field components.

$$P_e = \frac{\rho}{2\delta} \left(H_r^{\;2} + H_\theta^{\;2}\right)$$

where ρ = resistivity - ohm-metre.

and δ = skin depth - metres.

It is found that clamp plate loss reduces with diminishing cone angle, giving an approximate ratio of 2 to 1 for a change from 60^o to 30^o; this is comparable with Richardson's work.

In 1965, Reece and Pramanick (69) calculated the end region field in A.C. machines. As Lawrenson did, the authors consider the coil ends as consisting of a number of filaments but simplified in shape. The general simplification suggests that this work should be applicable to Induction and Salient Pole machines provided the boundaries are suitably modified. Again like Lawrenson, the authors consider that the end cover and casing do not contribute significantly to the generation of losses, and therefore neglect them. This cannot be true, and as seen in section 1.1, end-guard losses are not insignificant. To check their equations a model was used. The model was a small rotor-stator assembly wound with a single turn stator and rotor coil per pole. It is argued that since all coils in a 2-layer winding are identical, it is only necessary to derive expressions for the field produced by one coil per pole, and by assuming superposition, the field of a complete winding then obtained by applying a multiplier which is a function of an actual winding. From similar experiments documented in Chapter 5 of this thesis, it is seen that this assumption is likely to introduce considerable errors. If the authors are considering only two pole turbo-generators, then it may be possible to use a further multiplier which would correct any errors thus introduced. The authors claim that the use of their new equation for end-winding reactance has led to closer agreement between measured and calculated values of machine reactances.

As any study of clamp plates is not complete without some reference to shielding or screening this review will be terminated with a short study of the art. Attempts made to reduce heating and losses caused by the stray fluxes occurring at the ends of a generator are in general divided into three classes,

(1) by screening the metallic parts linked by the stray flux.

(2) by altering the properties of magnetic materials linked by the stray flux.

(3) by producing a magnetic field in opposition to that producing the stray flux.

When attempting to reduce clamp plate losses, only the first of these methods is usually considered. Methods of screening can be divided into two distinct classes.

(a) the provision of a low resistance screen in which the stray flux induces eddy currents, which in turn reduce the stray flux linking the parts being screened.

(b) the provision of a low reluctance path which diverts part of the stray flux away from the parts being screened.

Summarising the various views expressed on screening, there appears to be disadvantages, both when screening by means of laminated magnetic screens and by means of highly conducting screens. The use of a laminated magnetic screen adjacent to the stator winding to divert the fluxes away from the core end plate means that the reluctances of the path the flux originally travelled is reduced so that the amount of stray flux will increase. This additional flux could cause extra losses in the end windings themselves. However, the use of a laminated screen situated on the surface of the core end plate will probably only marginally increase the total stray flux. Conducting copper screens have the disadvantage that to be effective, very high currents must flow in these screens and due to their inherent resistivity, the resultant I^2R losses may be equal to or greater than the resultant decrease in losses in the core clamp plates. The current density in the screens is by no means uniform, the current tending to crowd into the edge of the shield nearest the bore of the machine, so that it is possible that a large part of the expensive and weighty screens are not used as conductors. However, due to the greater heat conductivity of copper, these screens can be more easily cooled thus they find a use as a form of heat sink on the surface of the clamp plate. With highly conducting screens, the eddy current loss tends to increase as the screen resistivity increases. Therefore, it is important to use very low resistivity material for the screen, and to ensure that no high resistance joints occur. Obviously, the usefulness of a low resistance screen depends on its own eddy current loss being lower than the reduction of loss in the parts being screened, as stated earlier.

Evidence as to the effectiveness of the various types of screening is very limited although it would seem that laminated screens offer more possibilities for loss reduction than do conducting screens. However, since the majority of the reported experimental work has been carried out on laboratory models it is impossible to draw any firm conclusions. Despite this, it is clear that as the machines increase in ratings, screening in one form or the other will be used.

Chapter II

2.0 Experimental Models.

Losses in core clamp plates are investigated in the present study by examining test results made on two experimental models. Thus a complex phenomenon is evaluated in such a way that the effect can be predicted for actual electrical machines. The success of such an extrapolation depends on the validity of the scaling rules used in transforming from model to machine. In this respect, difficulties arise because

(1) electromagnetic effects at boundaries between magnetic and non-magnetic, conducting and non-conducting materials may not follow the same scaling rules as the physical dimensions.

(2) parallel magnetic paths may be unavoidably out of proportion on the model.

(3) it may not be possible to account for magnetic saturation on a similarity basis.

These difficulties may account for the fact that fully scaled physical models are rarely used in solving problems in rotating electrical machines. Considering clamp plate losses, the problem of designing an acceptable model is somewhat simplified. The requirement is a typical end winding and adjacent clamp plate surface which together, must have representative profiling. Also, a main magnetic circuit similar to actual machines is necessary, to ensure similarity of end-region fields. Thus the model consists of a wound stator core formed of slotted laminations, and an un-slotted laminated rotor pack. Rotation is not required, so that the rotor is supported by air-gap wedges, which also ensure a uniform air-gap. For structural reasons, the stator is carried in a mild steel plate frame of minimum dimensions.

This construction allows the model to represent both salient pole sychronous machines and squirrel-cage induction motors, although it is recognised that the model does not simulate possible rotor winding effects. It is believed that at the clamp plate surfaces, the effect of rotor winding m.m.f. is negligibly small. Two model assemblies are shown in the photograph Fig. 2.0 - 3.

The study of clamp plate loss adopted follows two distinct paths;

(1) Evaluation of clamp plate loss from tests carried out on models.

(2) Investigation of flux density distribution on clamp plate surfaces.

The input power to the model stator winding consists of

(a) stator winding copper loss
(b) clamp plate loss
(c) stator and rotor core iron loss

If the winding is designed such that supplementary copper loss is minimal and can be neglected, loss (a) can be calculated and extracted from the total measured loss. By having two models, identical in every respect except core lengths, loss (b) can be considered equal for both models, and loss (c) can be considered proportional to core length. Thus at any given current taking the core lengths to be in the ratio 3:1, and letting W_1 and W_2 be the input power corrected for basic copper loss, for the short and long core respectively, then

$$W_1 = \text{Iron loss} + \text{Clamp plate loss}$$

$$W_2 = 3 \times \text{Iron loss} + \text{Clamp Plate loss}$$

$$\boxed{\therefore \text{ clamp plate loss } = \frac{3W_1 - W_2}{2}}$$

Thus, having obtained tha clamp plate loss from the models, the result would be proportioned dimensionally for direct use on actual machines.

The clamp plate surface flux density studies were carried out by means of Hall effect probes. In view of the fragility of these probes, it was necessary to design suitable mounting jigs, which enabled the flux density to be measured radially, axially and circumferentially.

The models and Hall-probe jigs are shown in photographs, Fig. 2.0 - 1 to 3. Fig. 2.0 - 1 shows the end view of the short-core model; points to be noted are,

(a) the stator winding overhang, with its finely stranded conductors.

(b) Hall probe jig located at the shaft centre and capable of circumferential movement. This jig is toothed (See Fig. 5.2 - 6) and carries six probes for measuring axial and radial flux densities in the vicinity of the stator teeth.

(c) Hall probe jig located on a circumferentially slotted carrier mounted on the stator frame. This jig carries ten probes for measuring axial flux densities either on the core or clamp plate radial surface.

Fig. 2.0 - 2 shows a close-up of the third jig, designed to carry the single probe shown in position on the clamp plate. Half the clamp plate is removed to show the half-lap joint and the bevel. Points to note on the single-probe jig are:

(a) dovetail slot on horizontal carrier to allow axial movement.

(b) Slit on vertical carrier to allow radial movement.

(c) the stator frame-mounted carrier (see also Fig. 2.0 - 1) which allows circumferential movement of the jig assembly.

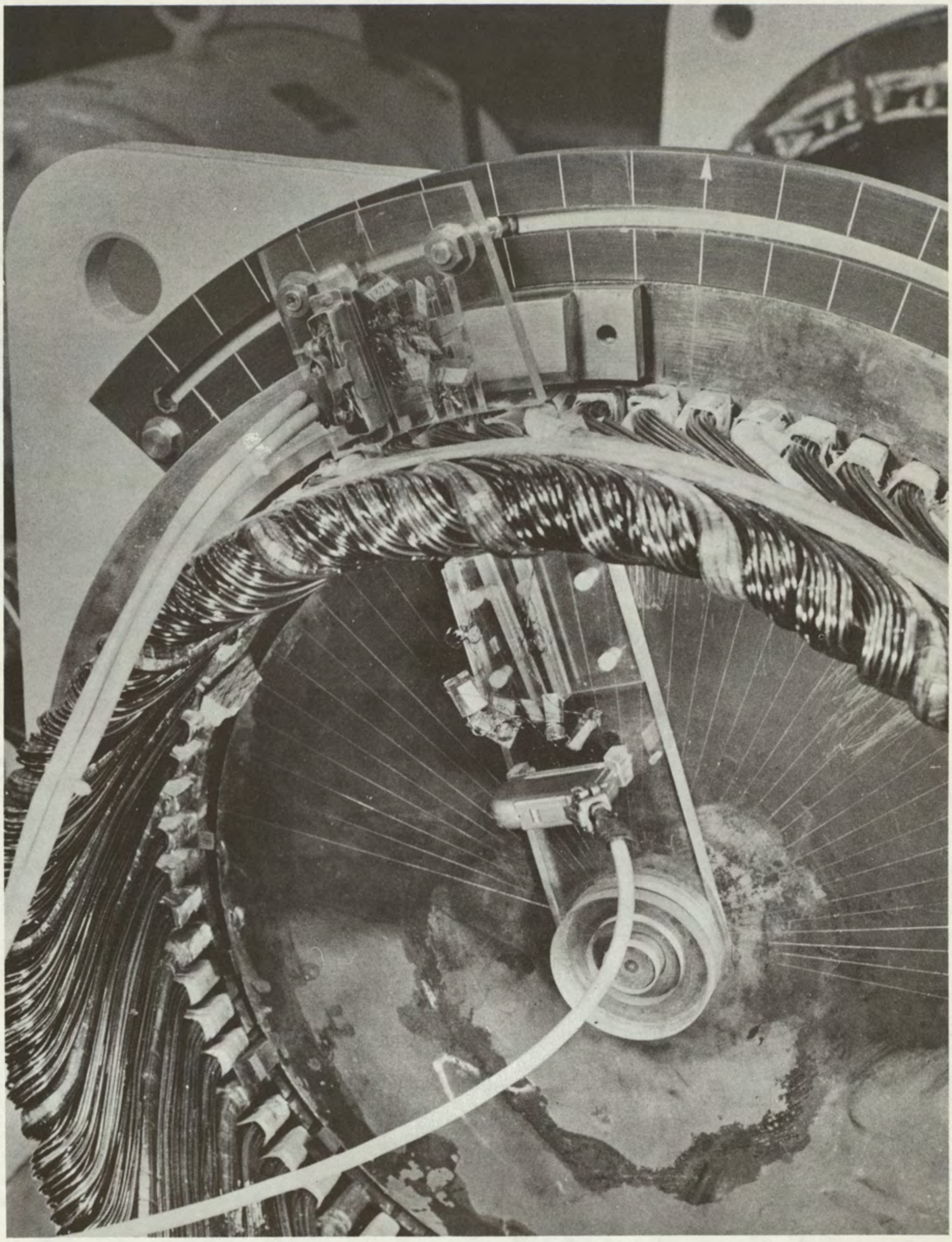

FIG 2·0-1

SHORT CORE STATOR WITH HALL PROBE JIGS IN POSITION. NOTE HALF LAP JOINT ON CLAMP PLATE.

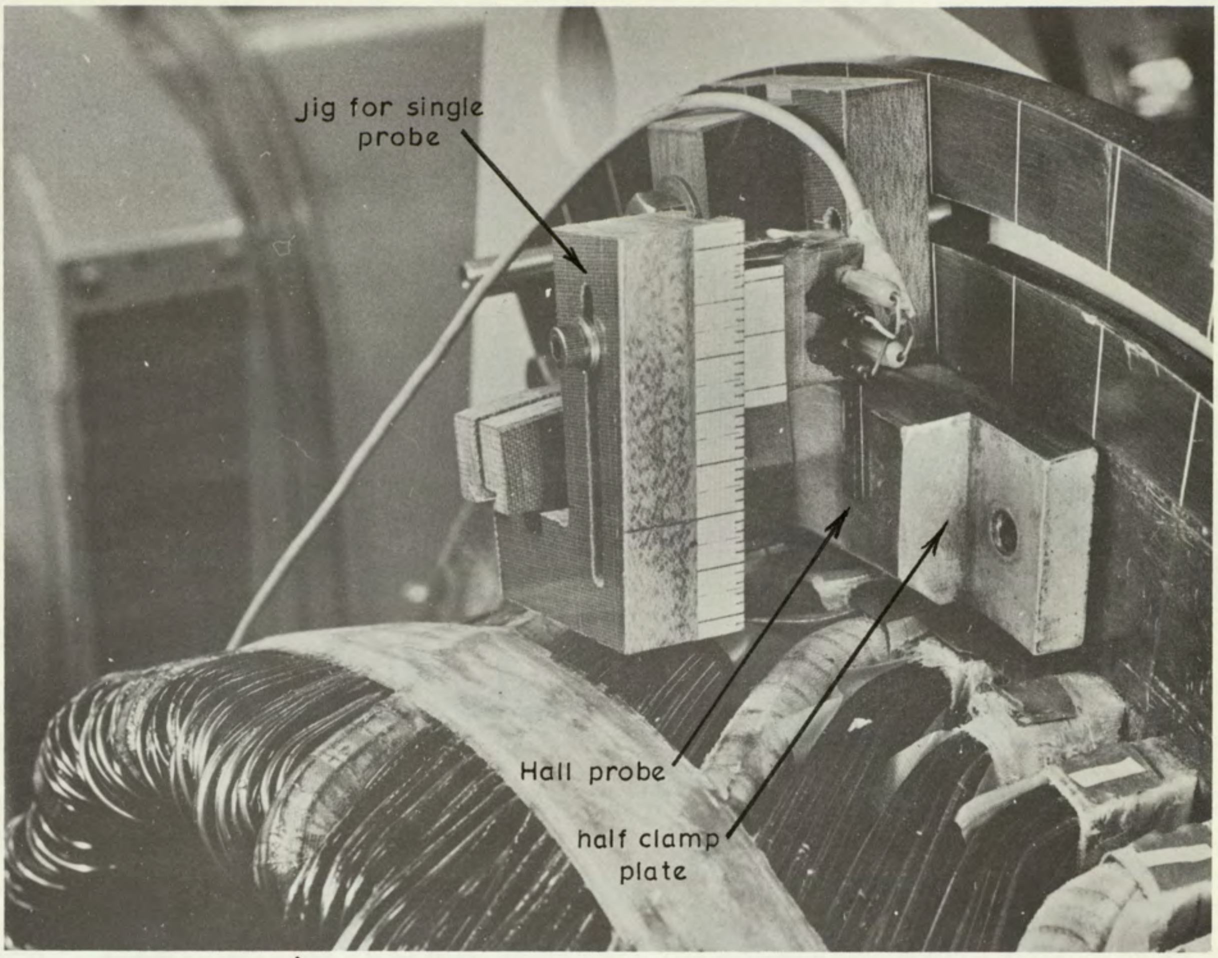

FIG 2·0-2

FIG 2·0-3

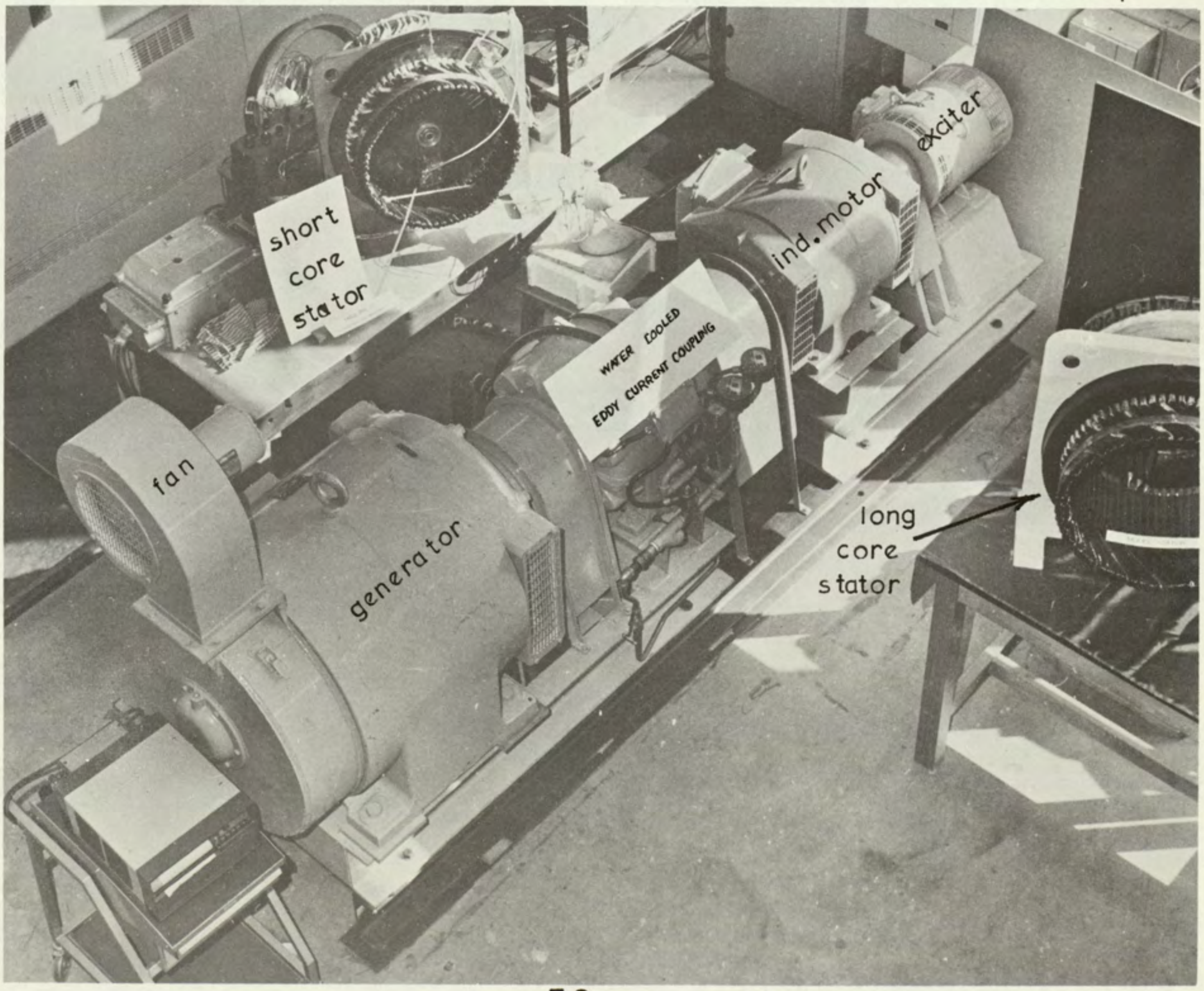

Fig. 2.0 - 3 is a general view of the motor-alternator set used to give a variable voltage and frequency supply, and shows also the two models. Note thin plate frames on the models.

2.1 Design of Model Stators

Having made the decision to use two experimental stators on which the various clamp plates would be mounted, the design of the windings had to be carefully considered. It was necessary to establish the power supply availability, before establishing the frame size of the model stators. Preliminary checks soon indicated an upper limit in the region of 200 Amperes 3 phase 415 Volts at 50Hz. With this in mind, the starting point was taken to be the core lengths, 50mm and 150mm being considered. At the time of design, it was felt that a working loading of 525 Ampere conductors per centimeter (AC/cm.) would be sufficient to produce measurable clamp plate losses. Working at a maximum air gap density of 0.7 webers/square metre a few preliminary calculations quickly showed that an existing standard stamping would be suitable. The stamping had the leading dimensions given in Fig. 2.1 - 1, which gave an AC/cm of 535 and air gap density of 0.675 wb/m^2.

The magnetic loading in the iron circuits was deliberately kept at a low level to ensure that the majority of the ampere turn requirement lay in the air gap. The resultant larger than normal air gap of 10mm. is more compatible with large sychronous machines working at 525 AC/cm loadings. The 470mm. bore design normally operates at 375 AC/cm with air gaps between 2.5 to 4.0 mm.

The stator and plain disc rotor stampings were blanked from a medium resistance silicon sheet 0.020" thick. The stampings were carefully deburred, insulated and glued together with a thermo-setting epoxy resin, thus avoiding the need for any through-bolts. The back of the stator pack

Stamping Details FIG 2·1-1

(To Scale)

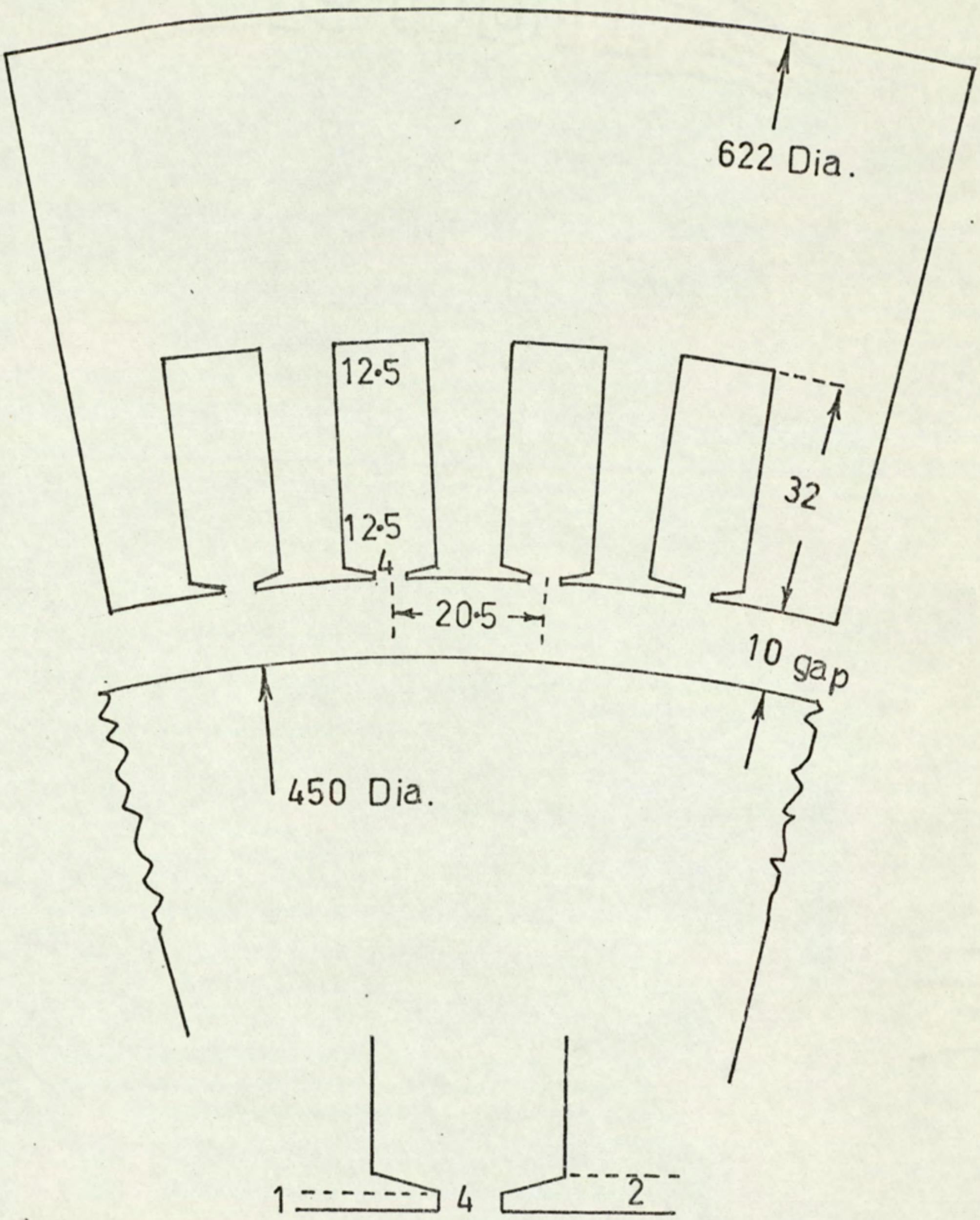

Slot Detail.

Enlarged.

All dimensions are in millimetres.

however, has three equally spaced axial seam welds to secure it. The stator pack is held in a narrow mild steel plate frame, Fig. 2.1 - 2, and is separated from the frame by a 6.5mm. radial air gap. Brass wedges hold the pack securely in the frame. With this construction, it was hoped that iron losses and leakage into the stator frame could be kept to a minimum.

The 72 slot stamping was chosen to ensure a balanced six pole three phase winding that could be short pitched 83.3% which results in a rotating m.m.f. having a low harmonic content; also, a balanced m.m.f. pattern over every pole pitch is obtained. The windings in this frame size are normally of the bar (strip) type, with single conductor depths of 13m m. in the radial direction. This gives a commercially acceptable level of eddy current loss in the slot copper. It was felt that this level was not acceptable in the model as eddy current losses in the stator conductors would be difficult to extract with any degree of confidence from overall test figures. A six conductor per slot winding with 9 strands per conductor of $14\frac{1}{2}$ S.W.G. round wires was selected. Normal manufacturing pactice discourages the use of more than 6 strands per conductor due to the difficulty of jointing between coil ends. However, to ensure good joints, the 18 strands in each joint were cleaned, seperately tinned, then bound together with tinned copper wire and the whole joint flooded with soft solder. The star-point was similarly made by staggering the joints between pairs of phases. Subsequent testing showed no hot joints, indicating that no erratic loss generation would occur in the joints. The winding end dimensions and connection details are

Stator Pack Details. FIG 2·1-2

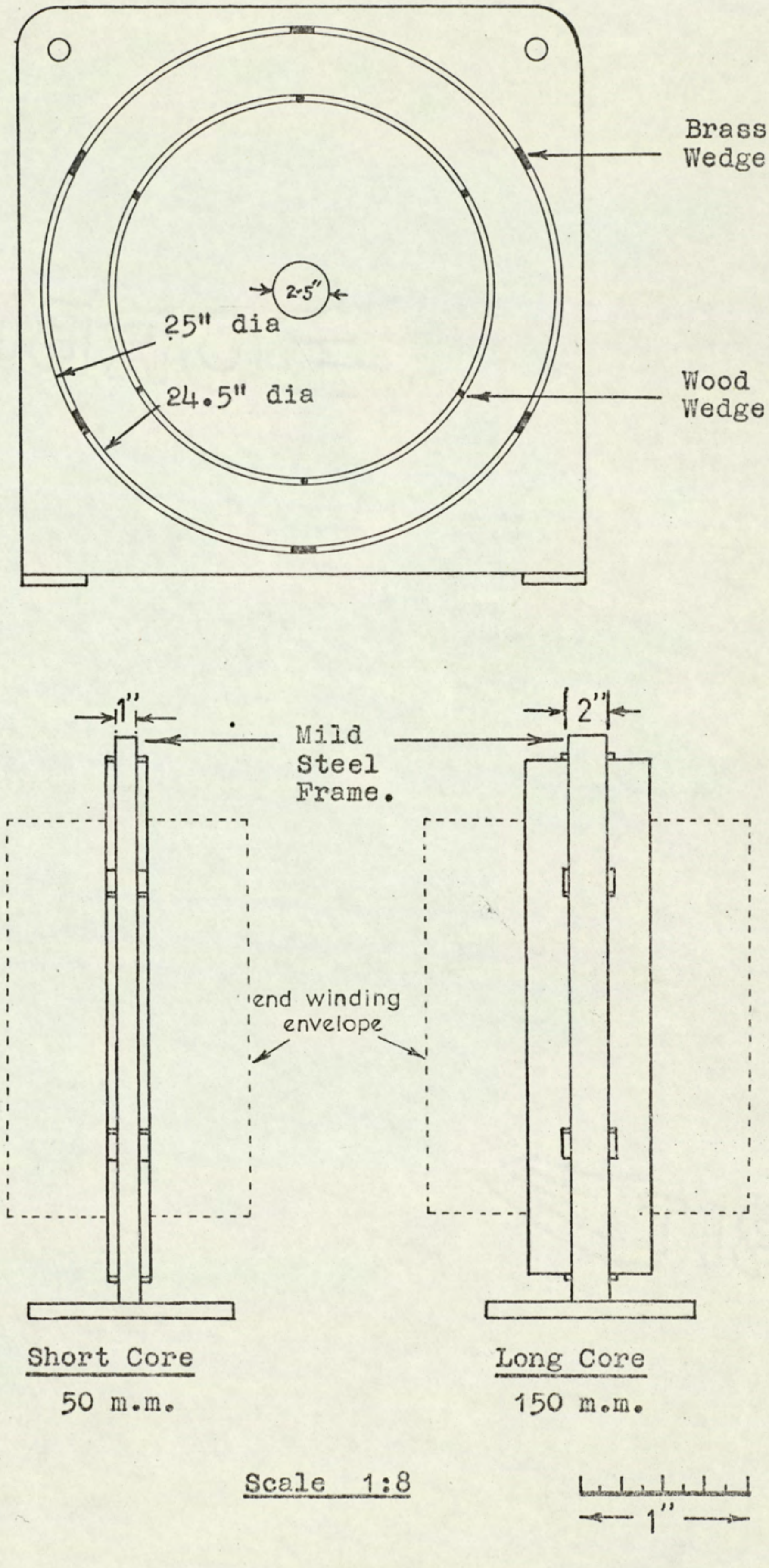

given in Fig. 2.1 - 3.

Due to the high AC/cm loading and also high degree of conductor subdivision, the quantity of copper in the slot was limited giving current density of 6.95 amp/mm^2. Normal design practice is not to exceed 5 to 5.5 amp/mm^2 on a continuously rated rotating machine. With a short-time rated static model, and assuming that eddy current losses in the copper would be far lower than in the conventional windings this value was considered acceptable. As seen later, this value was raised to 9.1 amp/mm^2 giving a 0.5°C per second rate of temperature rise.

Design Calculations

The following calculations are based on the 50 mm core length. The longer core would be proportioned directly.

1) Resistance Calculation

$$\text{Res/ph} = \frac{0.0173 \times 0.458\text{m} \times 144}{26.28} = 0.0435 \text{ Ohm}$$

2) Reactance Calculation ref: Kuhlmann (38)

$$W^2 f\ 10^{-8} = 432^2 \times 50 \times 10^{-8} = 0.09325$$

$$\text{Slot permeance} = \frac{26}{3 \times 12.5} + \frac{3}{12.5} + \frac{1}{8} + \frac{1}{4} = 1.308$$

$$\text{Slot Reactance} = \frac{.09325 \times 50 \times 1.308 \times .875 \times .238}{72}$$

$$= 0.176 \text{ Ohms}$$

$$\text{End Wdg. Reactance} = \frac{.09325\ (25 + 64) \times .966^2 \times .0885}{6}$$

$$= 0.1145 \text{ Ohms.}$$

Total Primary Reactance = 0.1760 + 0.1145 = 0.2905 Ohms.

3) From iterative trial calculations, it was estimated that a current of 170 amps would flow if a balanced 3 phase 120 volts per phase 50 Hz supply was impressed across the stator terminals.

FIG 2·1-3

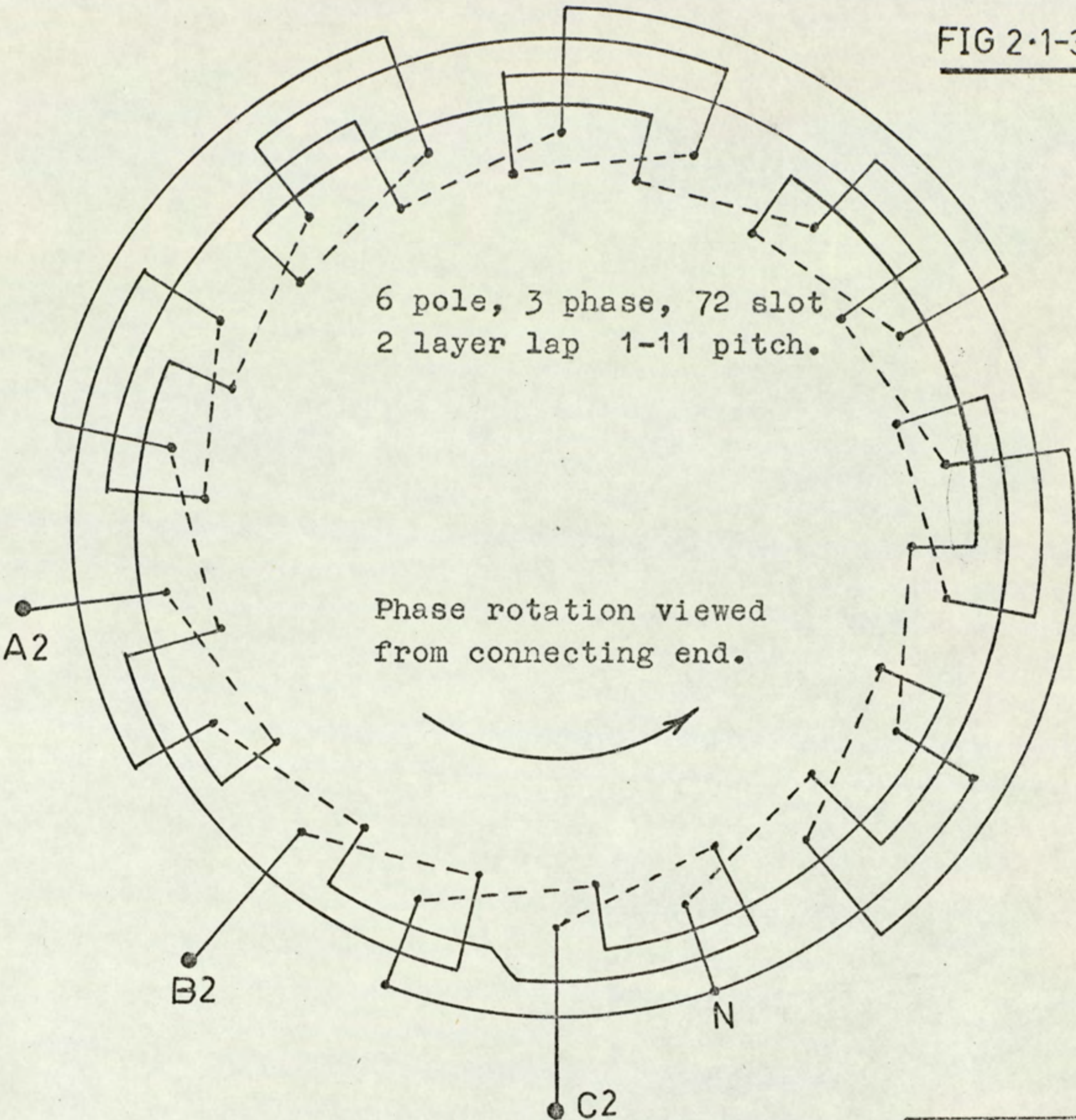

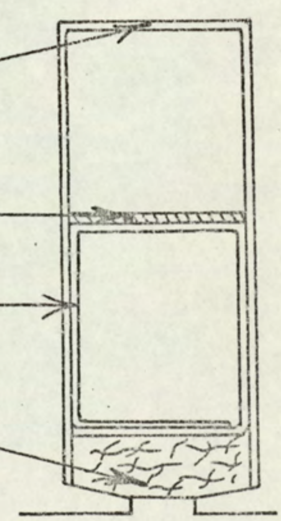

Scale 2:1

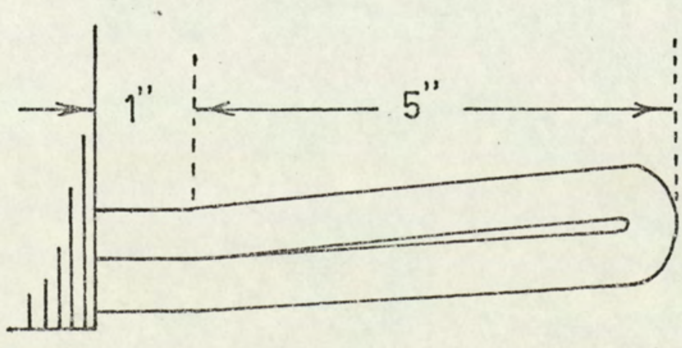

Scale 1:2

WINDING DETAILS FOR
THE MODEL STATORS

4) Magnetic Calculation (Final iteration)

Try 170 A/ph

$E_{flux} = 120 - (170 \times .2905) = 70.5V$

$\text{Flux/pole} = \dfrac{70.5}{2.22 \times .956 \times .966 \times 144 \times 50} = 0.00477 \text{ Wb.}$

$B_{gap\ (av)} = \dfrac{0.00477}{0.01205} = 0.396 \text{ Wb/m}^2$

$AT_{gap} = 1.28 \times 0.3960 \times 0.0796 \times 0.01015 \times 10^7 = 4100$

$I_{gap} = \dfrac{4100}{1.025 \times 24} = 166.5 \text{ Amps a.c.}$

Path	Density Wb/m^2	AT/m	Path lt. m.	AT.
Core	1.15	300	0.10 1	30
Teeth 60°	1.14	300	0.03 2	10
Rotor Ignored:			Total	40

$I_{MAG} = \dfrac{4140}{1.025 \times 24} = 168.3 \text{ Amps a.c.}$

The iteration was concluded at this level. The above resistance and reactance values indicate a power factor of 0.07.

From experience it can be assumed that the actual power factor will not be better than 0.1 lag. This fixed the power requirements at

120V/ph 170 A/ph P.F. 0.1 for the short core giving 61.25 KVA, and approximately three times this value for the long core.

As the power supply was modified at a later date by the purchase of a 200 KVA 3 ph motor - generator set, the original limitations imposed on the design of the model stators no longer held true. It was decided to leave the design of the models untouched. Subsequent requirements of a higher load current, up to 240 Amps, fully extended the motor generator set.

2.2 Design of clamp plates.

The design of the clamp plate dimensions depends on the magnetic conditions at the clamp plate surface in the model being representative of a typical range of machines. Since the important parameters are surface flux density and resulting effective loss per unit surface area, the inside diameter of the clamp is not important. Neither is the outside diameter, provided the ratio of winding overhang length to core depth is representative. The axial thickness depends invariably on the mechanical requirements of clamping the core, and cannot be easily fixed for the model. However, it is suggested that depth of penetration is an important parameter, and a clamp plate thickness at least equal to the depth of penetration was chosen. The relevance of increasing the axial dimension above this limit forms part of the present investigation. As it was decided to base the design on the depth of penetration, a problem arose. Classical formulation (ref: 9, 10, 11) used to compute eddy current losses in magnetic materials are derived from equations based on the condition of constant permeability. This assumption is unfounded since in each cycle the permeability of modern materials will undergo changes of at least 1 to 100. It can therefore be expected that large differences of losses can occur between calculated and tested values based on classical formula. This led to a search in all existing published literature and data to decide on the maximum value of surface flux density that could be expected on the clamp plates face. This value appeared to be in the region of 0.2 to 0.25 webers/m^2. The formulation finally used was

$$\delta = \left(\frac{\rho}{\pi f} \times \frac{Hm}{Bm} \right)^{\frac{1}{2}}$$

where

δ = depth of penetration metres.

f = frequency Hz

ρ = resistivity ohm metre.

Bm = flux density Wb/m^2

Hm = peak magnetisation Amp/metre.

Initially, five commonly used clamp plate materials were considered, Mild Steel (EN 4A), Meehanite G.E., Brass, Cast Aluminium and No-du-mag, a very high resistivity (ρ = 1.0 - 1.2 ohm - m) non-magnetic cast material. It was found that on the basis of the above formulation, it was impractical to use No-du-mag as a thickness of over 7.1 cm would be required. The Brass and Aluminium plates required depths of 1.75 cm. and 1.21 cm respectively which were considered practical, and a common casting pattern having a 2.5 cm thickness was decided upon. The magnetic materials required thicknesses of 0.15 to 0.25 cm over the working range of flux density considered. The mild steel plates were made a ¼" thick solely for mechanical handling purposes, whilst the meehanite plates were cast to the same pattern as the non-ferrous plates. At a later stage when evaluating initial test results it was felt that a mild steel plate having the same cross-section as the three castings was necessary. This was obtained and included in the test programme. When considering the two magnetic materials it was noticed that the magnetising characteristics were very dissimilar Fig. 2.2 - 1. It was felt that these differences could be of importance, particularly the lower saturation level and higher resistivity of meehanite compared with mild steel.

In deciding to use the depth of penetration as a basis for design, it is implied that the radial surface of the clamp plate is of most importance. Subsequent phenomena observed during testing has shown that this is not true. It is felt that the inner axial surface of the clamp plates also contributes to losses, particularly if the radial clearance between the winding and clamp surface is small. To test this latter point a set of $\frac{1}{4}$" plates with varying radial clearances was manufactured. The cross-section of all the plates used is given in Fig. 2.2 - 2, the more significant properties being listed in Fig. 2.2 - 3. In passing, it will be noticed that all the test plates have a radial depth greater than the depth of penetration.

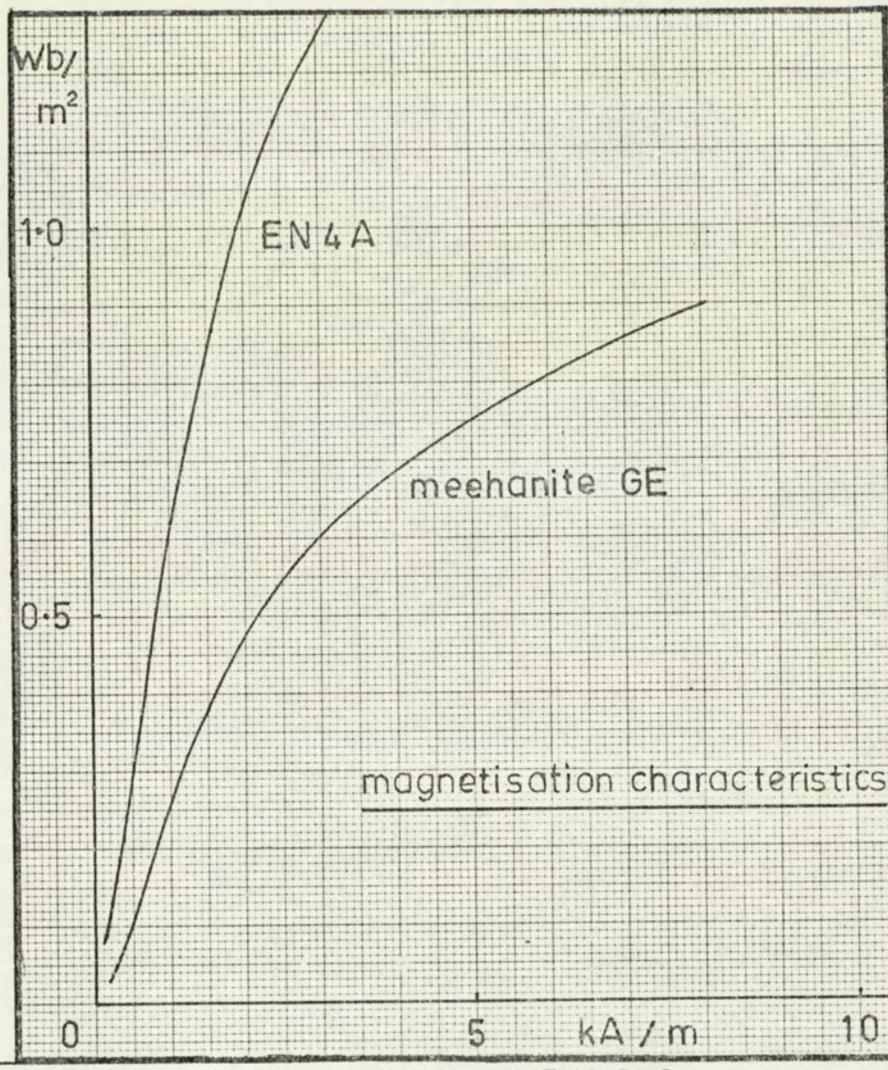

FIG 2·2–1

CLAMP PLATE DIMENSIONS

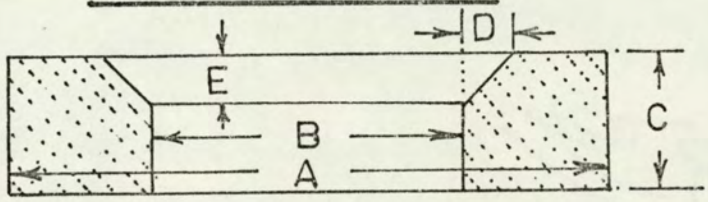

all cast rings and bevelled mild steel.

A	B	C	D	E
24·5"	21·5"	1·0"	8 mm	10mm

FIG 2·2–2

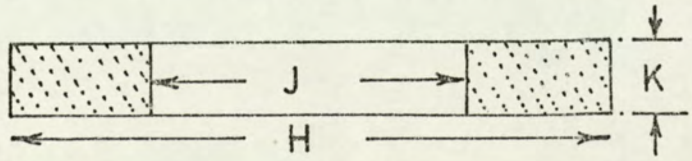

mild steel rings - no bevel

type	H	J	K	radial clearance
1	24·5"	21·5"	1"	6·05 mm
2	24·5"	21·5"	1/4"	6·05 mm
3	24·5"	21·125"	1/4"	1·28 mm
4	24·5"	21·875"	1/4"	10·80 mm

Material Specification

Type		A Cast Si Aluminium	B Cast Brass	C Mild Steel	D Meehanite
ohm/cm^3 x 10^{-6}(20°C)	ρ	2.83	7.50	18.0	70.0
Temp. coeff of res. 0-100°C	$\propto$	.0039	.002	.003	.002
Chemical analysis per cent.		Si 11.5	Sn 9.5	C 0.26	C 3.2
		Fe 0.6	Zn 0.05	Si 0.13	Si 1.7
		Mn 0.5	Pb 0.25	Mn 0.74	Mn 0.9
		Al remainder	P 0.25	S 0.035	S 0.1
		excluding 0.75 % residues	Cu remainder excluding 0.3 % residues	P 0.04	P 0.2
Ult Strgth. T/in^2		10.5	15	29.5	28
B.S.S.		1490/1963	1400/1961	970/1955	-
Quality		LM 6 - M	PB 3C	EN 4A	G.E.

FIG 2·2–3

2.3 Power - Instrumentation

At a very early stage in the general survey of problems that had to be considered, it was apparent that the instrumentation for power measurements required careful attention. From the design of the model stators a quick summation of expected losses ignoring possible clamp plate losses gave a wide range of requirements.

Power: On the short core the power loss varied from 2 to 6 kilowatts at 0.04 to 0.08 power factor while on the long core, 3.5 to 12 kilowatts at 0.03 to 0.06 power factor.

Current: 0 to 240 amp, virtually sinusoidal over the range.

Voltage: 0 to 300 volts between lines for the short core and 0 - 700 volts on the long core.

The measurement of voltage presented no problems, due to a good selection of meters available in the laboratory. The current range offered problems in so far that current transformers had to be used with virtually no phase angle error. This was resolved by purchasing two current transformers with a 1200/5 ratio with a single conductor threaded through the window. Thus by using an ammeter with 1 amp scale, full scale deflection was obtained at 240 amp.

Power measurements presented the greatest difficulties. Due to the very low power factor two special wattmeters had to be purchased, it being decided to use the two-wattmeter method of measuring power. An added advantage is that from curves and the ratio of readings, power factor is quickly obtained. This was checked against the value obtained by dividing kilowatts by kilovolt-amps. All sets of readings giving power factor by the two methods differing by more than 4 to 5 percent were rejected and retaken immediately.

The basic wattmeter had voltage ranges 0 - 150, and 0 - 300, with 5 and 10 amp series/parallel current coil connection with a 20% overload on any scale. For all readings, the current coils were set permanently in series for the 5 amp scale. This resulted in the need for using multiplier boxes in series with the voltage coil, extending the range of the product, giving overall wattmeter multipliers of 240, 480, 720 and 960 watts per scale division. Assuming that scales can be read to 0.1 of a scale division and considering the majority of readings being taken on the 720 and 960 watt scales, the intrinsic error was therefore 72 - 96 watts. As will be seen later this value is considered when evaluating clamp plate losses.

Whenever it became necessary to change from one scale to another, check readings were taken on both scales. The need for this degree of accuracy becomes necessary because of the small proportion clamp losses could represent in the total reading. Typically, at 200 Amp the percentage distribution of losses was estimated as shown in the table below.

Watts	%	Allocation
10700	100	Total input
8800	82.2	Copper I^2R
460	4.35	Iron loss
1440	13.45	Stray loss

Frequency was measured indirectly. The motor-generator set had a tacho-generator driven by a timing belt embodied in its design. The output was fed to a digital voltmeter, on which it could be observed directly that 100.00 volts corresponded to 1000 r.p.m., (50 Hz).

In general, to avoid errors due to accelerated heating up of the models, 5 instruments had to be read in under 7 to 10 seconds, which was extremely difficult. The wattmeters have the illuminated galvanometric spot type indicator, the voltmeter and ammeter were standard pointer deflection units and the tachometric unit a digital device. It was found that the digital device could be read instantaneously, the illuminated spot devices only marginally slower, and the pointer units were the most tedious to read.

2.4 Power Supply Requirements

Preliminary estimates of power requirements indicated that the power factor of the load would be very low, lying in the range 0.04 to 0.08. At these low power factors, the strong de-magnetising effects would tend to distort the output voltage waveform from the supply generator. It was felt necessary to check the waveforms on no-load and on load. It will be seen in Fig. 2.4 - 1, that there is very minor distortions. The waveforms were analysed and found to be virtually sinusoidal, Fig. 2.4 - 2 lists the individual harmonic analysis. For these tests the generator was connected in the two parallel star connection and the tests were carried out in detail on the short core model. The waveforms were checked visually and recorded for the series star connection and on the long core. As the results were similar they have not been reproduced here.

The supply motor-generator set purchased for the experimental investigation consisted of a four pole squirrel cage induction motor (1460 r.p.m.) coupled to a six pole salient-pole generator through an eddy current coupling. The D.C. exciter for the A.C. generator was coupled to the outboard end of the induction motor. The eddy current coupling derived its excitation from a rectifier bank, the overall scheme having a closed loop speed control circuit which enabled the speed to be held constant at 800, 1000 and 1200 rev/min to within $\pm$ 5 rev/min. The generator was rated at 415/550 volts, 208 amps 150/200 KVA 1000/1333 r.p.m. The generator had a synchronous reactance X_d = 1.065 per unit with a leakage reactance X_1 = 0.04 per unit. As can be expected, these low values helped to keep distortion to a

FIG 2·4-1

PHASE VOLTAGE
NO LOAD.

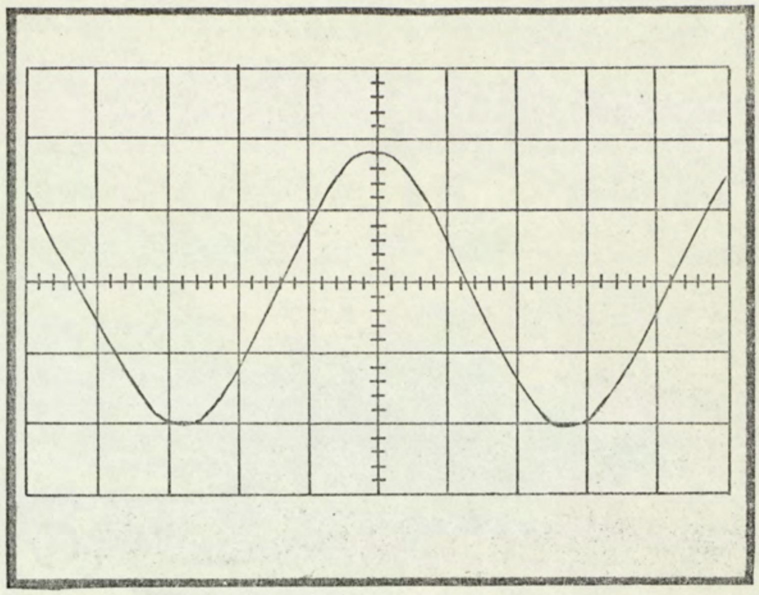

PHASE VOLTAGE.
224 amps .09 Pf.
234 Volts.

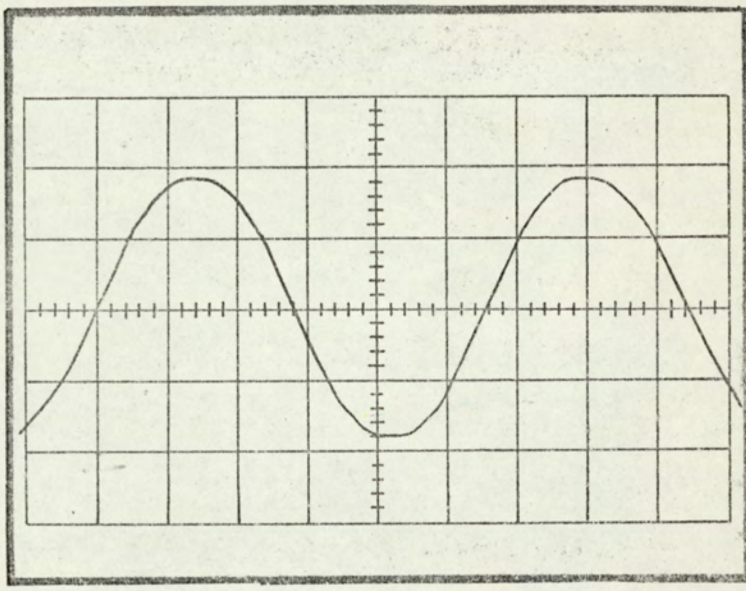

PHASE CURRENT.
224 amps .09 Pf.
234 Volts.

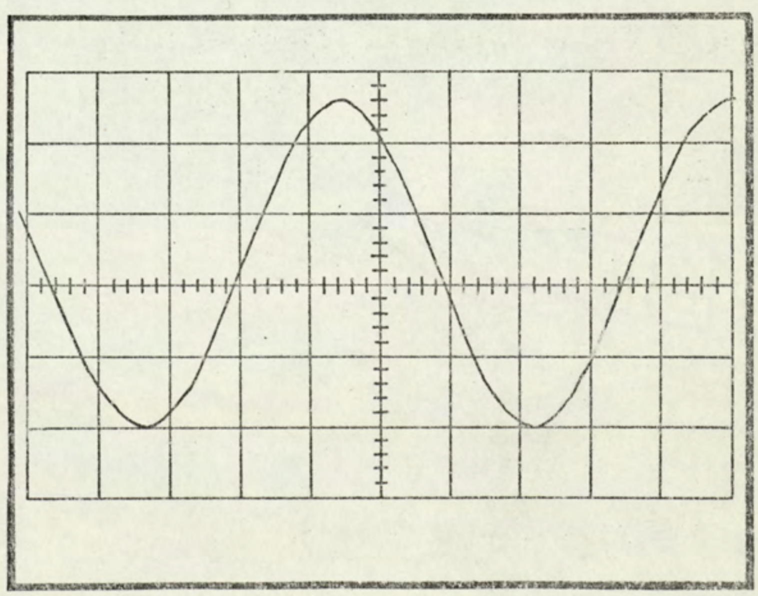

SUPPLY GENERATOR WAVEFORMS

FIG 2·4-2

Harmonic Analysis.

Harmonic No.	F.L. Ph. V.	N.L. Ph. V.	F.L. Ph. C.
1	100.00	100.00	100.00
2	1.2900	0.4900	0.7860
3	3.2400	2.7400	0.7900
4	0.9230	1.5900	0.1960
5	2.0150	0.7710	0.1600
6	0.3980	0.4770	0.0870
7	0.5120	0.4410	0.0485
8	0.1510	0.1890	0.0460
9	0.4760	0.7900	0.0163
10	0.2060	0.2900	0.0103
11	0.1400	0.2630	0.0585
12	0.0930	0.0838	0.1410
13	0.0696	0.0484	0.0442
14	0.0719	0.0823	0.1482
15	0.1230	0.1135	0.1405
16	0.0755	0.0314	0.0547
17	0.0725	0.0190	0.0714
18	0.0783	0.0586	0.0781
19	0.0129	0.0643	0.0012
20	0.1395	0.1990	0.0212
21	0.0192	0.0643	0.0166

HARMONIC ANALYSIS OF SUPPLY GENERATOR WAVEFORMS. HARMONIC AMPLITUDES GIVEN AS A PERCENTAGE OF THE FUNDAMENTAL.

minimum.

As stated earlier, tests were extended to 240 amp. on the short core but the motor generator set was unable to deliver more than 220 amp. on the long core due to limited exciter capacity. Test curves had to be extrapolated beyond 220 amp. for the long core.

<u>Chapter III</u>

3.0. Flux measuring techniques

In rotating electrical machines the problem of measuring the magnetic quantity under investigation always presents problems. It is therefore opportune to consider the various principles employed for magnetic measurements. One of the most common is the use of Faraday's law of induction.

$$e = - N \, (d\phi/dt) \text{ volts.}$$

where ϕ is in webers. Now, when the flux existing in the region of space enclosed by a coil is to be measured, the flux linkage must vary. Either the coil can be moved in a stationary field on the coil is held stationary in a time varying field. Since interest centres on the total change of flux linkage, the above equation could be rearranged and then by integrating,

$$\triangle N \phi = - \int e \, dt.$$

This principle is employed in conjunction with a ballistic galvanometer which basically is a moving - coil permanent magnet type of instrument. Alternatively, the coil output could be connected to an instrument such as a Grassot flux meter, the main difference being that it has a heavily damped element.

A second principle involves the force experienced by a conductor carrying a current in a magnetic field

$$F = B \, l \, i \text{ newtons}$$

where B is in webers per square metre l is in metres "i" in amperes. This principle is not widely used for direct measurements of flux, but it is extensively used in instruments such as the d'Arsonval galvanometer. An extension of this principle is the magnetometer type of instrument which utilizes the torque exerted on a magnet in a field to produce a deflection. Here, for a given volume of permanent magnetic material V, torque T is given by the expression,

$$T = B\ V\ H\ \text{Sin}\,\theta \text{ newton metres.}$$

where H is the ampere turns per metre, and θ the angle of rotation away from the direction of the field.

Another use of physical properties is the change of resistance of materials in a magnetic field. The A.C. resistance of a bundle of high permeability wires either carrying an alternating current or in an alternating field gives a convenient method for obtaining the change in resistance. The change in resistivity of a Bismuth spiral in strong magnetic fields has been the basis for another form of detection for measuring magnetic fields. At the present time magneto - resistance probes, which are usually in the form of modified (doped) Indium Arsenide wafers with very much stronger resistance variation characteristics, have started to come into greater use for weak and strong field measurements.

A further physical effect which is used to great advantage is the Hall-Effect in materials. Briefly, consider a rectangular plate of semi-conductor material, e.g. germanium. If the plate carries an excitation current across two opposite side edges, then if a magnetic field crosses the plane of the plate, a voltage will be induced across the remaining side edges. This phenomena is discussed in greater detail in the following chapters.

Finally, probably the most modern method of field strength measurements is the nuclear resonance method. Here the nuclei of many atoms act like spinning magnets, the axis of spin being the same as the axis of the magnetic pole. The magnitude of both the angular momentum and the magnetic moment are unchanging characteristics of the nucleus. It follows that a magnetic field produces a torque on the nucleus which tries to align it with the field. Since the spin energy produces the action of a gyroscope, the nucleus whirls round the axis of the magnetic field with a speed proportional to the strength of the magnetic field. As can be expected, this method requires complex equipment and is scarcely practical for normal laboratory usage. The method chosen for the present study is discussed in the following section.

3.1 Choice of flux measuring devices

In the preceeding section, a brief survey was carried out, covering the principles involved in existing flux measuring techniques. From this survey and considering the relative dimensions of the models and the sensors for flux measuring techniques, it soon became apparent that a final choice had to be made from three, namely

a) Search Coils

b) Magneto-resistor probes

c) Hall Effect Probes

To evaluate correctly the merits and disadvantages of the above three methods, a number of factors had to be considered, the most important being economics, availability, ease or convenience of use, physical size and limits of accuracy.

Physical Size:

All three sensors essentially integrate flux density over their active areas. Thus, to measure flux densities at points in a magnetic field which may be neither uniform nor uniformly graded, it is essential to keep the active areas of the sensors as small as possible. The Hall probe can be obtained readily in sizes down to 2.0 mm by 2.0 mm, the magneto-resistor 4.0 mm by 4.0 mm but with difficulty, whilst a search coil to give a reasonable output could be wound round a 1.5 mm by 1.5 mm former. There is one major snag, in that the radial dimensions of the search coils can not be maintained accurately on such a small former. Further, it would be difficult to assess the mean area encompassed by the various turns making up the coil.

Availability:

Both the Hall effect and magneto resister probes are readily available. Search coils need to be wound to suit, but present no problem.

Convenience of Use:

The search coil is probably the most inconvenient for handling. There is little to choose between the other two sensors. All three sensors can be accomodated with instrumentation existing in the laboratory.

Accuracy:

It is felt that the search coil probably has the greatest degree of error due to the uncertainty of the area covered by the sensor. Error introduced by the instrumentation for the three sensors would be more or less equal. The Hall Effect probe instrumentation is described in detail in section 3.3.

Economics:

The Hall Effect probes were definitely the most expensive sensors available at the time of purchase, costing approximately eighteen pounds (sterling) each. The magneto-resistors were approximately one third of this figure and the search coil one tenth of the Hall Effect price.

Considering all the above, and finally taking into account the importance of repeatability in carrying out tests it was decided to use the Hall Effect probe. Subsequent use of the equipment on the Factory Test Floor and in the Laboratory more than justified this choice on the major points of convenience in setting up apparatus, varying the probe mountings as discussed later, and by the ability to obtain test points quickly. In concluding this chapter the author would like to comment on the fact that while economics must be considered, it should never be the deciding factor in the decision to purchase experimental equipment. The use of the more expensive Hall probes was fully justified as will be apparent from tests carried out later.

3.2 The Hall-Effect Probe

If a conductor or semi-conductor plate carrying an electric current I is placed with its plane at right angles to a magnetic field of constant density B, and electric potential V is generated across the opposite

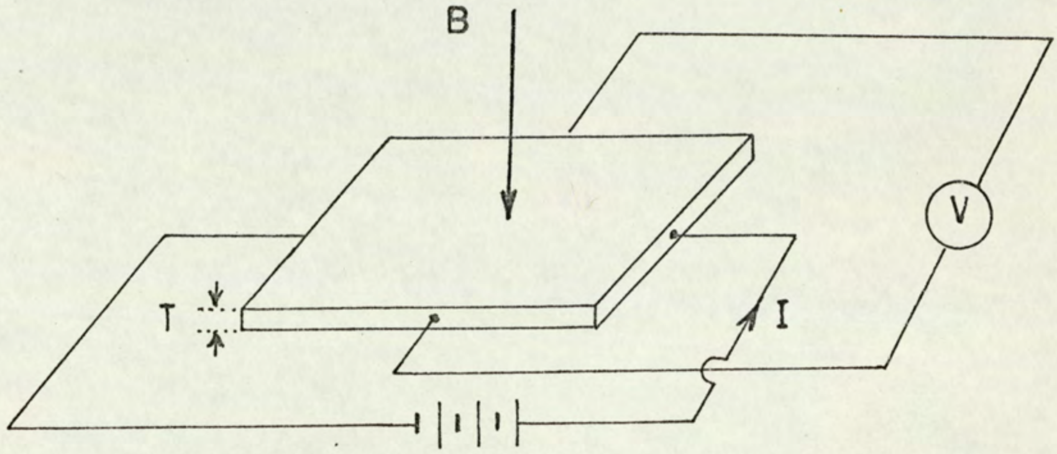

edges perpendicular to both current and magnetic fields. This phenomena, known as the Hall effect was first observed in 1879. The value (V) may be expressed by the equation.

$$V = \frac{K.\ I.\ B.}{T}$$

where K is a constant, I is the current through the plates, B is the magnetic field strength and T the thickness of the plates.

In conducting metals, the Hall Voltage is not significant. This is not so for semiconductors with their lower values of electron mass and consequent higher electron mobility. Indium arsenide and indium antimonide have the distinction of possessing the highest electron mobility among known semiconductors, Typical values are given overleaf.

Electron Mobility

Material	EM. at 20°C (cm^2/V. sec)
Germanium	3600
Silicon	1300
Indium Antimonide	65000
Indium Arsenide	25000

Consider the commercially practical Hall Probe. As it must have a finite width and length the current flow across the plate is non-uniform. There will also be effects due to change in magnetic field strengths and temperature. The semiconductor used must be chosen to keep these side effects to a minimum. Indium Arsenide is most commonly used for Hall Probe manufacture.

When considering the use of Hall Probes in A.C. fields, care must be excercised in making measurements. The element has four leads attached to it, and, of necessity, these leads create an inductive loop around the Hall element. The pick-up from the inductive loop can become appreciable in high fields at medium to high frequencies. At power frequencies this effect can generally be neglected. As the induced voltage is in quadrature with the Hall output voltage, it can be separated by using a phase discrimination circuit. This inductive voltage can be calculated as shown.

$$V_{ind.} = A \frac{dB}{dt} \text{ volts}$$

A = effective area m^2.

B = Wb/m^2

t = seconds.

The area A is not the area of the Hall probe, but is the area covered by the loop. The effective values of A can be obtained for each probe from the manufacturer.

A further phenomenon peculiar to Hall effect devices is the "turn-over" or reversal effect. This involves any difference in readings when the probe is reversed in a given static field. It is similar to polarity sensitivity and is generally caused by electrical unbalance in the Hall element. It can generally be discounted except where measurements of a very high degree of accuracy are required. On the probes selected, this effect was hardly discernable and has therefore been ignored.

Hall Probes Selected.

It was found that there were only a few manufacturers producing Hall probes commercially. For A.C. fields in particular, commercial units available were limited in use up to 0.3 Wb/m^2. It was therefore necessary to use the probes in conjunction with a milli-volt meter and suitable calibration curves for high A.C. field measurements.

Specification for Mk 111 Probes.

Thickness of plate.	0.001" approx.
Input resistance.	4-20 ohms.
Output resistance.	4-20 ohms.
Max. plate exciting current in free air.	100 mA
Max. plate exciting current with heat sink.	200 mA
Sensitivity	4 - 8 $V/A.\,Wb/m^2$
Temperature Coeff. 20°-$60^\circ C$.	0.1% /$^\circ$C
Misalignment Voltage	$\pm$ 0.75 m V at 50 m A.
Drift of Misalignment Voltage	300 V at 10 mA
Dimensions:	3 by 12 mm 0.41 mm Thk.
Effective element Area:	2 by 2 mm

After a survey of available probes, the Miniature Field Probe manufactured by Associated Electrical Industries at Lincoln, England was selected. These probes were found to be extremely sensitive and had the advantage of being easily available.

The A.E.I. probe consists of a thin semi-conductor plate mounted on a Beryllia backing. Evaporated silver leads are used for connections to the plate and these, in turn, are joined to a flexible printed circuit lead-out connected to 12" of lead wires.

The use of a high impedance electronic volt meter and Hall probes having an open circuit linearity of better than 1%, eliminated the need for linearising resistors. Tests were carried out to check side effects in an A.C. (50 c/s) and D.C. field. Typically, the A.C. reading was found to be 2.8% low compared with a 'standard' D.C. reading. Some of this error was actually due to the lower accuracy of the A.C. milli-volt meter used when compared with the D.C. digital voltmeter. As a check, the inductive voltage was calculated and found to be less than 0.1%.

It was decided that a possible error of 1.5% could be obtained if the D.C. calibration curves were used for 50 cycle per second A.C. field use.

Twenty probes were specially selected. Of these probes, sixteen had a sensitivity within 3% of each other and four within 6%. Linearity was checked at 40, 100 and 200 mA exciting currents and found to be within $\pm$ 1.0%. Fig. 3.2 - 1 lists the calibrations for all the probes selected. As all tests will be carried out with temperature variations not exceeding 10°C, a further 1% error could be expected. Considering all possible variations, it is felt that an overall accuracy to within $\pm$ 4% could be expected, with a repeatability within 2.0%.

In concluding this chapter, it should be mentioned that

TABLE I

MKIII HALL PROBE CALIBRATION DATA - FEBRUARY 1967.

OHMS		Millivolts output into high impedance load, test current = 40.0 mA.			Sensitivity $\times 10^{-1}$ V/A.Wb/m^2			Probe No.
R_{CC}	R_{HH}	Wb/m^2 0·0991	0·2936	0·9985	0·0991	0·2936	0·9985	
7	11	21.43	63.93	206.6	.541	.544	.517	1334
7	8	19.68	58.36	189.4	.496	.497	.474	1335
7	7	19.54	57.80	185.6	.493	.492	.465	1370
6	7	20.01	60.21	204.5	.505	.513	.512	1371
8	9	20.37	59.65	186.5	,514	.508	.467	1372
7	7	20.26	60.50	198.3	.511	.515	.496	1373
8	8	20.28	59.86	193.1	.512	.510	.483	1374
7	7	19.14	56.85	183.7	.483	.484	.460	1375
7	6	19.06	57.20	192.1	.481	.487	.481	1376
7	8	19.99	59.06	189.2	.504	.503	.474	1378
7	8	20.21	60.48	198.6	.510	.515	.497	1379
7	8	20.33	60.93	201.5	.513	.519	.505	1380
8	8	19.74	58.87	191.0	.498	.501	.478	1383
7	7	19.67	59.10	197.3	.496	.503	.494	1384
7	8	20.42	60.86	198.7	.515	.518	.497	1386
9	8	20.96	62.36	201.7	.529	.531	.505	1387
8	8	20.87	61.88	200.8	.526	.527	.503	1389
10	10	21.18	63.03	202.4	.534	.537	.507	1395
10	10	20.70	61.90	198.8	.522	.527	.498	1397
11	9	20.58	60.93	197.9	.519	.519	.496	1398

R_{CC} = Input Resistance in OHMS.

R_{HH} = Output Resistance in OHMS.

due to the low level of output from the Hall Probes, the use of Hall Effect multipliers were considered briefly. Their use was rejected for two reasons. The first was physical size and the second was the additional errors that could be introduced by the hysteresis loop inherent with the multiplier.

3.3 Hall probe instrumentation.

The instrumentation and circuitry described here were designed and assembled primarily for the measurement and investigation of the magnetic fields in the region of the clamp plates and in the air gap of the experimental stators. However, with minor additions to the circuitry, there is no reason why it cannot be used for general measurements on machines. As the selected probes had a temperature coefficient of 0.1% per degree centigrade and the temperature variations during tests would be held to within 10 degrees, no circuits were required to compensate for temperature variations. Further, the specially selected probes had an open circuit linearity of better than 1% and therefore, no linearising resistances were used. These two characteristics helped to simplify the circuit.

The constant current circuit was designed to operate on a single phase 50 Hz. 0 - 230 volts variable power input. The circuit diagram is shown in Fig. 3.3 - 1. The Zener diodes ZD1 are applied to the base of a transistor TR1. R2 is a fixed resistor to limit the maximum output current, while R1 is variable to give fine control of the output. The network gives a constant current adjustable from 0 - 200 mA.

Initially it was found that the ripple frequency of the D.C. output introduced a corresponding ripple in the output of the Hall probe when measuring D.C. fields. This in turn gave erroneous readings of milli volt output, and when measuring A.C. fields, would lead to distortion of output wave forms. A seperate stabilised ripple-free D.C. supply was used for calibration purposes. After experimenting with smoothing circuits, the "pi" form finally used was found to give a ripple of 0.25 mV on a 57.2 mV output (0.44%). In terms of

HALL PROBE
constant current
circuit

FIG 3·3-1

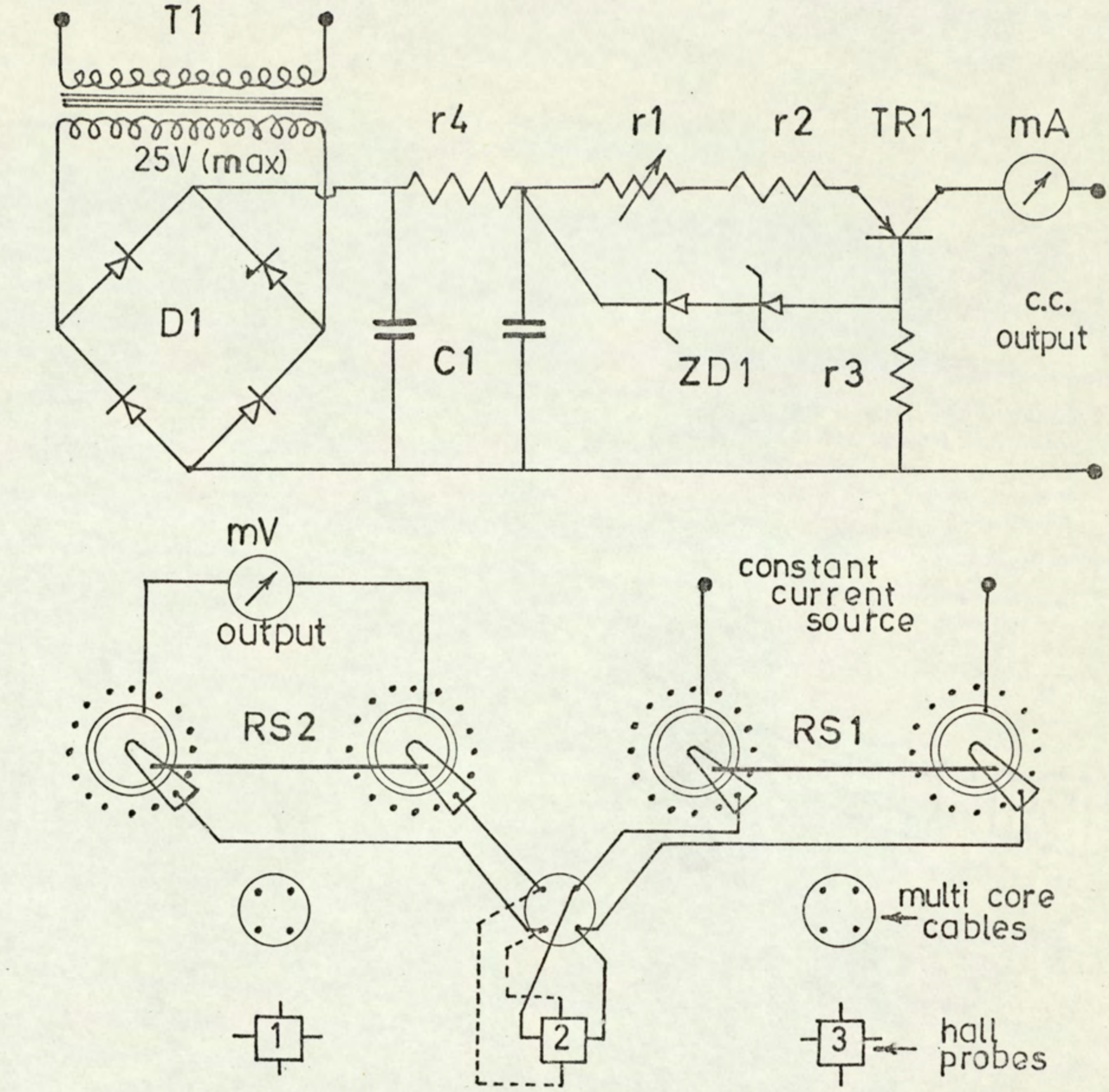

r1	0 – 200 ohmn	TR1	OC29 transistor
r2	100 ohmn	C1	1000 μF electrolytic
r3	470 ohmn	ZD1	OAZ 269 zener (5·6V ± 10 %)
r4	22 ohmn		
RS1, 2	rotary switches	D1	HG5005 diodes
T1	variable 0 – 230 Volt 1 ph 50 watt		

comparison with the stabilised power source there was no discernable difference in the Hall probe output voltage. Fig. 3.3 - 2. is a record of the output voltage. The circuit was checked for temperature stability by switching on, and allowing to warm up. The output current was then set at 40mA and held for a period of one hour. At the end of this period virtually no adjustment was required to obtain 40mA exactly.

The constant current source is connected through a ganged silver contact rotary switch RS 1 so that each of the 20 probes can be switched into circuit as required. The ganged rotary switch RS 2, also with silver contacts introduces the probe output terminals across a high impedance electronic milli-voltmeter. The rotary switches are coupled to six foot lengths of multicore conductors giving 12, 6 and 1 single probe banks. These in turn are connected to gold plated multipoint jack plugs to keep contact effect to a minimum. The complete set gives a great degree of freedom and makes the set portable for use outside the laboratory (if necessary) as seen later.

Trace of hall probe output waveform when excited from the constant current circuit, using the permanent magnet test field.

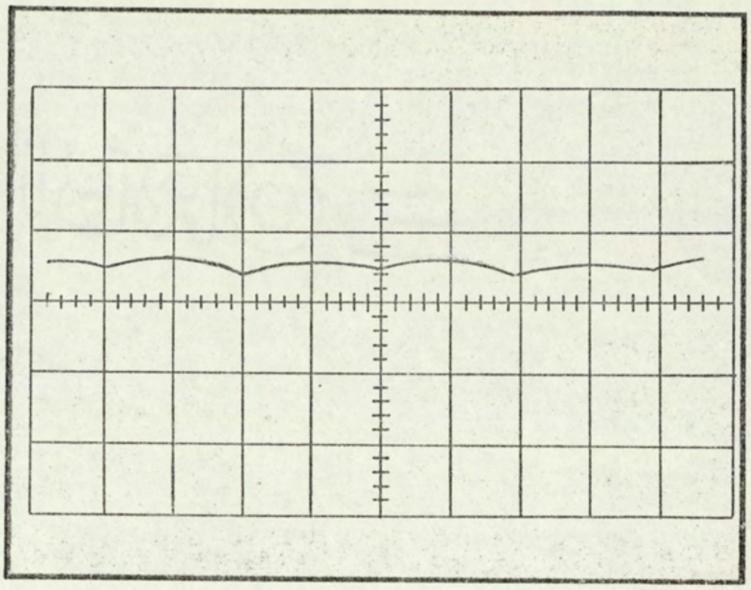

Scale : 1 mV/cm.

Test Field : 2.98 Kilogauss.

Exciting Current : 40 milliamps.

Output Voltage : 57.2 millivolts.

(Equivalent to 58 mV at 41.3 mA).

Ripple Content : 0.25 mV in 57.2 mV.

(Equivalent to 0.44%).

Probe No. 1334.

Note : On a stabilised D.C. source 41.3 mA excitation gave 58 mV output in a 2.98 Kilogauss test field.

3.4 Evaluation of probe output data.

When the calibration data for each probe is considered in detail, it is apparent that each reading must be referred to a calibrating reading which is taken at the start and end of each set of data. This is to ensure that there has been no drift in the flux metering circuits. As the number of readings taken daily could easily exceed 100 - 150, it became necessary to devise a digital computer programme to assimilate this vast quantity of data. The programme had to accept the data, the probe calibrations and excitation values before and at the end of each test run.

The programme will select the correct probe constants from a table. Correcting for zero datum, and assuming the sensitivity for zero flux density, an approximate flux density is calculated. Three neighbouring values of densities and corresponding sensitivities are selected from a table. Then by interpolation and reiteration, the accurate density is obtained. It was decided that three interations would generally be sufficient; however, this number can be changed by varying the input data.

In this era of common computer usage, it is of no great interest to study the programme in its programme language form. The simplified flow diagram given in Fig. 3.4 - 1., shows clearly the functions, orders, and programming sequences. The programme was written in Fortran IV language and can be easily made compatible for use on any computer having Fortran IV facilities. Probably one instruction in every twenty may need adjusting.

DATA CONVERSION FLOW DIAGRAM

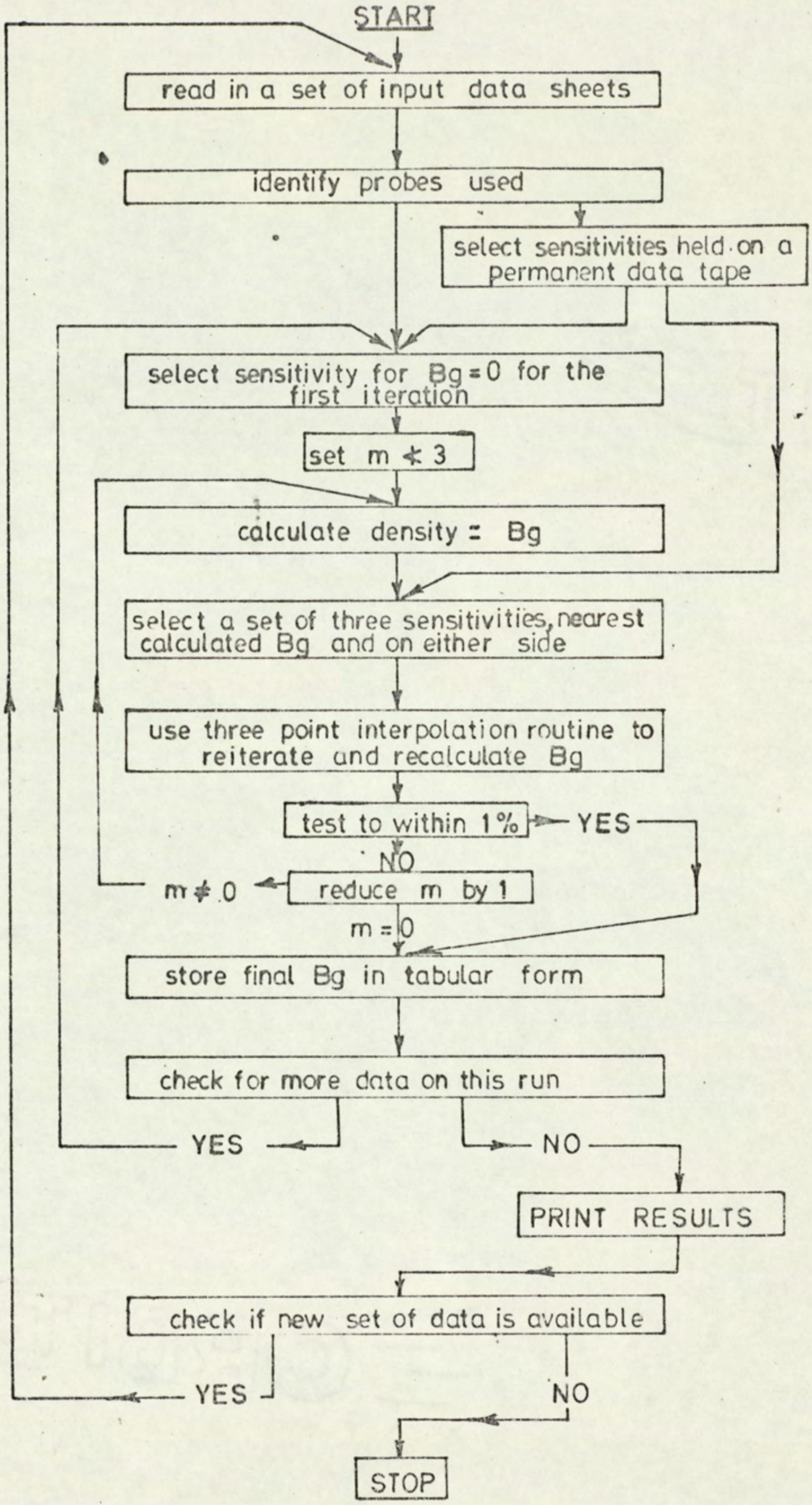

m = number of iterations desired.

3.5 Hall probe linearity tests in an alternating current field.

Although the basic Hall probes had been tested at the manufacturer's works to check their suitability for alternating current work, it was felt necessary to carry out a similar test with the associated instrumentation. Accordingly, a 200 turn solenoid was wound onto the centre limb of a small open-ended E - type stack of punchings. The end surface of the centre limb was carefully marked out and each probe in turn was clamped parallel to this surface. The excitation to the solenoid was obtained from a sinusoidal 50 Hz source through a variable ratio transformer.

A series of magnetisation curves were taken with a constant 50mA D.C. excitation to the probes. The results of the test are given in Figure 3.5 - 1 where the probe outputs are converted to flux density on the associated digital computer programme. Four of these results are plotted to show their linearity. The particular four were selected to cover the band width inside which all probes fall. The deviation of ± 4% is due entirely to the inability to locate the probe precisely on the target.

Probe 9 was selected at random to carry out a linearity test at constant flux density across the probe, and with varying probe excitation currents. This is shown in Fig. 3.5 - 2. At the same time, the probe output was recorded for average, r.m.s., and peak values. As can be expected, with a sinusoidal input, the output is reasonably sinusoidal. It can also be reasonably assumed that the Hall probe behaves linearly under the conditions of test.

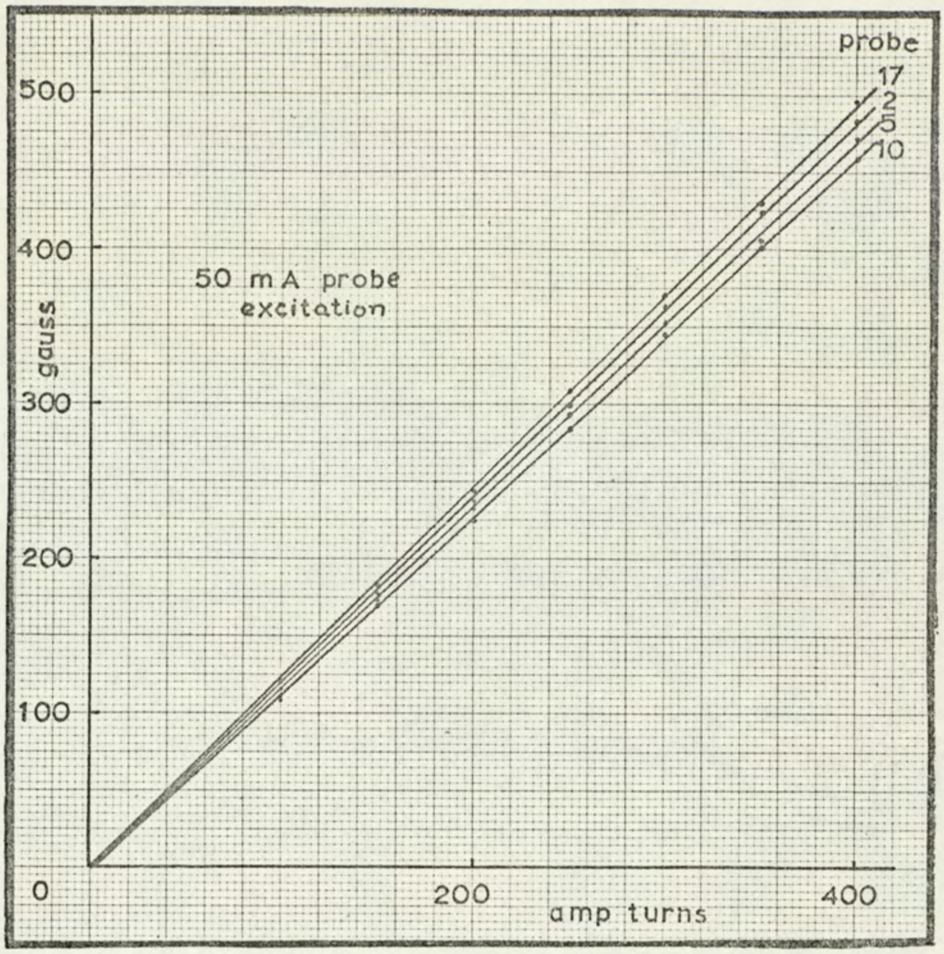

FIG. 3·5-1

A.C. CALIBRATICN TESTS

FJ.1661,FIELD MEASUREMENT DATA CONVERSION

probe ↓ \ SET →	1.	2.	3.	4.	5.	6.	7.
1	487.24	417.23	366.69	304.53	236.57	176.41	110.47
2	484.53	424.04	363.53	298.97	238.42	177.84	115.62
3	487.06	422.14	365.33	304.46	239.53	182.70	115.72
4	481.39	418.01	362.48	298.94	239.30	177.59	117.81
5	472.35	405.94	353.22	292.70	232.18	173.64	110.02
6	478.68	416.03	363.14	300.42	235.70	178.79	113.99
7	487.80	423.07	370.06	307.20	242.31	183.28	116.33
8	469.46	408.97	357.91	294.72	234.92	178.12	112.96
9	476.63	415.30	361.59	298.24	237.91	181.01	115.59
10	458.14	401.94	345.70	283.79	225.61	170.01	109.12
11	.00	.00	.00	.00	.00	.00	.00
12	.00	.00	.00	.00	.00	.00	.00
13	476.37	416.84	361.28	299.76	238.23	178.68	117.14
14	489.75	427.24	370.73	308.10	241.35	182.63	115.73
15	451.11	389.44	337.40	279.58	223.67	166.61	108.76
16	457.89	397.43	344.72	286.11	228.22	170.66	107.95
17	495.09	430.82	370.54	308.61	244.23	183.03	120.99
18	496.11	432.02	373.72	311.51	245.38	187.00	116.91
19	.00	.00	.00	.00	.00	.00	.00
20	543.10	464.42	398.14	327.70	257.23	197.11	128.66

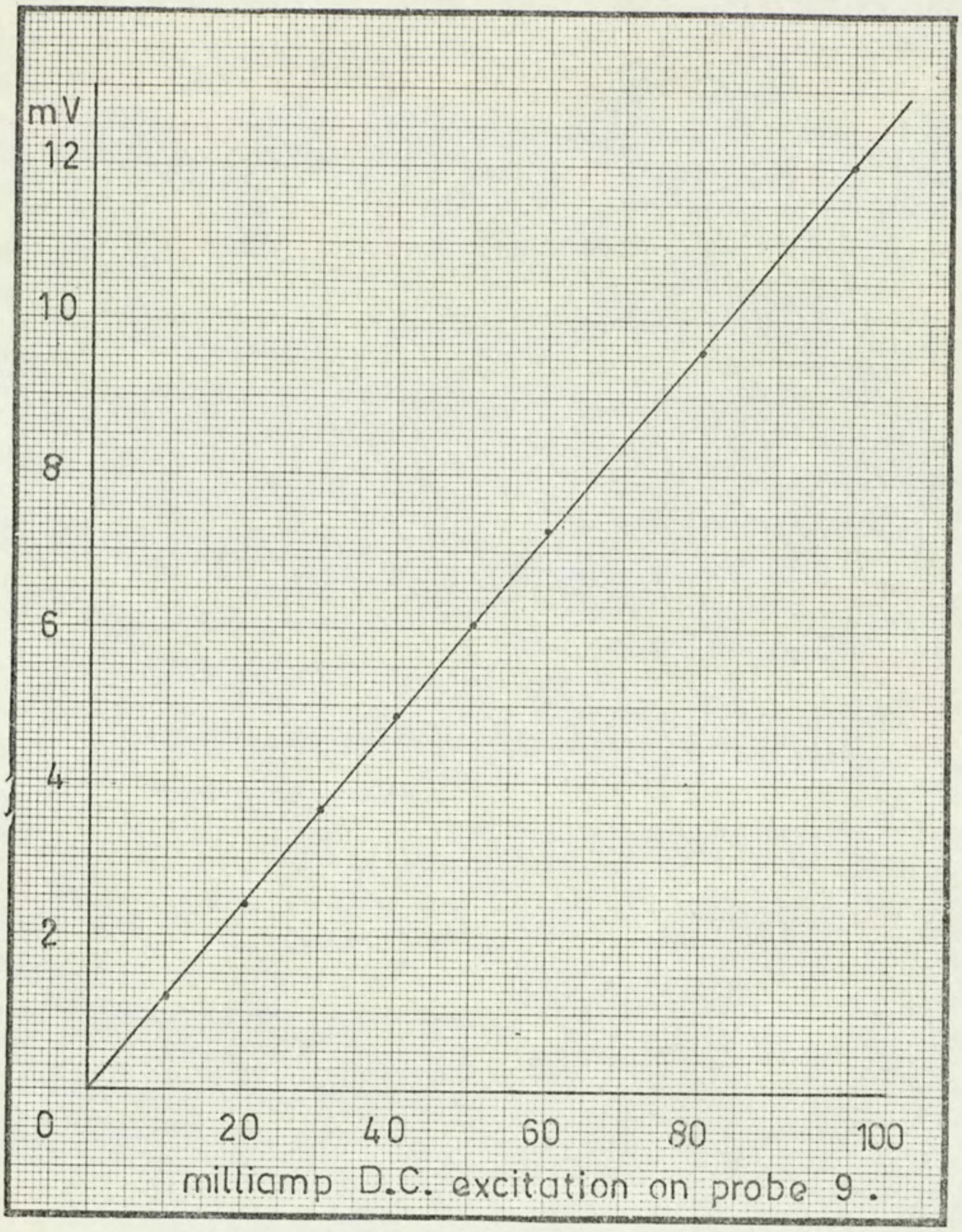

FIG 3·5-2

AC linearity tests
200 amp turns = 235 gauss (·0235 Wb/m^2)
(on solenoid)

relative test readings		
peak value	= 8·42 mV	ratio = 1·412
rms	= 6·00 mV	
average value	= 5·36 mV	form factor = 112

3.6 Possible Improvements to Hall Probe Instrumentation

From the experience gained using the instrumentation described in this thesis, both in the Laboratory and in the factory test area, various limitations were encounted. It was often felt that the requirement of working over a limited temperature range was a serious handicap. A machine on no-load would be at a total temperature of about 20°C while at full load, hot, the total temperature of the area under investigation could easily reach 110°C on a class B insulated machine; this would introduce a 9% error if not corrected either mathematically in the associated computer programme described earlier, or by a temperature compensating circuit which could adjust the excitation current proportionally. This development of an automatic temperature compensating circuit is not easy and can be quite expensive and as far as this author is aware, no commercially available Hall Effect equipment has this feature inherent in the design.

A further improvement would be the provision for a parallel output for direct display on an oscilloscope. If the oscilloscope or recorder used has a high impedance to match the electronic meter already being used, calibration can be obtained directly.

Finally, for the instrumentation to be universally used for frequencies up to 2400 Hz, it is imperative that correction circuits are included to correct for the inductive voltage pick-up. While this effect can be calculated by using the calibration data as described in section 3.2., it is felt that the use of a phase discrimination circuit is advisable. Only the component directly proportional to the field under investigation is then monitored.

It is not proposed to enter into details of the temperature and inductive voltage correcting circuits, as this could be the subject for future investigation into Hall-Effect measuring techniques. All the above remarks will of course apply equally to magneto resistance devices.

Chapter IV

4.0 Preliminary Testing.

It is intended to test two models at various excitation current, and at each of three different frequencies (40, 50 and 60 Hz). Consequently the number of variations possible would require an impractical length of testing time. It is recognised that a few simple preliminary tests will indicate certain similarities which reduce the volume of testing necessary. Thus, by comparing flux densities at the clamp plate surfaces at each of the three frequencies, at one specific location and with one value of stator excitation current, it was considered sufficient to make flux density measurements at one frequency only. Similarly, comparing flux densities at the clamp plate surfaces on each model in turn, for one specific set of conditions, indicated that the patterns are virtually identical, so that full scale flux density measurements can be confined to one model only.

Under certain conditions of flux density testing, the wave form of the Hall probe output voltage indicated considerable distortion. At the outset, it was necessary to check that this was a genuine representation of the flux density being measured, and not a spurious effect produced in the probe device itself.

4.1 Variation of probe output with frequency.

Throughout this study, loss tests were carried out at 40, 50 and 60 Hz to obtain the dependence of loss with frequency. With regard to the flux density patterns which were examined in detail, it was decided to restrict all tests to 50 Hz as it would be both expensive and wasteful in time to repeat tests at 40 and 60 Hz. In order to justify this decision, it was decided to take a typical set of test results at all three frequencies. Tests were carried out using the $\frac{1}{4}$" mild steel clamp plates. The Hall probe was placed 38mm radially from the winding, on the clamp plate surface. To enable ease of comparison, tests were taken at 50 and 60 Hz on one oscillogram and then at 40 and 50 Hz on the other oscillogram. This is clearly seen in Fig. 4.1 - 1. To complete the comparison the r.m.s. output of the probes was recorded directly. From these results, it was felt that the decision to carry out tests at 50 Hz only was quite justified.

variation of probe output with frequency for a fixed position on the clamp plate surface with constant excitations on stator and probe.

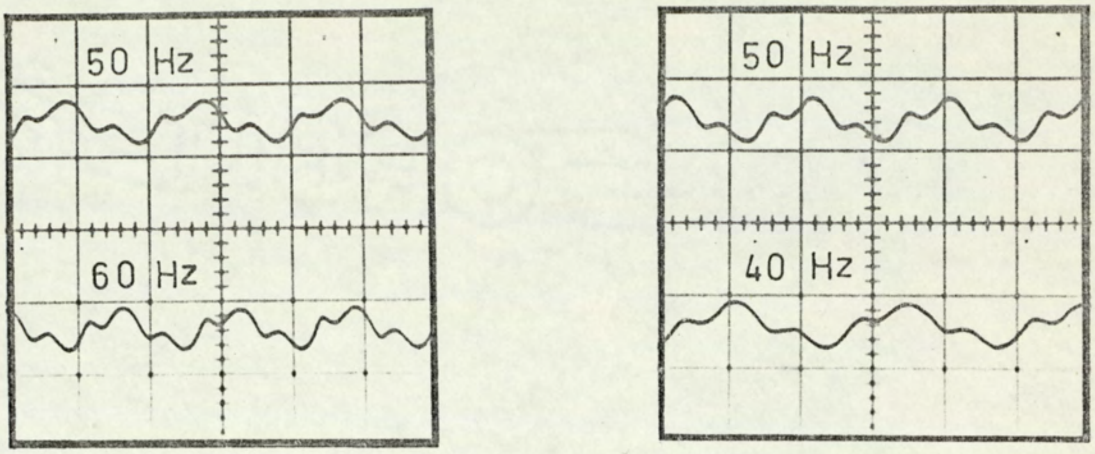

10 mV/cm
10 ms/cm

probe positioned 38 mm from winding
stator excitation 240 amp
probe excitation 50mA
1/4" mild steel

Hz	mV rms
40	2·12
50	2·05
60	2·01

FIG
4·1-1

4.2 Hall probe comparison with search coil.

Bearing in mind the comment made earlier regarding the difficulty in determining the true dimensions of a multi-turn search coil, it was decided to carry out this test visually. As the Hall probe measures 2.0 x 2.0mm it was decided to produce a search coil with similar dimensions. The final coil used had 20 turns wound on a 2.0mm diameter former. To obtain a good visual comparison meter scales were adjusted to give reasonably similar envelopes for both tests which are recorded in Fig. 4.2 - 1. On the oscillographic record of search coil output, both the search coil voltage output and its integrated wave were recorded simultaneously. From a close examination of the integrated wave shape compared with the Hall probe output wave, it can be concluded that the results are sensibly similar.

The site chosen for this comparison is where the flux density wave indicates maximum distortion. The close similarity of the traces shown in Fig. 4.2 - 1 verifies that the distortion does not originate within the Hall probe equipment.

comparison of Hall probe output with the integrated output from a twenty turn search coil.

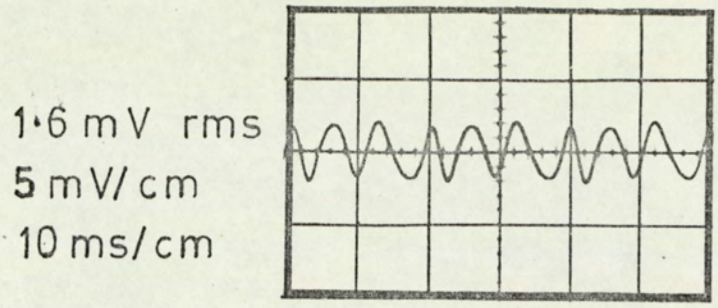

FIG 4·2-1

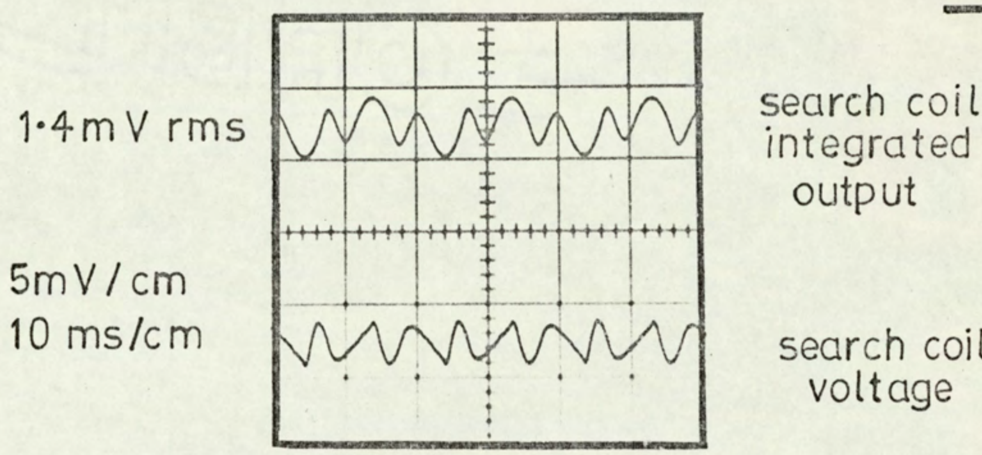

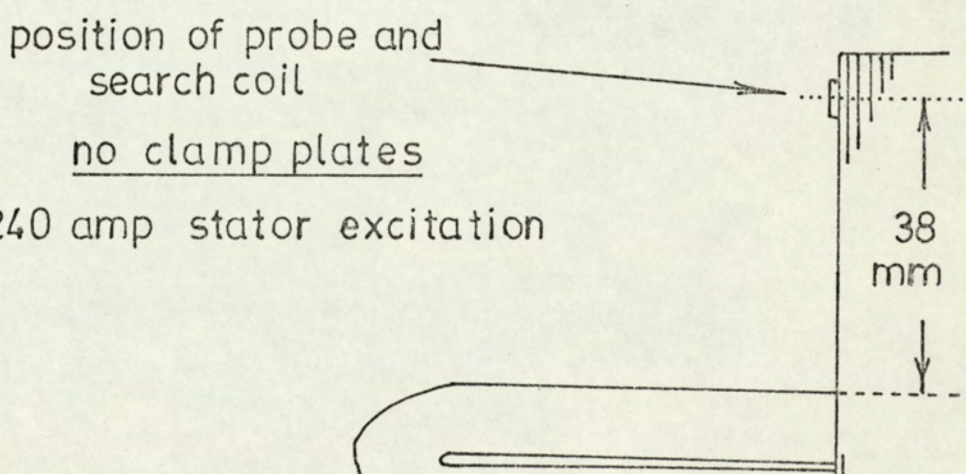

4.3 Similarity test for end region field on long and short cores.

Probably this is the most important of this series of preliminary tests. In the design philosophy of the model stators, it is assumed that provided end windings are electrically and dimensionally identical, the resultant flux density patterns on the clamp plate surfaces on the two models would be identical. Accordingly, tests were carried out on the long and short cores at 204 amp excitations with the one inch unbevelled mild steel clamp plates. Traces were taken along the radial and axial surfaces of the clamp plates. Fig. 4.3 - 1 and 4.3 - 2 show that for all practical purposes, the traces are identical.

At this point it was suggested that it would be opportune to wind a single turn search coil round the clamp ring and record output. At the same time oscillographic records were taken, Fig. 4.3 - 3. It was surprising to find that the short core appeared to have more flux trapped in the clamp plates. This suggests the possibility of the clamp plates also carrying part of the main flux diverted from the core, and that the proportion diverted is different for the two cores. It was decided to trap the Hall probe between the clamp ring and the core stamping face and record the output. This is shown in Fig. 4.3 - 4. Here again, more core flux appears to be diverted from the short core than from the long core. Further, the probe output from the short core test appears to show more distortion than from the long core test. As will be seen later, when evaluating clamp plate losses there is a similar discrepancy between long and short core tests. This problem is dealt with in detail in chapter 6.0 and 7.0.

similarity tests on long and short cores to compare radial and axial surface flux density traces on the 1" unbevelled mild steel clamp plates with 204 amp stator excitation.

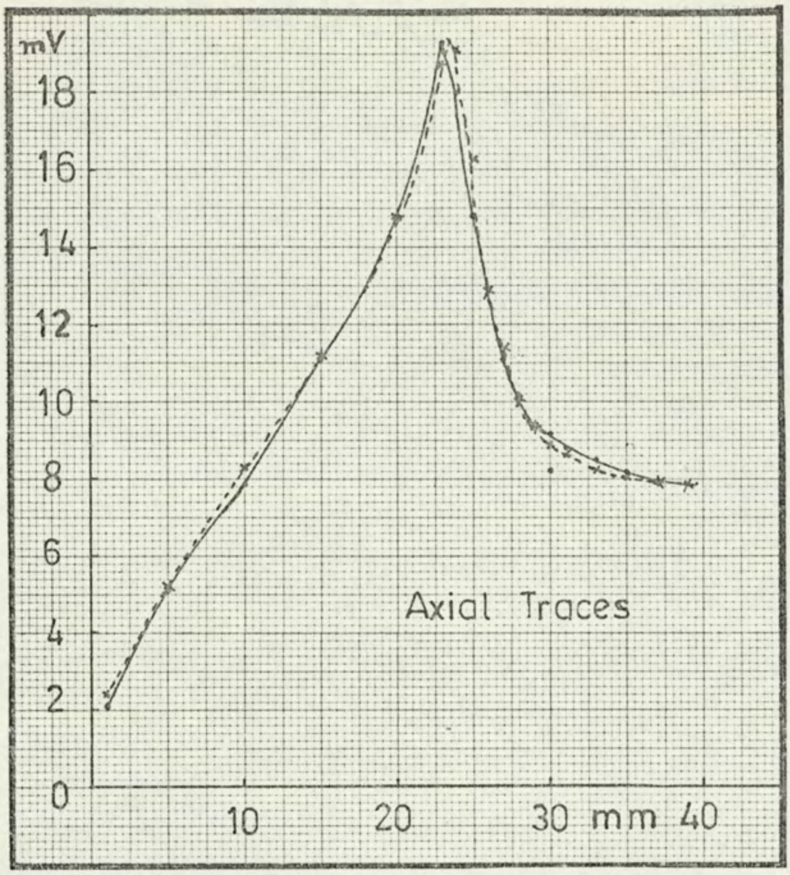

FIG 4·3-1

long core
short core
1mV=4·15m.Wb/m^2

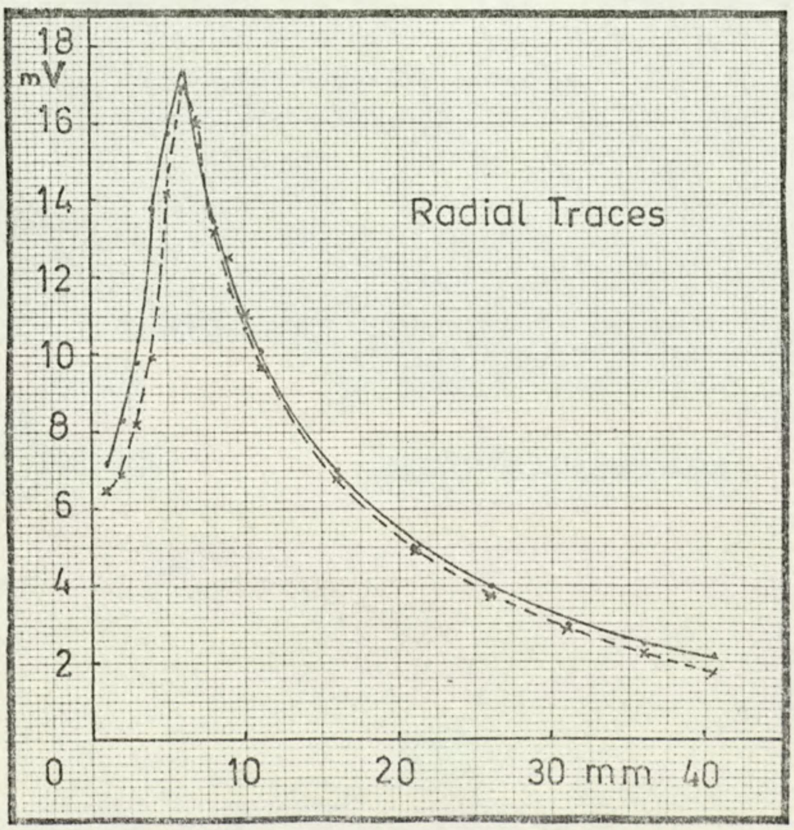

FIG 4·3-2

similarity test on long and short cores with a single turn search coil wound round the 1" unbevelled mild steel clamp ring with 204 amp stator excitation.

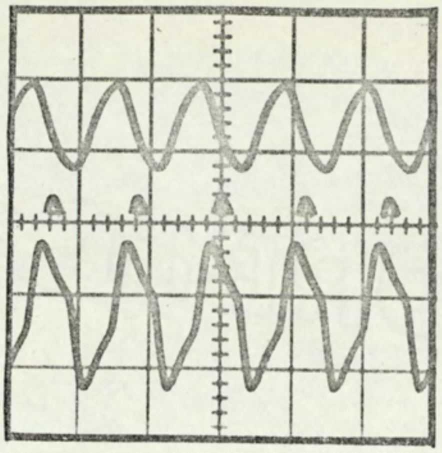

flux trace 1 mV/cm
($\int v dt$)

(v) volt trace 2 mV/cm

long core

FIG 4·3 -3

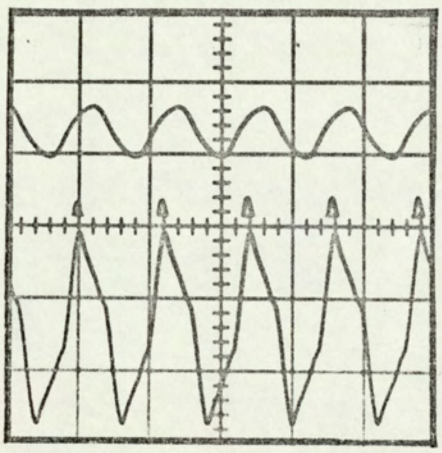

flux trace 2 mV/cm
($\int v dt$)

(v) volt trace 2 mV/cm

short core

	volt trace	
	mV rms	mV peak
long core	50	75
short core	68	102

similarity test on long and short cores with Hall probe trapped between the 1" unbevelled mild steel clamp and the stamping pack, with 204 amp excitation, probe positioned 8mm radially from winding

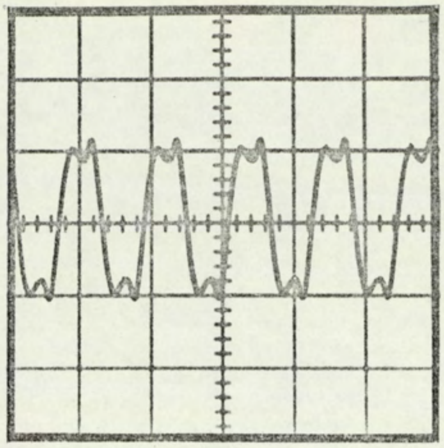

2 mV/cm
long core

FIG 4·3-4

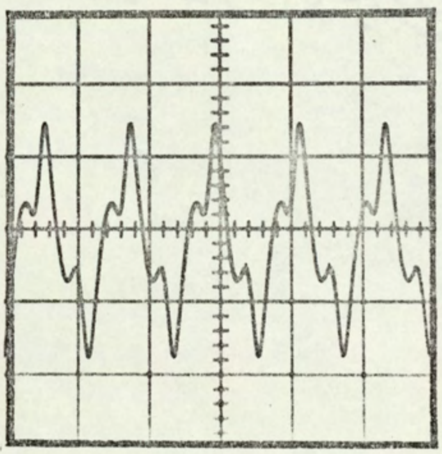

2 mV/cm
short core

	mV rms	mV peak
long core	6·3	8·05
short core	6·85	12·1

Chapter V.

5.0 Preliminary investigation of the general m.m.f. and flux density distributions.

In the salient pole synchronous machine, the air gap and the interpolar regions have been studied extensively. The techniques of hand flux plotting in these two regions has become a standard design office proceedure. In fact, the use of analogue aids such as the Teledeltos paper plots rarely find an application, except for exceptional boundary conditions.

To verify these flux plots, the use of search wires axially positioned in the air gap has become a standard feature of commercial testing. The verification of the interpolar plots can be carried out laboriously using search coils but is more often carried out indirectly by checking the overall magnetisation characteristics. There is also the clamp plate boundary which is of importance, but this is neither easy to analyse nor to check experimentally. It is true that test plots have been carried out using small multi-turn search coils, but this is not a commercially practical test due to the setting up and calibration time for the associated equipment. With the Hall probes used in this study, it was decided to take advantage of the fact that testing is relatively simple and to carry out a series of preliminary fundamental tests.

Initially, tests were carried out with direct current excitation on the winding with the following conditions of test excitation,

a) A single coil
b) All coils in one pole pair (4 coils)
c) All coils in one phase
d) All coils in two phases
e) All coils in the three phases

All these patterns could have been derived by using the well known Fourier expression for a rectangular wave, which represents the m.m.f. of a single coil carrying direct current. However, since it is not easy to take into account the conductor disposition, it was felt that it would be better to actually measure the flux density patterns rather than assume the patterns exist. Since the main interest lies in the relative magnitudes of the flux density patterns, it is sufficient to present the results in actual Hall probe output voltage.

5.1 Air gap flux density distribution with direct current excitation.

a) The single short pitched coil.

The coils on the model stators are short pitched, slot 1 to slot 11 (83.3%) for the conventional six pole winding. Exciting a single coil would therefore constitute setting up a very short pitched coil on a two pole system (27.8%). It was felt that regardless of this extreme short pitching, the theoretical rectangular m.m.f. pattern would give rise to a similar form of air gap flux density wave. A direct current of 75 amperes was passed through the coil. The single Hall probe was held centrally against each stator tooth face in turn. The plot of a complete traverse is shown in Fig. 5.1 - 1. A study of this air gap flux density distribution shows a very marked cusp, where, a rectangular distribution had been expected. Magnetic saturation effects were discounted due to the very low (o.o2 Wb/m^2) flux density level of this test. To study this phenomenon, a full scale flux plot was carried out by hand, assuming gap flux density to be uniform within the coil pitch. The result of a series of relaxations and iterative calculations is given in Fig. 5.1 - 2. The deviation between the measured values and the predicted value is seen in Fig. 5.1 - 3. For convenience only half the plot is shown.

b) Four consecutive coils excited.

As with the single coil, there was a noticeable cusp in the air gap distribution, although it was not quite so pronounced. The resultant plot is shown in Fig. 5.1 - 4, the current per coil being 82 amps. It will be noted that at this higher level of magnetisation (o.112 Wb/m^2) there is less deviation from the expected rectangular gap density air gap flux density pattern with a single single short pitched coil excited with d.c.

FIG 5·1-1

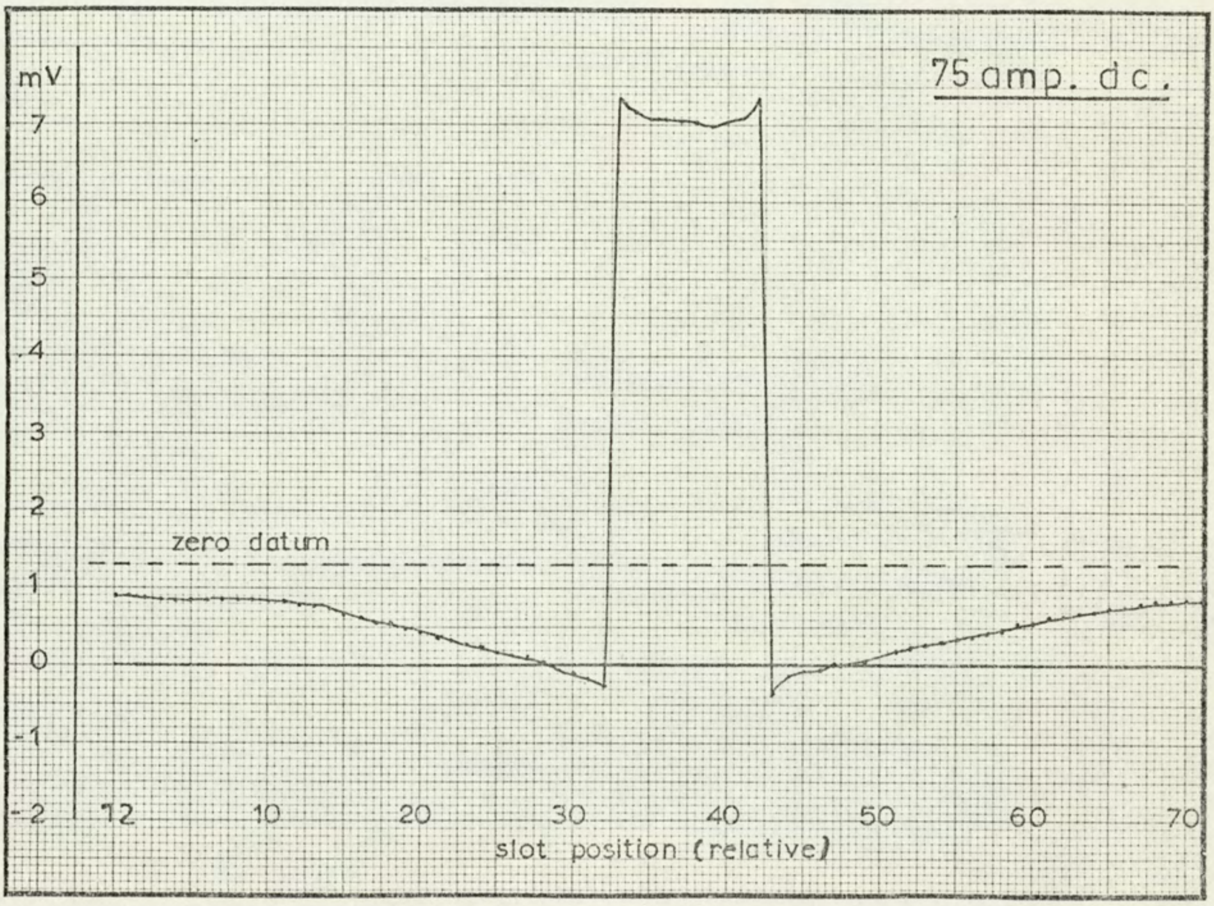

FIG. 5·1–2

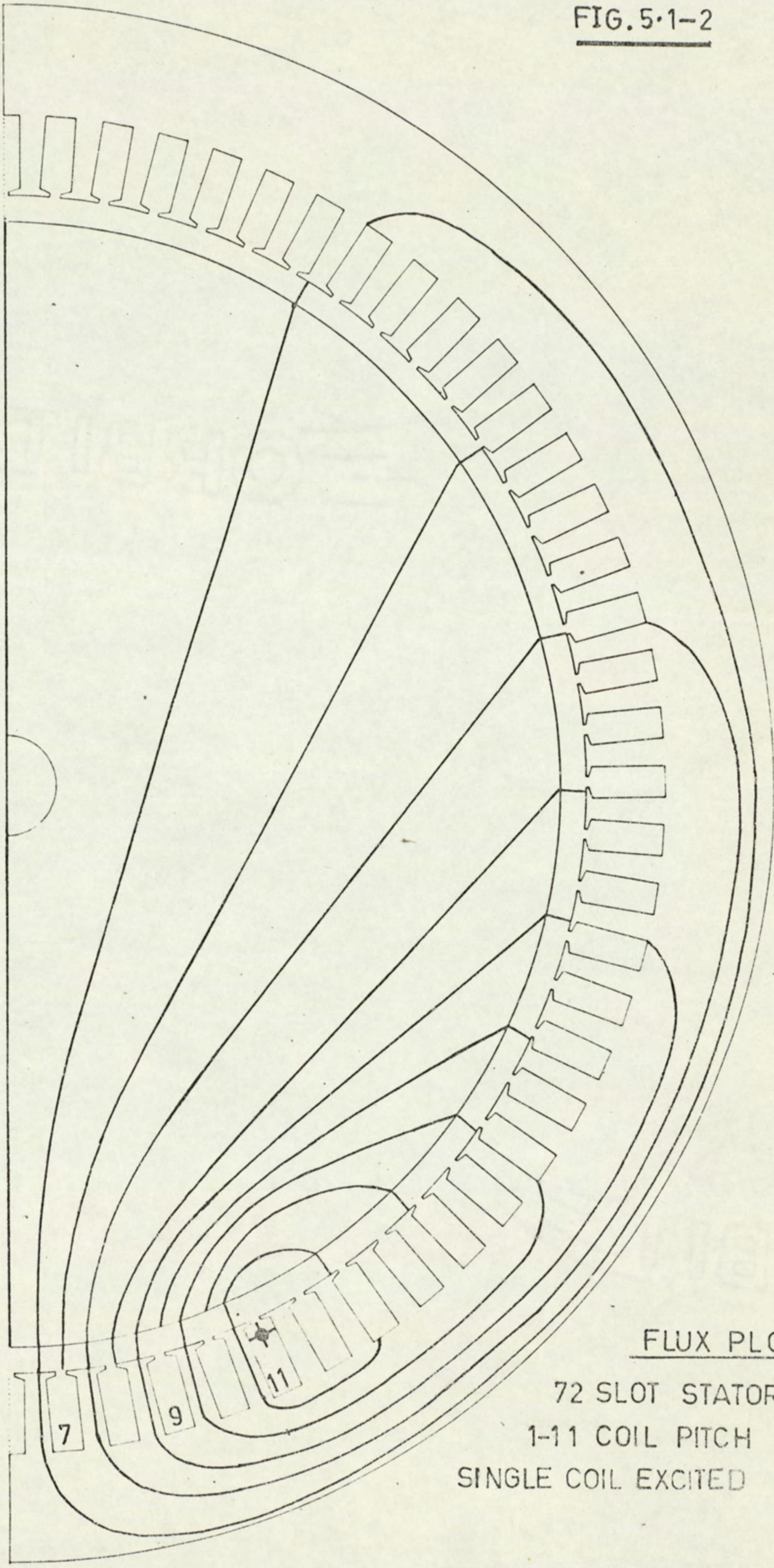

FLUX PLOT

72 SLOT STATOR

1-11 COIL PITCH

SINGLE COIL EXCITED

comparison of measured and estimated air gap flux density distribution with a single short pitched coil excited with d.c.

FIG 5·1-3

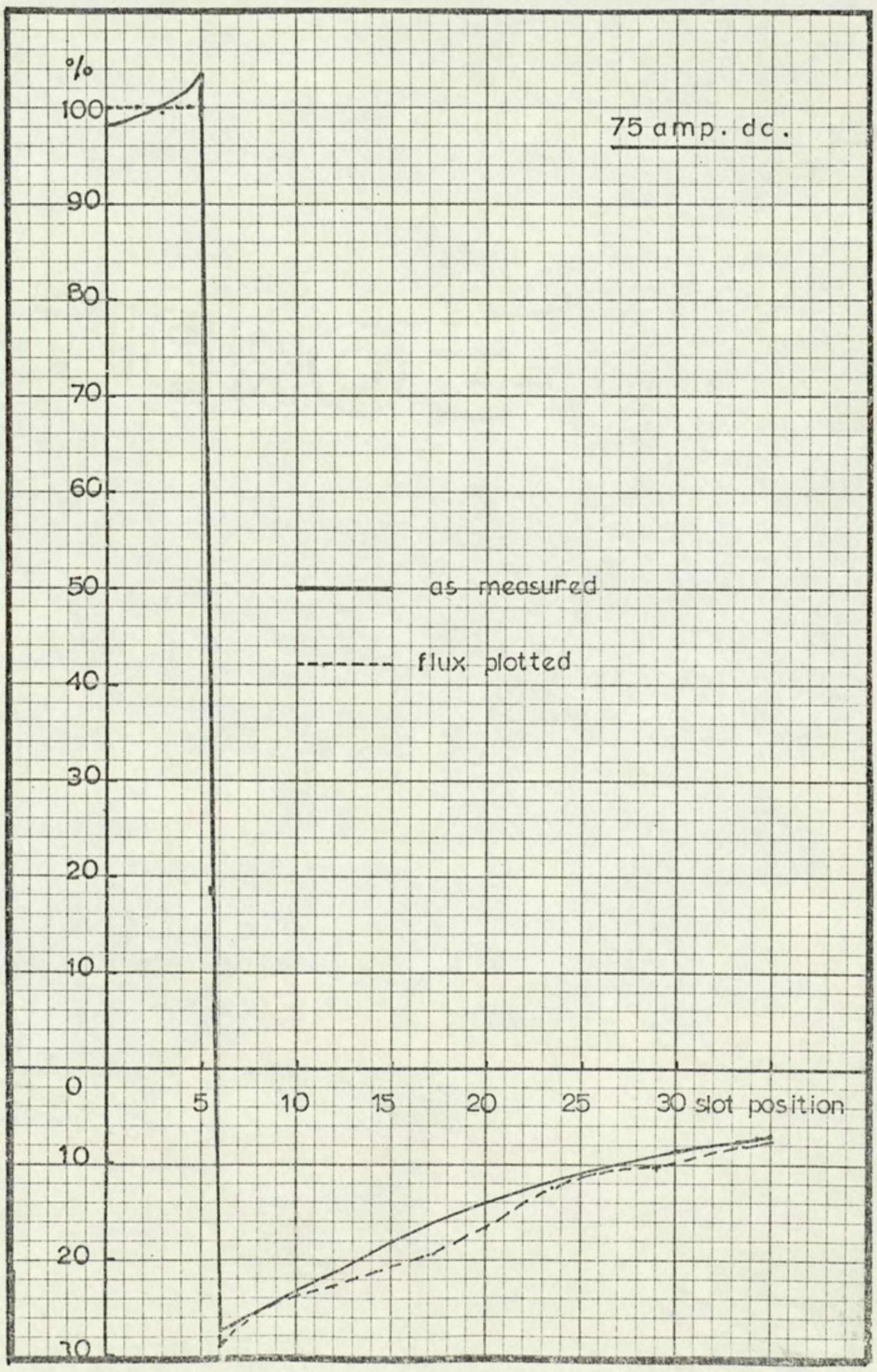

air gap flux density pattern with four consecutive coils excited with d.c. - 82 amps. FIG 5·1-4

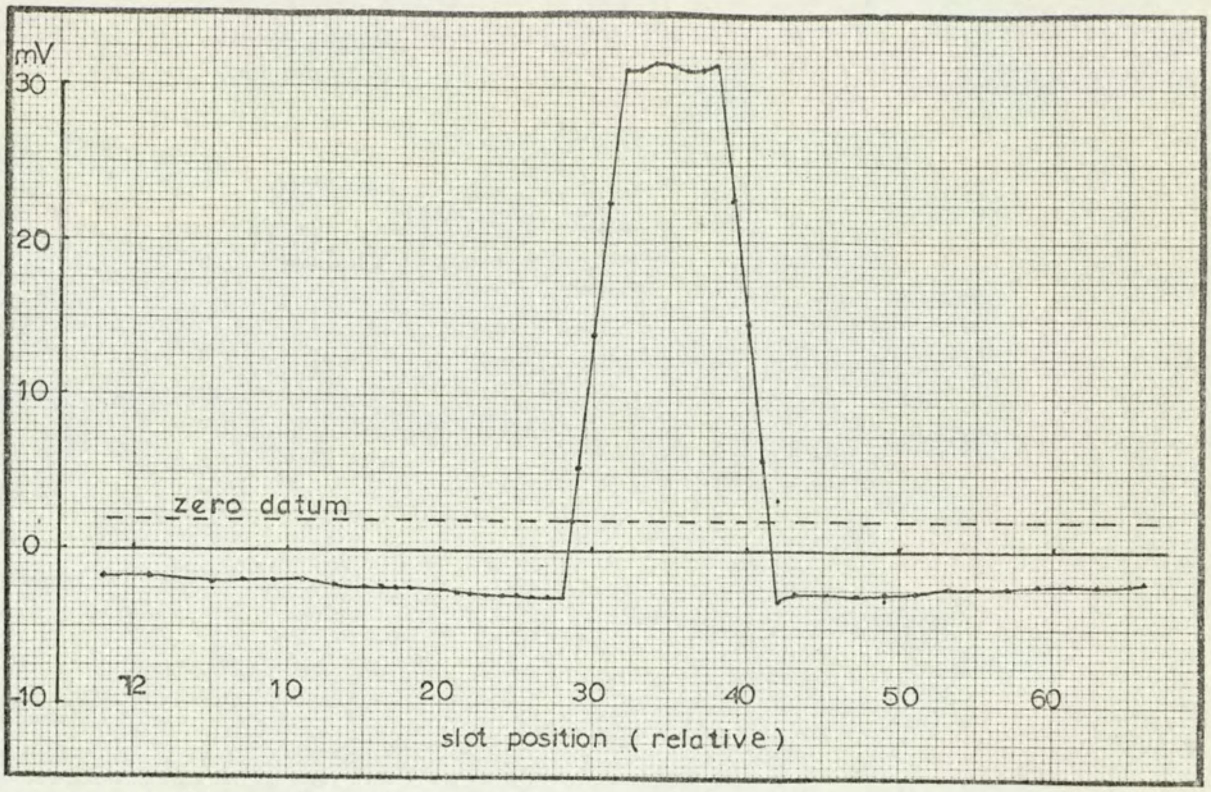

air gap flux density pattern with all coils in one phase excited with d.c.-80 amps. FIG 5·1-5

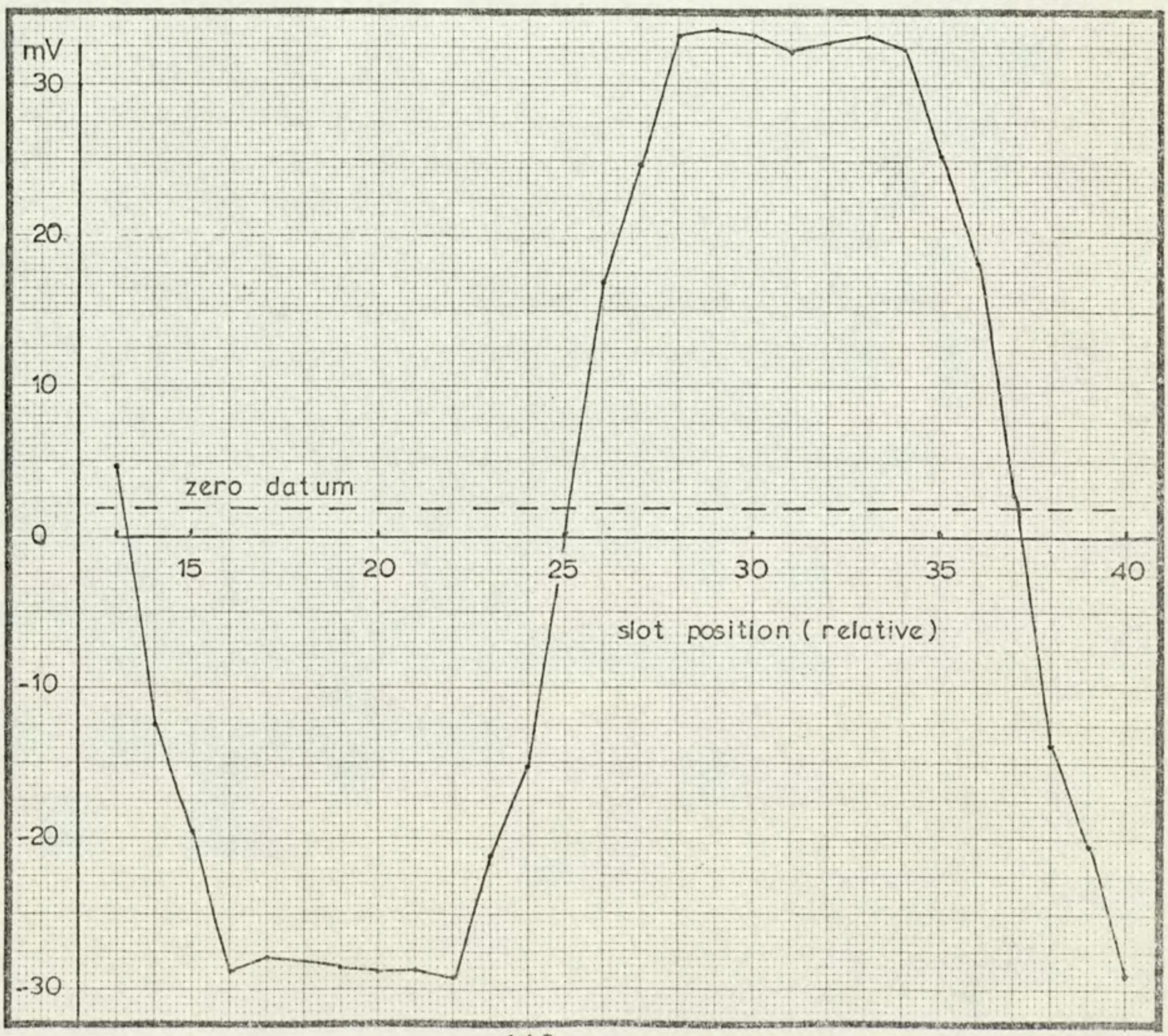

pattern.

c) All coils in one phase excited.

With the true six pole pattern being set up, the air gap pattern was approximately trapezoidal as would be expected. The slight irregularities at the crest of each pole group were due to a slightly loose probe mounting. The resultant plot is shown in Fig. 5.1 - 5., the current per coil being 80 amps.//In the three preceeding tests, the current source was a large bank of batteries. It was difficult to maintain these currents constant for long periods, and it was necessary to make slight proportional corrections. It is felt, however, that the study has served the original purpose of obtaining a reasonable pictorial representation of the air gap flux density patterns.

At this point in the test proceedure, a motor generator set in the laboratory was modified to obtain high stable values of current at very low voltages, for example 7 volts at 140 amperes, the generator being originally designed to work at 240 volts 200 amperes. The next three sets of tests were carried out with 140 amp. excitation. As a result of the difficulties experienced in the earlier tests the single probe carriage was modified so that the probe would be held central in the air gap opposite the tooth face and not hard up against it. For ease of comparison the results are shown together on Fig. 5.1 - 6.

d) Single phase excited.

This is test (c) repeated at higher values of excitation and with the probe central in the gap. The red phase was excited and used as a reference phase for this and the following tests.

e) Two phases excited in series.

It will be noted that this connection is sometimes used for the secondary connections of synchronous induction motors.

f) Three phases excited, series - parallel.

Here, the red phase was used as the series phase, the other two being connected in parallel. This connection is commonly used on synchronous induction motor secondary windings. Theoretically the m.m.f. per ampere compared with (e) above should be in the ratio of 0.875. From the tests, the corresponding flux density ratio is found to be 0.883. From Fig. 5.1 - 6 the areas under the plots for tests (e) and (f) have the ratio 0.86 approximately. For (d) and (f), the measured ratio of m.m.f. is 1.65 compared with the theoretical value of 1.75. Further, a shift of 2 slot pitches (30° Electrical) is observed for the peak positions of the respective waves, as expected.

Conclusions.

Apart from the unexpected cusp on the short pitched coil tests, the distribution on the air gap has followed the expected theoretical patterns. The ratio of m.m.f. for the different connections appears to follow theory. One interesting feature of these tests was that when the probe was held flat against the tooth face, slight deviations in the plane of the probe from that normal to the radius were reflected in the probe output. With the probe in the centre of the air gap minor deviations were barely discernable in the probe output. At the time of testing no significance was attached to these observations. However, air gap flux density pattern with d.c. excitation of 140 amp, varying stator connections.

FIG 5·1-6

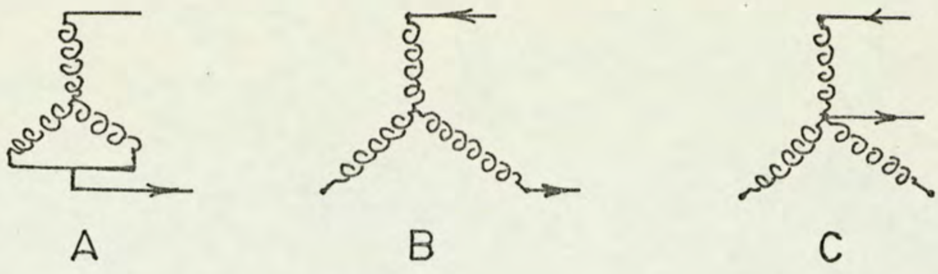

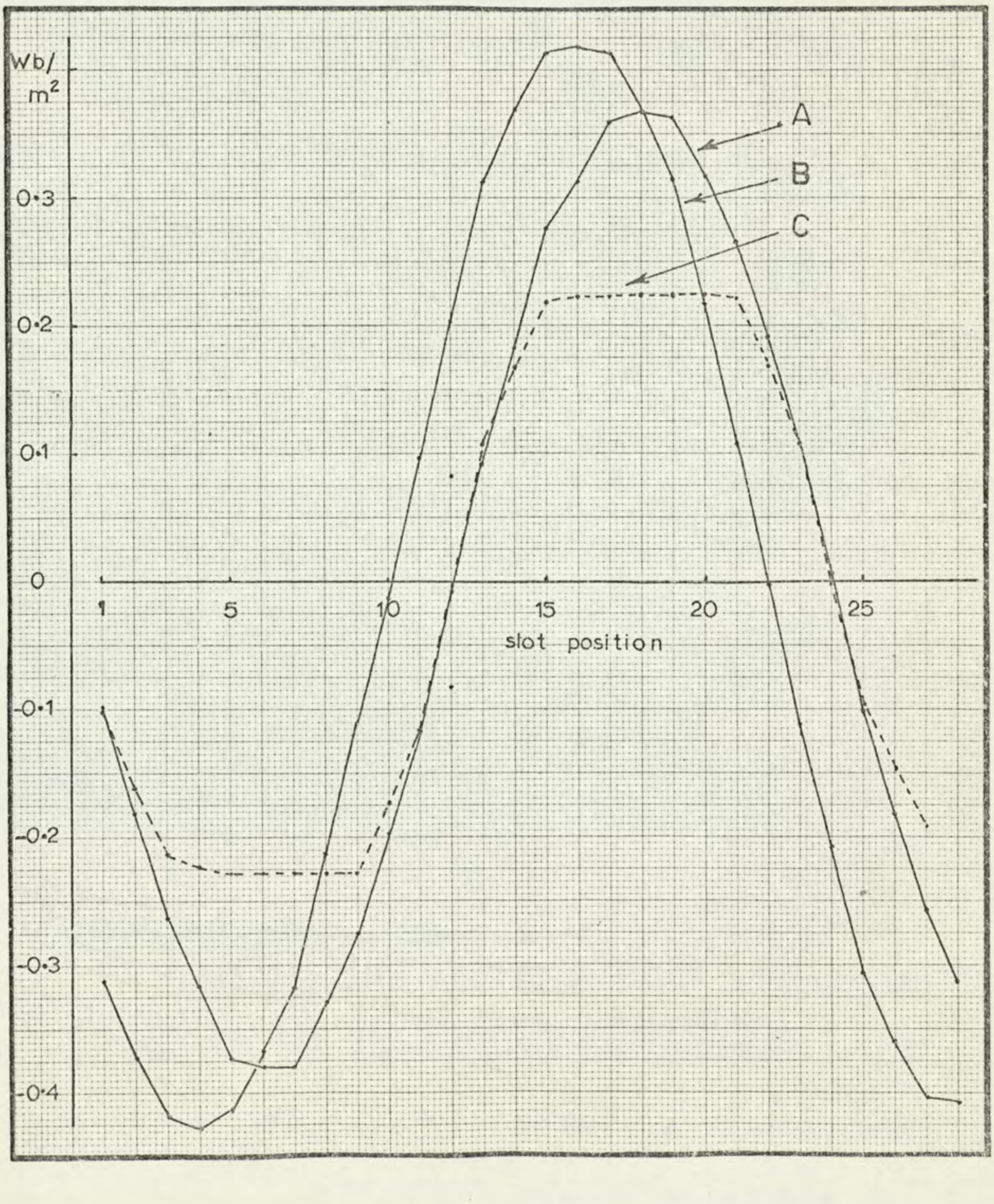

considering that the probe (2.0mm x 2.0mm) is being placed on a surface made up of 0.5mm laminations it appears plausible that the probe was picking up "tufting" or flux concentration at the edges of individual stampings due to roughness of the stator pack.

5.2 Core stamping surface flux density distribution with direct current excitation.

a) The single short pitched coil.

Using the single probe jig, see Fig. 2.0 - 2, the single probe was located on the stamping surface at three radial positions in turn along a slot centre line as illustrated in Fig. 5.2 - 1. The resultant flux density distribution normal to the stamping face for a series of slot positions is shown in Fig. 5.2 - 2. Although the probe was not mounted precisely, nevertheless there is clear evidence that the flux density over the coil pitch is tilted or skewed.

When examining the conductor disposition in the slot, it is observed that the high point coincides with the slot in which the current-carrying coil side is nearer the bottom of the slot while the low point corresponds to the slot in which the excited coil side is nearer to the stamping bore (air gap). It is seen that this skew effect weakens as the probe moves radially away from the slot. This proximity effect of conductor position in the slots is referred to later, in connection with Fig. 5.2 - 8.

b) Four consecutive coils excited.

As with the single coil test, there is still a tendency for the plot Fig. 5.2 - 3. to skew in the same manner. In this test the skew is not so pronounced, since the effect is spread over four slot pitches.

c) All coils in one phase excited.

With the true six pole pattern being set up, a symmetrical density distribution pattern would be expected. In Fig. 5.2 - 4. it will be noticed that there is still a tendency to skew. Further, considering the trace (1), the test positioning for probes.

FIG 5·2-1

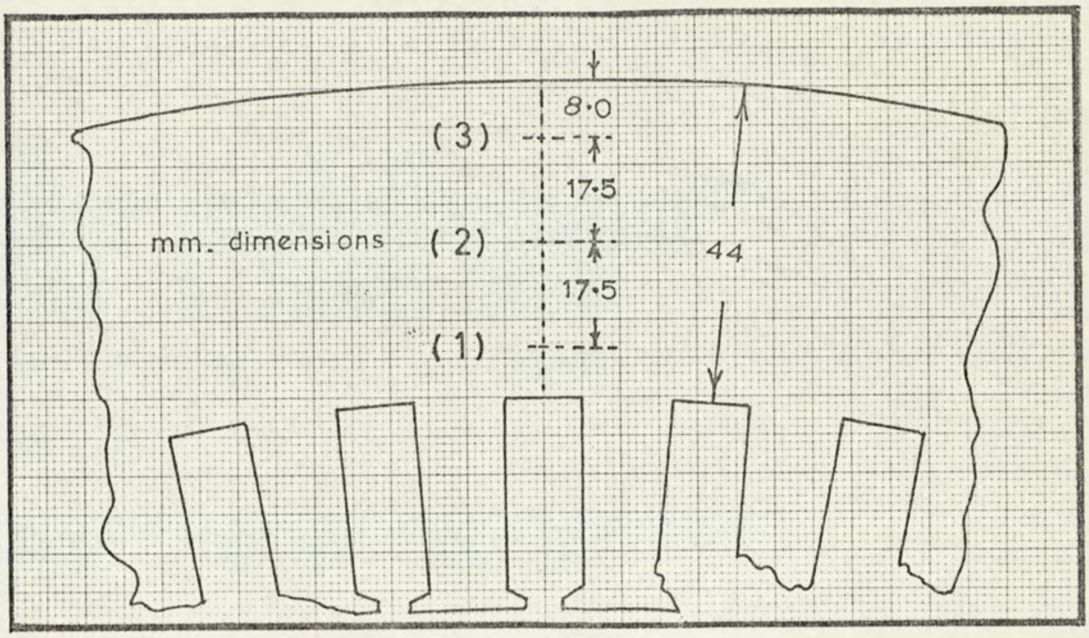

core surface flux density plot for a single coil excited with d.c.

FIG 5·2-2

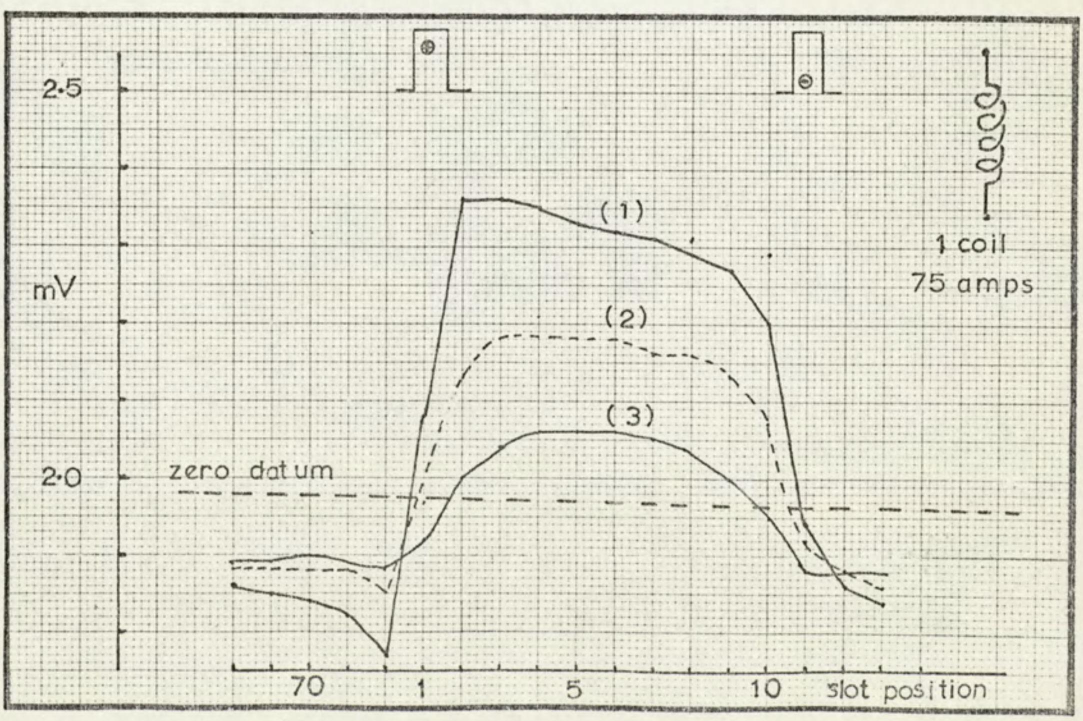

core end surface flux density plot — four consecutive coils excited with d.c. FIG 5·2-3

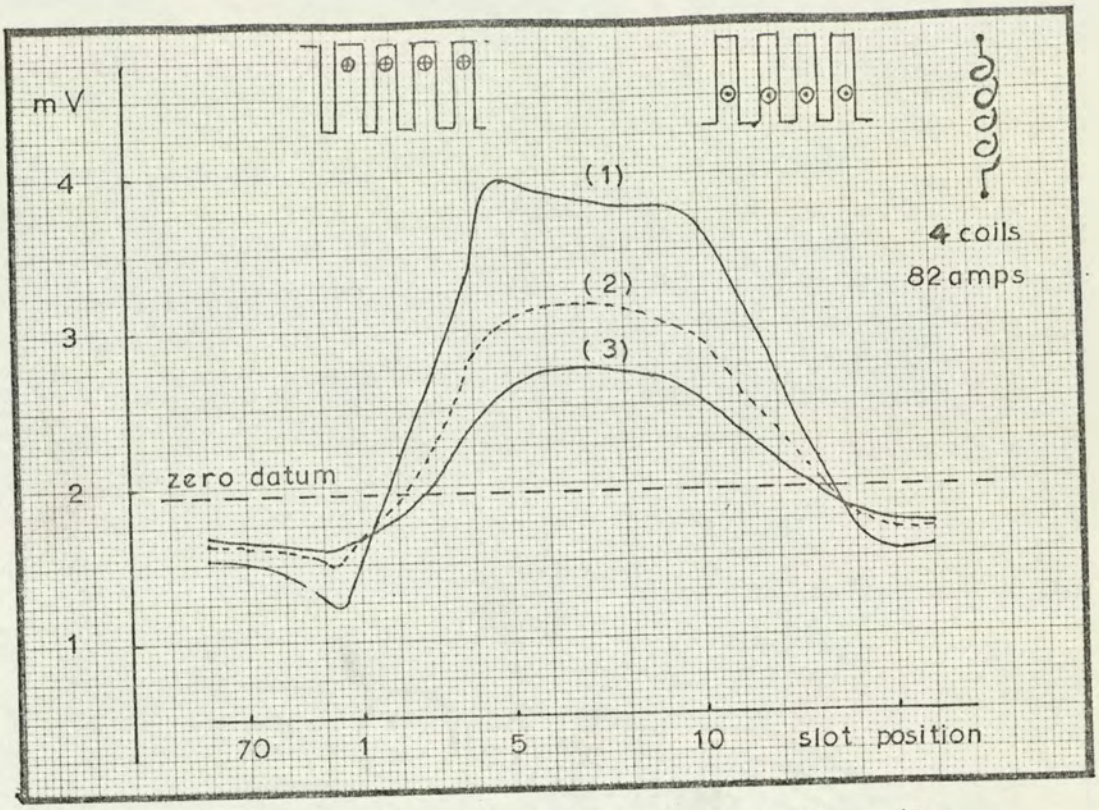

core end surface flux density plot — all coils in one phase excited with d.c. FIG 5·2-4

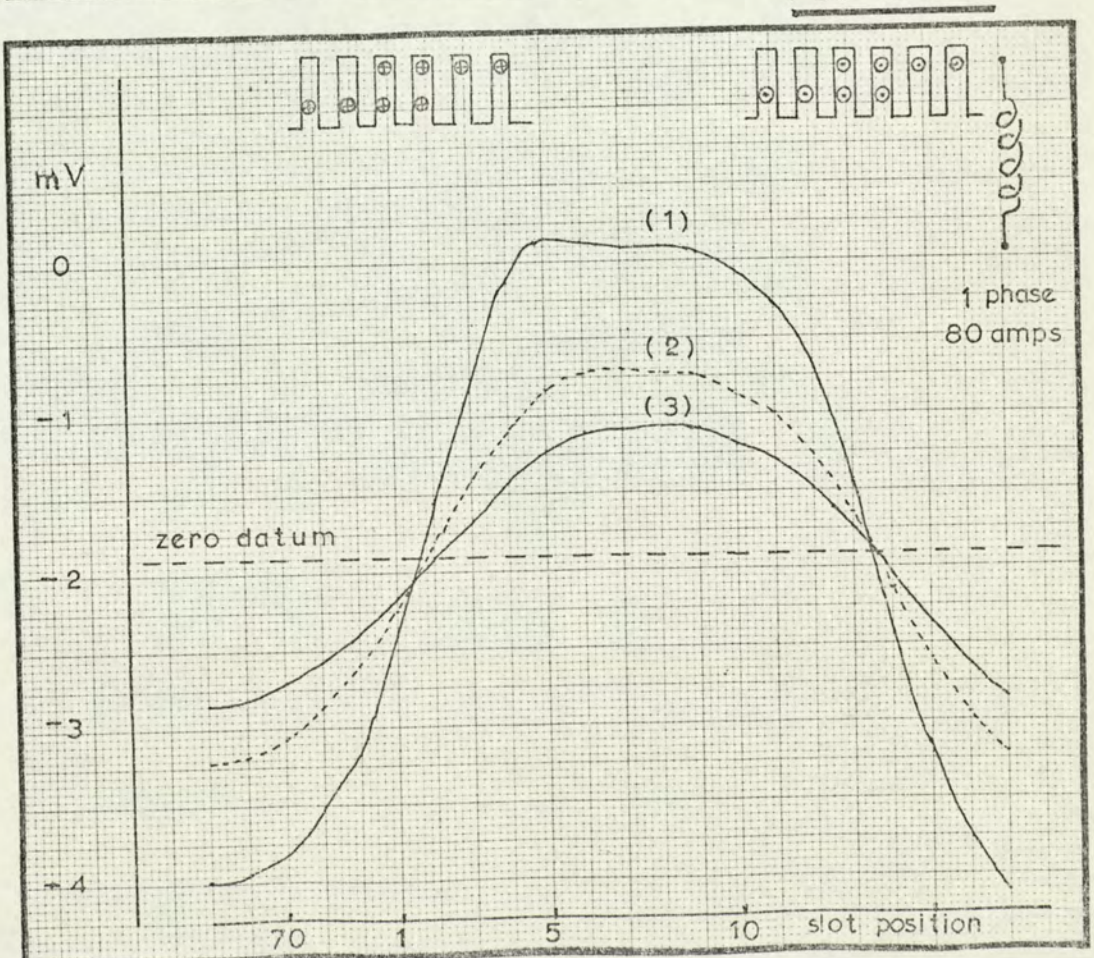

pattern between slot position 1 and 6 is the mirror image of that between 13 and 18, while the pattern between slot position 6 and 13 is the mirror image of that between 18 and 24. This is more than coincidence, and it is reasonably assumed that this phenomena is not due to faulty probe positioning. The pattern of trace (2) and trace (3) is extremely good, and more like the expected symmetrical pattern. Similar assymmetry of flux density distribution was also noticed on the end surfaces of the teeth, which again underlines the conclusion that conductor-slot-position does influence the flux density pattern.

The influence of slot ampere-conductor content was investigated by examining the core end-surface flux density, with three-phase excitation of the stator winding. The Hall probe positions are shown in Fig. 5.2 - 5, which also shows the resulting Hall probe output plotted as a function of circumferential displacement. In the vicinity of the stator conductors (positions A and B), the flux density is seen to peak every fourth slot, which is the spacing of slot-pairs carrying conductors of the same phase. The coil phase-grouping is illustrated in Fig. 5.2 - 8. The author is aware of a 200 MW turbo-generator in which the stampings at the back of the slot were badly burnt. The burnt areas showed a pattern which corresponded to the ampere-conductor concentration pattern as referred to here.

The Hall probe jigs are shown in the photograph, Fig. 5.2 - 6. The individual probes are clearly seen in the stator core jig, B, their numbering and relative positioning being indicated diagramatically in Fig. 5.2 - 7. The ten probes are arranged along four radial lines, exactly one-third slot pitch apart, and so that seven circumferential flux density plots showing effect of grouping of conductors.

FIG 5·2–5

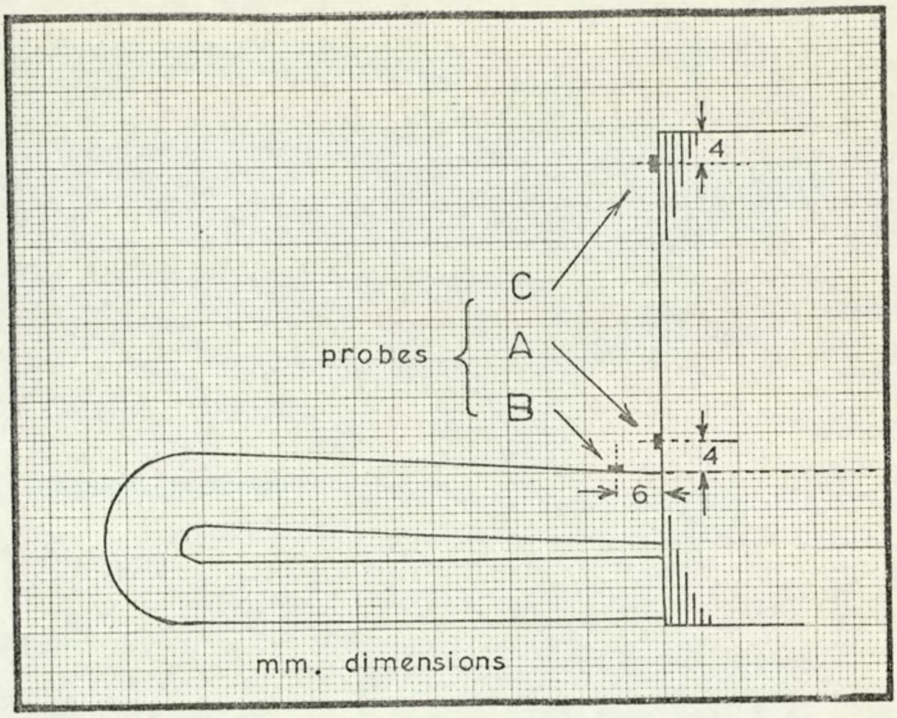

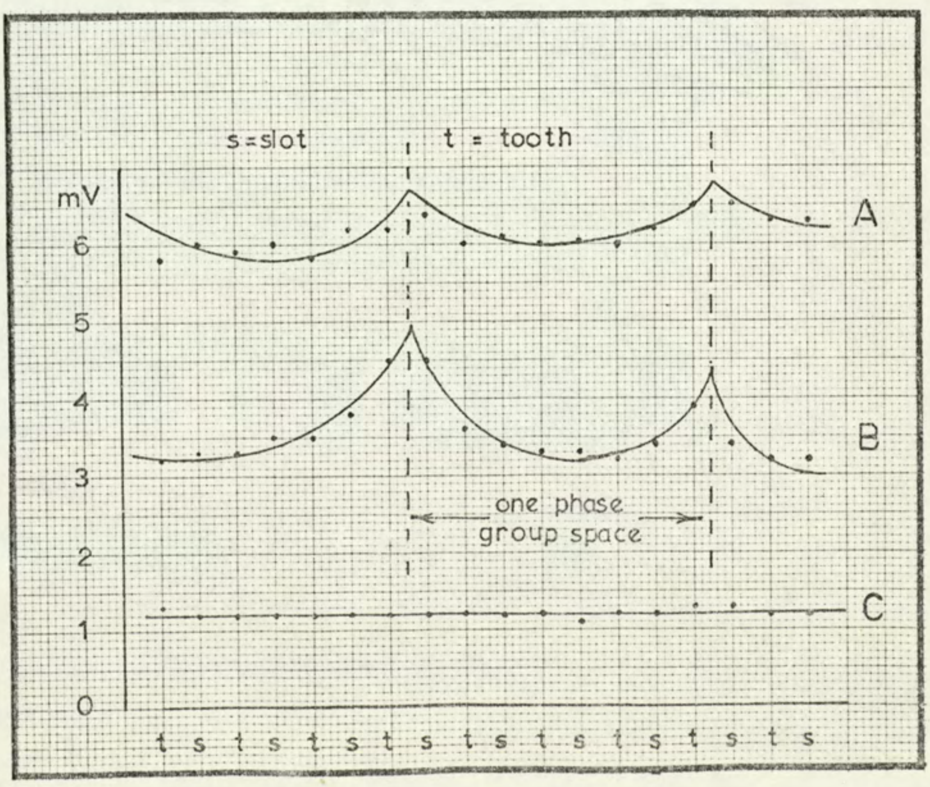

FIG 5·2-6

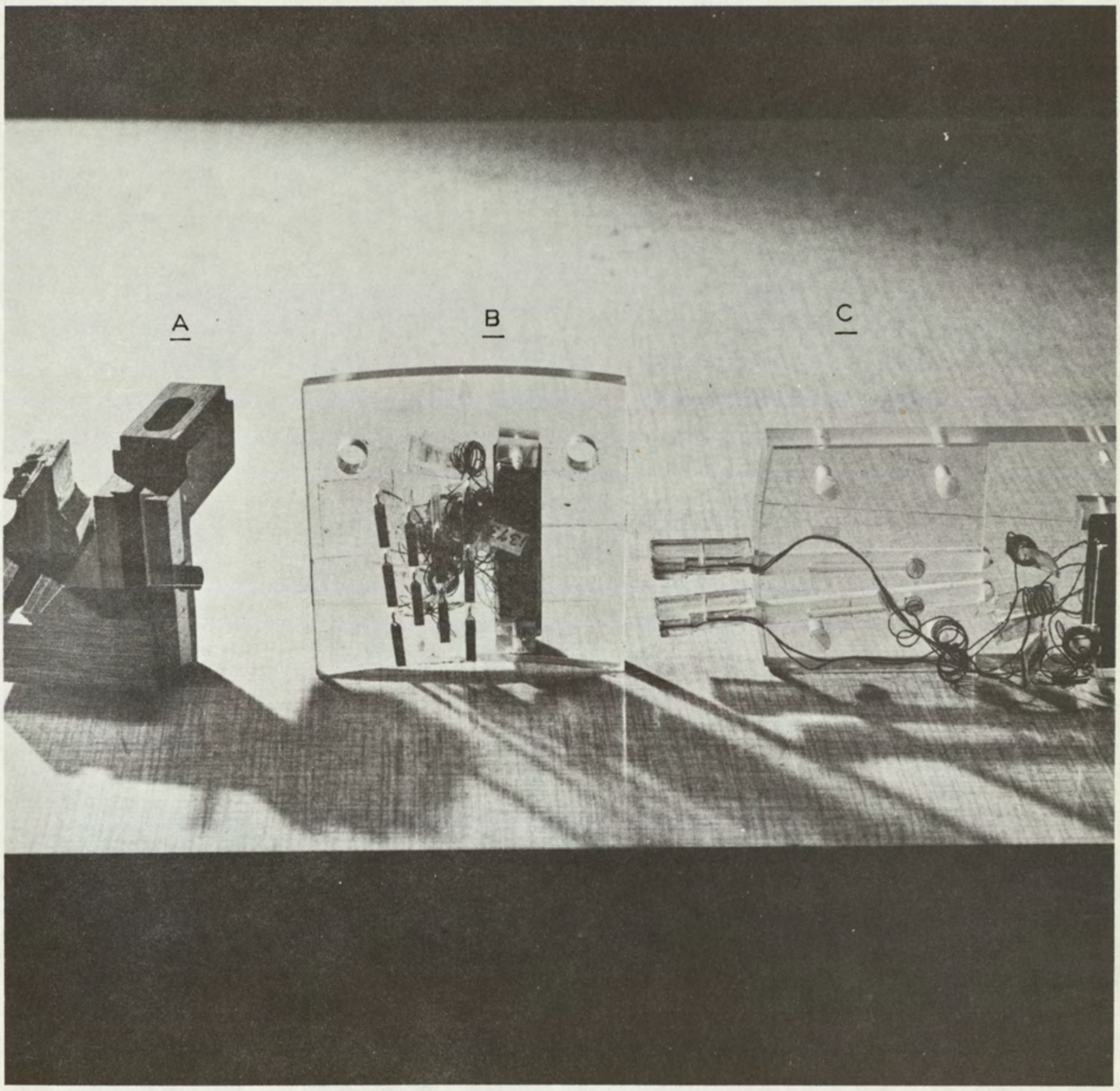

A – SINGLE PROBE JIG

B – STATOR CORE JIG

C – STATOR TOOTH JIG

JIGS USED FOR MOUNTING PROBES

slot numbering with relative phase disposition.

FIG 5·2-8

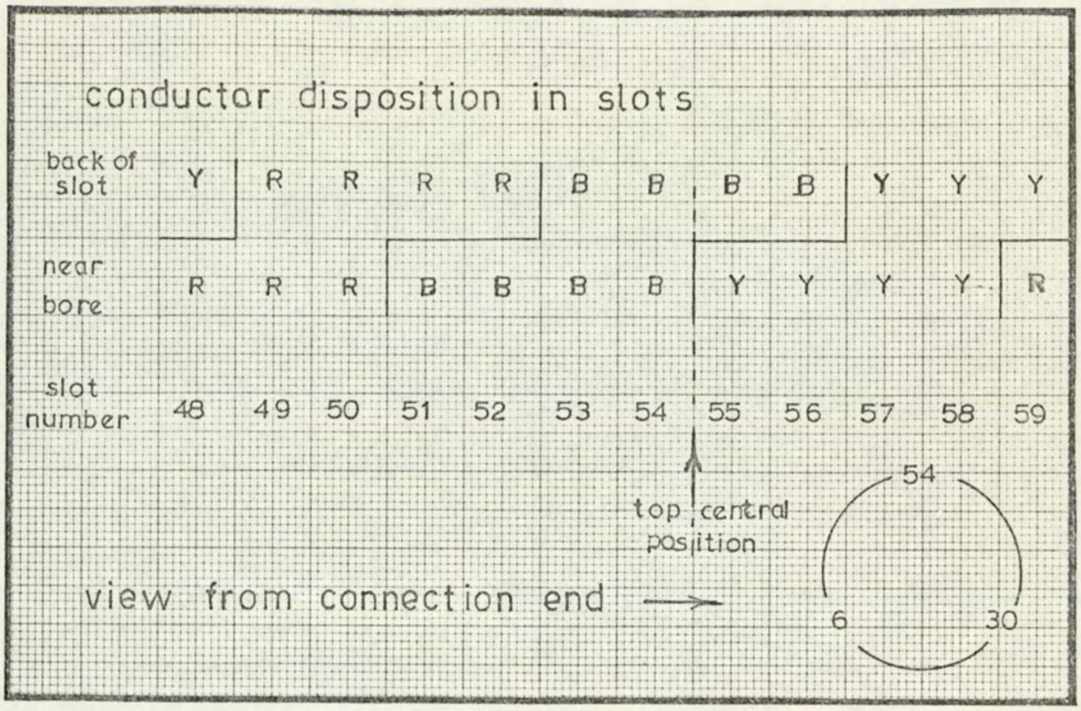

probe numbering on jig shown in figure 5·2-6

FIG 5·2-7

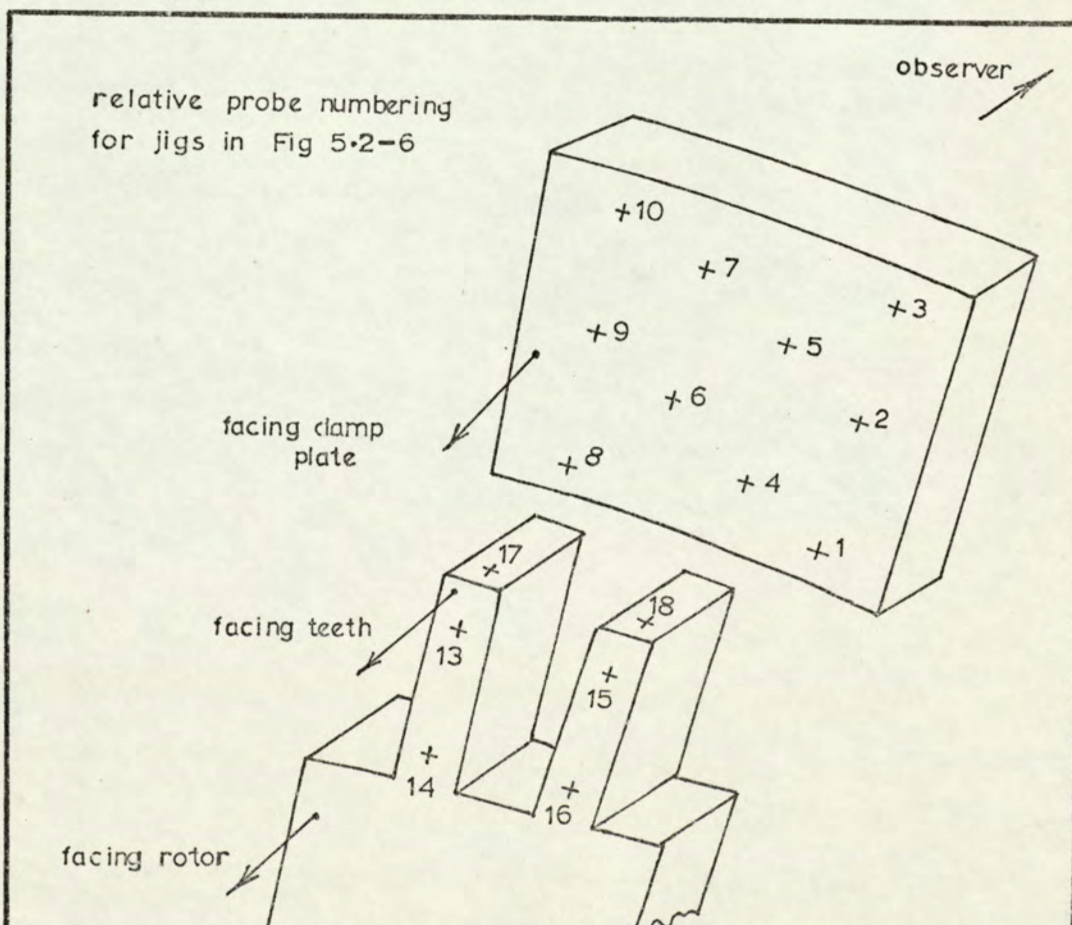

loci of different radii are described when the jig is moved in its mounting. This gives a reasonable scan of the core and clamp plate end surface. Fig. 5.2. - 6A shows the single-probe jig, which provides a means of similar scanning using one probe only. The positioning of the six probes and the stator-tooth jig (Fig. 5.2 - 6C) is shown diagramatically in Fig. 5.2 - 7. Probes 17 and 18 are intended to measure flux density on the inner circumferential surface of the clamp plate.

5.3 Comparison of clamp-plate surface flux-density distribution with a.c. and d.c. excitation of the stator winding.

In the preceeding section, flux density plots normal to the stator stampings end surface were examined in some detail. To complete this preliminary study, a clamp-plate surface flux density investigation was carried out using the quarter inch mild steel, and the one inch aluminium clamp plates.

Using the single probe universal jig, plots of clamp surface flux density against radial distance were obtained for various d.c. excitations with both the three-phase series parallel, and two-phase-series connections of the stator windings. For both connections, the circumferential position of the Hall probe was such as to give maximum output voltage.

The Hall probe measurements were repeated with three phase a.c. excitation of the stator windings, and so that the results could be conveniently compared with the d.c. tests, the same circumferential position as for the series parallel d.c. connection was chosen (i.e., along the axis of the red phase), and the peak value of probe output voltage recorded. With this arrangement the peak value of a.c. phase excitation is equivalent to the d.c. red phase excitation, series-parallel connection, and the Hall probe peak output stage can then be compared directly with the output of the d.c. case.

The test curves obtained are recorded in detail, in Fig. 5.3 - 1 to 3, as it was hoped to use them in the future to correlate this experimental work with the analysis carried out by Davies (8) on eddy-current couplings.

radial surface density traces with varying d.c. stator excitation. stator connected series-parallel with aluminium and mild steel clamp plates.

FIG 5·3-1

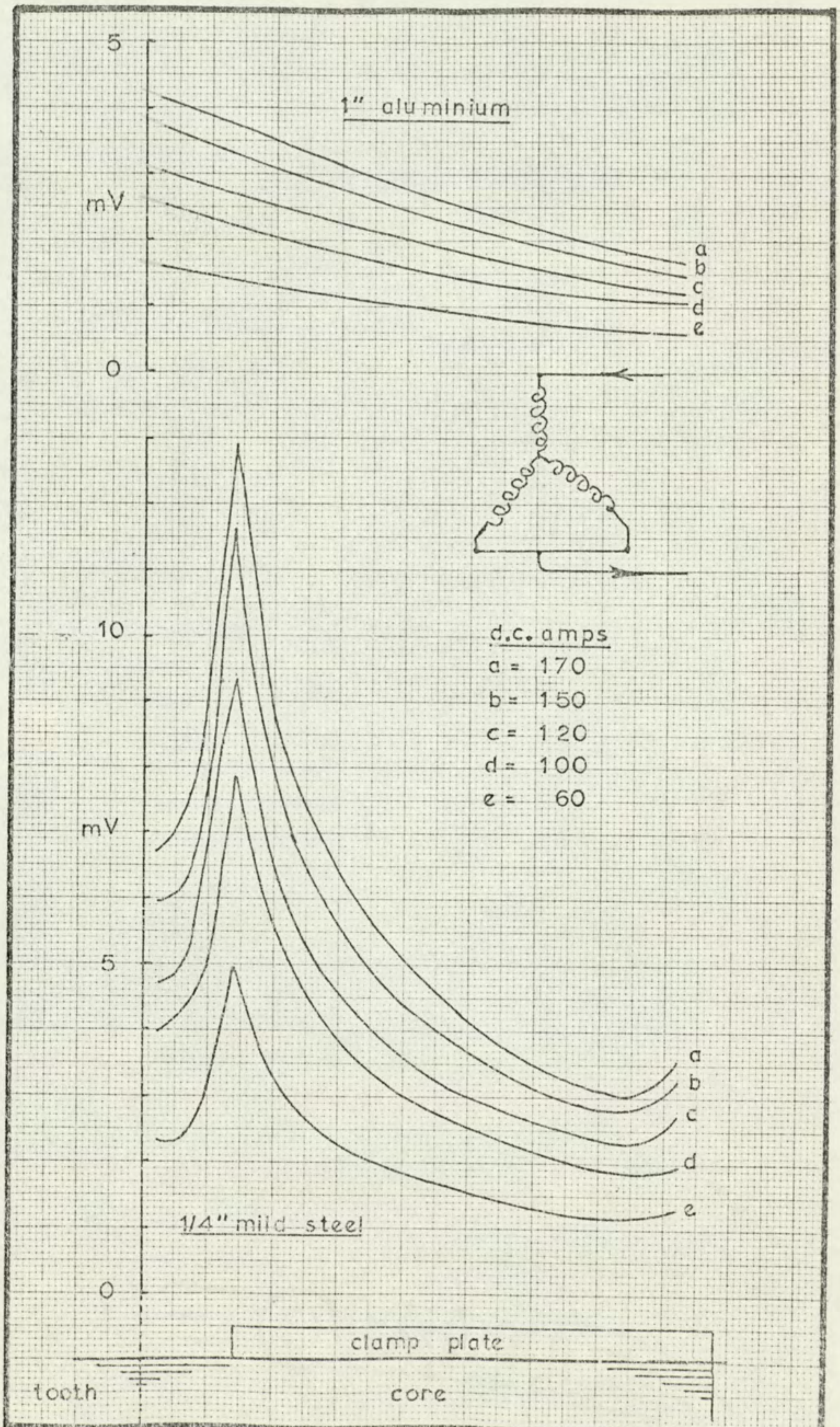

radial surface density traces with varying d.c. stator excitation. stator connected 2 phases in series, with aluminium and mild steel clamp plates.

FIG 5·3-2

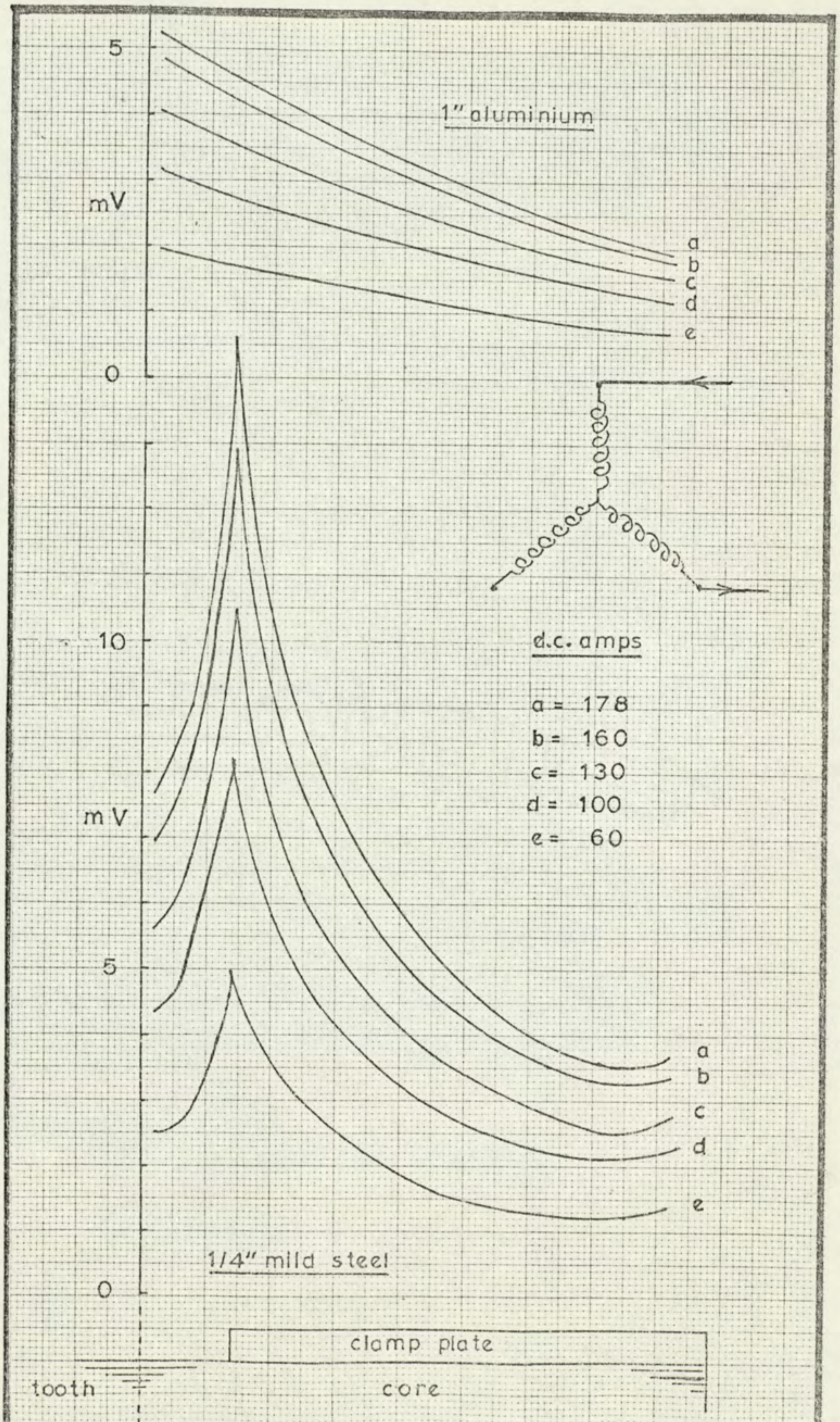

radial surface density traces with varying a.c. stator excitation, excited 3ph 50Hz with aluminium and mild steel clamp plates.

FIG 5·3–3

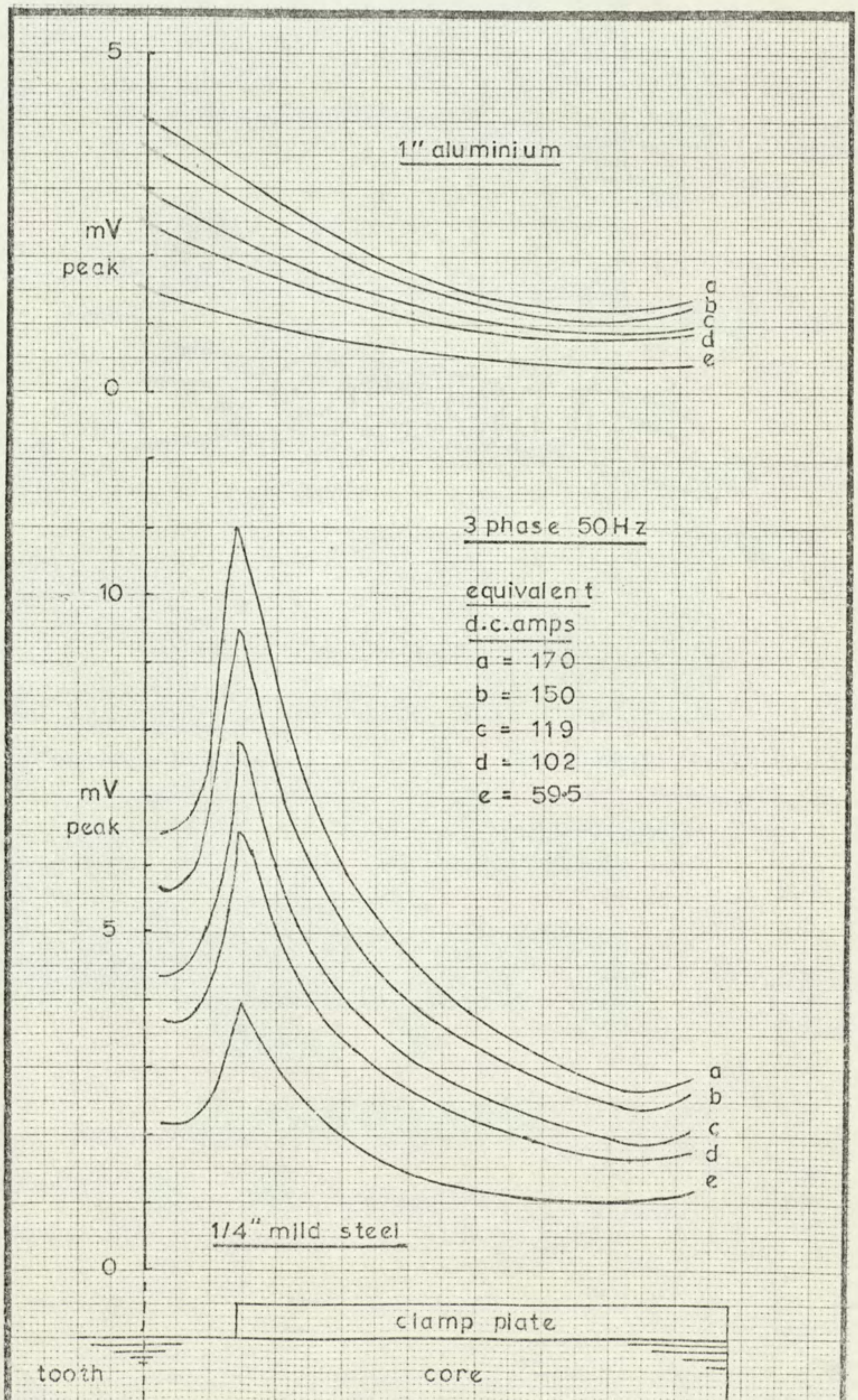

To make a comparison of (a) the two d.c. connections, and (b) the a.c./d.c. excitation, the Hall probe output voltages were plotted against excitation for several radial positions. In the case of the aluminium clamp-plates this relationship showed good linearity in all cases, and enabled the comparison ratios to be listed as shown in the left hand section of the following table.

Ratios of Hall Probe Output Voltages.

	1" Aluminium			$\frac{1}{4}$" Mild Steel	
Radial Distance from Winding Surface	15mm	25mm	35mm	19mm	25mm
$\frac{\text{d.c. 3ph. series parallel}}{\text{d.c. 2ph. series}}$	0.84	0.83	0.87	0.925	0.925
$\frac{\text{a.c. 3ph.}}{\text{d.c. 3ph. series parallel}}$	0.71	0.60	0.64	0.88	0.90

For the quarter inch mild steel plates, linearity of the Hall-probe-output/stator-excitation-current relationship, although generally good, allowed reliable comparison ratios to be calculated only at the middle (radial) part of the clamp plate. These ratios are given in the right hand section of the above table. The slight deviation from linearity in the case of the mild steel plates was thought to be due to the flux-concentrating effect of the sharp edges, an effect shown clearly by Figs. 5.3 - 1 to 3.

With respect to the ratios of Hall probe outputs for the two d.c. conditions, it is interesting to compare these with the corresponding theoretical ratio of maximum m.m.f. per ampere, which is 0.875. For the aluminium plates, which must give similar results to measurements in air, 1" axial distance from the core, the flux density (Hall probe output) difference exaggerates the winding m.m.f. difference, while the ferrous plate tends to even out the difference.

When considering the a.c./d.c. ratios, the fall-off from unity is an indication of the induced eddy currents present in the clamp plates, and it is evident that these eddy currents have a greater proportionate effect of the resultant flux density in the case of aluminium than in the case of mild steel. Further, the eddy current effect is more marked in the middle (radial) section of the aluminium plate, than towards the radial boundaries. Figs. 5.3 - 1 to 3 in general show very clearly the strong tendency for the flux to concentrate at the sharp inner edge of the unbevelled ferrous clamp plate. Such an effect is entirely absent for the non-ferrous (metallic) clamp plate, the axial flux density continuing to rise slightly as the Hall probe leaves the clamp plate surface, moving towards the winding overhang. The ratio of flux densities at the radially inner and outer edges is approximately 4:1 for the M.S. clamp plate, and approximately 2.5:1 for the aluminium clamp plate. Assuming that the loss distribution in the clamp plate is related to the distribution of external surface flux density, and that the loss magnitude is proportional to the square (at least) of the magnitude of this density, the loss is heavily concentrated at the inner radial edge of ferrous clamp plates. Thus the clamp plate loss can be considered as being proportional to the inner diameter of the clamp plate, all other things being equal. For non-ferrous metallic clamp plates, the loss is less heavily concentrated, but a diameter slightly in excess of that at the inner surface may be taken, for similar proportionate scaling.

Finally, it is worth noting that the level of excitation for all these tests was sufficiently low for any additional effects from the stator core (referred to in Section 7.1) to be negligible. That is, the clamp surface flux densities measured (as Hall probe output voltages) in these tests are believed to be due solely to the overhang m.m.f., and any resulting eddy currents.

Chapter VI.

6.0 Clamp plate loss investigation - introduction.

Originally, it had been intended to carry out the loss measurements on the models with stator currents up to 180 amperes. This figure corresponded to an ampere conductor per centimeter loading of 527. In initial tests, the stray losses were barely discernable. A quick check showed that after 200 amp loading, these losses were more pronounced. It was found possible to work up to 240 amp on the short core, and up to only 220 amp on the long core. At these higher loadings, the stator winding heated up very quickly, making it impossible to take readings as a series of points on a curve. Accordingly, it was decided to work at a reasonably constant temperature for all readings. The model was pre-warmed to approximately 30°C; the load current was brought up rapidly and a set of readings taken, and the current then reduced to zero value. The core, clamp plates and the winding temperatures were continually monitored. The copper losses were corrected for the winding temperature. By this technique it was possible to achieve a degree of consistency in the observations, provided readings of meters were taken quickly. The model was allowed to cool before the next set of readings. In general, it took nearly 20 minutes before the next set of readings could be recorded.

During the preliminary tests, the clamp plate surfaces were explored using the single probe. The concentration of flux at the corner edges of the ferrous clamp plates was observed as described earlier and as a result, a series of extra tests were carried out. These are described in detail in Section 7.0. At the same time during these tests, quite by accident one of the quarter inch mild steel rings had been badly centred, such that one side of the ring was almost touching the winding. It was noted that this side of the ring was appreciably hotter than the diametrically opposite side.

At about the same time, the author had the opportunity of taking the Hall Probe equipment into the works test area of the Parson's Witton Factory to investigate an 8,350 horse power induction motor which had been exhibiting high iron losses. These tests are described in detail later. The point of interest however was that the author observed that the mild steel clamp plates were very close to the winding and showed a number of hot spots round the circumference. As a result of these independent sets of observations, the scope of the present tests was extended. The additional quarter inch mild steel rings with small and large clearances were manufactured, as was a one inch mild steel ring with no bevel. These rings are detailed in Fig.2.2 - 2 in section 2.2.

The extension of the test range to 240 amp. gave a working value of 700 amp conductor per cm., which applies to conventionally air cooled salient pole machines of over 400 MVA rating.

During the various exploratory tests with the Hall probe, it was noticed that when the Hall probe was inserted in the air gap of the two models, the long core appeared to produce more flux per ampere, over the working range of 160 - 240 ampere. Making allowances for the different core length and leakage reactance, it was noticed that the short core required relatively more voltage to pass a given current. This had been initially attributed to the inaccuracy of the estimation of leakage reactances on these very short core lengths. However, it became clear that this discrepancy was the result of the two cores possesing different magnetising characteristics. This is illustrated in section 6.1, and leads to a modification in the clamp plate loss formula.

6.1 Loss measurements - tabulations.

From Section 2.0 the test expression for clamp plate loss is given as

$$\text{Clamp plate loss} = \frac{3\,W_1 - W_2}{2}$$

where W_1 and W_2 are the input powers at the same current, less calculated copper losses, for the short and long core models respectively. This expression assumes that flux densities in the core and teeth of the two models are equal, at the same excitation current. Taking the air-gap flux densities to be an indication of the densities in the iron, Fig. 6.1 - 1 shows that there is in fact a difference. Fig. 6.1 - 1 is the relationship between air-gap flux density and stator current for the two models, the flux density was measured directly, using a single Hall probe, held midway in the air-gap, perpendicular to the centre-line of a stator tooth. Over the working range of 160 to 240 amps, the flux density in the long core model for a given current is greater than that in the short core model. If the ratio of long-core/short-core flux densities at a given current is 'r', then the ratio of long-core/short-core iron losses at the same current is $3r^z$. From loss curves for silicon steel, plotted on a log-log basis, the value of 'z' is seen to be 2.0 for densities up to 1.0 Wb/m^2, and 2.5 above 1.15 Wb/m^2. The design parameters of the models show that over the working range, the densities in teeth and core are greater than 1.15 Wb/m^2. Thus,

$$r^z = r^{2.5} = K_1$$

where K_1 is referred to as a correction factor, and is independent of frequency. The modified loss equations now

CALCULATION OF CORRECTION FACTOR K_i FROM MAGNETIC CHARACTERISTICS OF THE TWO MODELS

FIG 6·1-1

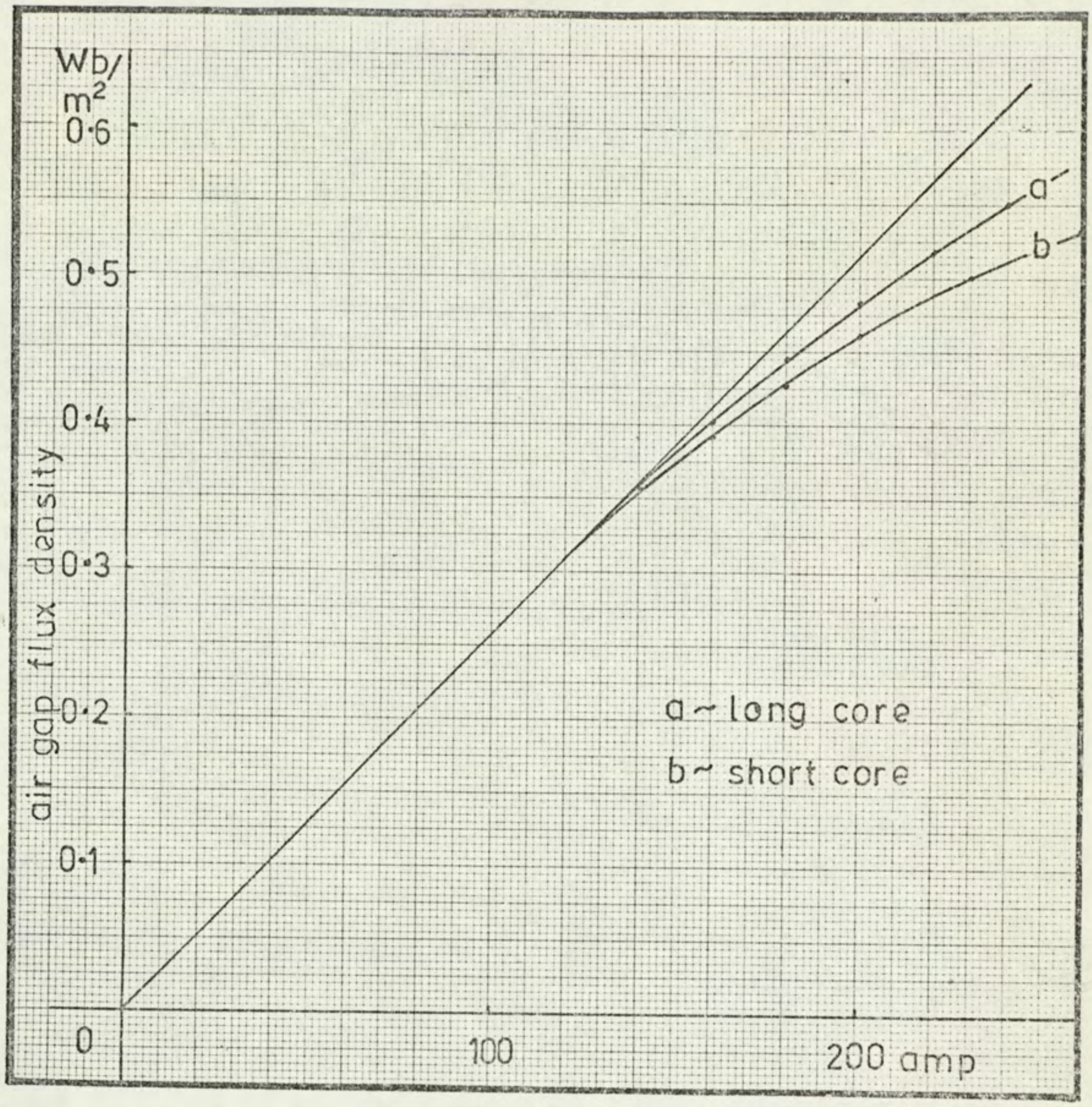

amp	$\frac{B_{long}}{B_{short}} = r$	$Ki = r^{2\cdot5}$
160	1·025	1·064
170	1·027	1·068
180	1·035	1·089
190	1·039	1·099
200	1·050	1·132
210	1·054	1·144
220	1·060	1·157
230	1·065	1·171
240	1·073	1·193

become,

$$W_1 = \text{Iron loss} + \text{Clamp plate loss}$$

$$W_2 = 3\,K_i \times \text{Iron loss} + \text{Clamp plate loss}$$

$$\boxed{\text{Clamp plate loss} = \frac{3\,W_1\,K_i - W_2}{3\,K_i - 1} = W_c}$$

Obviously, when $K_i = 1.0$, the expression reduces to the form given in Section 2.0.

The input power to each model in turn was measured, corrected for stator winding copper loss, and plotted against stator current. From these curves, values of W_1 and W_2 were taken and are tabulated in Fig. 6.1 - 2 to 9, which also derive the losses for various clamp plates using the above expression.

1/4" mild steel - 6·05 mm radial clearance					FIG 6·1-2
amps	W1 watts	W2 watts	3Ki	3Ki W1	total clamp loss
40Hz	(1)	(2)	(3)	(1)x(3)=(4)	$\frac{(4)-(2)}{(3)-1\cdot 0}$
160	395	458	3·191	1260	366
170	477	541	3·204	1530	448
180	570	632	3·267	1862	542
190	670	733	3·297	2205	643
200	775	840	3·396	2630	748
210	890	960	3·432	3050	860
220	1035	1080	3·471	3590	1019
230	1175	1220	3·513	4130	1159
240	1330	1365	3·579	4760	1318
50Hz					
160	503	610	3·191	1608	455
170	606	722	3·204	1940	552
180	719	850	3·267	2350	662
190	844	985	3·297	2780	783
200	985	1135	3·396	3340	922
210	1140	1300	3·432	3910	1075
220	1310	1480	3·471	4545	1242
230	1500	1680	3·513	5270	1430
240	1700	1890	3·579	6080	1625
60Hz					
160	625	820	3·191	1995	537
170	750	975	3 204	2405	648
180	886	1140	3·267	2900	776
190	1040	1330	3·297	3420	912
200	1210	1540	3·396	4110	1075
210	1400	1765	3·432	4800	1250
220	1600	2015	3·471	5550	1432
230	1830	2290	3·513	6430	1648
240	2080	2550	3·579	7440	1900

1" mild steel with bevel					FIG 6·1-3
amps	W1 watts	W2 watts	3Ki	3Ki W1	total clamp loss
40Hz	(1)	(2)	(3)	(1)x(3)=(4)	$\frac{(4)-(2)}{(3)-1\cdot0}$
160	420	508	3·191	1340	380
170	505	605	3·204	1620	460
180	600	706	3·267	1965	555
190	705	830	3·297	2330	652
200	830	960	3·396	2820	776
210	955	1110	3·432	3280	895
220	1100	1290	3·471	3815	1020
230	1260	1490	3·513	4420	1165
240	1445	1715	3·579	5190	1345
50Hz					
160	580	820	3·191	1850	470
170	675	955	3·204	2160	547
180	790	1115	3·267	2580	646
190	920	1295	3·297	3030	756
200	1070	1500	3·396	3640	895
210	1245	1720	3·432	4275	1050
220	1455	2005	3·471	5050	1230
230	1700	2350	3·513	5980	1445
240	1975	2755	3·579	7090	1680
60Hz					
160	720	1065	3·191	2300	563
170	855	1270	3·204	2740	668
180	1025	1520	3·267	3355	810
190	1210	1830	3·297	4000	945
200	1425	2180	3·396	4850	1115
210	1680	2540	3·432	5780	1335
220	1930	2970	3·471	6700	1510
230	2200	3410	3·513	7710	1715
240	2550	3930	3·579	9130	2015

1" meehanite with bevel					FIG 6·1-4
amps	W1 watts	W 2 watts	3Ki	3Ki W1	total clamp loss
40Hz	(1)	(2)	(3)	(1)x(3)=(4)	$\frac{(4) - (2)}{(3) - 1{\cdot}0}$
160	435	480	3·191	1385	414
170	510	565	3·204	1638	486
180	595	665	3·267	1945	563
190	690	775	3·297	2275	653
200	800	905	3·396	2720	758
210	925	1050	3·432	3175	876
220	1065	1220	3·471	3700	1005
230	1222	1410	3·513	4370	1180
240	1400	1640	3·579	5000	1300
50Hz					
160	555	720	3·191	1770	480
170	660	860	3·204	2120	571
180	780	1020	3·267	2550	674
190	920	1200	3·297	3030	798
200	1085	1410	3·396	3680	950
210	1265	1670	3·432	4330	1100
220	1480	1980	3·471	5130	1275
230	1735	2330	3·513	6090	1500
240	2020	2750	3·579	7220	1730
60Hz					
160	740	1085	3·191	2360	580
170	880	1295	3·204	2820	692
180	1030	1535	3·267	3370	810
190	1205	1810	3·297	3980	945
200	1405	2115	3·396	4770	1110
210	1620	2450	3·432	5540	1275
220	1875	2825	3·471	6500	1490
230	2150	3240	3·513	7550	1720
240	2420	3660	3·579	8680	1950

1" mild steel - no bevel					FIG 6·1-5
amps	W1 watts	W2 watts	3Ki	3Ki W1	total clamp loss
40Hz	(1)	(2)	(3)	(1)x(3)=(4)	$\frac{(4) - (2)}{(3) - 1{\cdot}0}$
160	406	600	3·191	1300	320
170	495	715	3·204	1590	397
180	595	850	3·267	1950	484
190	720	990	3·297	2375	600
200	850	1150	3·396	2885	724
210	1000	1320	3·432	3432	868
220	1170	1505	3·471	4060	1034
230	1360	1715	3·513	4775	1220
240	1575	1940	3·579	5650	1440
50Hz					
160	535	865	3·191	1710	386
170	640	1015	3·204	2050	470
180	765	1190	3·267	2500	578
190	910	1392	3·297	3000	700
200	1085	1630	3·396	3690	860
210	1290	1900	3·432	4430	1040
220	1525	2210	3·471	5300	1250
230	1790	2540	3·513	6290	1495
240	2080	2900	3·579	7480	1780
60Hz					
160	750	1210	3·191	2390	539
170	890	1455	3·204	2850	631
180	1050	1720	3·267	3440	758
190	1260	2010	3·297	4160	935
200	1510	2330	3·396	5120	1165
210	1750	2655	3·432	6000	1380
220	2020	3010	3·471	7000	1615
230	2300	3380	3·513	8090	1880
240	2580	3820	3·579	9280	2120

1" brass with bevel					FIG 6·1-6
amps	W1 watts	W2 watts	3Ki	3KiW1	total clamp loss
40Hz	(1)	(2)	(3)	(1)x(3)=(4)	$\frac{(4)-(2)}{(3)-1\cdot0}$
160	370	450	3·191	1180	335
170	430	540	3·204	1380	380
180	500	640	3·267	1633	439
190	570	755	3·297	1880	490
200	645	880	3·396	2200	550
210	730	1030	3·432	2510	609
220	820	1185	3·471	2850	675
230	915	1370	3·513	3215	736
240	1025	1570	3·579	3665	810
50Hz					
160	485	725	3·191	1545	374
170	570	870	3·204	1830	435
180	660	1040	3·267	2165	495
190	755	1220	3·297	2485	552
200	865	1430	3·396	2940	631
210	985	1650	3·432	3380	712
220	1110	1890	3·471	3850	794
230	1250	2160	3·513	4380	885
240	1405	2435	3·579	5035	1010
60Hz					
160	670	1145	3·191	2140	454
170	765	1330	3·204	2450	508
180	865	1550	3·267	2830	564
190	970	1790	3·297	3205	615
200	1100	2070	3·396	3740	699
210	1240	2380	3·432	4250	770
220	1390	2740	3·471	4830	848
230	1570	3130	3·513	5510	950
240	1720	3495	3·579	6150	1030

1" aluminium with bevel					FIG 6·1-7
amps	W1 watts	W 2 watts	3Ki	3Ki W1	total clamp loss
40Hz	(1)	(2)	(3)	(1)x(3)=(4)	$\frac{(4)-(2)}{(3)-1\cdot0}$
160	395	475	3·191	1280	367
170	452	555	3·204	1450	405
180	515	645	3·267	1685	459
190	592	745	3·297	1960	530
200	670	870	3·396	2265	582
210	760	1000	3·432	2605	660
220	850	1150	3·471	2950	730
230	945	1325	3·513	3325	798
240	1050	1525	3·579	3765	870
50Hz					
160	500	750	3·191	1595	385
170	585	875	3·204	1880	455
180	675	1020	3·267	2210	523
190	770	1180	3·297	2540	592
200	880	1375	3·396	2990	675
210	1000	1585	3·432	3432	762
220	1130	1815	3·471	3920	852
230	1270	2060	3·513	4460	958
240	1435	2320	3·579	5150	1095
60Hz					
160	690	1170	3·191	2200	470
170	785	1360	3·204	2520	526
180	885	1580	3·267	2890	579
190	1015	1840	3·297	3350	659
200	1150	2105	3·396	3900	750
210	1310	2395	3·432	4500	870
220	1470	2710	3·471	5100	970
230	1650	3060	3·513	5800	1095
240	1835	3410	3·579	6580	1225

no clamp plates					FIG 6·1-8
amps	W1 watts	W 2 watts	3Ki	3Ki W1	total clamp loss
40H	(1)	(2)	(3)	(1)x(3)=(4)	$\frac{(4)-(2)}{(3)-1\cdot0}$
160	285	317	3·191	910	270
170	335	370	3·204	1075	318
180	390	425	3·267	1274	373
190	450	486	3·297	1482	433
200	513	553	3·396	1741	495
210	580	621	3·432	1990	562
220	648	692	3·471	2245	628
230	717	765	3·513	2520	698
240	790	840	3·579	2825	769
50Hz					
160	405	490	3·191	1292	367
170	465	560	3·204	1490	422
180	537	642	3·267	1755	490
190	615	731	3·297	2025	562
200	700	830	3·396	2375	648
210	800	945	3·432	2745	740
220	912	1076	3·471	3160	845
230	1035	1215	3·513	3640	968
240	1160	1360	3·579	4155	1085
60Hz					
160	542	675	3·191	1730	482
170	640	780	3·204	2055	579
180	742	897	3·267	2425	674
190	858	1026	3·297	2830	789
200	985	1165	3·396	3340	910
210	1115	1345	3·432	3830	1010
220	1250	1505	3·471	4340	1150
230	1400	1698	3·513	4920	1284
240	1560	1910	3·579	5580	1428

1/4" mild steel, varying radial clearances					FIG 6·1–9
amps	W1 watts	W2 watts	3Ki	3Ki W1	total clamp loss
δ=1·28 mm	(1)	(2)	(3)	(1)x(3)=(4)	$\frac{(4)-(2)}{(3)-1\cdot0}$
160	520	790	3·191	1660	397
170	629	910	3·204	2016	501
180	754	1045	3·267	2460	623
190	895	1195	3·297	2950	764
200	1050	1350	3·396	3560	924
210	1220	1510	3·432	4190	1102
220	1420	1680	3·471	4930	1316
230	1630	1875	3·513	5725	1532
240	1865	2065	3·579	6680	1790
δ=6·05 mm					
160	485	724	3·191	1549	376
170	588	834	3·204	1886	477
180	705	955	3·267	2300	593
190	835	1090	3·297	2750	723
200	980	1230	3·396	3325	875
210	1140	1375	3·432	3920	1048
220	1325	1530	3·471	4600	1242
230	1520	1690	3·513	5340	1452
240	1735	1925	3·579	6210	1660
δ=10·8 mm					
160	445	670	3·191	1420	342
170	540	768	3·204	1730	436
180	646	882	3·267	2110	541
190	756	1000	3·297	2520	662
200	900	1140	3·396	3050	798
210	1050	1275	3·432	3605	957
220	1220	1420	3·471	4230	1138
230	1400	1575	3·513	4920	1334
240	1600	1730	3·579	5730	1550

6.2 Clamp Plate losses - a presentation.

The clamp plate losses evaluated in section 6.1 were plotted on a log-log basis and are presented in Fig. 6.2 - 2 to 9. This presentation indicates that the clamp plate loss W_c can be expressed in the form

$$W_c = k A^x f^y$$

where A is the stator current, f is the supply frequency, and x and y are constant for each clamp plate, over the test range of current and frequency. The values of x and y for the various clamp plates are summarised in the table of Fig. 6.2 - 1. Clearly, on a loss basis, the clamp plates can be divided into three groups, thin ferrous plates (stamping thicknesses), thick ferrous plates, and non-ferrous (metallic) plates. Fig. 6.2 - 1 suggests mean values of x and y for the three groups, although it must be emphasised that the relatively high value of 3.85 for the 1" unbevelled mild steel plate is not necessarily in error. The result for thin ferrous plates is implied from the tests with no clamp plate present, the end region field penetrating into the first few stampings at the core end.

Classical work on eddy current losses indicates that the loss should be proportional to $B^{2.0}$. In the non-ferrous group, brass and aluminium give $x = 2.2$ and 2.4 respectively, which are somewhat higher than the 2.0 applied to flux density. Considering the ferrous groups, Davies (6) shows that losses in the drum of eddy current couplings are proportional to $B^{2.98}$. Also, for silicon stampings with flux densities above 1.15 Wb/m^2, conventional iron losses are proportional to $B^{2.5}$ (see section 6.1). Again, test values for x on comparison, are somewhat higher, being 3.0 to 3.85 for thick plates, and 2.7 for the laminations.

summary of clamp plate loss tests, variation of loss with frequency and current.

FIG 6·2-1

$$\text{clamp loss} = k\,A^{x}\,f^{y}$$

test exponents	x	y
1/4" mild steel	3·2	0·95
1" mild steel with bevel	3·2	1·00
1" meehanite with bevel	3·0	0·90
1" mild steel - no bevel	3·85	1·10
1" brass	2·2	0·64
1" aluminium	2·4	0·70
no clamp plates	2·7	1·50

averaged results	x	y
no clamps ≃ thin plates	2·7	1·5
non ferrous	2·3	0·67
ferrous ≃ thick plates	3·3	1·0

Considering the variation with frequency, from classical work, the value of 'y' should be 0.5 for non-ferrous materials. For ferrous materials, Grieg (21) proposed that 'y' should lie between 1.5 and 2.1 for thin plates, and <1.5 for thick plates. Miles Walker (33) and Rockwood (51) suggest values of 1.4 and 1.5 respectively for thick plates. The present work gives values of 'y' which are slightly high for non-ferrous plates, 0.64 for brass and 0.70 for aluminium, and considerably low values for thick plates, 0.9 to 1.1. For laminations (no clamp plates) the results give y = 1.5, which can be compared with Grieg's measured value of 1.7 for stampings of thickness 0.016" (0.406 mm), and also for punchings of up to 0.125" (3.18 mm) thickness.

Figure 6.2 - 9 shows that increasing the radial clearance between the bore of the clamp plate and the winding surface decreases the total clamp plate loss. The total loss reduction is less than 20% compared with an increase of more than 8:1 in the radial clearance. This appears to indicate that most of the clamp plate loss occurs on the radial surface, the radial clearance affecting only the loss on the bore surface.

In the following sections, clamp plate losses as derived from the test results are considered in more detail, concentrating on the variation of loss with excitation current. The above brief comparison shows that the loss increases more rapidly with excitation current than with flux density. Thus, either

(a) the effective flux density within the clamp plate increases more rapidly than the excitation current, or

(b) supplementary losses not taken into account are present.

It is believed that some part of the increase of clamp plate losses with current is certainly due to supplementary losses.

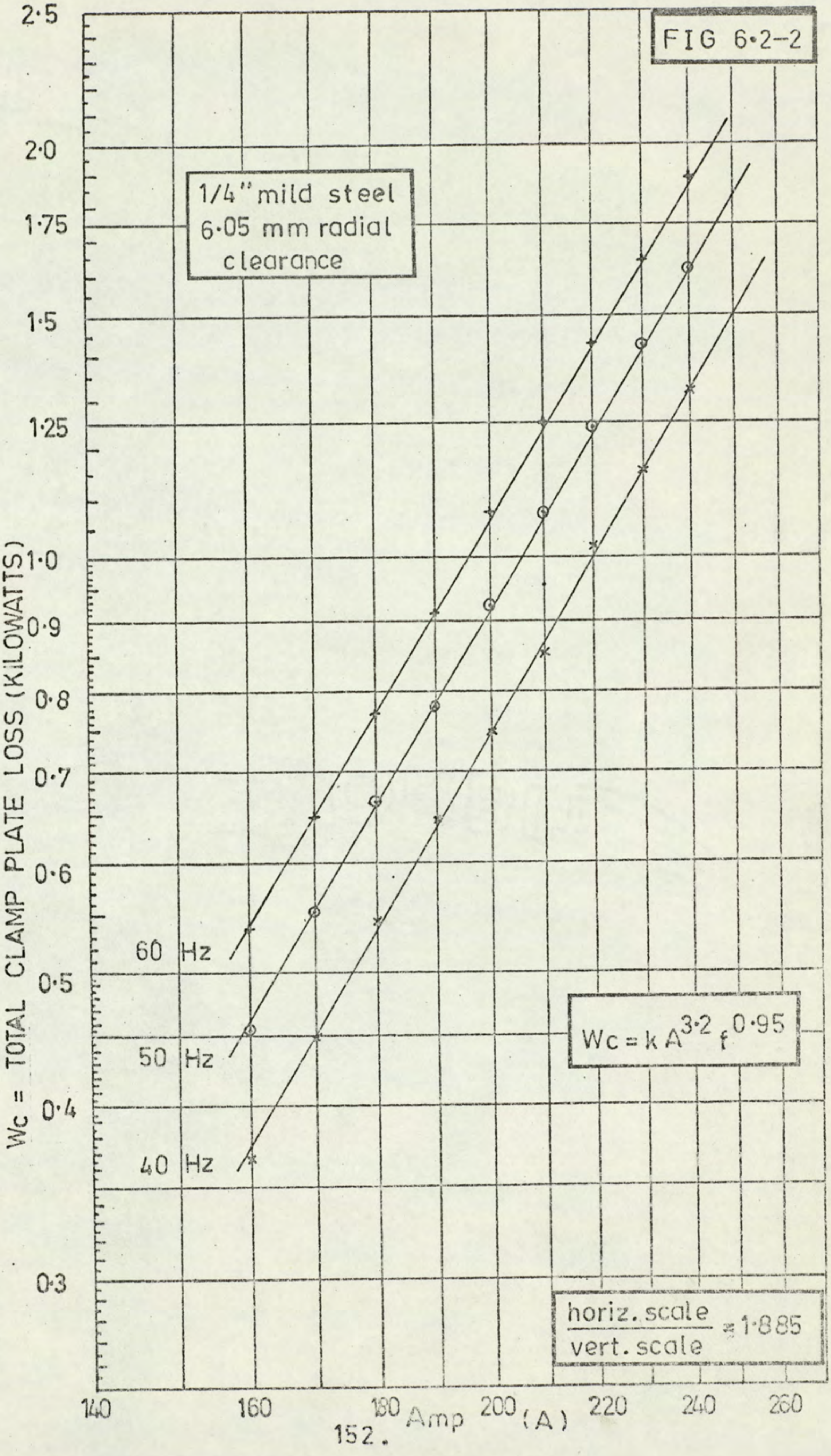
FIG 6·2-2
1/4" mild steel
6·05 mm radial
clearance
60 Hz
50 Hz
40 Hz
Wc = k A3·2 f0·95
horiz. scale / vert. scale ≈ 1·885
Wc = TOTAL CLAMP PLATE LOSS (KILOWATTS)
Amp (A)
2·5
2·0
1·75
1·5
1·25
1·0
0·9
0·8
0·7
0·6
0·5
0·4
0·3
140
160
180
200
220
240
260

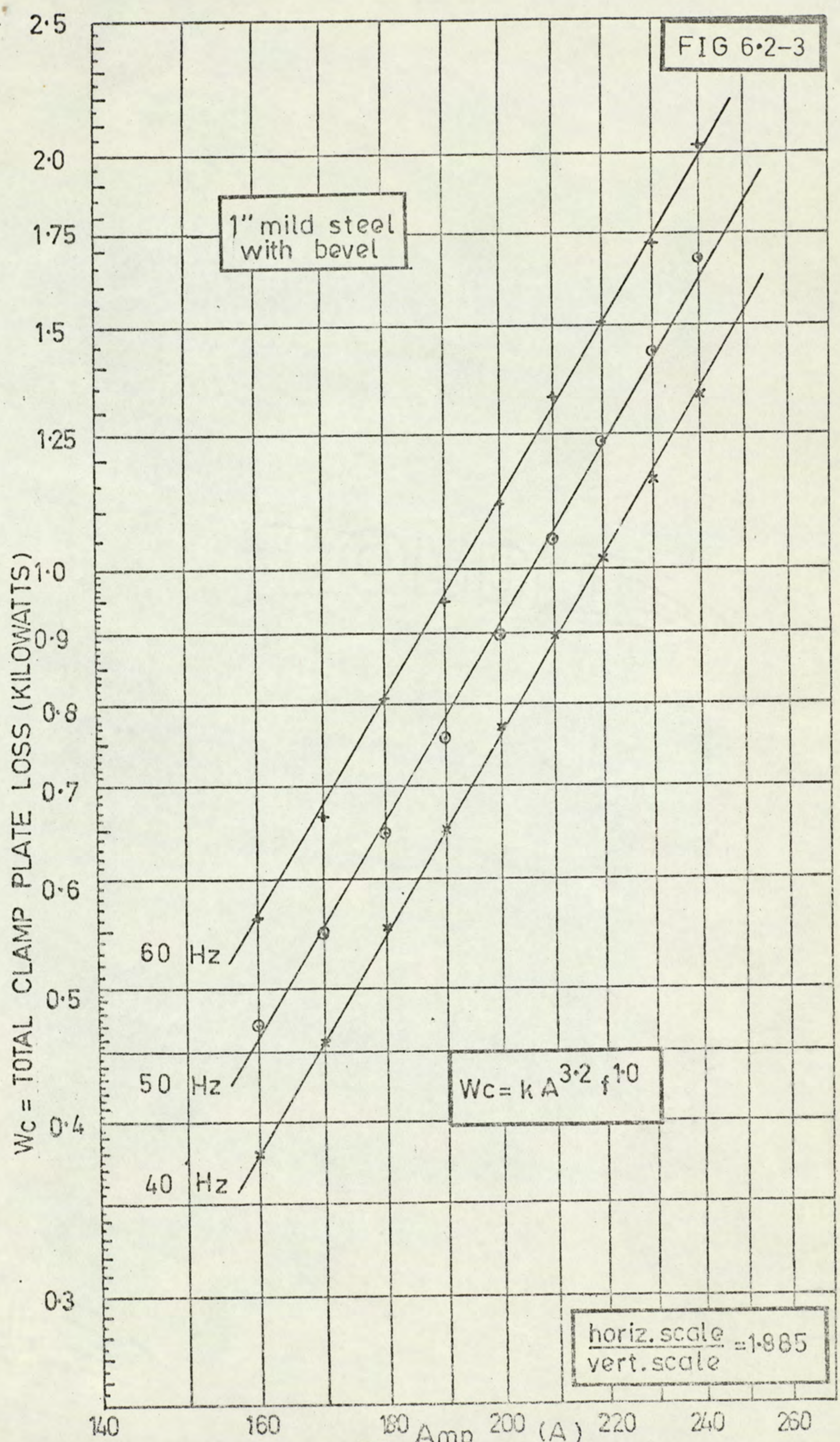
FIG 6·2-3
1" mild steel with bevel
Wc = TOTAL CLAMP PLATE LOSS (KILOWATTS)
2·5
2·0
1·75
1·5
1·25
1·0
0·9
0·8
0·7
0·6
0·5
0·4
0·3
60 Hz
50 Hz
40 Hz
Wc = k A^3·2 f^1·0
horiz. scale / vert. scale = 1·885
140
160
180
200
220
240
260
Amp (A)

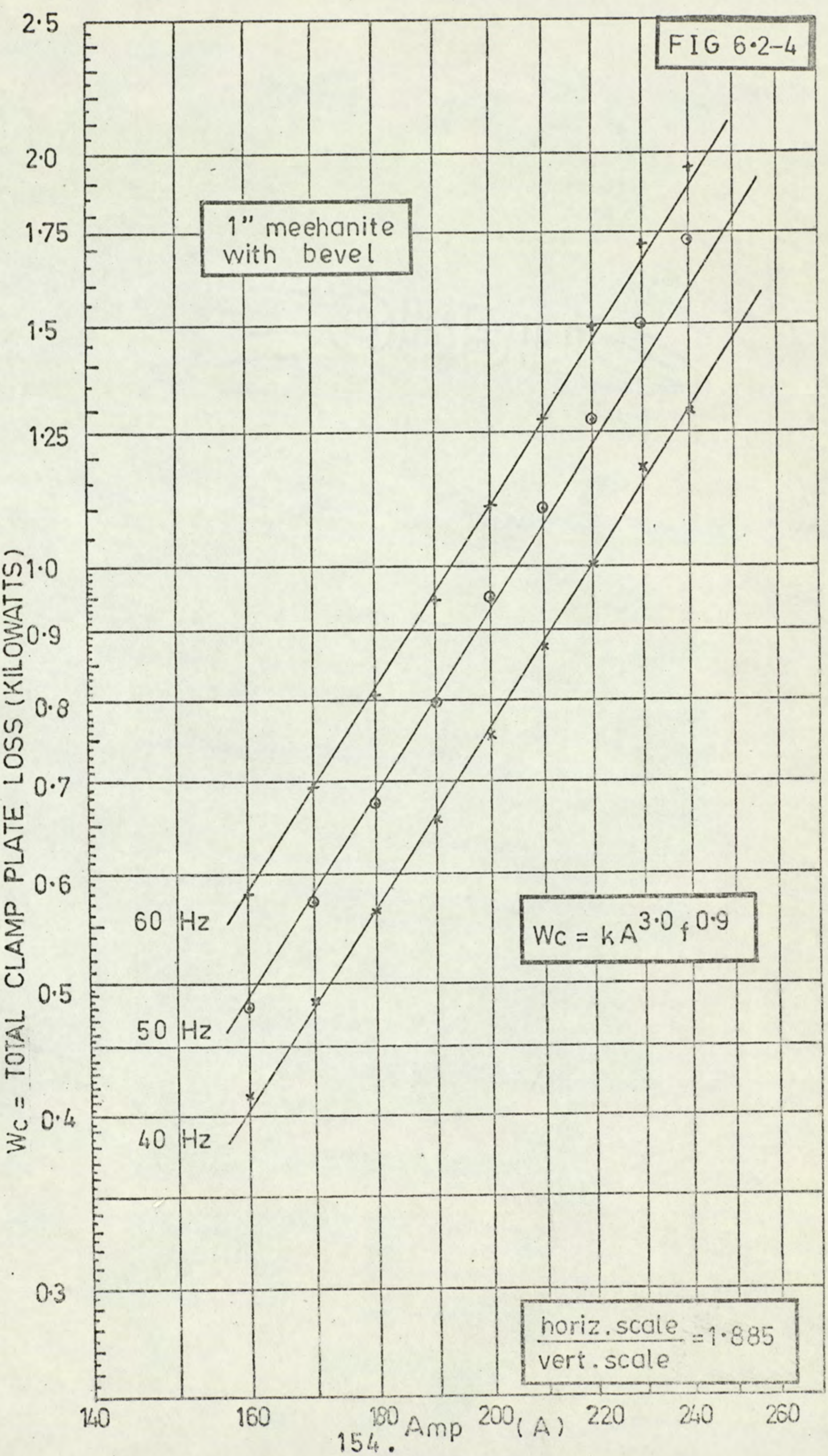

FIG 6·2-4
1" meehanite with bevel
Wc = TOTAL CLAMP PLATE LOSS (KILOWATTS)
2·5
2·0
1·75
1·5
1·25
1·0
0·9
0·8
0·7
0·6
0·5
0·4
0·3
60 Hz
50 Hz
40 Hz
$Wc = kA^{3.0} f^{0.9}$
$\frac{\text{horiz. scale}}{\text{vert. scale}} = 1{\cdot}885$
140
160
180
200
220
240
260
Amp (A)

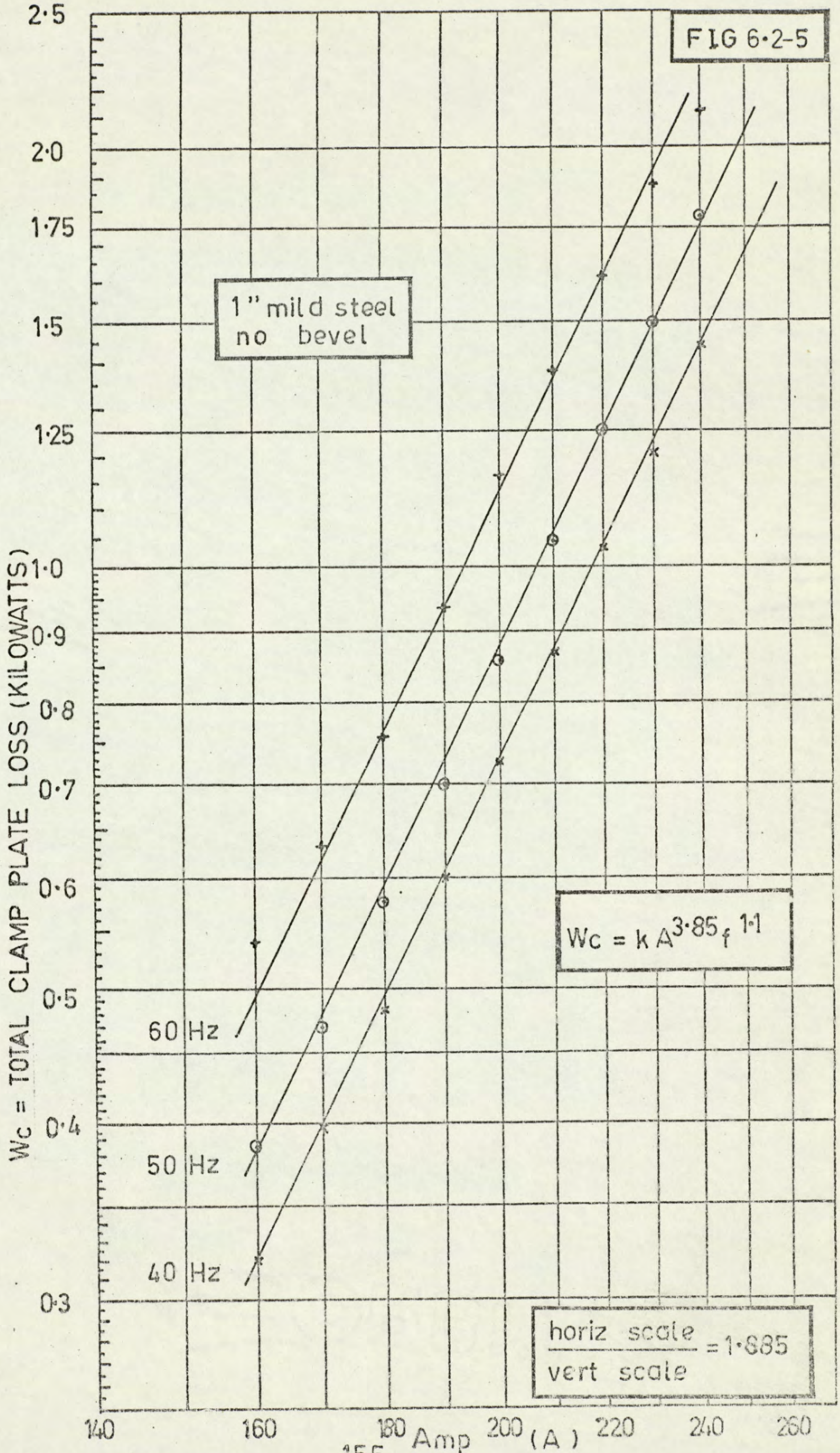
FIG 6·2-5
1" mild steel
no bevel
Wc = k A^3·85 f^1·1
horiz scale / vert scale = 1·885
60 Hz
50 Hz
40 Hz
Wc = TOTAL CLAMP PLATE LOSS (KILOWATTS)
2·5
2·0
1·75
1·5
1·25
1·0
0·9
0·8
0·7
0·6
0·5
0·4
0·3
140
160
180
200
220
240
260
Amp (A)

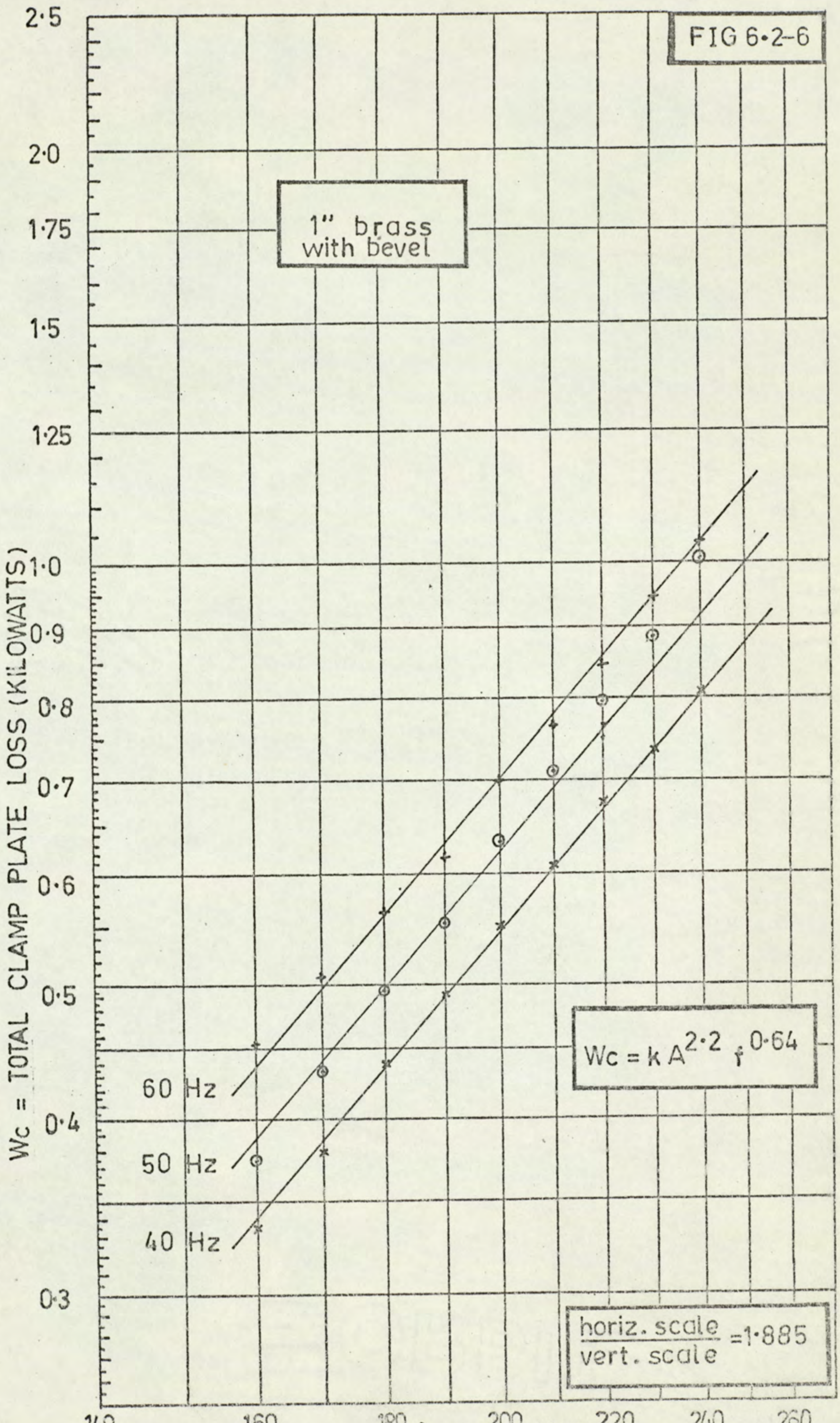

FIG 6·2-6
1" brass with bevel
Wc = TOTAL CLAMP PLATE LOSS (KILOWATTS)
2·5
2·0
1·75
1·5
1·25
1·0
0·9
0·8
0·7
0·6
0·5
0·4
0·3
60 Hz
50 Hz
40 Hz
Wc = k A^2·2 f^0·64
horiz. scale / vert. scale = 1·885
140
160
180
200
220
240
260
Amp (A)

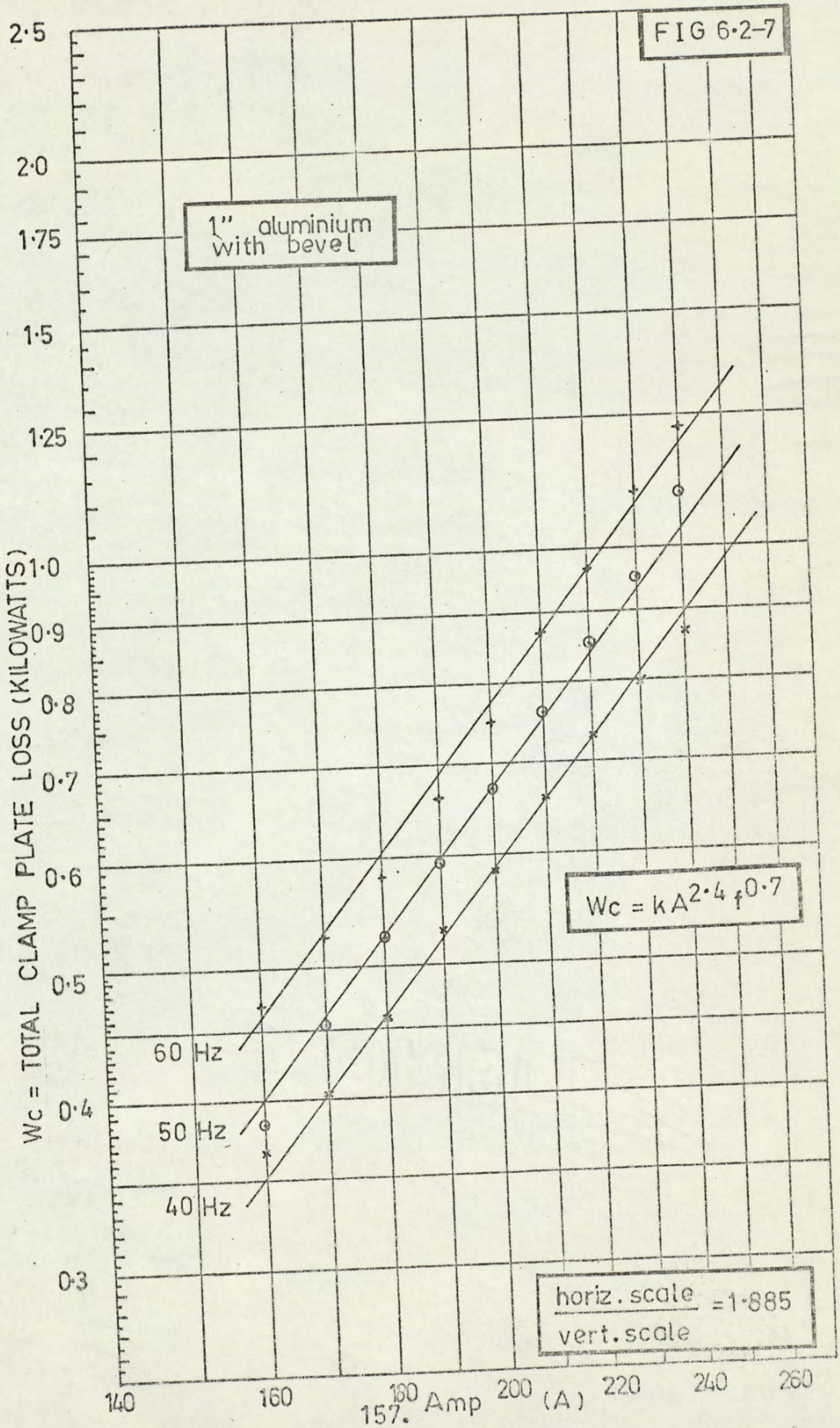
FIG 6·2–7
1" aluminium with bevel
$W_c = kA^{2 \cdot 4} f^{0 \cdot 7}$
horiz. scale / vert. scale = 1·885
60 Hz
50 Hz
40 Hz
Wc = TOTAL CLAMP PLATE LOSS (KILOWATTS)
2·5
2·0
1·75
1·5
1·25
1·0
0·9
0·8
0·7
0·6
0·5
0·4
0·3
140
160
180
200
220
240
260
Amp (A)

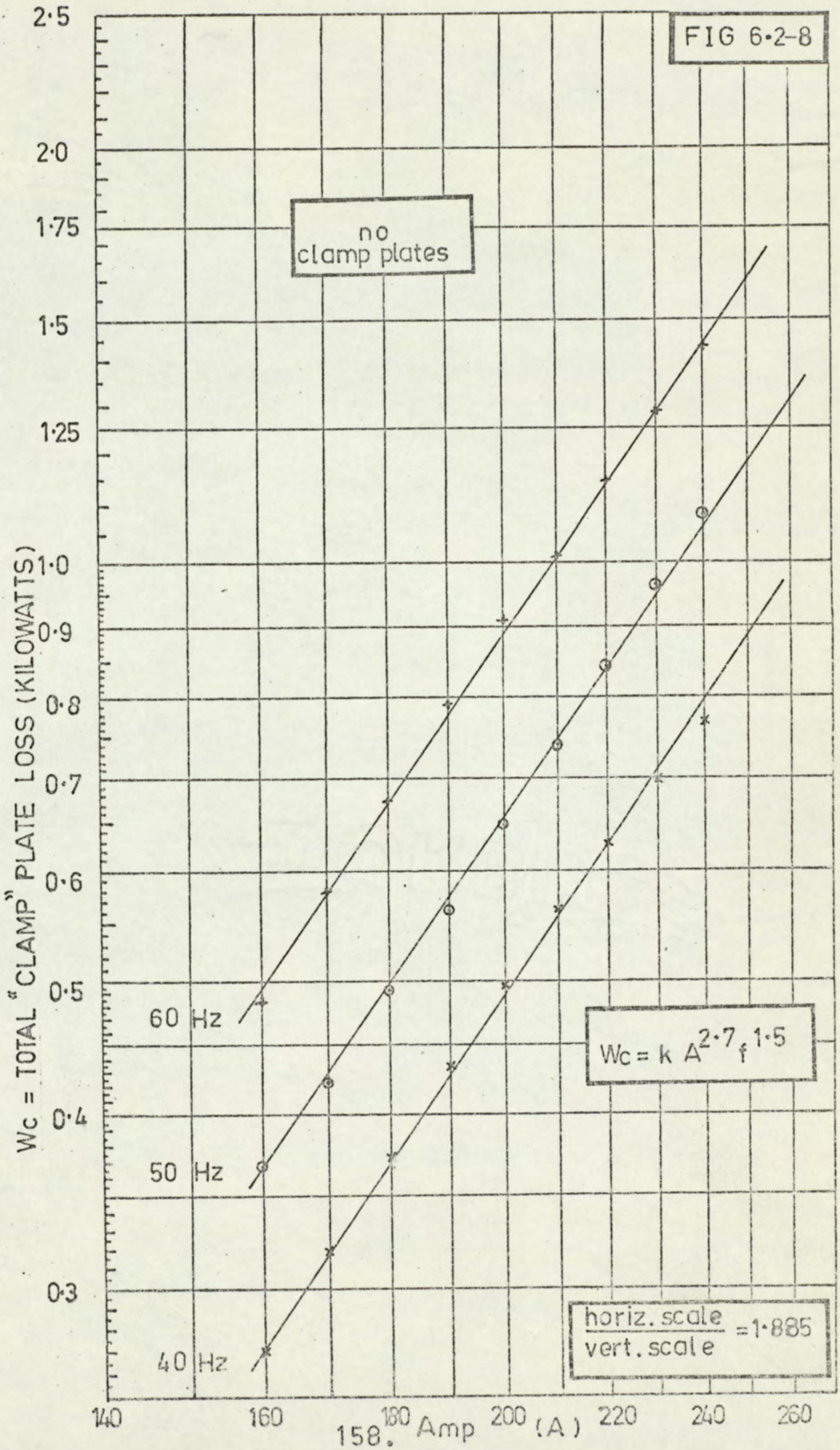
FIG 6·2-8
no
clamp plates
60 Hz
50 Hz
40 Hz
Wc = k A^2·7 f^1·5
horiz. scale / vert. scale = 1·885
Wc = TOTAL "CLAMP" PLATE LOSS (KILOWATTS)
2·5
2·0
1·75
1·5
1·25
1·0
0·9
0·8
0·7
0·6
0·5
0·4
0·3
140
160
180
200
220
240
260
Amp (A)

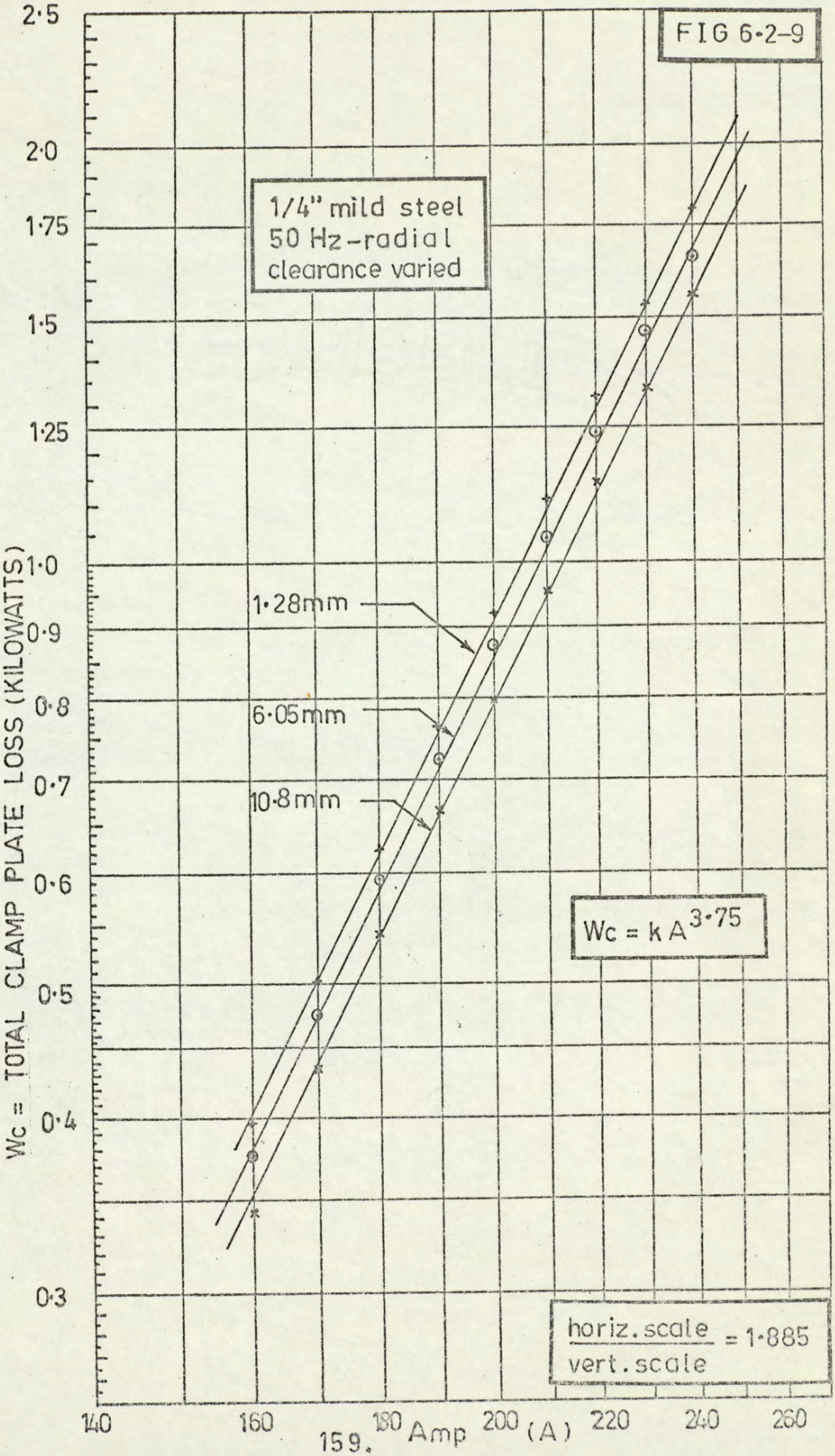
FIG 6·2-9
1/4" mild steel
50 Hz-radial
clearance varied
1·28mm
6·05mm
10·8mm
Wc = k A^3·75
horiz. scale / vert. scale = 1·885
Wc = TOTAL CLAMP PLATE LOSS (KILOWATTS)
2·5
2·0
1·75
1·5
1·25
1·0
0·9
0·8
0·7
0·6
0·5
0·4
0·3
140
160
180
200
220
240
260
Amp (A)

6.3 General survey of dissimilarities in the two models.

At this stage it seemed possible that unintentional differences in the two models were sufficient to affect the clamp plate loss results. Before further discussions of these results, it was decided to examine the possible dissimilarities in the models in some detail.

Initially, the magnetisation voltage-current curves for both models under all conditions were plotted and examined, the results for "no-clamp plates" are shown in Fig. 6.3 - 1. By simultaneously viewing the curves for the various clamp plates, for both models using an illuminated ground-glass plate, it was noted that there was hardly any difference. Any deviation could be attributed to the inaccuracy of plotting points and drawing curves through these points. On comparing results for the two cores, it was seen that the short core required more excitation in the iron circuits compared with the long core. This characteristic was also observed in Fig. 6.1 - 1 when plotting the air gap density curves. It is clear from the tests that the source of this difference is a function of the cores and not the clamp plates.

The possibility of the air gap flux density wave shapes being different due to unequal degrees of saturation existing in the two cores was checked. Fig. 6.3 - 2 is a record of the air gap flux density wave shape on the short core. A check on the long core gave similar results.

The effect of unequal core ampere turns is also apparent in Figs. 4.3 - 3 and 4.3 - 4 under the section on preliminary testing. In both tests, more flux is diverted into the magnetic clamp plates on the short core than on the long core. (Part of the search coil voltage is of course due to overhang magnetisation characteristics for the long and short cores at 40, 50, and 60 Hz

FIG 6·3-1

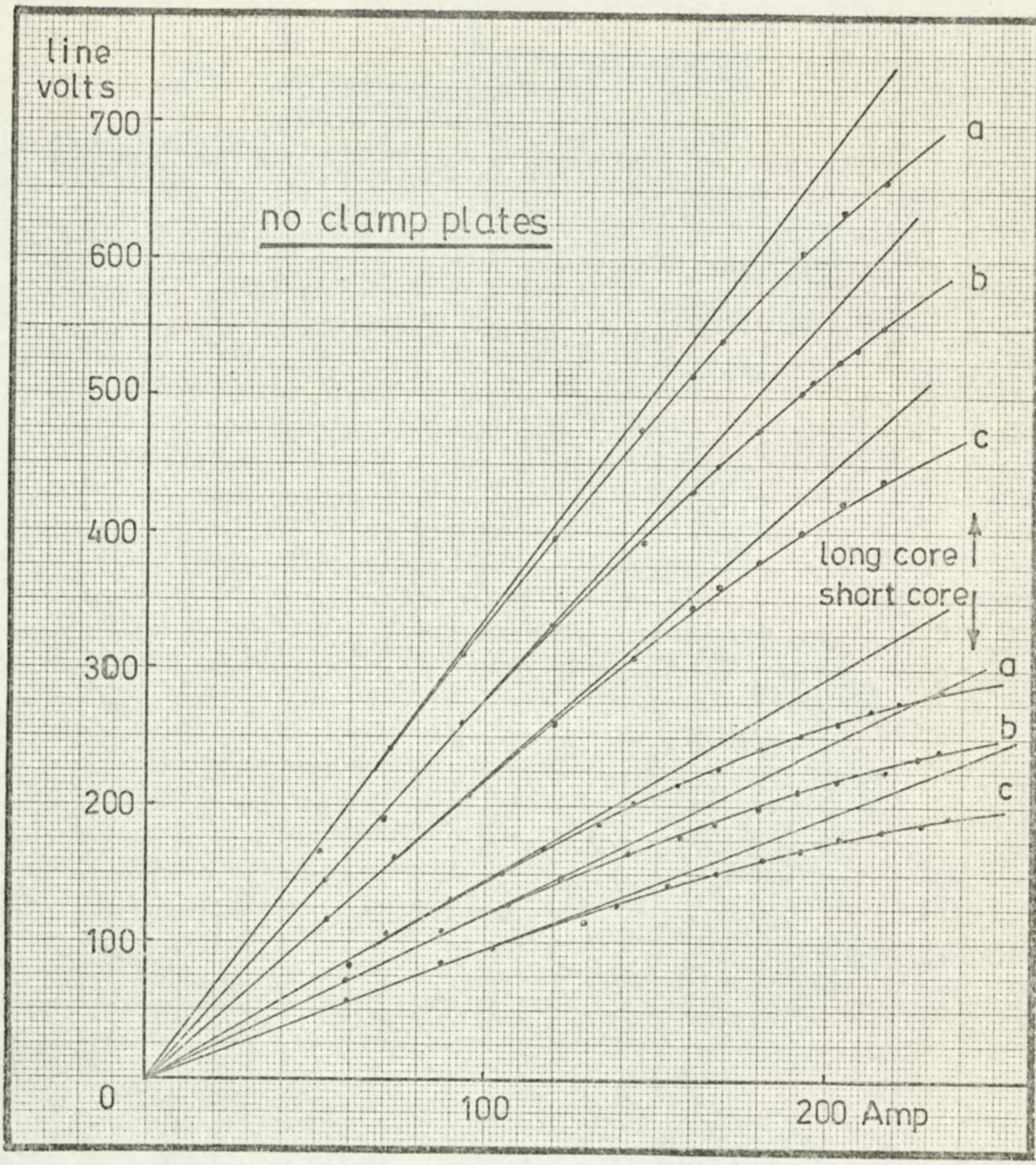

(a) 60 Hz (b) 50 Hz (c) 40 Hz

with both ferrous and non ferrous clamp plates the mag. curves correlate to within 5 volts at 240 amp.

air gap flux density waveform on the short core with 50 Hz supply on stator

FIG 6·3-2

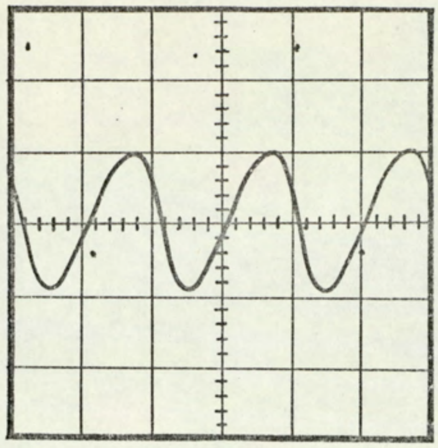

240 Amp

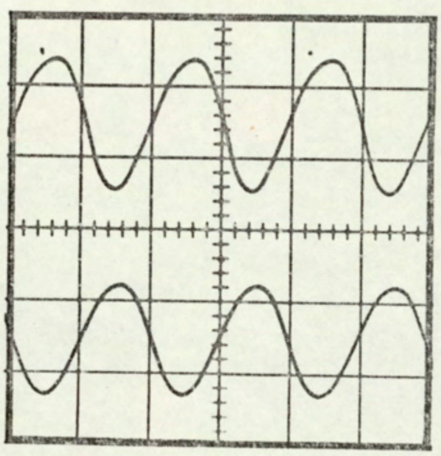

240 Amp

180 Amp

5 mV/cm

10 ms/cm

air gap flux density = 0·506 Wb/m^2
at 240 amp 50 Hz

leakage flux, which is considered equal for both cores). If the clamp plates are thus considered to form parallel paths with the core stamping path, then less iron ampere turns would be required in the case of ferrous clamp plates. However, as pointed out earlier, comparing the various total magnetic characteristics did not reflect any significant difference. Nevertheless the ferrous clamp plates do carry part of the main flux, and to examine this effect further, tests were carried out on the short core using a single-turn search coil wound round the aluminium and $\frac{1}{4}$" M.S. clamp plates respectively. The results are detailed in Fig. 6.3 - 3.

Taking the r.m.s. value of search coil voltage to be representative of the total circumferential flux within the clamp plate, the ferrous plate contains nearly 20 times more flux than the aluminium plate. Part of the increase is in flux resulting from the overhang m.m.f., but Fig. 5.3 - 3 shows that this increase cannot be more than 3 times. This indicates that appreciable flux is being shunted from the core with ferrous clamp plates.

In the next test, a Hall probe was inserted in the centre of the air gap between the stamping pack and the frame to check the magnitude of flux leaking into the frame. Details of the test carried out on the short core are recorded in Fig. 6.3 - 4, a visual check having been made on the long core for similarity. When plotting these magnetisation curves, it was noticed that up to approximately 150 amp. excitation, the leakage flux into the frame was insignificant. Above this value the level rose sharply, a characteristic which would be expected on examining the magnetisation curves of Fig. 6.1 - 1.

tests on short core with a single turn search coil round the 1" aluminium clamp ring and the 1/4" mild steel ring with 240 amp stator excitation.

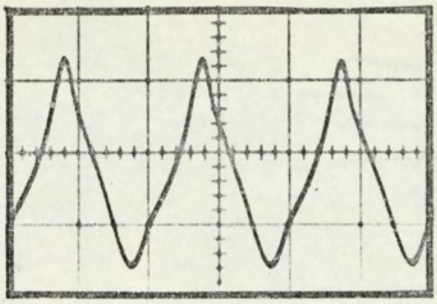

1" aluminium

flux trace ($\int v\,dt$)

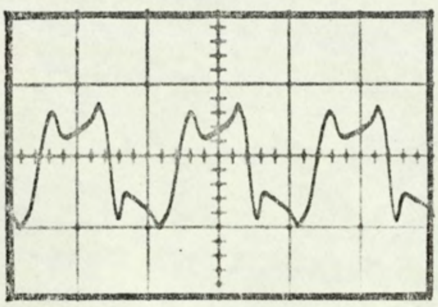

voltage trace (v)

5 mV/cm

FIG 6·3-3

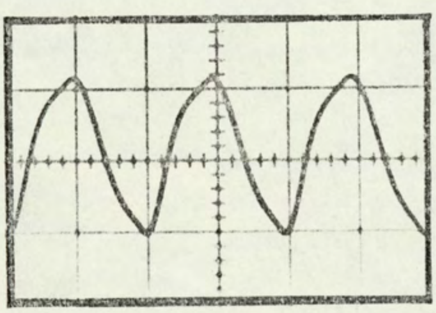

1/4" mild steel

flux trace ($\int v\,dt$)

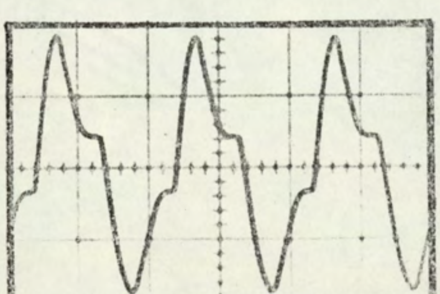

voltage trace (v)

50 mV/cm

	voltage trace	
clamp ring	mV rms	mV peak
aluminium	3·15	4·15
1/4" mild steel	61·2	98·2

waveform of flux density in airgap between stamping pack and stator frame on the short core, top central position

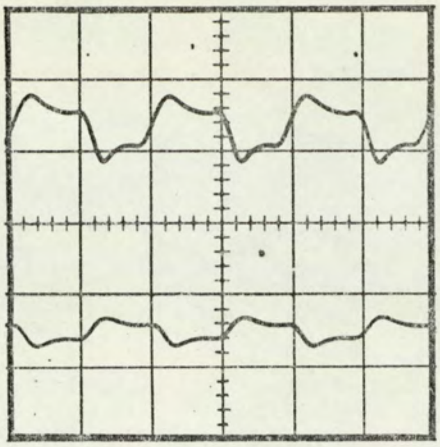

240 amp

180 amp

tests at 50 Hz

FIG 6·3-4

back gap magnetisation characteristics.

Note that the 50 mm core is mounted in a one inch thick frame while the 150 mm core has a two inch frame. With this in mind, further search coil tests were carried out on the frame and also the 1" unbevelled and $\frac{1}{4}$" mild steel clamp plates. The frame search coils were positioned round both the maximum section (radial plane through lifting holes, Fig. 2.1 - 2) and the minimum section (vertical radial plane). The resulting magnetisation curves are shown in Fig. 6.3 - 5 and 6.3 - 6, and each frame considered separately, exhibits similar characteristics regardless of clamp plate thickness. However, at currents exceeding about 150 amps., more flux is diverted into the frame and clamp plates of both thicknesses in the case of the short core than in the case of the long core. Furthermore, in the case of the short core frame, the maximum section indicates more flux than in the minimum, suggesting that some leakage flux from the overhang penetrates into the frame. (This effect appears negligible for the long core frame, since the frame vertical surface is more remote from the overhang).

To complete this study, frame search coil magnetisation curves were taken with no clamp plates present. The results showed that flux leaking into the frame of the long core model is virtually independent of the clamp plate used. For the short core model, with no clamp plates, and presumably with non-ferrous clamp plates, slightly more flux leaks into the frame than with ferrous clamp plates. Again, there are differences because on the short core model, the frame is much nearer the model end regions.

magnetisation curves with a single turn search coil on clamp plate and frame on the short core, tests at 50 Hz

FIG 6·3-5

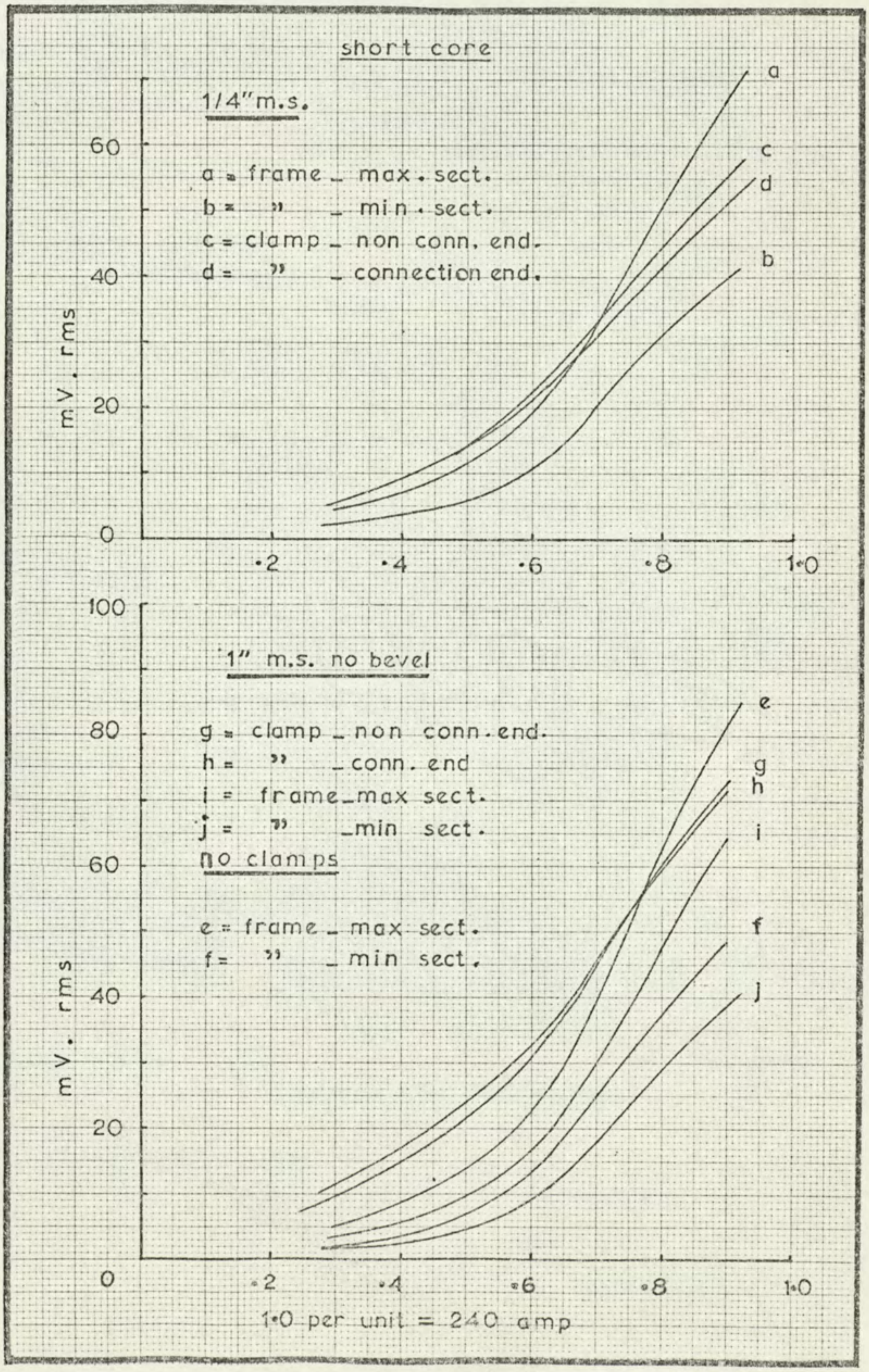

magnetisation curves with a single turn search coil on clamp plate and frame on the long core, tests at 50 Hz

FIG 6·3-6

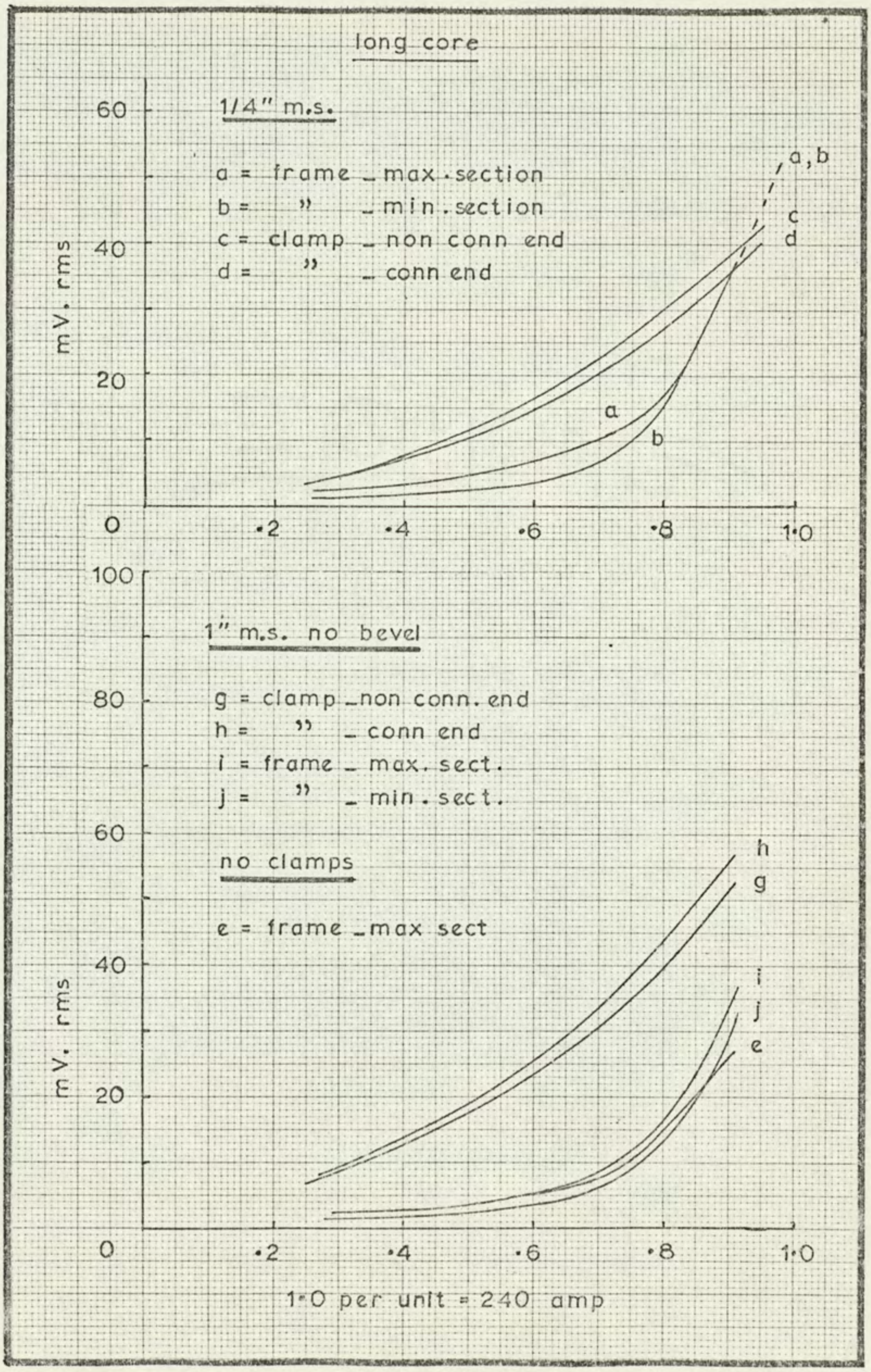

6.4 A critical appraisal of the results.

Conclusions drawn from the clamp plate loss results presented in section 6.2 can be summarised as follows:

(1) Thick mild steel plates, unbevelled, Figs. 6.2 - 2 and 5.

With a current exponent of 3.85, the loss in the 1" plate increases with current more rapidly than the loss in the $\frac{1}{4}$" plate, which has a current exponent of 3.2. The curves intersect at 210A, such that below this value, the $\frac{1}{4}$" plate loss is greater than the 1" plate loss.

(2) 1" thick mild steel plates, Figs. 6.2 - 3 and 5.

The loss in the unbevelled plate increases more rapidly with current than the loss in the bevelled plate, current exponents being 3.85 and 3.2 respectively. These curves intersect at 210A, such that below this value, the bevelled plate loss is greater than the unbevelled plate loss.

(3) $\frac{1}{4}$" thick mild steel plates, Figs. 6.2 - 2 and 9.

Current exponents of 3.2 and 3.75 are obtained from two separate tests, for the same clamp plate, under apparently identical conditions. The clamp plate losses at 50 Hz are compared in the following table.

Amps	160	200	240
Watts (1st Test)	460	920	1620
Watts (2nd Test)	380	860	1680

(4) 1" thick ferrous plates, bevelled, Figs. 6.2 - 3 and 4.

The mild steel and meehanite clamp plates give virtually the same loss.

(5) All thick ferrous plates.

Exponents of frequency in the loss expression lie within the range 0.9 to 1.1, and are considerably lower than expected.

(6) No clamp plates, Fig. 6.2 - 8.

The end region loss in this case is proportional to $I^{2.7}$ and $f^{1.5}$, and is regarded as representing the loss in thin clamp plates. The exponents are in good agreement with published results.

(7) Non-ferrous plates.

Although the loss in the aluminium plates increases more rapidly than in the brass plates, with respect to both current and frequency, the loss is generally higher in the brass plates.

The intersection of loss curves referred to in (1) and (2) above, together with conclusion (3), indicate the possibility of errors in the method used to obtain clamp plate losses. Alternatively, the models may not be functioning exactly as assumed. As shown in section 6.3, there are differences in the models other than in core lengths, and this must affect the loss calculation.

The loss equations used in section 6.1 are

$$W_1 = W_i + W_c$$

$$W_2 = 3K_i W_i + W_c$$

where W_i = iron loss in the short core.

$$\text{Therefore} \quad W_i = \frac{W_2 - W_1}{3K_i - 1}$$

This equation was used to calculate the short-core iron loss, from the tests with various clamp plates given in section 6.1. The results are shown plotted against per iron losses derived from test curves for the short core for the various clamp plates, all tests at 50 Hz.

FIG 6·4-1

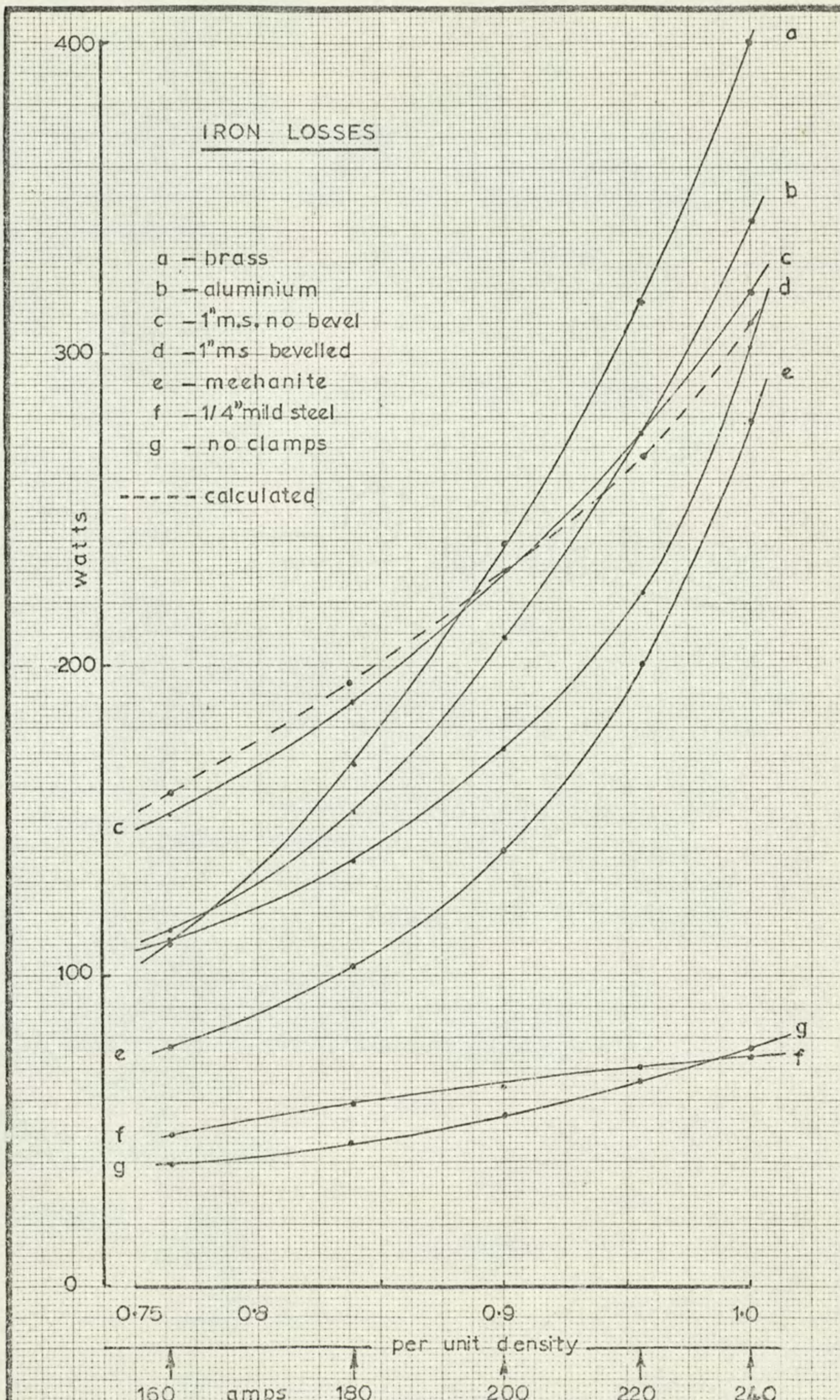

unit flux density (gap) in Fig. 6.4 - 1, the gap flux density at 240 amps excitation is taken as 1 p.u. If the loss evaluation is correct, then clearly these curves should coincide; for comparison, a calculated iron loss curve is included. The iron loss calculation was made at 240 amps, using the stamping makers' iron loss curves, and then assuming the loss to vary as $B^{2.5}$.

When considering discrepancies referred to above, possible errors in measurements must not be eliminated entirely. Such errors are listed as follows:-

(a) Errors in wattmeter readings. The wattmeters were used with resistance multiplier boxes in series with the voltage coils (see section 2.3). Depending on the multiplier box used, each scale division on the meters is equivalent to 480, 720, 960 or 1200 watts. Accepting that the meters were read to within 0.1 of a scale division (0.2 mm approximately), there may be inherent errors of $\pm$ (48, 72, 96 or 120) watts in each wattmeter reading.

(b) Errors in extrapolating the long-core losses to 240 amps. Extrapolation was necessary from 200 to 240 amps for the long core results, and this was made both on a linear and a logarithmic basis. Accuracy is considered to be within the limits of curve-plotting in general.

(c) Errors due to curve-plotting. All values of W_1 and W_2 in tables 6.1 - 2 to 9 were taken from curves drawn through actual test points (i.e., input power less winding copper loss). This process virtually eliminates random wattmeter errors, and errors (a) above. In general, the scatter of the test points with respect to the drawn curves was of the order of $\pm$ 100 watts in 2,500 watts, so that errors due to the positioning of the curves are well within this limit.

(d) Errors in measuring winding resistances. Resistance measurements were made by two methods, one using an accurate resistance bridge, and the results agreed to within 0.5%.

The relative importance of these possible errors is seen in the following table, where the magnitudes of the clamp plate losses and core iron losses are compared with the wattmeter reading (2-wattmeter method).

Stator amps	Long core, watts				Short core, watts			
	wattmeter reading		clamp loss	iron loss	wattmeter reading		clamp loss	iron loss
	+ve	-ve			+ve	-ve		
150	33,000	28,200	350	100	14,400	10,900	350	300
192	52,200	45,100	760	180	23,300	17,050	760	540
215	66,000	55,700	1,150	240	28,100	20,450	1,150	720

These results are for 50 Hz supply, the clamp loss being for the $\frac{1}{4}$" MS plate, (mean, from Figs. 6.2 - 2 and 9), and representative values of iron loss taken from Fig. 6.4 - 1. It is seen that the maximum difference at 215 amps, between the iron loss curves of Fig. 6.4 - 1 (230 W) is less than 1.2% of the minimum wattmeter reading at the same current.

It is possible therefore, that the scatter of the iron loss curves of Fig. 6.4 - 1 is within the limits of test accuracy, especially if the $\frac{1}{4}$" MS clamp plate and no clamp plate results are excluded. However, it is seen that generally, the iron loss appears to increase more rapidly than in proportion to $B^{2.5}$, and this fact is taken as an indication of the presence of an extra loss.

It is believed that the results are affected by two factors not properly taken into account at the outset. These are (1) end leakage effects and (2) core saturation effects.

(1) End leakage effect. For the same air-gap flux density in the two models, the total overhang leakage fluxes are approximately equal. Also, approximately equal proportions of this leakage enters into the core. Consequently, the flux density in the short core must be higher than it is in the long core, with a corresponding difference in the excitation currents. The magnitude of this effect is evaluated in Appendix A1, where the leakage flux entering the core-ends is estimated by summing the Hall probe output over the core-end surface corresponding to one pole pitch. With a d.c. excitation of 140 A in one phase and 70 A in two phases (= 99 A r.m.s.), the end leakage is shown to be 21.4% of the total air-gap flux per pole for the short core model.

Assuming the end leakage flux to be proportional to excitation current, and calculating the air-gap flux from Fig. 6.1 - 1, the end leakage at 200 A a.c. is 24.0% This compares with 22.6% calculated entirely from the two magnetising characteristics of Fig. 6.1 - 1. This shows that the comparitively large end leakage accounts for the difference in the magnetisation characteristics of the two models.

This effect is taken into account in the clamp loss calculations by introducing the factor K_i (see section 6.1), which is calculated from magnetisation characteristics of the models with no clamp plates in position. Since the end leakage must be affected by the type of clamp plate used, it is possible that it is incorrect to use the same values of K_i for all the clamp plate loss calculations. However, the comparison of the various magnetisation voltage-current curves discussed in section 6.3, indicated that changes in end leakage are negligibly small. The significance of errors in K_i can be judged by assuming $K_i = 1.0$ for say, the 1" mild steel clamp plates (with no bevel) loss calculation. The clamp loss at 160 A, 50 Hz is reduced by 16 watts (4.2%), and at 240 A, 50 Hz the loss is reduced by 110 watts (6.2%). Finally, Appendix A1 shows that most of the end leakage into the stator iron is by way of the teeth, and the presence of the clamp plates must have negligible effect on this part of the leakage flux. Errors due to incorrect evaluation of K_i therefore must be well inside the percentage errors obtained when taking K_i to be unity.

(2) Core Saturation Effects. As the excitation current increases, and flux densities across the stator iron sections become appreciable, flux diverted from the core into the clamp plates, and also into the model frames, is no longer negligible. Extra loss must therefore be generated at the clamp plate inner surface, and at the bore surface of the frames. Allowing for a total extra loss We1 and We2 in the short end long core models respectively, the loss equations become

$$W_1 = W_i + W_c + W_{e1}$$

$$W_2 = 3\,K_i\,W_1 + W_c + W_{e2}$$

$$\therefore \quad W_c = \frac{3\,K_i\,W_1 - W_2}{3\,K_i - 1} - \frac{3\,K_i\,W_{e1} - W_{e2}}{3\,K_i - 1}$$

$$\text{and} \quad W_i = \frac{W_2 - W_1}{3\,K_i - 1} + \frac{W_{e1} - W_{e2}}{3\,K_i - 1}$$

An attempt was made to suggest the order of magnitude of the error terms in these equations, but without success. Figs. 6.3 - 4, 5 and 6 show that the extra flux, and therefore extra loss, in both frame and clamp plate, is negligible up to about 140 A for the short core, and up to about 170 A for the long core. Therefore the extra loss may be expressed in the form

$$W_{e1} = \alpha \quad (I - 140)^{\gamma} \quad \text{for } I > 140 \text{ A}$$

$$W_{e2} = \beta \quad (I - 170)^{\gamma} \quad \text{for } I > 170 \text{ A}$$

where I is the excitation current, and α, β, γ may be constants over a limited range of currents.

Although the tests carried out in section 6.3 indicate the probability of the above approach, there is insufficient data to enable α, β and γ to be evaluated.

When considering the total loss associated with the clamp plates, the "extra" loss generated at the core-clamp-plate interface must be included. The test method of section 6.1 correctly includes this extra loss only when the magnetisation characteristics of the two models are identical, and the axial lengths of the frames are related in such a way that the calculation eliminates the extra losses in the frames. Neither of these two conditions apply, and the total clamp plate loss in the short-core model is given by

$$(W_c + W_{ecl}) = \frac{3 K_i W_1 - W_2}{3 K_i - 1} - \left[W_{efl} + \frac{W_{el} - W_{e2}}{3 K_i - 1} \right]$$

Where W_{ecl} is the extra loss at the core-clamp-plate interface in the short core model and W_{efl} is the loss in the frame of the short core model. The term in square brackets represents the error, the second part of which is also the error when extracting the core iron losses, Fig. 6.4 - 1, and is probably not more than 50 watts.

Chapter VII

7.0 Radial and axial clamp surfaces :- exploration.

Earlier studies on end region fields in the presence of clamp plates indicate that strong field concentrations exist at edges formed by sharp changes in direction in boundary planes of magnetic materials, as would be expected. This effect does not occur with non-ferrous clamp plates as has been seen earlier. In this section, three particular variations of clamp plate conditions are considered in order to illustrate this "edge concentration" effect, and its dependence on the proximity of the winding.

Fig. 7.0 - 1 gives measured field plots for quarter inch clamp plates with different inside diameters. The effect of clearance between the inside axial surface of the clamp plate and the winding is thus indicated.

The flux density normal to the inside axial surface of the clamp plate is of the same order as that normal to the outside surface, so that there is a loss associated with both these clamp plate surfaces. Further-more, during the loss tests the inside axial surface of the clamp plates with minimum clearance became considerably heated. In studying these surface flux density plots, it is clearly noticeable that the flux density rises to peaks at the edges of the clamp plates, and reduces sharply away from the edges. Again, when considering the radial plots, only the portion of the clamp face nearest the edge appears to be subjected to a high surface density.

Fig. 7.0 - 2 gives a direct comparison between a one inch mild steel clamp plate with and without a bevel. Not surprisingly, the unbevelled clamp plate exhibits higher peak values of surface flux density. It would be reasonable to expect that bevelling would reduce the clamp plate losses.

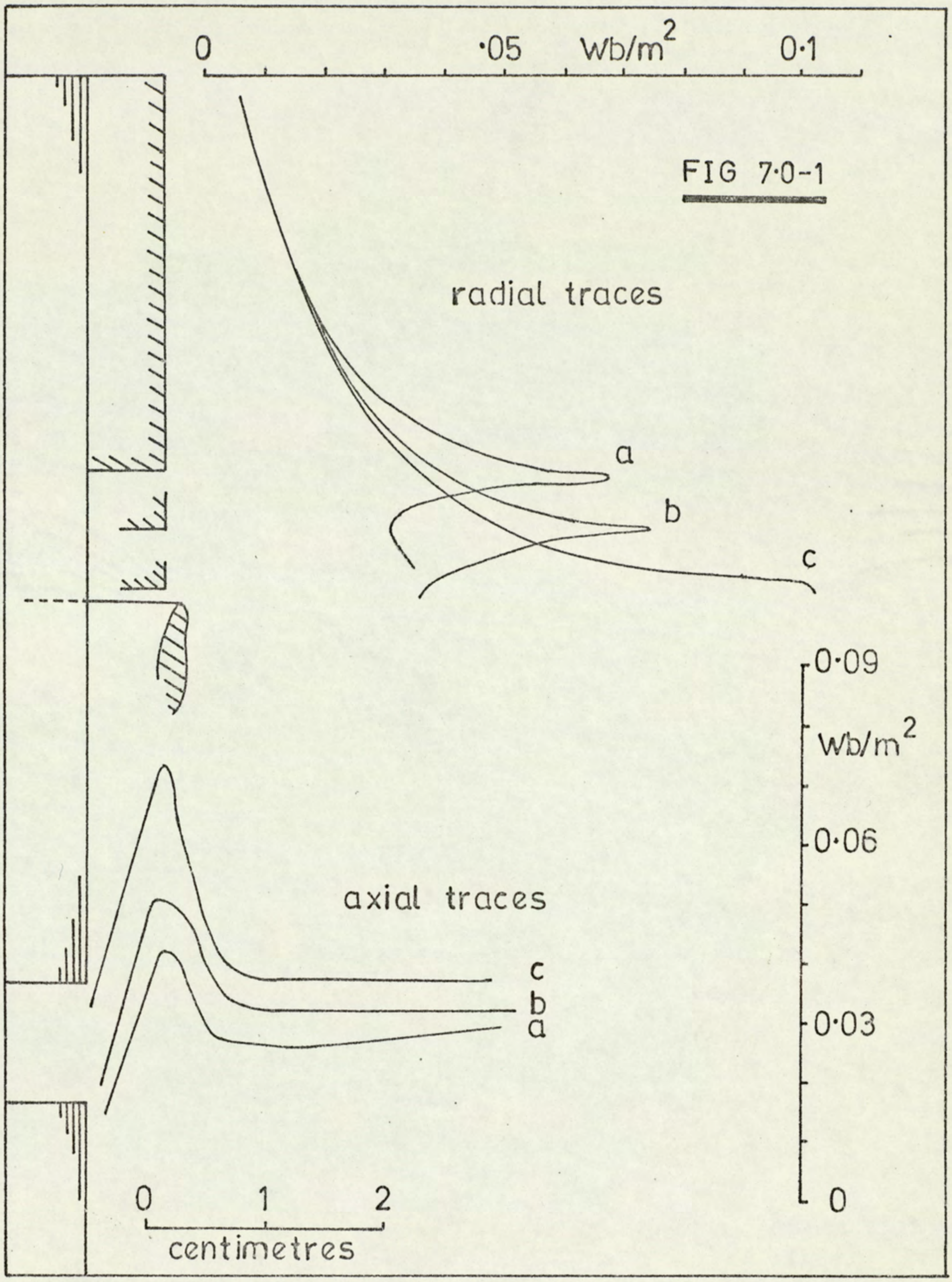

Flux density normal to radial and axial surface of clamp plate:— 1/4" mild steel clamp plates with varying inside diameters.

Radial Clearances from winding:-

a = 10·8 mm, b = 6.05 mm, c = 1·28 mm.

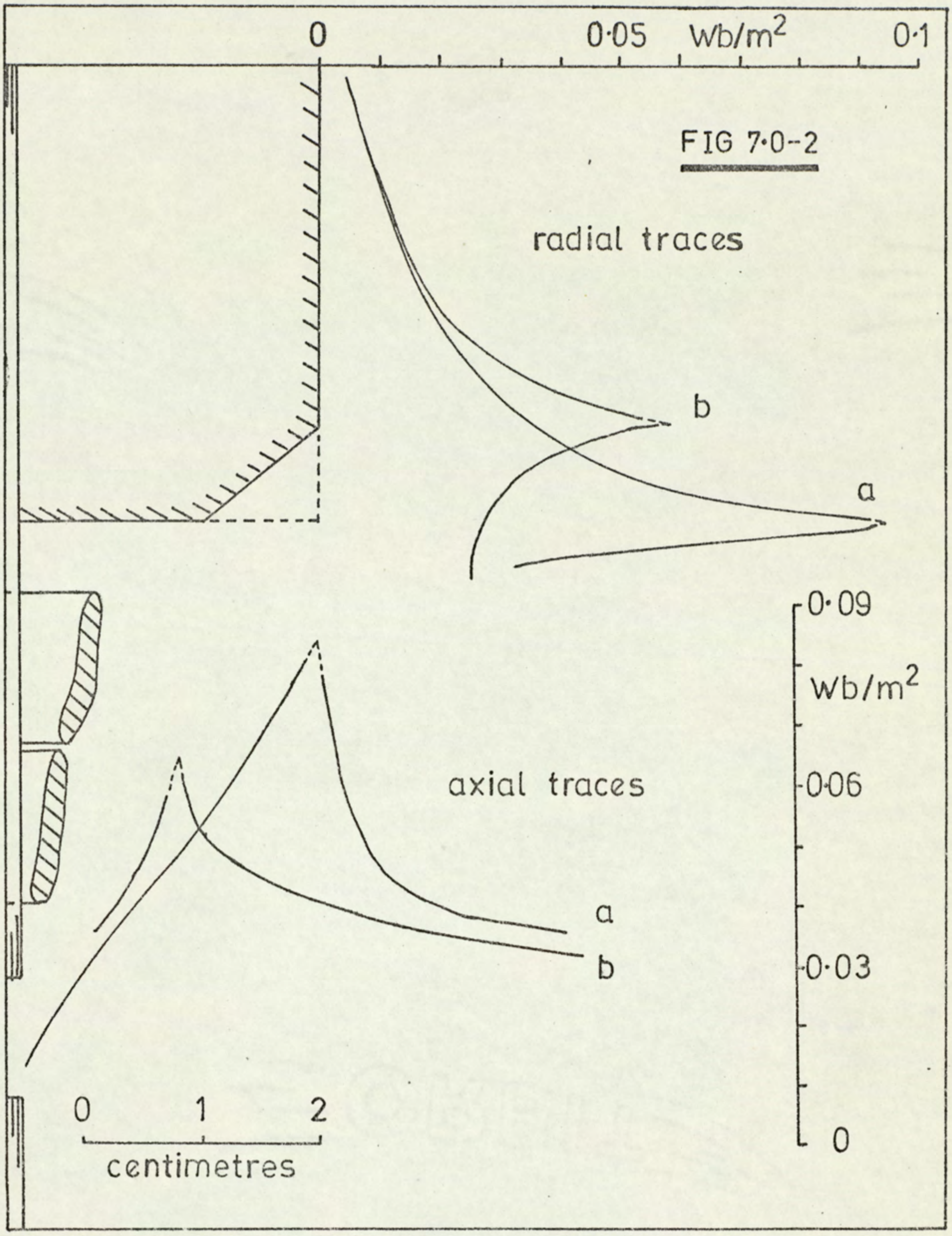

Flux density normal to radial and axial surfaces of clamp plate.

a = 1" mild steel (No Bevel).

b = 1" mild steel (Bevelled).

Radial clearance from winding 6.05 m.m.

Since the flux density over the bevelled surface is virtually constant at the edge value (not shown in Fig. 7.0 - 2) there is only a small difference between the total normal flux in the two cases, so that the total clamp loss in the bevelled plate is not necessarily less than that in the unbevelled plate. However, the loss studies in section 6.2 show that above 200 amp (585 A.C./cm) bevelling does in fact reduce the clamp plate loss.

When comparing the $\frac{1}{4}$" and 1" unbevelled clamp plates, the edge concentration of flux is less in the former indicating that the overall flux distribution depends on the relative distance between the edge and the main body of the stator rotor cores. Also, Fig. 7.0 - 1 and 7.0 - 2 show that the total flux normal to the radial and axial clamp plate surfaces is at least double, for the 1" clamp plate, but this difference is not accompanied by a corresponding difference in clamp loss; on the contrary Fig. 6.2 - 2 and 6.2 - 5 actually show more loss in the $\frac{1}{4}$" plate at currents lower than 210 amps.

Finally, to complete this study the quarter inch clamp plate was positioned 1.9cm from the stamping face as seen in Fig. 7.0 - 3. When comparing the axial surface plot with plot (b) in Fig. 7.0 - 1, the peak density in Fig. 7.0 - 3 is nearly twice that shown in Fig. 7.0 - 1. The radial plots however show somewhat lower flux density levels at the spaced-out plate, but in this case it was possible also to record the density on the inner radial surface. Though no losses were measured with the clamp plates in the position of Fig. 7.0 - 3, it was noticed that the clamp plates heated up extremely quickly. This is evidently the result of the higher flux density at the axial surface, and an effective

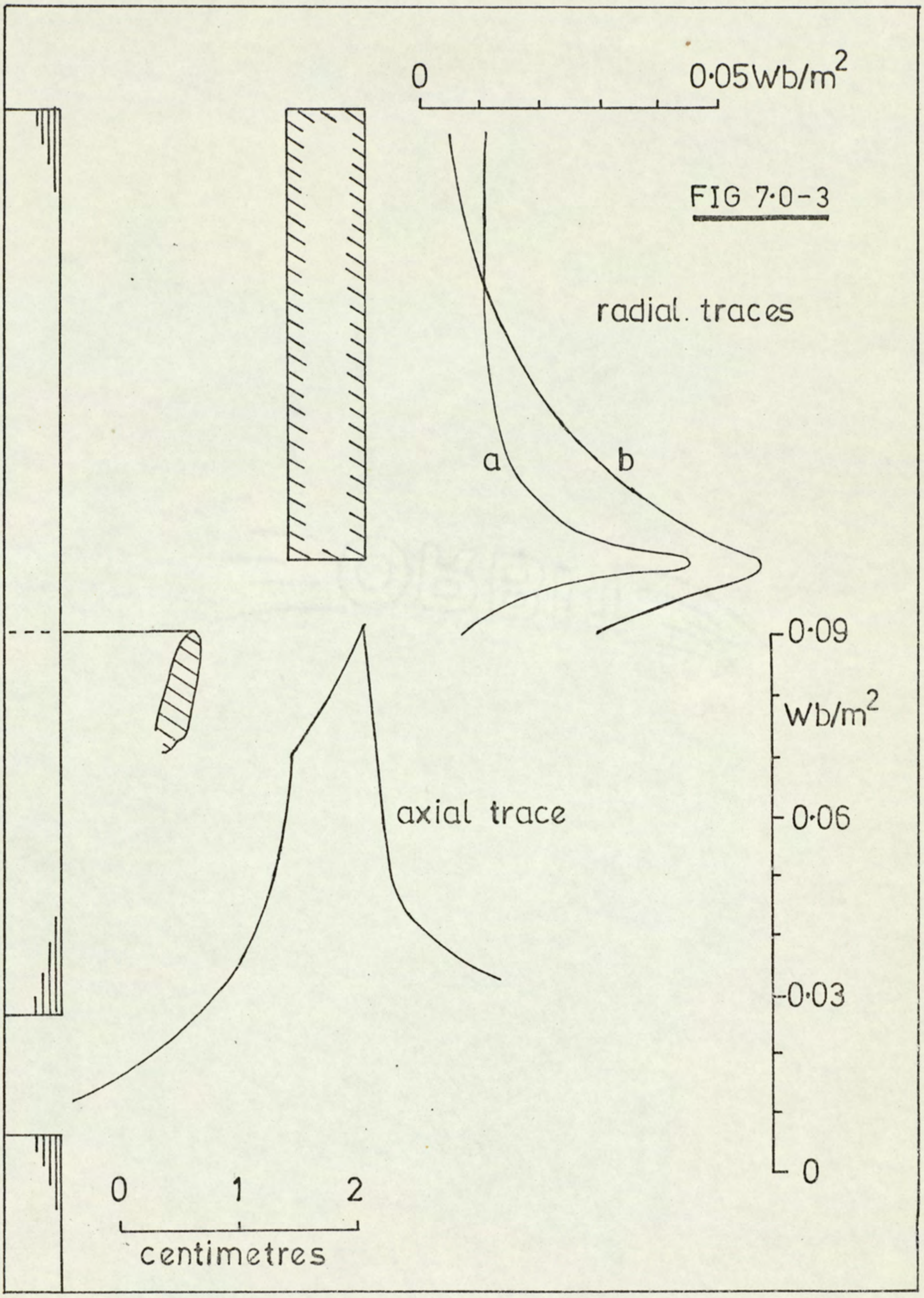

Flux density normal to radial and axial surcafes of clamp plate: — 1/4" mild steel clamp plates spaced 1.9 cm. from end of core. Radial clearance from winding 6.05 m.m.

a = Inner radial surface.

b = Outer radial surface.

doubling of the radial surfaces exposed to the overhang m.m.f. As seen earlier there exists a possibility that there is a further iron loss present in the interface between magnetic clamp and stamping core. It would appear possible to reduce this extra loss by fitting a layer of insulation (non metallic spacer) between the clamp plate and stamping pack. The test observations and Fig. 7.0 - 3 would suggest the reverse, though there may possibly be an optimum insulation thickness for which, extra losses are at a minimum level.

All the above tests were carried out with 240 amperes in the Stator winding corresponding to an electrical loading of 700 A.C./cm.

7.1 A study of clamp surface flux density waveforms.

It was noted in section 4.2 that the flux density at the clamp plates outer surfaces, as measured by the Hall probe, can show a considerable amount of time-dependent distortion. Since the current in the stator winding contains no time harmonic over 1.0% in magnitude (see Fig. 2.4 - 2), the source of this flux density distortion cannot be in the overhang. This was verified by examining the Hall probe output voltage visually on an oscilloscope, with the probe held flat on (parallel to) the winding overhang and moved axially away from the core towards the overhang nose. With stator currents up to 240 amp. 50Hz., the probe output voltage remained reasonably sinusoidal throughout.

To establish a qualitative relation between the flux density distortion at the core end surface (i.e. with no clamp plate), and end region position, the Hall probe was moved axially towards the core from a position 38mm radially above the overhang, and 25mm axially away from the core. The Hall probe surface was held in a plane parallel to the plane of the core end surface throughout, and again the probe output voltage waveform was examined visually.

a) 120 amp: The waveform was initially sinusoidal, with very faint distortion appearing as the probe approached the core face. The magnitude increased from 1.15mV to 1.75mV r.m.s.

b) 180 amp: Initially the waveform was slightly distorted, the distortion increasing considerably as the core surface was approached. The magnitude decreased from 1.55mV to 1.45mV r.m.s.

c) 240 amp: The waveform was initially badly distorted, with the third harmonic in clear evidence. On moving towards the core face, the distortion again increased, the fundamental content of the waveform appearing to decrease to zero at the core face, the waveform then being mainly third harmonic. The magnitude increased from 1.1mV to 1.65mV r.m.s.

From the above observations, the following comments can be made.

1) The flux density distortion appears to be the result of phenomena occuring at the core end surface, or within the core.

2) The phenomena are such that there is a cancellation of the fundamental component of flux density, at least over part of the core end surface.

3) Because of the varying degrees of distortion, there is no purpose in seriously considering the r.m.s. measurements taken.

To investigate these effects further, the various clamp plates were introduced and photographic records taken of all Hall probe output waveforms. The main interest lay in the clamp plate outer surface, and also the core end surface with no clamp plates. The tests were divided into two groups, Group I with the probe held on the clamp face at a fixed radial distance, and results taken for three different values of stator current; and Group II with the stator current held constant, and the probe moved to each of four radial positions on the clamp (or core) face.

<u>Group I.</u> The r.m.s. values of Hall probe output voltage are tabulated in Fig. 7.1 - 1, with the corresponding waveforms given in Fig. 7.1 - 1 (a -g). For comparison, some of the waveforms are collated in Fig. 7.1 - 2. With the possible exception of the no-clamp-plate case

variation of probe output with various clamp plate materials and varying stator current for a fixed position on the clamp plate.

FIG 7·1-1

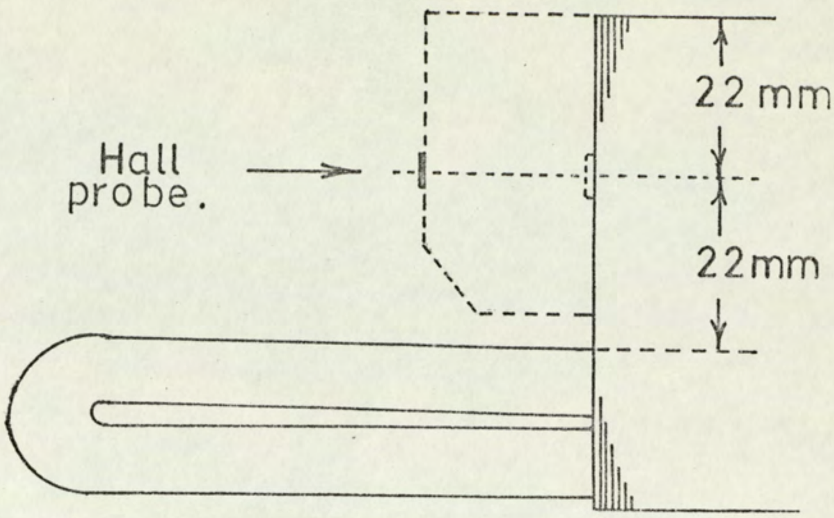

50 mA probe excitation.

output in millivolts (rms)

clamp type	50 Hz		
	120A	180A	240A
no clamps	2·60	3·20	3·50
brass	1·45	1·70	1·60
aluminium	1·25	1·50	1·50
meehanite	3·25	4·50	5·40
1/4" mild steel	3·00	4·30	5·10
1" mild steel (bevelled)	3·65	4·95	5·80
1" mild steel (no bevel)	3·10	4·15	4·80
1/4" mild steel with 10 mm copper shield	0·80	1·10	1·20

FIG 7·1-1a

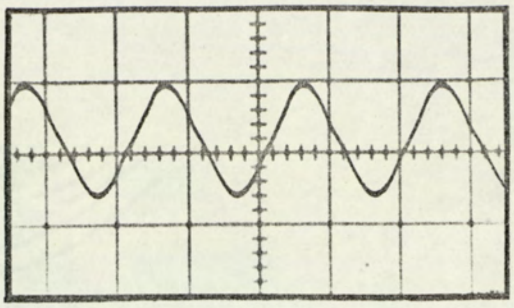

120 A

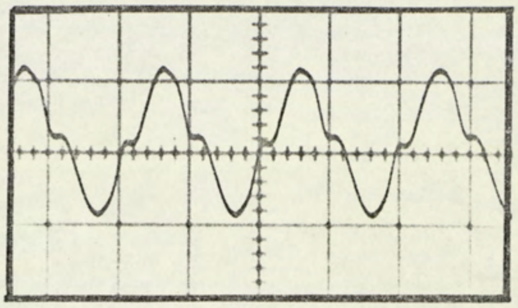

180 A

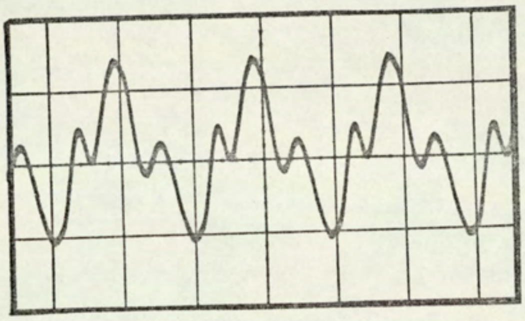

240 A

no clamp plates

0·005 v/cm

10 ms/cm

FIG 7·1-1b

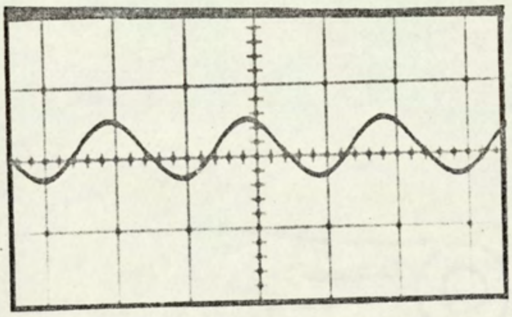

120 A

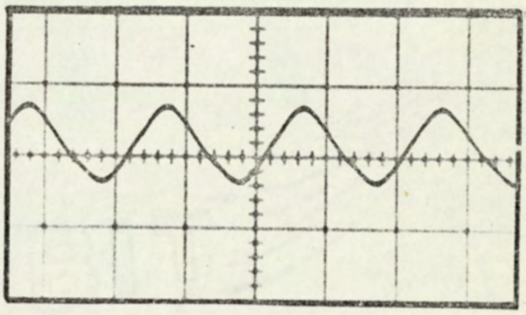

180 A

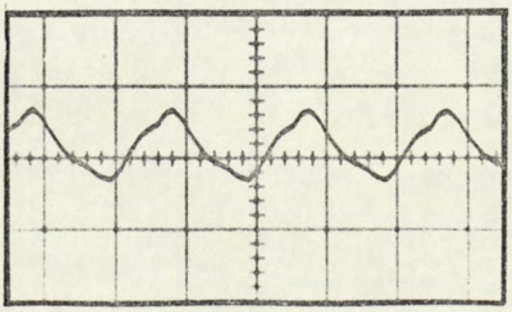

240 A

brass

0·005 v/cm

10 ms/cm

FIG 7·1–1 e

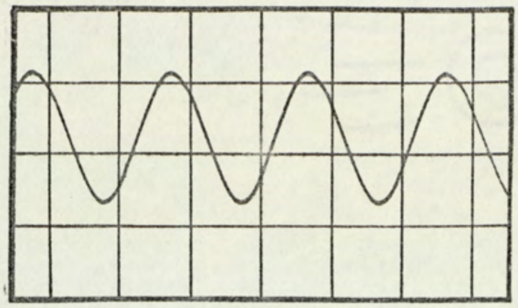

120 A

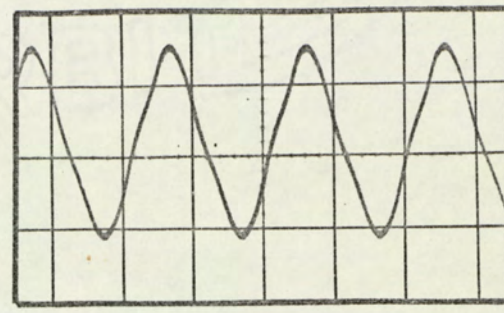

180 A

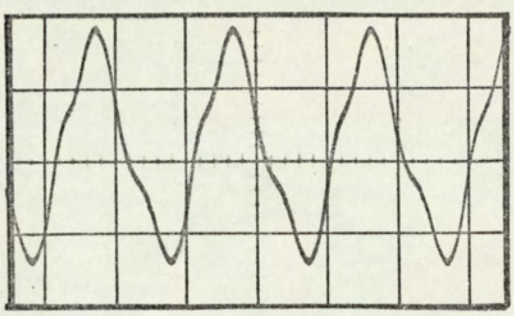

240 A

1/4" mild steel

0·005 v/cm

10 ms/cm

FIG 7·1–1 f

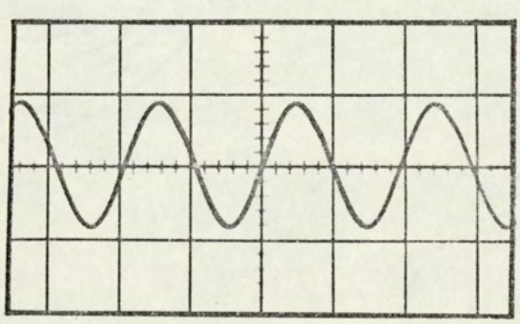

120 A

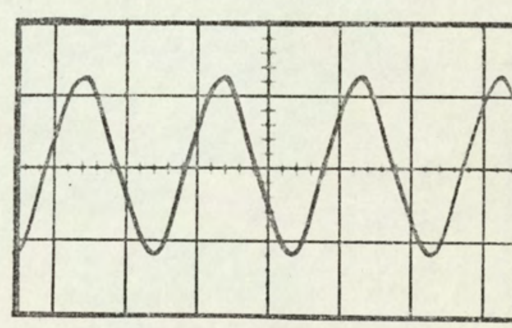

180 A

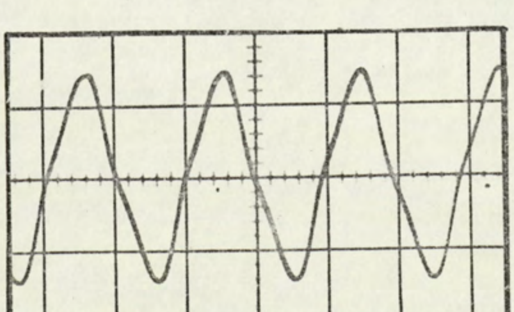

240 A

1" mild steel
(bevelled)

0·005 v/cm

10 ms/cm

FIG 7·1-1g

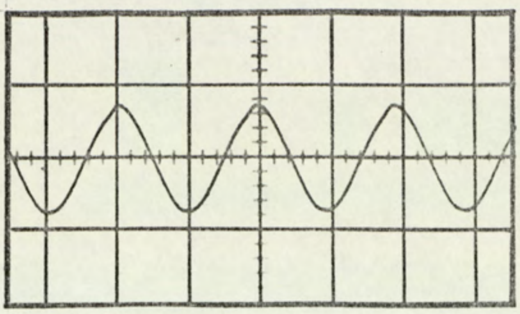

120 A

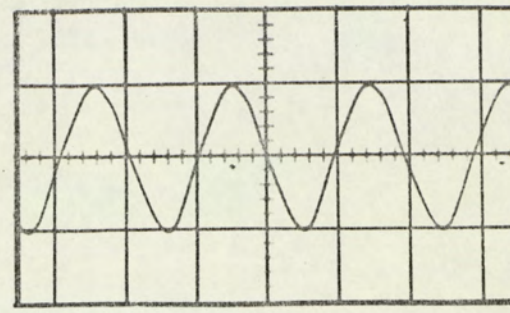

180 A

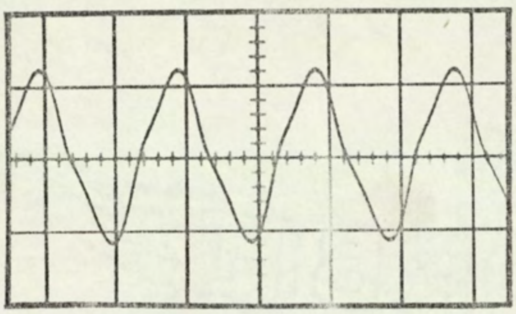

240 A

1" mild steel
no bevel
0·005 v/cm
10 ms/cm

FIG 7·1-1h

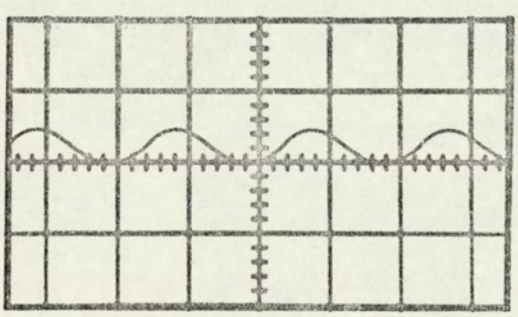

120 A

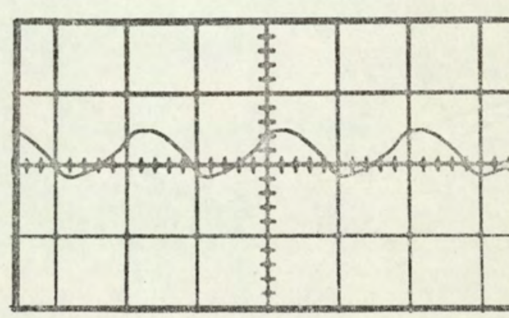

180 A

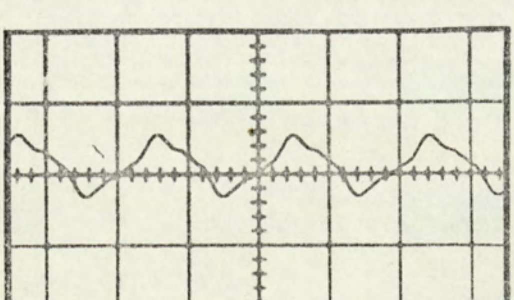

240 A

1/4" mild steel with
10mm copper shield
0·005 v/cm
10 ms/cm

FIG 7·1–2

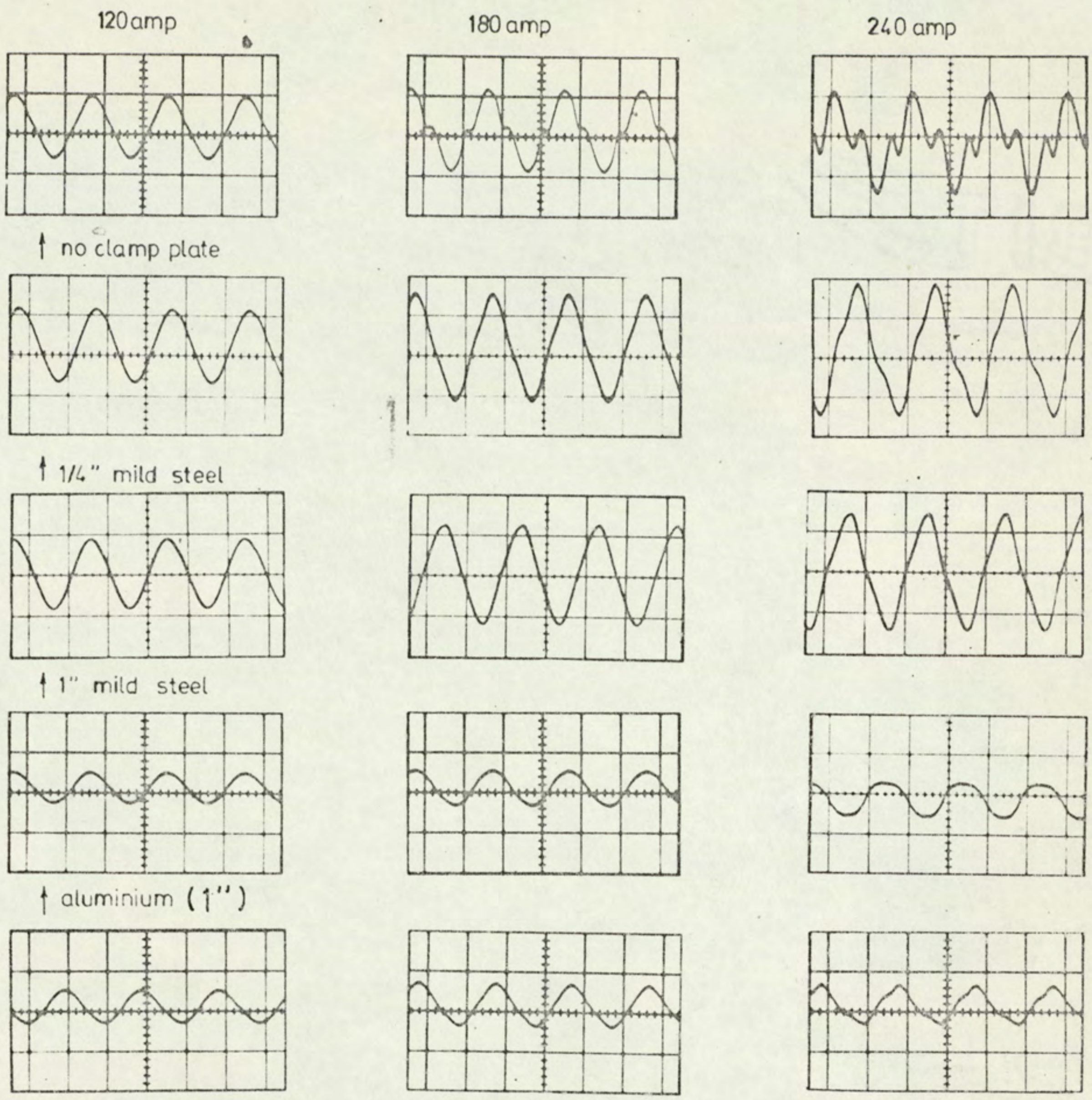

selection of oscillograms for comparison

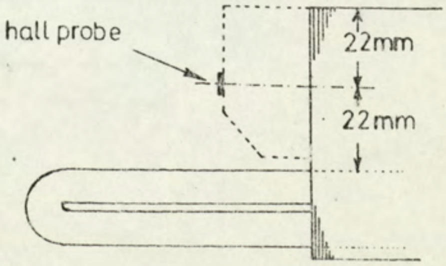

scale 5 mV / div.

(Fig. 7.1 - 1a), the fixed probe position is such that distortion in each case is limited, thus making the r.m.s. values in the table meaningful, and allowing the following argument to be developed.

Assuming the flux density normal to the clamp plate (or core) surface to be predominantly a function of leakage flux, it would be logical to expect the probe output voltage to be proportional to the exciting current, for any given clamp plate. The table in Fig. 7.1 - 1 shows clearly that this is not so. In fact, the measurements are consistent with an "opposing" effect originating from the core. By considering simple proportions, this effect, if it exists, can be shown to be negligible up to 146 $\pm$ 3 amps, for all cases except the no-clamp-plate case (139 amp, distortion not negligible) and the $\frac{1}{4}$" mild steel case (161 amp).

The resultant r.m.s. Hall probe output can be considered as consisting of two components, one the result of the overhang m.m.f. proportional to the exciting current, and the other a non-linear opposing effect issuing from the core. For example, for aluminium and 1" unbevelled mild steel, these component curves would be as shown in Fig. 7.1 - 3. The "effect from the core" is therefore seen to line up fairly convincingly with the build-up of m.m.f. at the stator core (and teeth) as represented in Fig. 6.3 - 4 and 6.1 - 1.

Considering further the results given in the table of Fig. 7.1 - 1, at 120 amps excitation there is negligible effect from the core, so that the corresponding Hall probe outputs are a true reflection of the overhang m.m.f., together with the accompanying reaction of the clamp plate eddy currents. It is immediately apparent that the reduction in surface flux density for the non-ferrous clamp plates, in the order brass, suggested component effects with hall probe in position shown in figure 7·1-1 (22 mm from winding) FIG 7·1-3

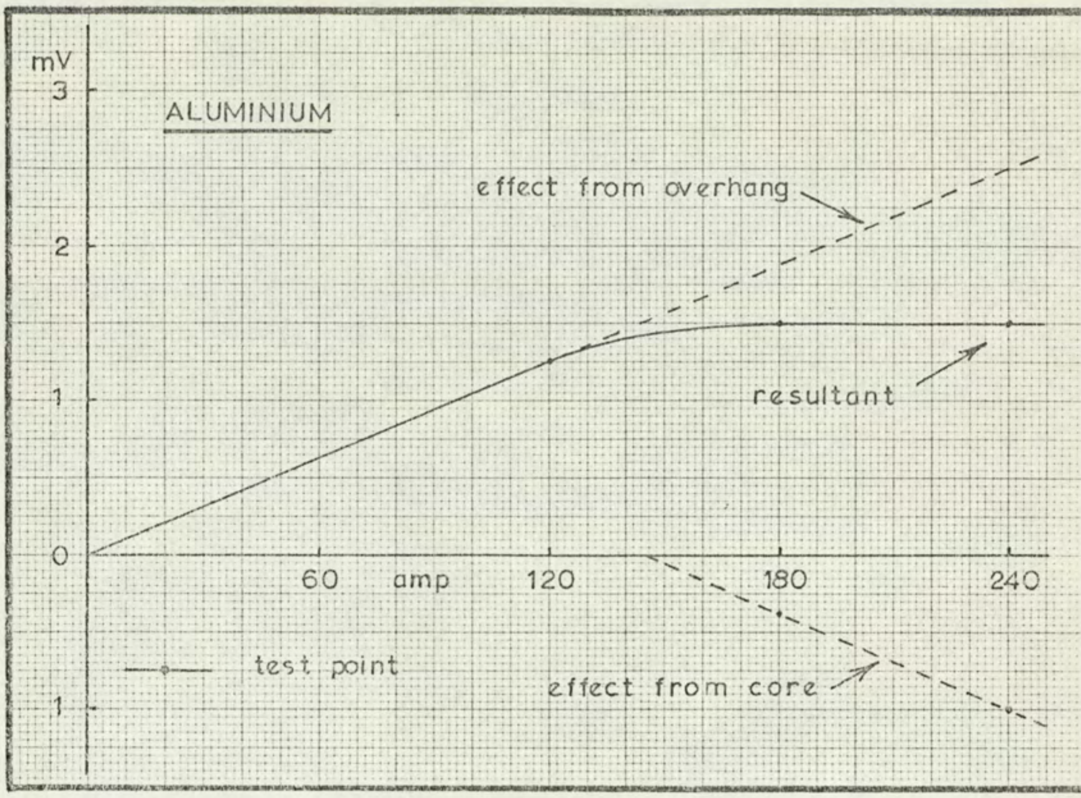

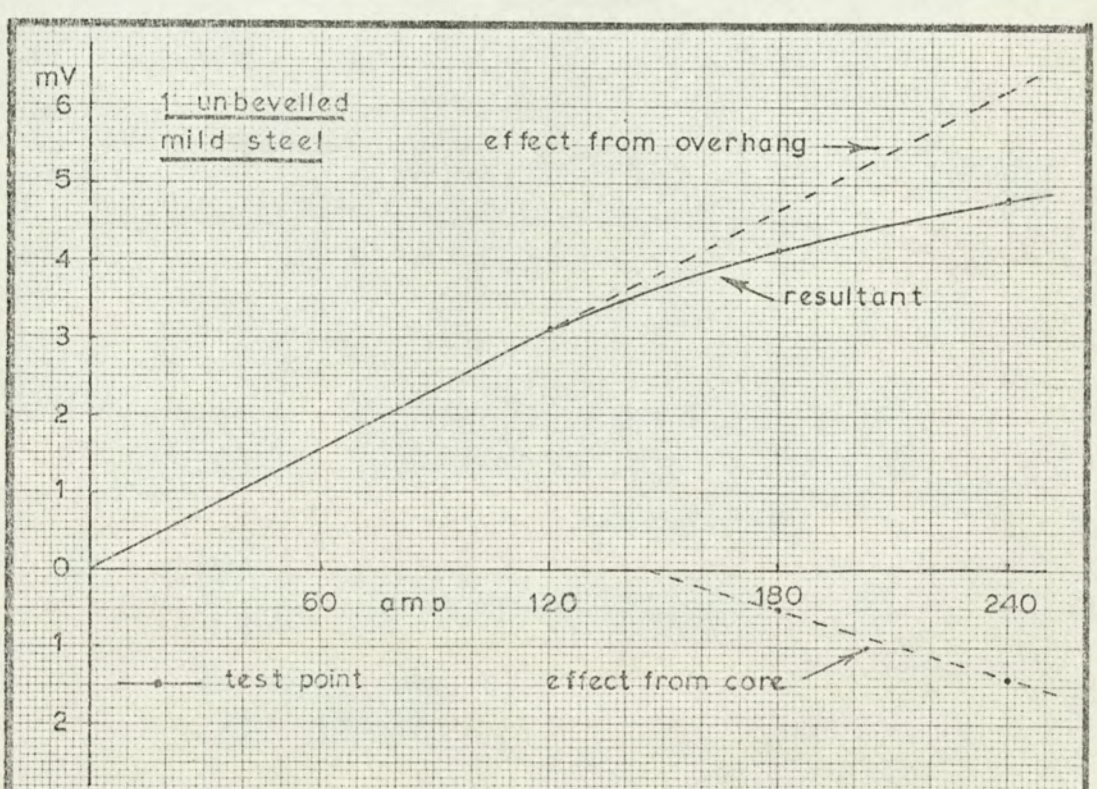

aluminium and copper is consistent with the level of eddy currents suggested by the respective specific resistances, which are 4.3 x the copper value for brass and 1.63 x the copper value for aluminium.

Compare the probe outputs at 120 amp excitation for aluminium clamp plates and no-clamp-plates. From the results of Fig. 7.1 - 4 and 7.1 - 1 the estimated probe output 1" axially from the core surface, with no clamp plates, (radial position of Fig. 7.1 - 1), is 1.84mV. With aluminium clamp plates, the corresponding value is 1.25mV, giving a ratio of 0.68 which can be compared with the a.c./d.c. ratio of 0.60 given for aluminium in section 5.3. It is assumed here that with no clamp plates the reduction in axial flux density due to the excitation being a.c. rather than d.c., is negligible.

Referring again to conditions at 120 A excitation,

a) The axial flux density 1" from the core surface is increased in the ratio 3.1/1.84 = 1.68 when the 1" unbevelled mild steel clamp plate is introduced. With the 1" bevelled M.S. clamp plate, the ratio increases to 1.98 due to the flux-concentrating effect of the surface discontinuity where the bevel commences (8mm radial from the Hall probe position). With the $\frac{1}{4}$" M.S. plates, the ratio lies between 1.15 and 1.63; Assuming the axial flux density to fall linearly from the core surface over an axial distance of 1", the ratio is

$$3.0/(2.6 - 0.25(2.6 - 1.84)) = 1.24$$

b) Comparing results for the meehanite clamp plate with the 1" bevelled M.S., the axial flux density reduces in the ratio of 3.25/3.65 = 0.89, which is obviously governed more by the permeability ratio 0.43 at 1.3 wb/m^2 (from Fig. 2.2 - 1) than by the inverse specific resistance ratio 0.26.

c) The effect of shielding the $\frac{1}{4}$" M.S. plate with a 10mm. thick copper plate is seen to reduce the axial surface flux density in the ratio of $0.8/3.0 = 0.27$ (or nearly 4 : 1). It must be pointed out that the copper plate was not a complete ring, shielding the whole of the M.S. clamp plate, but was limited to shielding up to two pole pitches, circumferentially. Further tests with the copper shield are given in section 7.2.

<u>Group II</u> At a constant winding excitation of 240 amps, the outputs of the Hall probe situated at each of four radial positions are tabulated in Fig. 7.1 - 4. The corresponding waveforms are given in Fig. 7.1 - 4 (a - g), with most of these collated in Fig. 7.1 - 5. In the cases of no-clamp-plates, aluminium and $\frac{1}{4}$" M.S. clamp plates, the oscillograms were enlarged photographically by 3 to 8 times, and a harmonic analysis made, measuring 80 ordinates per cycle. The results are given in Fig. 7.1 - 6.

It is seen at once that

1) The distortion (or percentage harmonic content) increases with radial distance away from the winding.

2) Both ferrous and non-ferrous clamp plates reduce the distortion visible compared with no-clamp-plates.

Note the reduction in distortion at the axial position of 1" from the core surface, when no clamp plate is present.

3) As previously suggested, the increase in distortion appears to be due to a reduction in the fundamental component, this being nearly zero at position D on the core surface.

variation of probe output with various clamp plate materials and varying radial position for a fixed stator excitation.

FIG 7·1-4

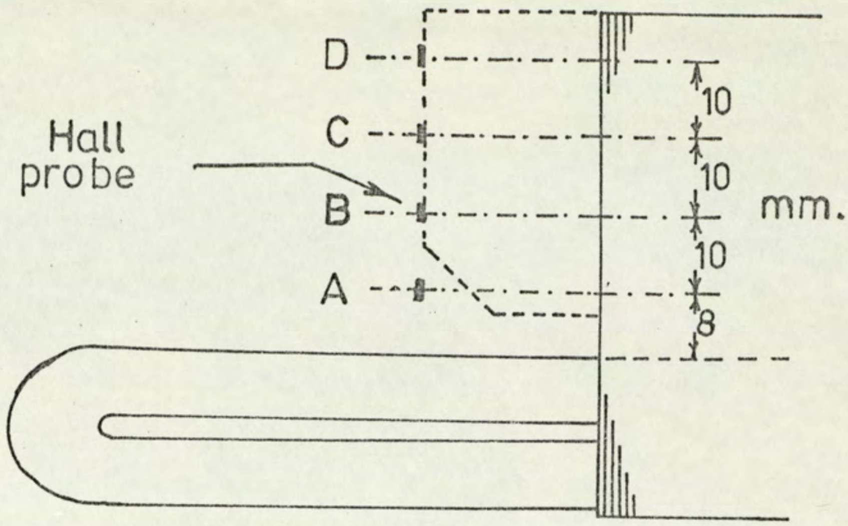

50 mA probe excitation

output in millivolts(rms)

240 Amp on stator

position	A	B	C	D
no clamps	7·45	4·35	2·65	1·60
brass	2·85	2·25	1·50	1·02
aluminium	2·80	1·70	1·05	0·85
meehanite	—	not	taken	—
1/4" mild steel	12·90	5·80	3·20	1·65
1" mild steel (bevelled)	8·35	7·00	3·35	1·60
1" mild steel no bevel	15·90	6·20	3·35	1·60
in air, 1" from stamping face	3·35	2·50	1·75	1·15

FIG 7·1-4a

no clamps

0·005 v/cm

10 ms/cm

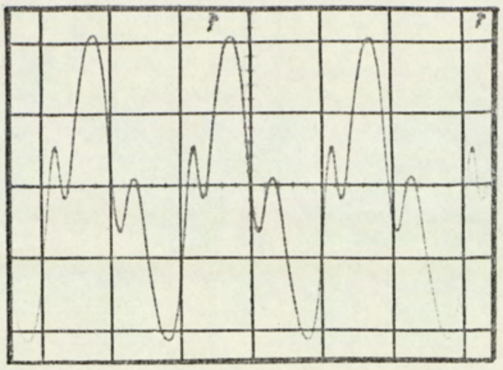

A

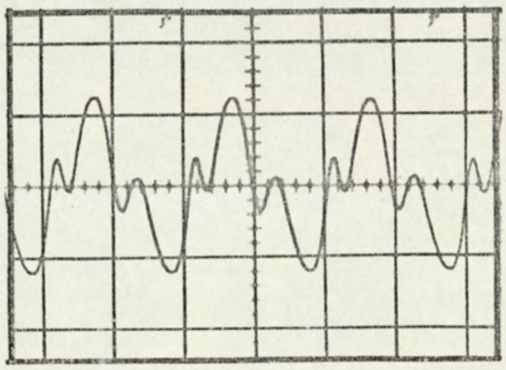

B

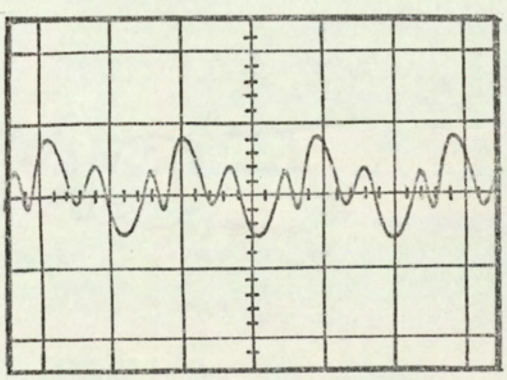

C

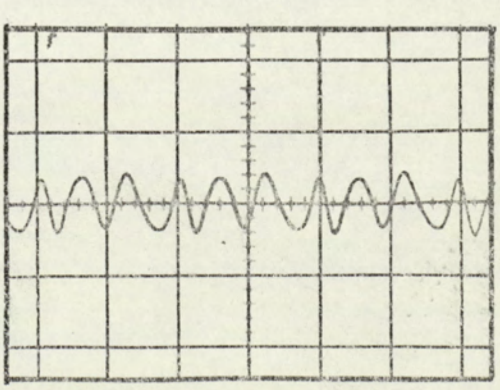

D

FIG 7·1-4b

brass

0·002 v/cm

10 ms/cm

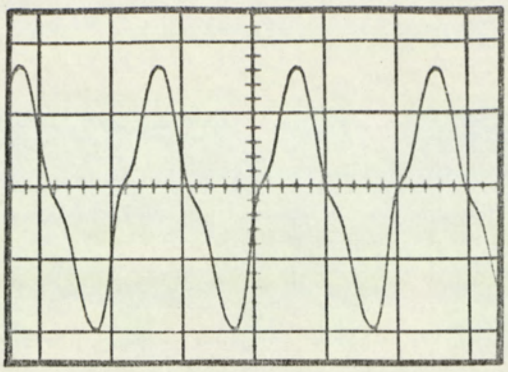

A

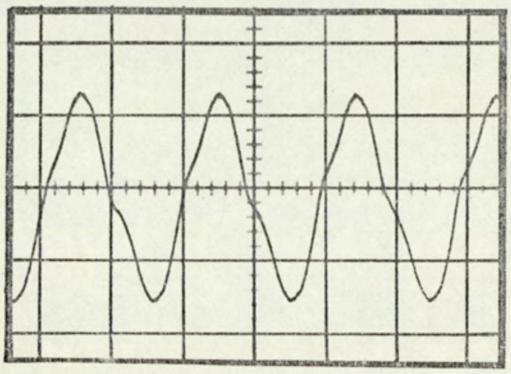

B

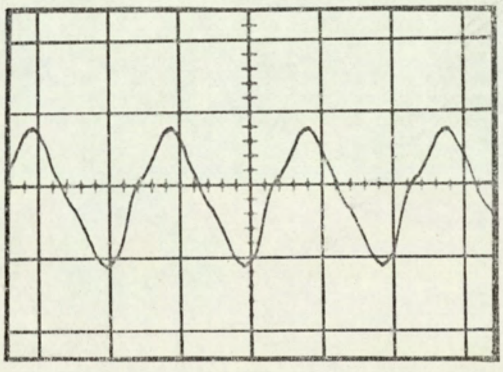

C

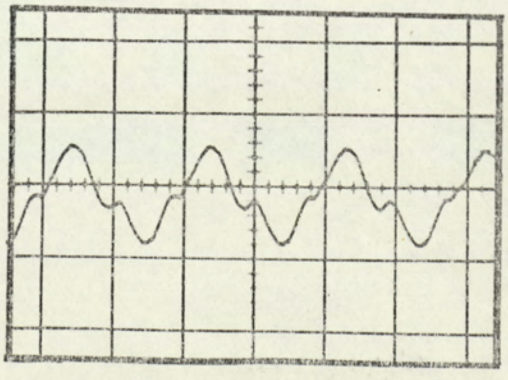

D

FIG 7·1-4c

aluminium

0·002 v/cm

10 ms/cm

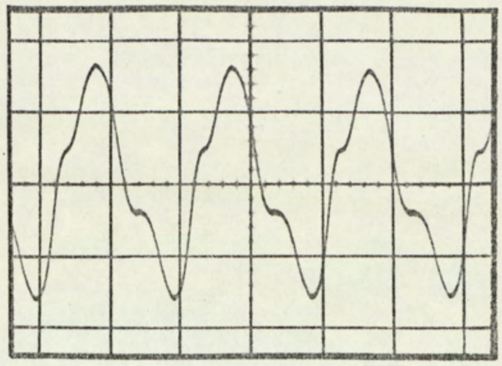

A

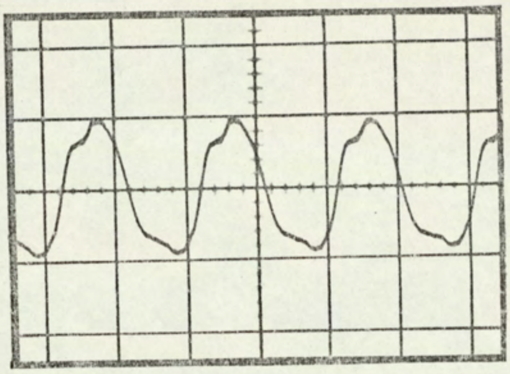

B

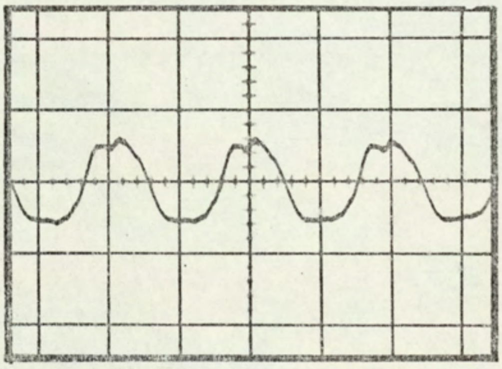

C

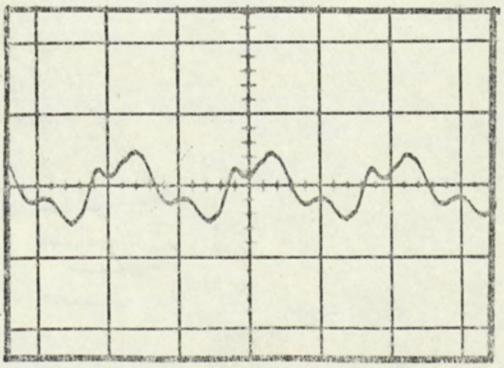

D

FIG 7·1-4d

1/4" mild steel

0·010 v/cm

10 ms/cm

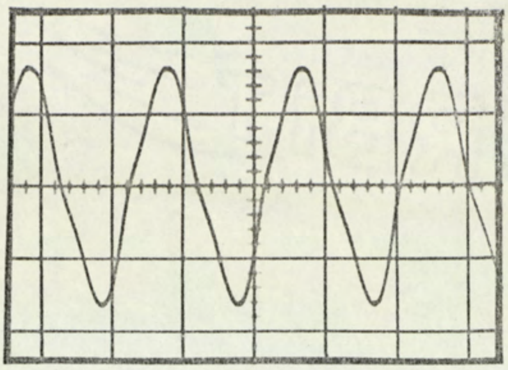

A

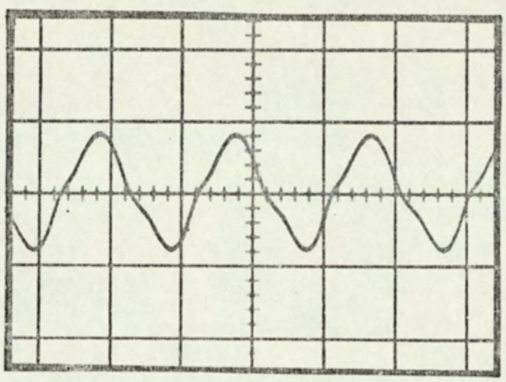

B

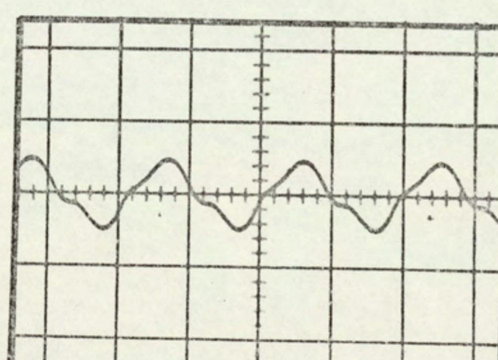

C

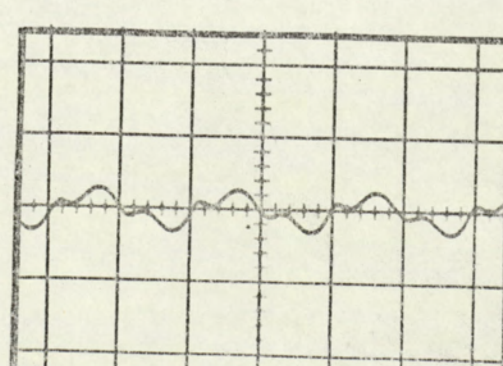

D

FIG 7·1-4e

1" mild steel
(bevelled)
0·005 v/cm
10 ms/cm

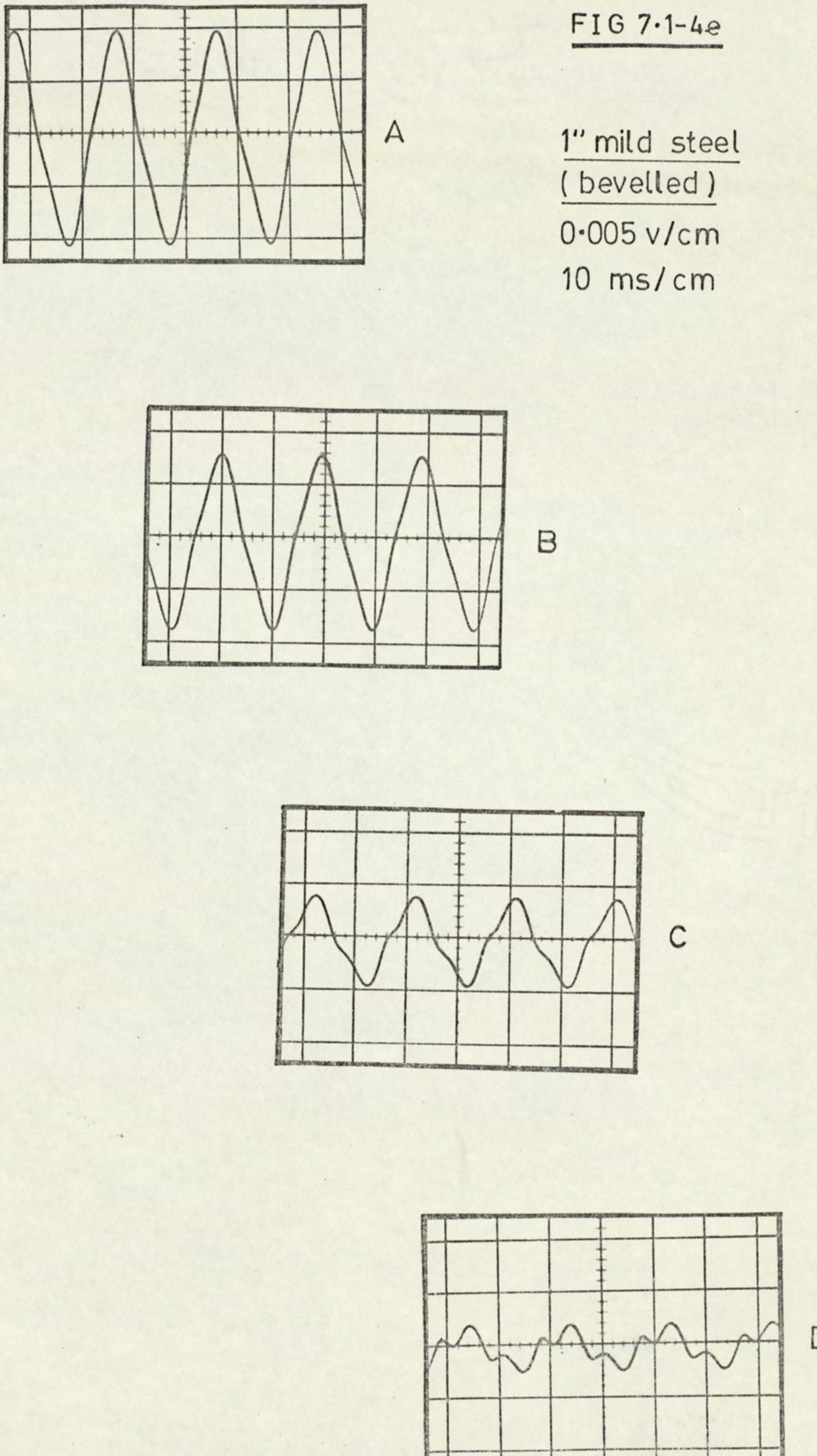

FIG 7·1-4f

1" mild steel
no bevel
0·010 v/cm
10 ms/cm

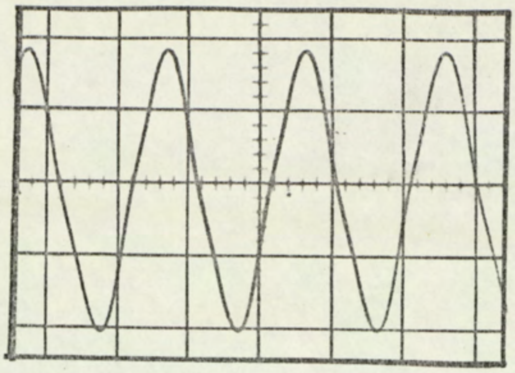

A

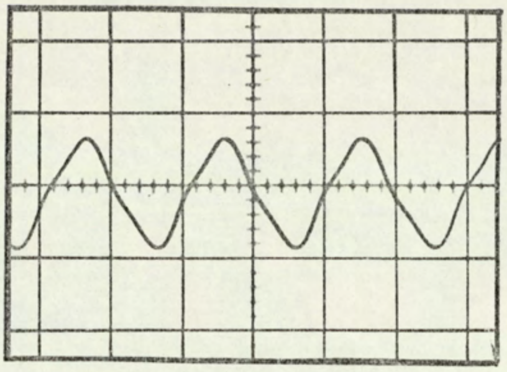

B

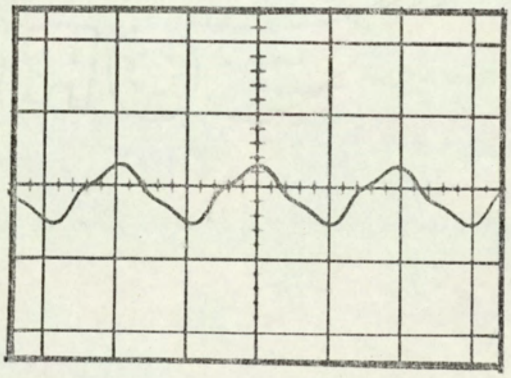

C

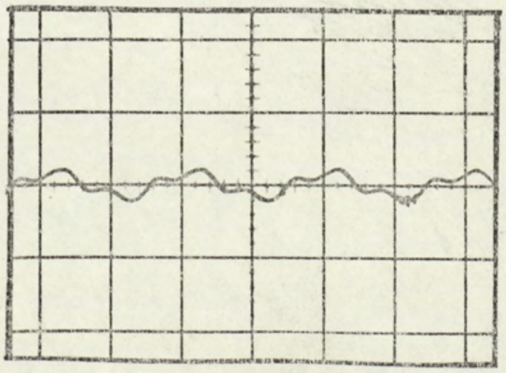

D

FIG 7·1-4g

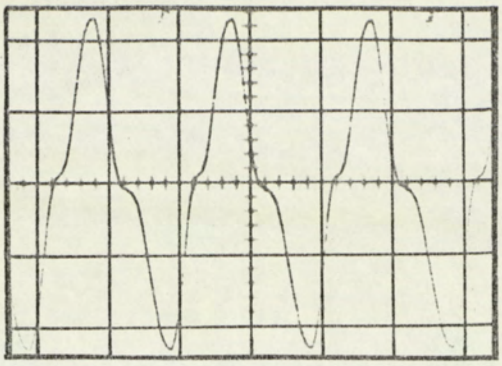

A

in air, 1" from stamping face

0·002 v/cm

10 ms/cm

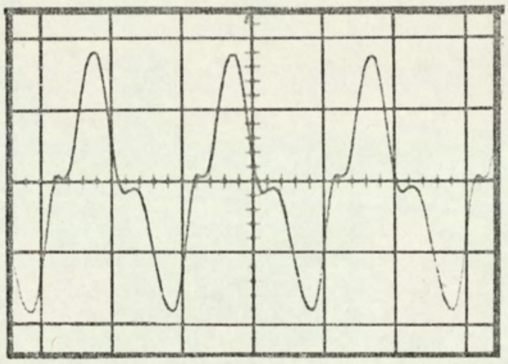

B

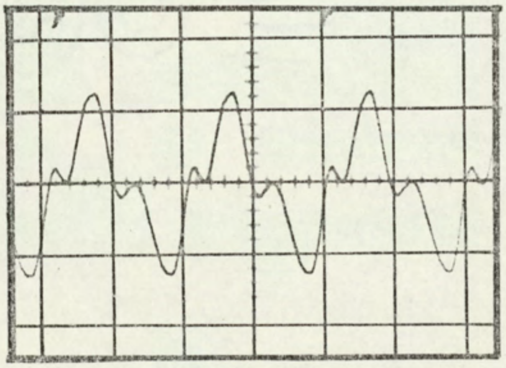

C

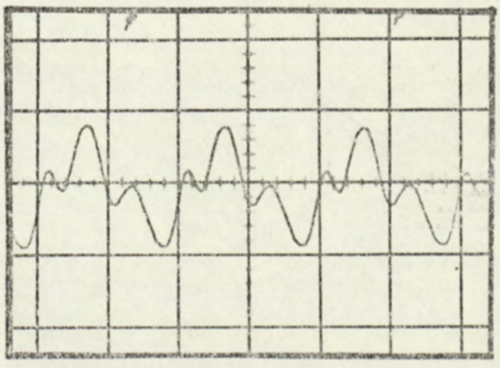

D

FIG 7·1-5

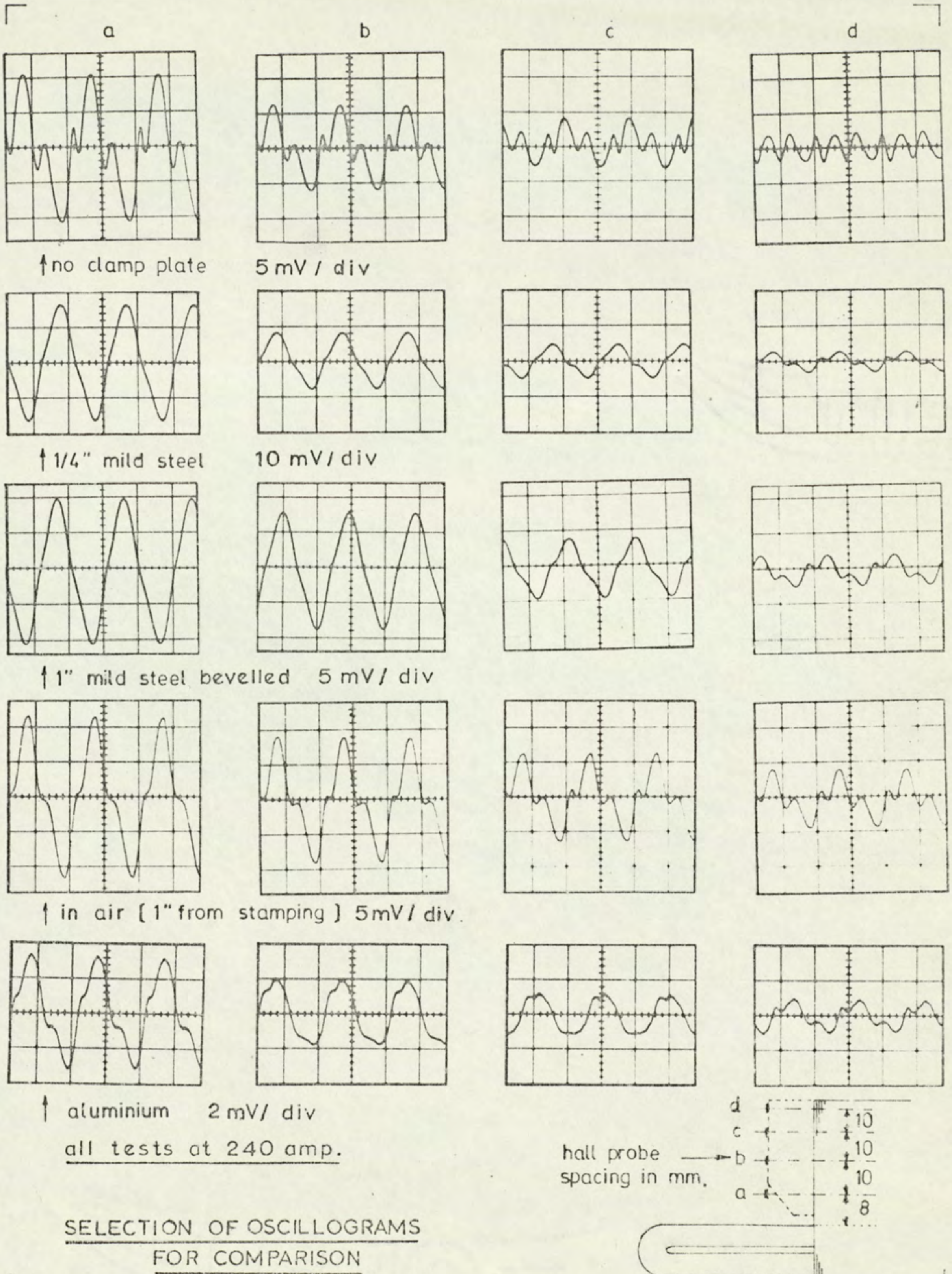

SELECTION OF OSCILLOGRAMS FOR COMPARISON

Extending the reasoning offered in sections 6.3 and 6.4, and again when discussing the results of Group I, it is suggested that primarily the Hall probe is measuring the resultant effect of magnetising forces (1) in the overhang, and (2) appearing across the stator core due to magnetic saturation of the main flux paths in the model. With no plates present there is also the secondary effect of reaction eddy currents flowing in the plane of the core stampings due to the overhang leakage flux. It is doubtful whether the eddy currents flowing in the core end stamping due to the main flux produce any external magnetic effects since the paths of these currents are toroidal. With this picture in mind, it seems likely that the distortion is associated with the way in which the core magnetising force is distributed.

Assuming (a) that the core magnetising force is entirely circumferential in direction, (b) that it is distributed sinusoidally with respect to angular position, at a given instant in time, (c) that the reluctance of the leakage path between two circumferential points on the core end is proportional to the circumferential distance, then it is shown in Appendix 2 that the leakage flux density B_{lc} at a point on the core end is given by

$$B_{lc} = \left\{ H_{cl} \; \frac{\sin \omega t}{\omega t} \right\}_{t=o}^{\frac{\pi}{2\omega}}$$

This expression applies to the first quarter of the positive half-cycle, and leads to the complete waveform of the flux density normal to the core end, illustrated below.

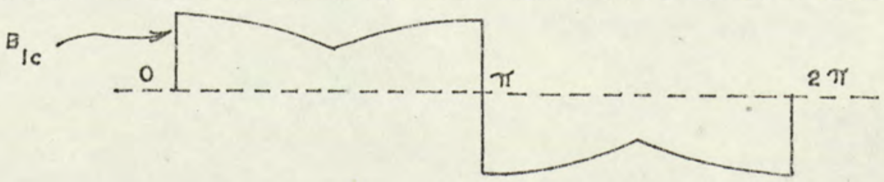

The fundamental, 3rd, and 5th harmonic components of this waveform are as follows:-

Fundamental :- 100%

3rd harmonic:- 52%

5th harmonic:- 20%

This result does not predict any even harmonics, but the odd harmonics calculated can be compared with values obtained indirectly from the test results. Extrapolating between positions B and C in Fig. 7.1 - 4, and using the results of Table 7.1 - 6., the harmonic values of normal flux density 22 mm. above the winding (i.e., position shown in Fig. 7.1 - 1) are as follows:-

Fundamental (resultant):- 4.3 mV (peak values)

3rd harmonic :- 2.25 mV

5th harmonic :- 0.7 mV

From the Table in Fig. 7.1 - 1, and using the argument illustrated in Fig. 7.1 - 3, the fundamental components of probe output voltage at 240 amps excitation are 2.6 x (240/120) = 5.2mV from the overhang, and 5.2 - 3.5 = 1.7 mV from the core (r.m.s. values). Allowing for the waveform distortion shown in Fig. 7.1 - 1a, the r.m.s. of the resultant fundamental is $4.3/\sqrt{2}$ = 3.04 mV rather than 3.5 mV. The fundamental component from the core is then 5.2 - 3.04 = 2.16 mV. Thus the harmonic components of the contribution from the core are

Fundamental :- 2.16 mV = 100% (r.m.s. values)

3rd harmonic :- 1.59 mV = 74%

5th harmonic :- 0.49 mV = 23%

Considering the assumptions made, these results compare favourably with the analysis of the calculated waveform.

FIG 7·1-6

harmonic analysis of probe output voltage on clamp plate surface

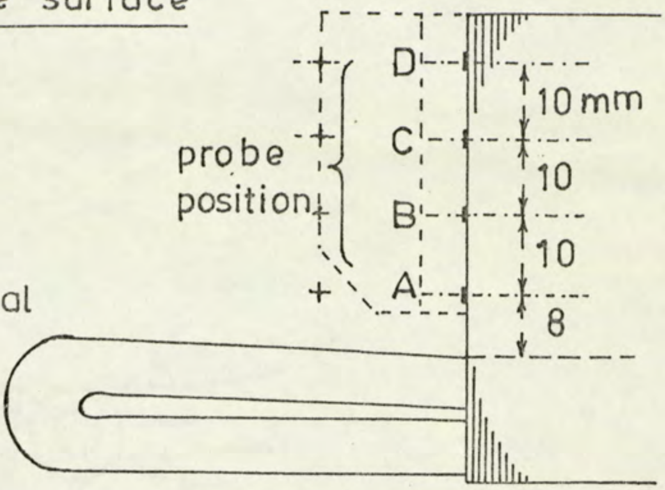

n = order of harmonic

row (a): actual mV.

row (b): % of fundamental

	no clamps				aluminium				1/4" mild steel			
n	A	B	C	D	A	B	C	D	A	B	C	D
↓ total r.m.s. millivolts	7·45	4·35	2·65	1·60	2·80	1·70	1·08	0·85	12·9	5·80	3·20	1·65
1 a	9·34	5·39	3·06	0·66	3·83	2·35	1·47	1·12	18·0	8·00	4·35	1·71
b	100	100	100	100	100	100	100	100	100	100	100	100
2 a	2·04	1·17	0·32	0·58	0·62	0·34	0·13	0·14	2·70	1·14	0·77	0·57
b	21·9	21·8	10·4	87·0	16·1	14·5	8·50	12·3	15·1	14·3	17·7	33·2
3 a	3·91	2·49	2·06	1·97	0·79	0·29	0·20	0·41	1·63	1·24	0·92	1·39
b	42·0	46·3	67·2	300·	20·6	12·2	13·3	37·0	9·00	15·4	21·2	82·0
4 a	0·92	0·66	0·11	0·49	0·11	0·14	0·05	0·10	0·30	0·28	0·26	0·28
b	9·90	12·3	3·50	74·0	2·90	5·90	3·90	8·90	1·70	3·50	5·90	16·6
5 a	1·36	0·77	0·60	0·50	0·22	0·10	0·06	0·08	0·47	0·33	0·20	0·38
b	14·6	6·50	19·5	76·0	5·60	4·40	4·60	7·40	2·60	4·10	4·60	22·2
6 a	0·60	0·35	0·09	0·20	0·07	0·07	0·04	0·05	0·24	0·16	0·08	0·10
b	6·50	1·70	2·80	29·7	1·90	3·10	2·70	4·60	1·30	2·00	1·90	5·80
7 a	0·33	0·09	0·06	0·06	0·04	0·03	0·02	0·04	0·10	0·05	0·03	0·06
b	3·60	1·65	2·10	9·60	1·04	1·50	1·20	3·40	0·54	0·70	0·75	3·50

Also, this calculated shape should be compared with the waveforms of Fig. 6.3 - 4, in particular the trace at 180 amps. The distortion indicated at the higher currents must be more than predicted, since the magnetising force in the core is then distorted due to saturation effects.

The effects discussed above are clearly complex, and an acceptable explanation would have to account for the magnetising force at the core, at the higher flux densities, appearingto penetrate through both ferrous and non-ferrous clamp plates. Table 7.1 - 6 shows that the harmonic components of the surface flux densities are reduced by the clamp plates, but they are still unexpectedly high.

7.2 Observations using copper shields.

Whilst a detailed study of the effect of copper shields on magnetic clamp plate is outside the scope of this work, a very limited investigation was made, as indicated in section 7.1. It was thought that this diversion might help to resolve some of the problems met with in the main clamp plate study.

The first test was a study of the waveform of flux density normal to the radial surface as detailed in section 7.1. When the quarter inch mild steel clamp plates carry a 10 mm thick copper shield on the outside radial surface, the surface density drops in magnitude by nearly 4 : 1 (see table 7.1 - 1). At the time, not much thought had been given to this phenomenon apart from noting the significant reduction in magnitude and change in waveshape. For the test illustrated in Fig. 7.2 - 1, the ratio of approximately 4 : 1 was obtained using the one inch mild steel clamp plates, the measurements here being made at a radial distance of 40 mm from the winding compared with 22 mm for the quarter inch plates. All the above tests were carried out with 240 amps. stator winding excitation.

At this stage it was considered necessary to investigate flux densities at the adjacent surfaces of clamp plate and copper shield and also whether the shield was equally effective when located in an approximate axial position close up and parallel to the winding. The conditions of the various tests are detailed in Fig. 7.2 - 2, with and without shields.

Although the radial copper shield shows a reduction of 4:1 in density at its outer surface, the magnetic

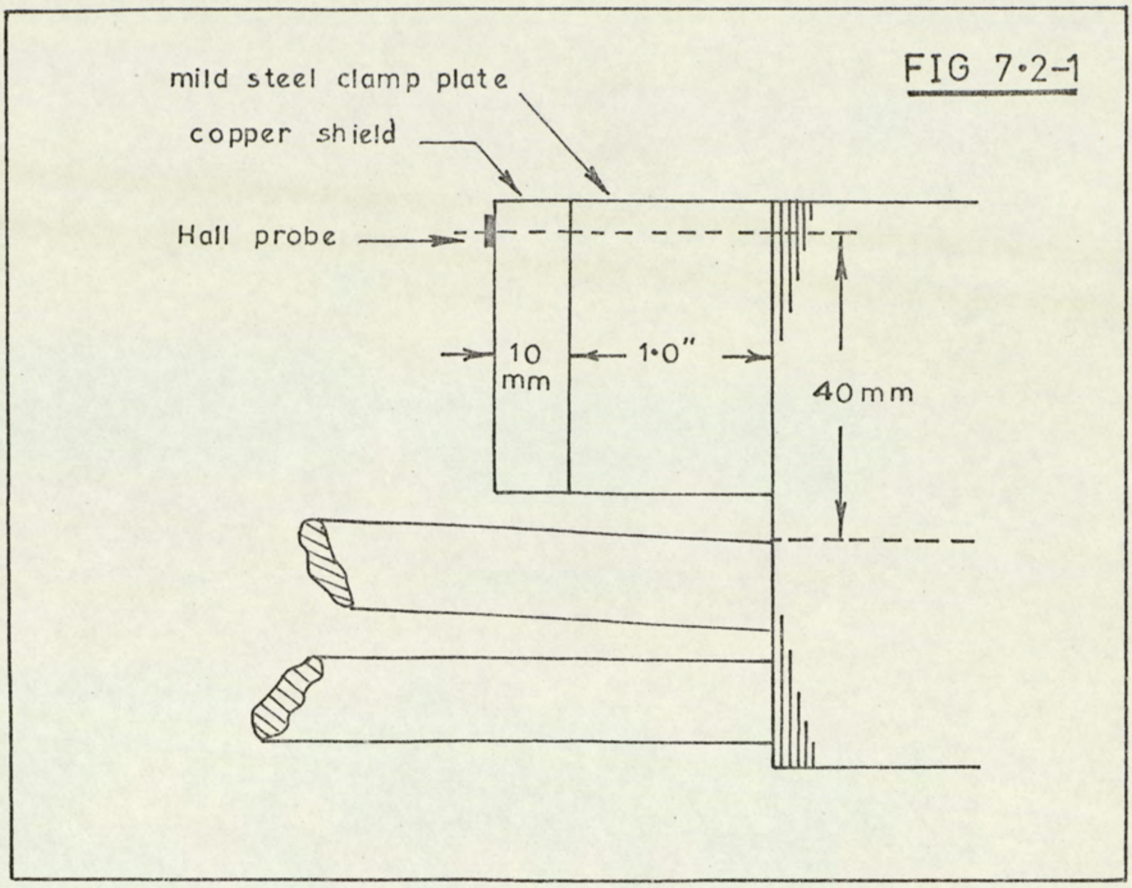

FIG 7·2–1& 2 POSITIONS OF HALL PROBE FOR TESTS WITH COPPER SHIELD

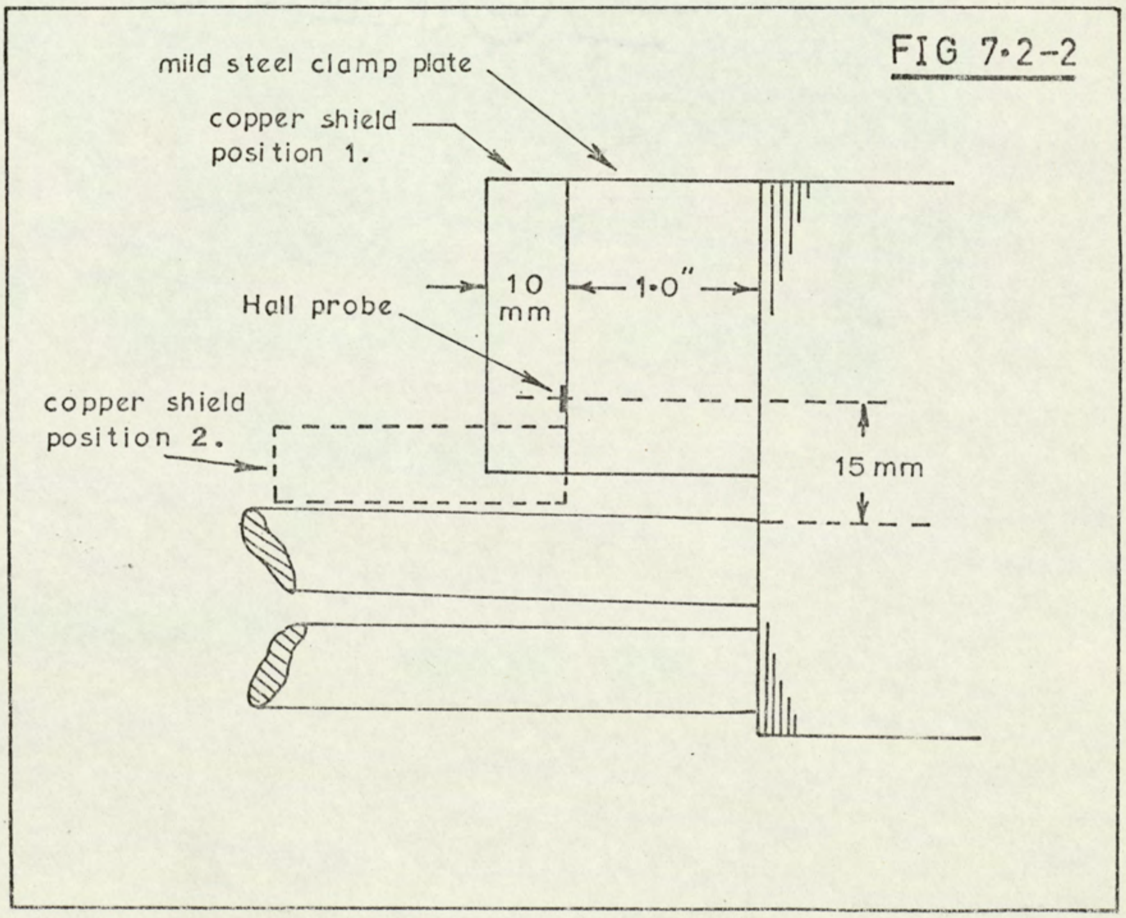

clamp plates do not benefit by the same amount. A reduction from 7.0 mV to 4.6 mV or approximately 1.5 : 1 results. Further, with the shield placed flat on the end winding the reduction at the clamp surface is from 7.0 mV to 5.4 mV or approximately 1.3 : 1. These results probably explain why some researchers have indicated that clamp shields do not significantly alter total losses. It is suggested, therefore, that in some cases, the heavy damping current loss in the copper is of the same order as the reduction in the clamp plate loss.

It is hoped that this brief study of the effect of copper shielding will provoke a more detailed study of the subject, including loss measurements. It is quite clear that the problems involved are complex.

7.3 Use of the Hall probe equipment in industry.

As the author's work was sponsered by industry, the Hall probe equipment developed for this study would offer an excellent means of exploring end region fields in production machines. Apart from the Hall probe equipment any phenomena relating to end winding regions and m.m.f. induced losses would be brought to the authors attention by the personnel of the various works test departments. For convenience these tests are documented as a series of projects.

Project 1.0 In this study the end region field of a 33,500 horse power, 1000 r.p.m. 50Hz, 11kV 1.0Pf. synchronous induction motor with non-magnetic stator clamp plates and rotor end bells was explored thoroughly. This machine is the largest industrial high speed three phase machine to be built at the Witton Factory of C.A. Parsons, and is also the largest sychronous induction motor in the world at the present time.

The Hall probe equipment described in section 3.3 was used to examine the end-region field, with reference to the following points:-

a) The use of solid brazed ferrules shorting all the strands at the end of the Roebel Transposed half-bars.

b) The use of non-magnetic clamp plates on six pole machines of this size.

c) The flux density normal to the conical surface of the winding overhang. (barrel surface).

d) The general pattern and magnitudes of the radial, axial and circumferential components of flux density in the end region.

The resultant tests proved the versatility and convenience of using the equipment. Over 300 test readings were taken in under 90 minutes of test time. Fig. 7.3 - 1 shows the resulting surface density plots on the tooth supports, clamp face and end winding surfaces. The tooth supports show a considerably higher surface density than the clamp face, the maximum value occurring nearest the stator bore.

The flux density normal to the surfaces of the ferrule did not exceed 0.02 Wb/m^2 (not shown in diagram). At this low value it was assumed that eddy current copper loss in the solid ferrules is negligible. The ferrules remained cool on a static heat run on the stator winding at rated current 50Hz. The low value of the flux density traces (a) and (b) on the winding surfaces justified the decision to use a 360° Roebel transposition in the slot portion only, in preference to the 540° Roebel transposition which extends into the end region, commonly used on Turbo-generators. At this low value of flux density, the eddy current copper loss in the end-winding must be negligibly small. Fig. 7.3 - 2 to 4 respectively show the radial, circumferential and axial components of flux density in the end region, with the rotor removed. Points of equal flux density are joined to form contours, which must not be confused with conventional two dimensional flux plots. The following points are apparent from these component contours.

1) In the region near the ferrules, circumferential components are low, and the radial and axial components indicate a toroidal-type field distribution.
2) Near the clamp plate surface, circumferential components are of the same order of magnitude as the axial components and are therefore not negligible, as would be the case with magnetic clamp plates.

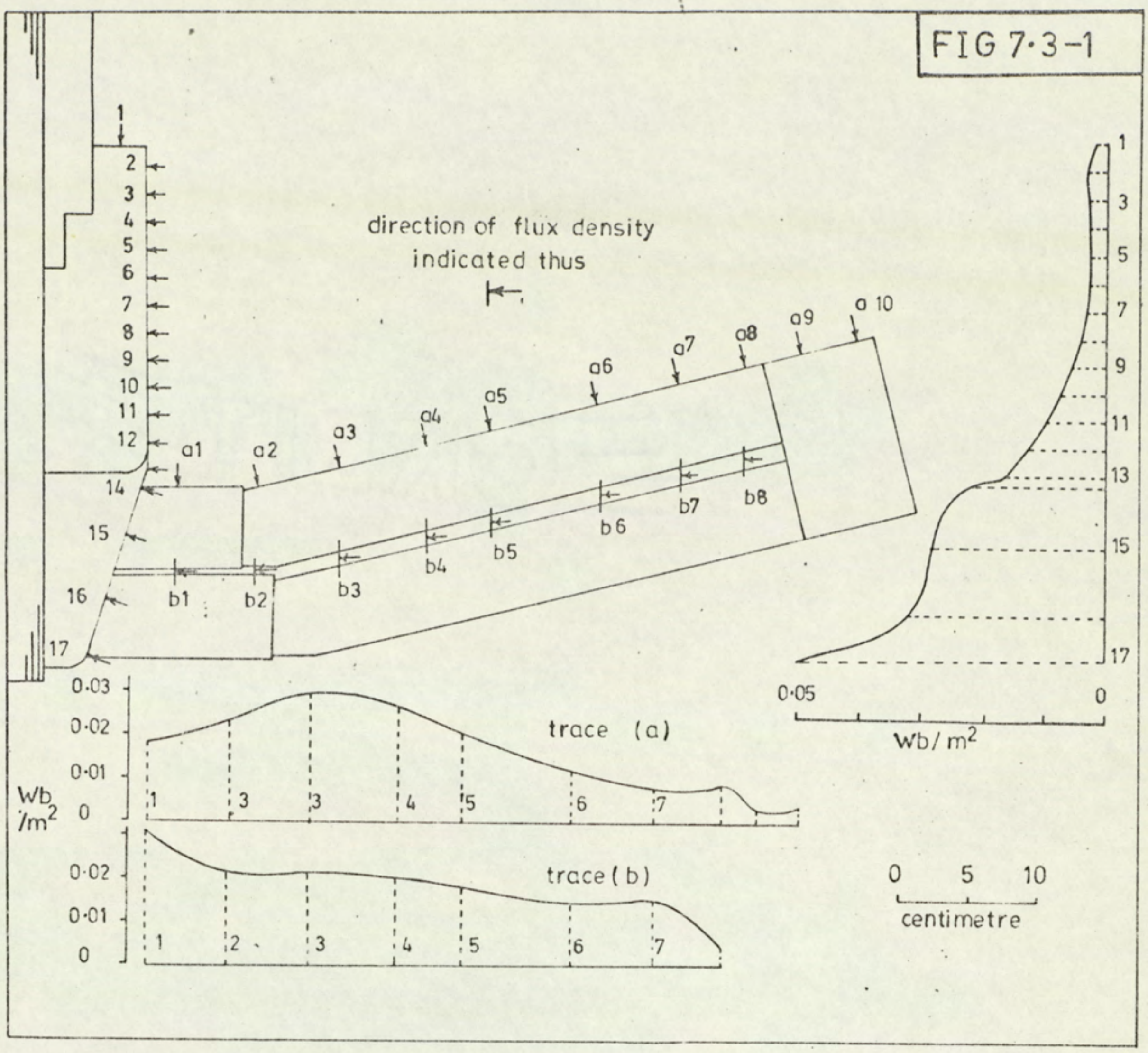

SURFACE FLUX DENSITY PATTERNS

PROJECT - 1

33500 H.P. synchronous induction motor

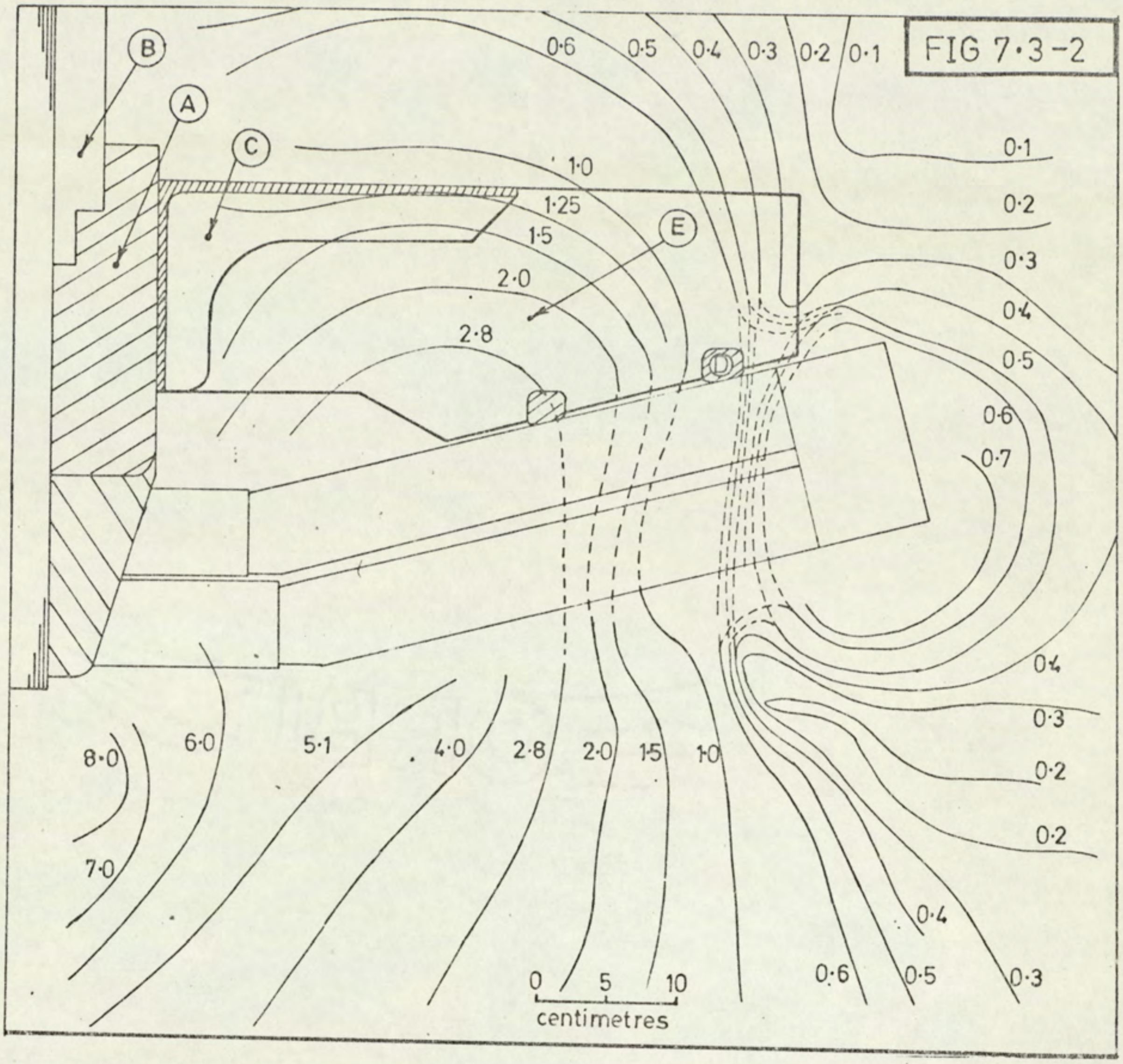

radial components of flux density contour values in millivolts 1mV = 0.006 Wb/m^2

Flux density plots for a 33500 H.P. 1000 r.p.m. synchronous induction motor.

Material Index.

A No-du-mag.
B Mild steel.
C Cast Brass.
D Fibre Glass
E Resin bonded fabric laminate.

FIG 7·3-3

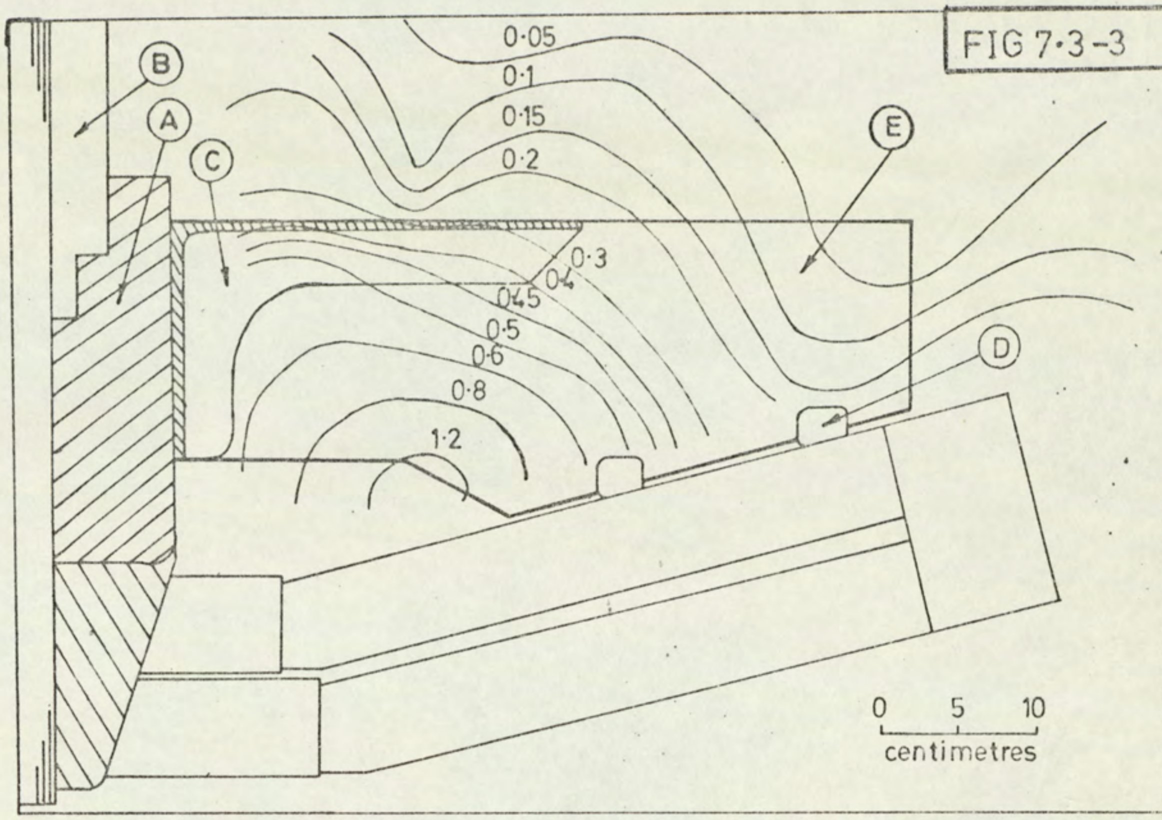

circumferential components of flux density
contour values in millivolts 1 mV = 0·006 Wb/m^2

FIG 7·3-4

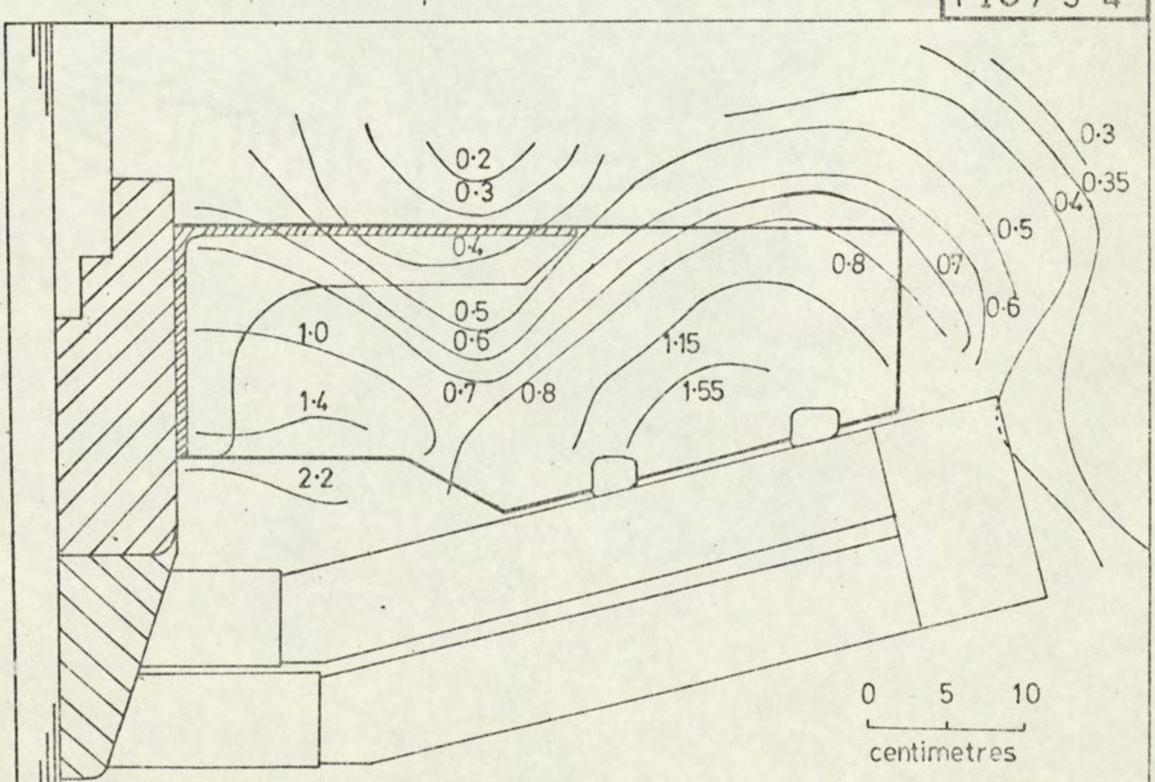

axial components of flux density
contour values in millivolts 1 mV = 0·006 Wb/m^2

3) On approaching the clamp plate surface, the axial components are virtually constant, while the radial components consistently decrease, but are not zero on reaching the clamp plate surface.

Finally, in view of (3) above, surface densities at the tooth supports and clamp plate given in Fig. 7.3 - 1, being axial components only, do not represent the total flux densities at these surfaces.

Project 2.0. This study originated from a report that the measured iron losses in a 8350 horse power 983 r.p.m. slipring induction motor were higher than expected, and that the mild steel balance discs at each end of the rotor were showing signs of heating. The relative positions of the end windings, clamp plates and balance disc are shown in Fig. 7.3 - 5. With the machine running light and 92 amperes on the stator, a general exploration of the end region gave very low values of field strength. After shut down, the balance discs and shaft were found to be faintly warm, but this was attributed entirely to the air friction within the machine. A cursory check on the mild steel clamp plate near region (a) in Fig. 7.3 - 5 indicated a definite warm region which was attributed to eddy losses, but due to the low level of stator excitation, it was not possible to draw positive conclusions. On examining the clamp plate, it was noted that the radial clearance of the clamp plate from the winding varied from 1.0 to 3.0 mm. Allowing for the insulation thickness, the copper-to-clamp plate clearance was probably 6 to 9mm. It was decided to lock the rotor and pass full load current through the stator windings. During this test, the clamp plate edge was heating steadily, indicating loss generation in this region. To enable a comparison of results the stator

FIG 7·3-5

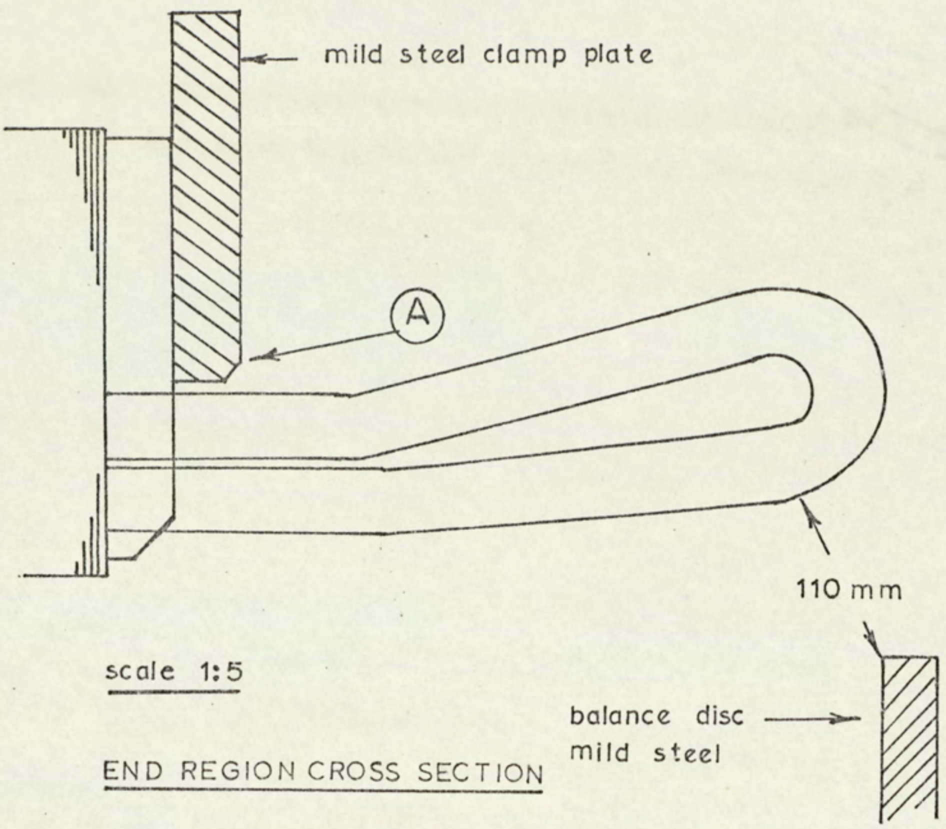

FIG 7·3-6

reference	33500 hp project 1		8350 hp project 2	
load	n.l.	f.l.	n.l.	f.l.
stator amps	595	1340	92	378
Amax. × 10^3	10·3	23·2	3·39	13·95
AC / cm	280	635	125	514
max flux. density normal to clamp plate surface (Wb/m^2) at position A in Fig 7-3-5	—	0·030	—	0·0348

COMPARISON OF DESIGN PARAMETERS AND TEST DATA.

m.m.f's for projects 1 and 2 were evaluated using the well known relationship;

$$A_{max} = \frac{1.35\ I\ W\ K_p\ K_d}{\text{no. of poles}}$$

Where: I = Phase current, amps.

W = Total series conductors in one phase.

K_p = Winding Chording Factor.

K_d = Winding Distribution Factor.

Table 7.3 - 6 gives the results obtained from observations in projects 1 and 2. It is apparent when examining these values and considering the lower losses obtained with non-ferrous clamp plates in section 6.3, that there is a good case for the use of non-ferrous clamp plates on large industrial machines. However, when economics dictates the use of magnetic clamp plates, then more attention must be given to details such as bevelling, increasing radial clearances and keeping magnetic materials to a minimum in the end region.

<u>Project 3.0</u> A 10,500 horse power 993 r.p.m. slipring induction motor was originally built with magnetic (steel wire) banding on the rotor overhang. This represented a magnetic cylinder placed inside the barrel of the stator overhang. On the light run test with the rotor running virtually synchronously, the banding heated, expanded and started to work loose. The replacement banding was made up of layers of fibre glass tape. Tests with this new banding showed a marked reduction in losses. This reduction represents the original banding loss and is show in Fig. 7.3 - 7. It is interesting to find that this loss, which can be attributed to stator m.m.f. is proportional to stator current raised to the power of 2.4.

losses in the banding wire on the rotor of a 10,500 h.p. slip ring induction motor running unloaded.

FIG 7·3-7

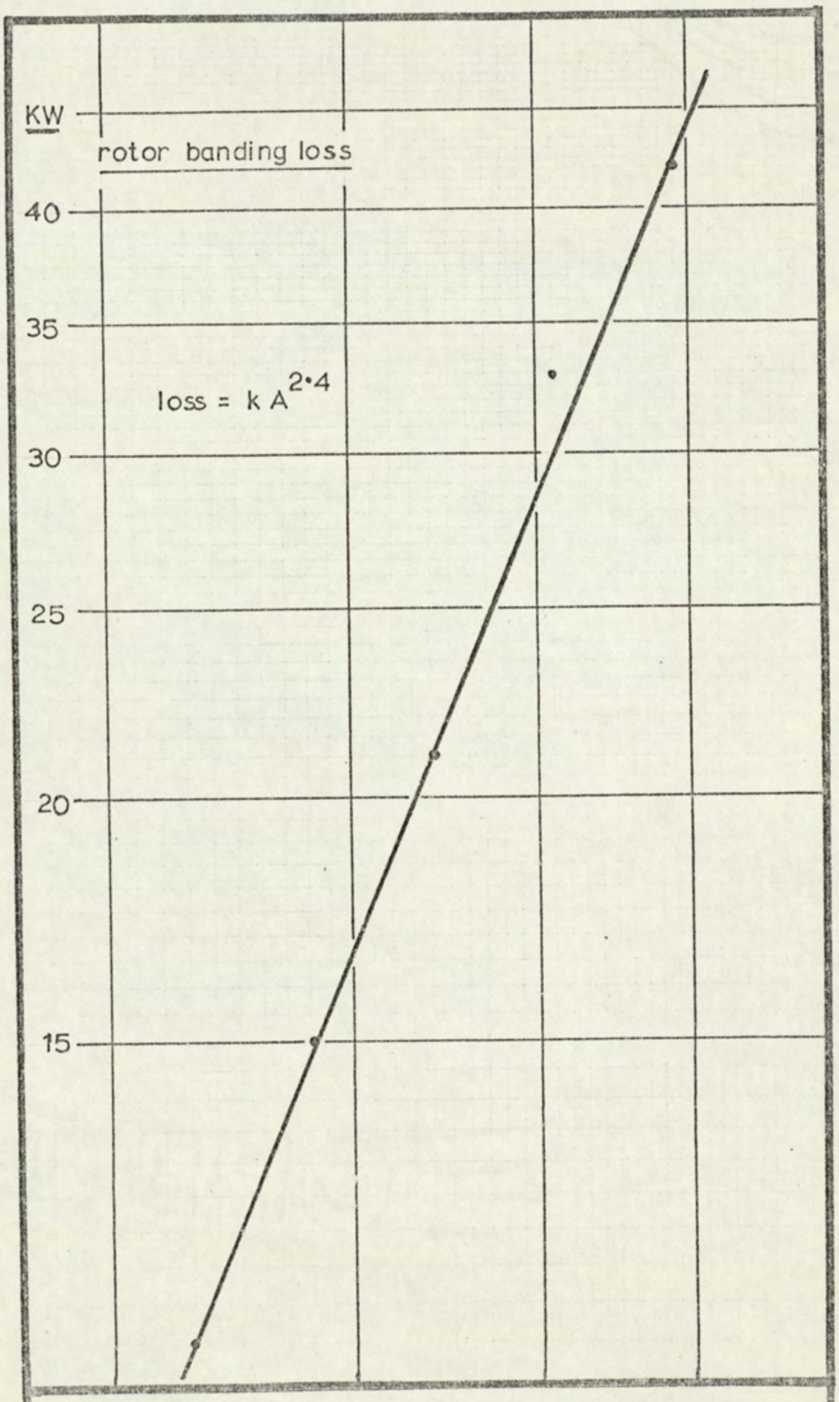

Conclusions: As a result of the various observations made in this section, and on experimental models detailed earlier, a series of instructions based on recommendations made by the author has been laid down, detailing exactly how all magnetic clamp plates and solid tooth supports are to be shaped for machines built within the organisation in which the author is employed. The main aspects concerned are, increasing radial clearances between clamp plates and windings, bevelling of the clamp plates, and removal of all sharp corners by smoothly merging all curves and planes. Tooth supports are to be cut back from the stator bore, radiused on the end to avoid sharp corners, and tapered back to where it meets the clamp plate. (See Fig. 7.3 - 1). As a further improvement, the use of non-magnetic clamp plates is being considered most seriously for all future large industrial machines.

Chapter VIII

8.0 Comparison of test results with earlier published formulation.

Even though the test results for clamp plate losses in section 6.2 include extra loss components, it is of interest to compare these results with values calculated from formulation derived by earlier authors. Richardson's work on ferrous clamp plates and Oberrettl's work on non-ferrous plates were selected for this exercise.

From Fig. 6.2 - 3 for 1" mild steel clamp plates with bevel, the clamp losses at 50 Hz are 0.92 kW at 200 A loading and 1.64 kW at 240 A loading. From Fig. 6.2 - 6 for 1" brass clamp plates with bevel, the clamp plate losses at 50 Hz are 0.62 kW at 200 A loading and 0.915 kW at 240 A loading.

Applying Richardson's work to the models.

$$d = 20''$$

$$h = 1.2''$$

$$l = 3.5''$$

$$AT = 6 \times 4 \times 200 = 4800 \text{ at } 200 \text{ A.}$$

$$K = 3.3$$

$$\text{Total clamp loss} = 2 \times 20 \times 3.3\,(1.2 + 3.5)\left(\frac{4800}{3.5}\right)^{1.6} \times 10^{-8} \text{ kW} = 0.665 \text{ kW}$$

For an overhang cone angle of 80° from the vertical, the loss reduction factor is 0.55, giving a loss of $0.665 \times 0.55 = 0.336$ kW at 200 A. The loss increases to $0.336 \times \left(\frac{240}{200}\right)^{1.6} = 0.49$ kW at 240 A.

Summarising;

Mild Steel Ferrous clamp plates.

Current, A.	200	240
Loss from tests kW	0.92	1.64
Richardsons', KW	0.366	0.49

Applying Oberrettl's work to the models.

$$\gamma \text{ (brass)} = 13.4 \times 10''$$

$$Rs_1 = 25.4 \text{ cms.}$$

$$Am = 6000 \text{ from model design parameters}$$

$$2\pi f \gamma Rs_1^{\,2} = 314.2 \times 13.4 \times (25.4)^2 \times 10^4$$

$$= 2.72 \times 10^{10}$$

Interpolating for a cone angle of 10° from the horizontal, for Fig. 1.2 - 9,

$$P_p = 9.2$$

$$\text{Total clamp plate loss} = \frac{10^4}{25.4 \times 13.4} \times 6000^2 \times 9.2 \times 10^{-3}$$

$$= \underline{0.097 \text{ kW at } 200 \text{ A.}}$$

$$\text{This increases to } 0.097 \times \left(\frac{240}{200}\right)^2$$

$$= \underline{0.14 \text{ kW at } 240 \text{ A.}}$$

Richardson suggests that the loss in non-ferrous clamp plates is simply $\frac{1}{3}$ of his calculated loss for ferrous plates.

Summarising;

Brass clamp plates.

Current, A	200	240
Loss from tests, kW	0.62	0.915
calc. Oberrettl, kW	0.097	0.14
Est. Richardson, kW	0.122	0.163

The loss calculation by both Richardson and Oberrettl appear low, particularly so in the case of brass clamp plates. Part of the reason must be that the losses obtained from results in the models include surface loss at the stator teeth, at the inner surface of the clamp plates, and at the surface of the stator frames. Also, the exponents of the stator current are different, making it impossible for the three evaluations to be comparable over a range of currents.

The clamp plate loss calculated from Richardson's work agrees with the model results at about 100 A, but this is equivalent to a much lower current loading than that for which Richardson's work is intended. The model results show that the loss in brass plates expressed as a percentage of the loss in mild steel plates at the same current varies from 83% at 160A to 56% at 240A. These values are higher than the single value of 33% suggested by Richardson.

Clamp plate loss evaluated for a 8350 H.P. motor.

The proposed method of evaluating clamp plate losses for a given machine is presented in Appendix A.3. The application is for salient pole synchronous machines, but provided the similarity rules given in A.3. are obeyed, the exercise can be applied to induction motors. Taking the 8350 H.P. slip-ring induction motor discussed in section 7.3, Project 2, as an example, the ratio of effective turns per pole is $(T1/To) = 1.23$. Thus the model current equivalent to a full load current of 378 A on the motor is

$$1.23 \times 378 = 465 \text{ A.}$$

Using the loss curve for 1" mild steel, bevelled clamp plate, given in Fig. 6.2 - 3, the loss at 200 A, 50 Hz is 0.92 kW. Extrapolating to 465 A, the loss is $\left(\frac{465}{200}\right)^{3.2} \times 0.92 = 13.8$ kW.

The ratio of effective diameters is (D_{e1}/D_{eo}) = (1516/567) = 2.67. The ratio of effective distance of clamp plate from overhang is (d_{eo}/d_{e1}) = (47/210) = 0.224. This gives a clamp plate loss of

$$13.8 \times 2.67 \times (0.224)^z \quad \text{i.e.}$$

z	1.0	1.6	2.0
Clamp loss kW	8.26	3.35	1.84

Applying Richardson's Work,

$$d = 59.5''$$

$$h = 6''$$

$$l = 13.5''$$

$$AT = 6 \times 5 \times 378 = 11340$$

Total clamp loss = $2 \times 3.3 \times 59.5\,(6 + 13.5)$ $\times \left(\frac{11340}{13.5}\right)^{1.6} \times 10^{-8} = 3.66$ kW.

The reduction factor for the overhang cone angle is 0.55, therefore, total clamp plate loss = 0.55×3.66 = 2.01 kW. Experience on machines of this size indicates that the value of 8.26 kW for $z = 1.0$, calculated from the model results is more realistic than 2.01 kW. If the loss is taken to be proportional to $l^{-1.0}$ and not to $l^{-1.6}$ in Richardson's work, his evaluation of clamp plate loss would increase to 17.4×0.55 = 9.6 kW, a value which is reasonably close to that calculated from the model results.

8.1 Conclusions and Recommendations for future work.

The investigation of losses in core clamping plates using two model stators is made more difficult by two factors which were not anticipated at the start. These are (1) the relationship between air-gap flux density and stator excitation current is different for the two models, (2) in both models the core saturation level is sufficiently high to cause flux to divert into paths in parallel with the cores, and result in extra losses being generated.

Differences in the magnetisation curves is believed to be the result of relatively high end-leakage fluxes, which give rise to different mean core densities at equal currents in the two models. The effect on the relative values of stator iron losses in the two models is partly taken into account by introducing the factor K_i (see section 6.1). The remaining relative differences in the iron losses are believed to be negligibly small.

To obtain appreciable clamp plate losses over a reasonable range of currents, it was necessary to increase the maximum current originally intended by about 30%. The resulting iron flux densities are still within the levels existing in modern machines, but are sufficiently high to cause considerable flux to cross the 6 mm radial gap between the cores and the ferrous frames of the models. Flux also diverts from the core-ends into the clamp plates.

Within the time available, it was not possible to extend the testing to enable the extra losses due to the core leakage fluxes to be evaluated. Since the loss at the inner radial surface of the clamp plates must also occur in machines where the saturation level is comparable to that in the models, it is logical to include this loss as part of the total clamp plate loss. This end is achieved in the loss derivation of section 6.1, but with some degree of error, probably small, due to unequal magnetisation curves and the presence of ferrous frames.

The clamp plate loss derivation also includes a possible loss component associated with end-leakage flux entering the stator core at the end surface of the teeth. Such a loss may be present in actual machines, and may be complicated by the presence of finger supports.

Future Work.

It is suggested that atleast five distinct lines of research into the problem should be continued in future.

(1) The extra losses referred to above can be virtually eliminated by (a) replacing the ferrous stator frames by say, timber frames, and (b) by doubling the air gap where-by iron ampere turns would be virtually zero for stator currents up to 240 A.

Alternatively, the magnetisation characteristics of two similar models can be made nearly identical by reducing the ratio of core lengths, and adopting longer lengths. This reduces the end leakage flux in relation to the air gap flux. For example, with core lengths of 150 mm and 300 mm, the end leakage flux would be 7.2% and 3.6% respectively, compared with 21.4% (50 mm core) and 7.2% (150 mm core) for the test models. To avoid an excessive power supply requirement, the stator bore of the new model may need to be reduced by one frame size. Tests on the new models would then give a more accurate assessment of total clamp plate loss (i.e. including the loss at the inner radial surface).

(2) The presence of magnetising influences on either side of each clamp plate makes the problem difficult. The surface flux density studies undertaken in section 7.1 indicates that the flux density at the outer radial surface of the clamp plate is influenced by magnetic potential gradient at the core end surface. As this potential gradient increases (with excitation current), the loss at the outer surface may level off, but the total clamp plate loss continues to increase with the appearance of an appreciable loss at the inner radial surface. Clearly, there is scope for investigation into the general problem of a plate of finite thickness influenced by magnetisation from both sides. A more fundamental model may be required for this purpose, and could include a further investigation into copper shields.

There is some practical significance in separating the two components of clamp plate loss, since in a machine the loss at the inner surface, due to iron saturation, is a stray no-load loss, while the loss at the outer surface is a true stray load loss.

(3) The work should be extended to indicate the relevance of some geometric distances. For example,

<u>(a) Radial height of clamp plate.</u> Because of the flux concentration at the inner (radial) edge of the ferrous plates, it is anticipated that the radial height has a more significant effect in the case of non ferrous plates. In relating the clamp plate losses in the models to actual machines (see Appendix A.3), allowance for clamp plate height is made only for non-ferrous plates,

and this in an intuitive way.

(b) Length of overhang. In Appendix A.3. this is taken into account by defining, empirically, the effective distance between the overhang and the clamp plate. It is suggested that clamp plate losses vary inversely with this distance, but this may not be the case.

(4) Fig. 6.2 - 3 and 4 indicate that there is virtually no difference between the losses in Meehanite and Mild Steel clamp plates. In view of the difference in their respective magnetisation characteristics, Fig. 2.2 - 1, this is surprising. It is suggested that tests with these clamp plates should be extended to include ampere conductor per centimetre loadings of up to 1500, equivalent to 535 A on the model windings. Tests with such high current loading are possible on the existing models, provided transient temperatures are kept under control by adopting automatic data logging. In this respect, the use of liquid nitrogen as a coolent may be seriously considered as a practical possibility.

(5) In spite of the numerous difficulties encountered in the present work, it is suggested that the two stators should be used to study the effects on boundaries other than clamp plate surfaces. For example,

(a) End guard around windings. These could be made up of cylinders and discs of appropriate materials.

(b) Metallic bracing rings on the overhang. In industrial machines it is not always enconomical to use fibre-glass bracing rings, and steel or brass rings are often used.

Any future work carried out on the existing, or new models, would benefit from improvements in experimental techniques. For example, the adoption of digital metering throughout, and possibly automatic data logging. It is believed that as much as 75% of testing time could have been saved in the present work.

In conclussion, it may be said that in production design offices, a steady change in emphasis of design effort is taking place. With the increased usage of computers, the day to day drudgery of design work is being reduced, and designers are spending more time on basic loss problems, introduced by increasingly higher design loadings made necessary by commercial competition. The use of experimental models is invaluable in this respect, even though the solution gained may be a semi-empirical one. The derivation of the constants of proportionality from live model testing rather than from approximate mathematical models, must give better correlation, at least until all related phenomena are sufficiently understood to make it possible to develop an adequate mathematical analysis.

ACKNOWLEDGEMENTS

The author wishes to express his sincere gratitude to Professor E.J.Davies for his guidance and encouragment at all stages of the project; also for making available facilities in the electrical engineering department of the University of Aston in Birmingham. He would like to thank the staff of the Electrical Machines Centre in particular for their unstinted help in the design and manufacture of the various jigs and fixtures required for the Hall probe instrumentation and power measurements.

He wishes to thank the management of C. A. Parsons and Company Limited - Witton Factory - Birmingham for their generosity in granting facilities for the project, the experimental models and for the day release for attendance at the University, without which this investigation would not have been possible. In particular, the author wishes to thank.

Mr. F.C. Krause, the former General Manager of the Witton factory of C.A. Parsons and Company Limited for his sanction of the project financially and by allowing use of the works facilities.

Mr. G. Campbell, General Manager of C.A. Parsons & Company Limited for his interest and support throughout the project.

Dr. I. Thomas for his extreme patience, help and guidance throughout the project, and in particular for first suggesting the ideas presented in sections 6.4,7.1 and appendicies A.1 and A.2.

Mrs. J. Mulholland for all the care and effort involved in typing this manuscript.

Appendicies

Appendix A.1. Evaluation of end leakage flux.

Part of the end leakage flux in each model stator enters the stator core at the core end surfaces. Assuming that this flux is normal to the end surfaces, then it can be evaluated by summating the Hall probe output, with the probe moving over the surface concerned.

Fig. A 1 - 1. gives the end surface flux density for both tooth and core sections, along a radial line corresponding to maximum stator m.m.f. The excitation is 140 A d.c. with the series-parallel connection shown in Fig. 5.1 - 6A.

Fig. A 1 - 2 gives the end-surface flux density along two fixed circumferences, again with 140 A d.c. excitation. Assuming this flux density to be sinusoidally distributed in the circumferential direction, then leakage flux per pole entering the core ends is given by:

$$\Phi_{1c} = 2.\frac{2}{\pi} B_{c.av} \; h_c \frac{1}{6} \pi D_c \quad \text{for the core back-of-teeth}$$

$$\Phi_{1c} = 2.\frac{2}{\pi} B_{t.av} \; h_t \frac{1}{6} \pi D_t \frac{W-S}{W} \quad \text{for the teeth.}$$

where B_{av} is the average flux density taken from Fig. A 1.1

h is the radial height

D is the mean diameter

c and t refer to core back-of-teeth and teeth sections respectively.

W is the tooth pitch at D_t

S is the slot width at D_t

The gap flux per pole is given by

$$\Phi_g = \frac{2}{\pi} B_{gmax} \; L_c \; \frac{1}{6} \pi \; D_g$$

maximum flux density normal to stator end surface, taken along a radial line.

140 Amp DC excitation

FIG A1-1

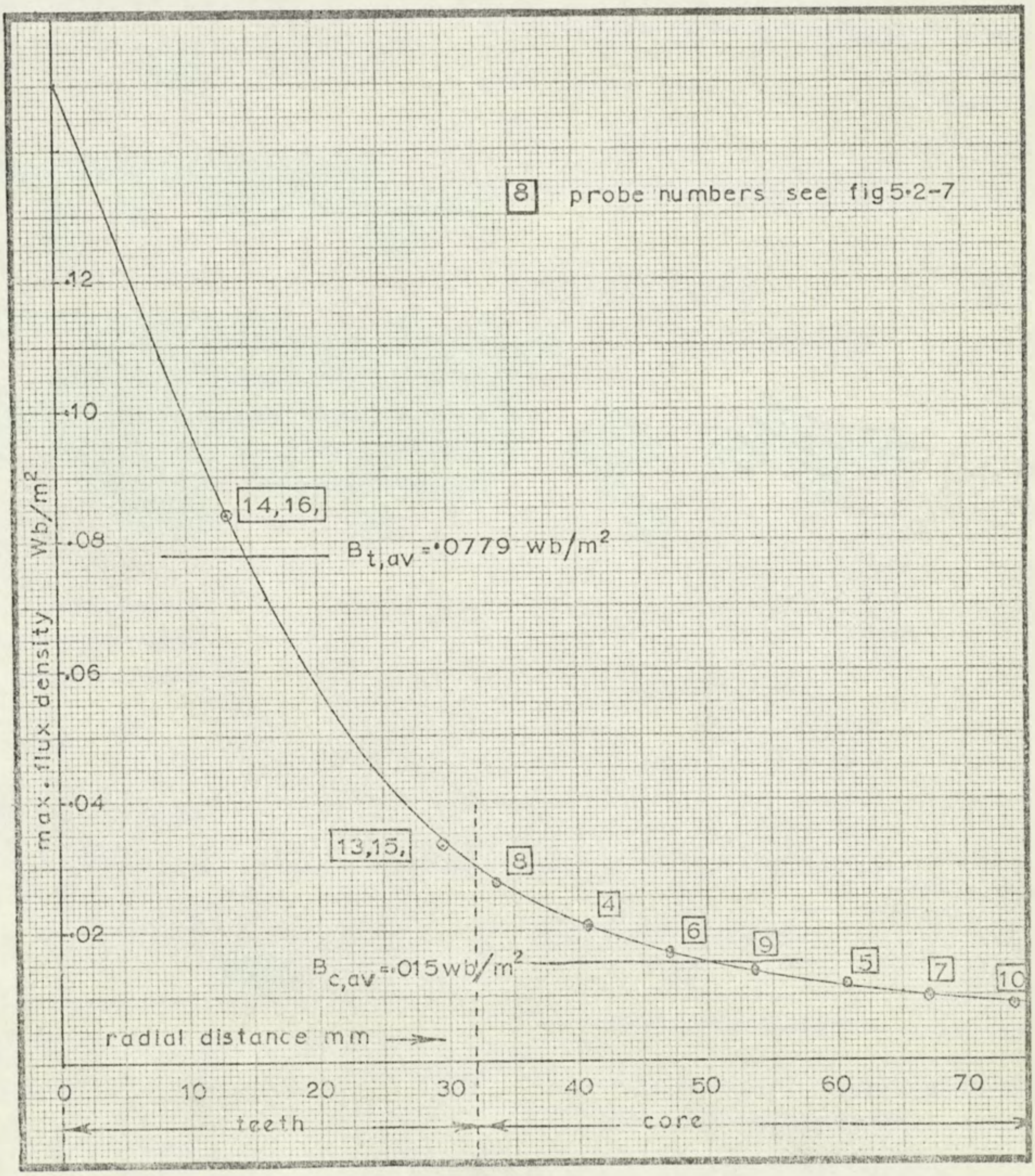

flux density normal to stator end surface, taken along two circumferential lines.

140 Amp DC excitation

FIG A1-2

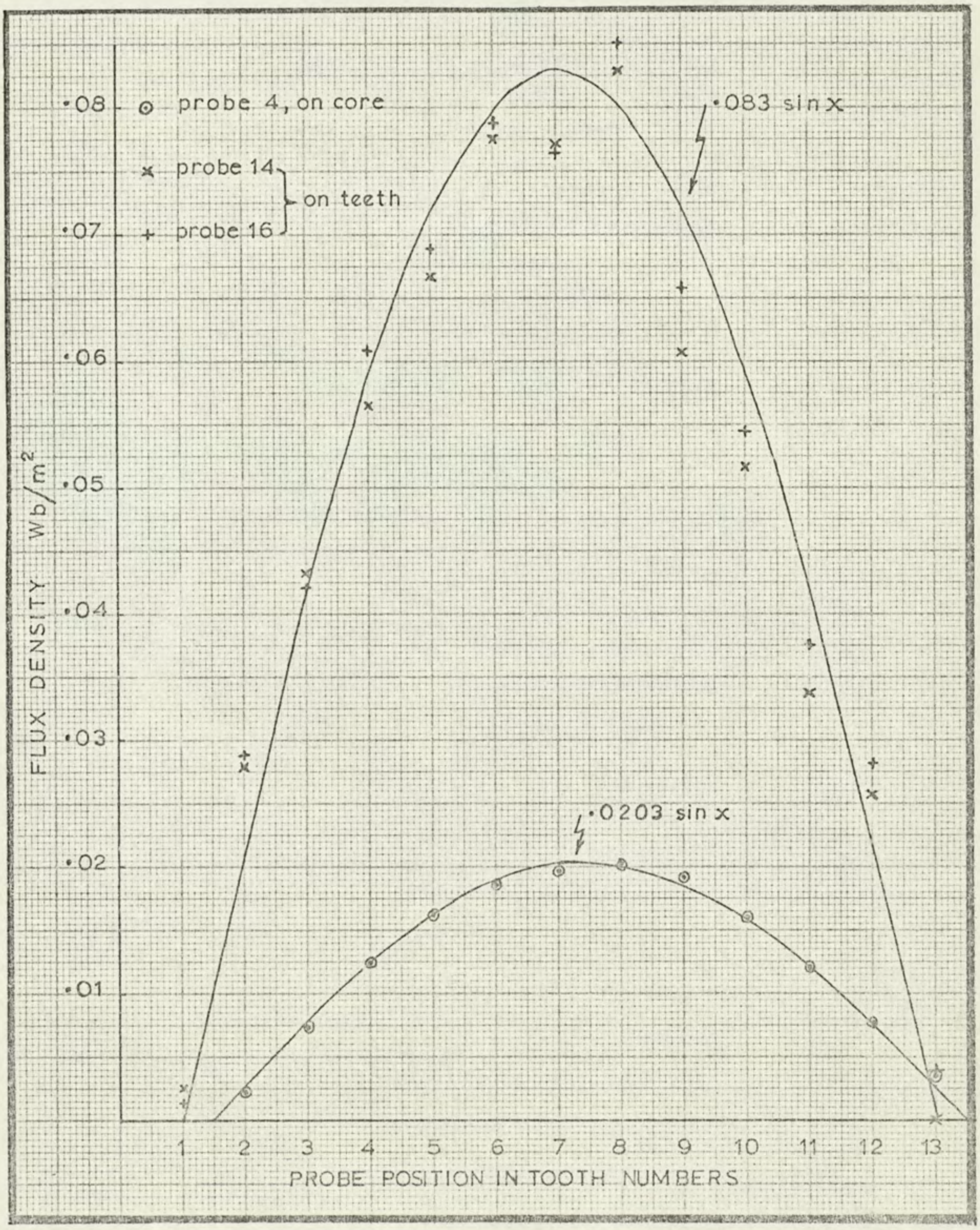

where L_c is the axial core length, B_{gmax} is the maximum air gap flux density, taken from Fig. 5.1 - 6 for the present evaluation. (140 A d.c. excitation).

Alternatively, the gap flux per pole is given by

$$\Phi g = \frac{2}{\pi} \sqrt{2} \quad B_{g.rms} L_c \frac{1}{6} \pi D_g$$

where $B_{g.rms}$ is the air gap flux density with a.c. excitation taken from Fig. 6.1 - 1, at 99 A a.c. which is equivalent to 140 A d.c. excitation.

Evaluating the above fluxes, for the short core model,

$$\Phi_{1c} = \frac{2}{3} .0150 \times .044 \times .578 = 0.254 \times 10^{-3} \text{ Wb}$$

$$\Phi_{1t} = \frac{2}{3} .0779 \times .032 \times .502 \times \frac{9.4}{21.9} = 0.359 \times 10^{-3} \text{ Wb}$$

$$\Phi_g \begin{cases} = \frac{1}{3} .365 \times .05 \times .470 = 2.86 \times 10^{-3} \text{ Wb @ 140A d.c.} \\ = \frac{\sqrt{2}}{3} .255 \times .05 \times .470 = 2.85 \times 10^{-3} \text{ Wb @ 99A a.c.} \end{cases}$$

Expressed in percentages of the air gap flux per pole, for the short core at 140A d.c. or 99A a.c. excitation,

End leakage flux into core back-of-teeth	=	8.9%
End leakage flux into teeth	=	12.5%
Total and leakage flux into stator core	=	21.4%

Assuming the end leakage flux to be proportional to stator current, and reading the air gap flux off the magnetisation curve, then the end leakage at 170A a.c. = 22.8%

" 200A a.c. = 24%

The total end leakage flux calculated at 170A a.c. from the design parameters of section 2, is 27.6% of the air gap flux per pole (i.e. the overhang reactance voltage expressed as a percentage of the air gap reactance voltage).

The main consequence of this high level of end leakage flux is believed to be different magnetisation curves for the two models. On this basis, the percentage leakage flux can be calculated from the magnetisation curves of Fig. 6.1 - 1 in the following way.

Consider the magnetisation of the two stators at two stator currents I_1 and I_2, such that

$$(I_1 - I_{g1}) \text{ for the short-core stator}$$

$$\equiv (I_2 - I_{g2}) \text{ for the long-core stator,}$$

where I_{g1} and I_{g2} are corresponding currents taken off the common air-gap line.

Then it can be said that

short core iron flux density at stator current I_1

$\equiv$ long core iron flux density at stator current I_2

Therefore, since the core lengths are in the ratio 3:1,

$$\frac{\text{total stator iron flux in the short core at } I_1 \text{ amps}}{\text{total stator iron flux in the long core at } I_2 \text{ amps}} = \frac{1}{3}$$

$$\therefore \quad \frac{\Phi_{g1} + \Phi_{l1}}{3\,\Phi_{g2} + \Phi_{l2}} = \frac{1}{3}$$

where Φ_{g1} = short-core air-gap flux at I_1

Φ_{g2} = short-core air-gap flux at I_2

Φ_{l1} = end leakage flux entering either core at I_1

Φ_{l2} = end leakage flux entering either core at I_2

Now assuming the leakage flux to be proportional to the stator excitation, $\Phi_{l2} = \frac{I_2}{I_1} \times \Phi_{l1}$

Therefore,

$$\frac{1 + \dfrac{\Phi_{11}}{\Phi_{g1}}}{\dfrac{\Phi_{g2}}{\Phi_{g1}} + \dfrac{I_2}{3I_1} \times \dfrac{\Phi_{11}}{\Phi_{g1}}} = 1$$

Again, $\dfrac{\Phi_{g2}}{\Phi_{g1}} = \dfrac{B_{g2}}{B_{g1}}$ which is the ratio of the corresponding air-gap flux densities, each of which can be obtained from Fig. 6.1 - 1

Therefore, $$\frac{\Phi_{11}}{\Phi_{g1}} = \left[1 - \frac{B_{g2}}{B_{g1}}\right] \Big/ \left[1 - \frac{I_2}{3I_1}\right]$$

Evaluating this expression for $I_1 = 200A$, for which

$I_2 = 225A$,

$$\frac{\Phi_{11}}{\Phi_{g1}} \times 100 = 100 \left[1 - \frac{.525}{.460}\right] \Big/ \left[1 = \frac{225}{600}\right]$$

$$= \frac{14.1}{0.625} = \underline{22.6\%}$$

Appendix A.2. Waveform of core end leakage flux density. A qualitative study.

In section 7.1 it is suggested that flux density normal to the core end-surface of the model stators is the combined result of overhang m.m.f. and m.m.f. appearing across the core. The effect of the latter m.m.f. can be analysed as follows.

In magnetic calculations on normal industrial machines, it is usual to neglect the radial components of flux density in the core back-of-teeth. Also assuming that the air gap flux density is sinusoidally distributed round the air gap, the core flux density can be taken as circumferential in direction, and sinusoidal in magnitude. This condition of air gap and core, taken instantaneously is illustrated in the top half of Fig. A.2 - 1a.

From the magnetisation characteristic of the core material, circumferential magnetising force H_θ at the angle θ is obtained, and analysed (harmonically) with respect to θ ($\theta = 0$ when core flux density B is maximum). Thus, at the angle θ , where the circumferential flux density is $B_m \cos\theta$, neglecting hysteresis, the magnetising force is

$$H_\theta = \sum_{n=1}^{n=\alpha} H_{cn} \operatorname{Cos} n\theta \quad \text{where n is odd.}$$

Therefore, between points a and a' in the core, the m.m.f. is given by

$$2 \int_0^\theta \sum_{n=1}^{n=\alpha} H_{cn} \operatorname{Cos} n\theta \, R d\theta$$

$$= 2R \sum_{n=1}^{n=\alpha} \frac{H_{cn}}{n} \operatorname{Sin} n\theta$$

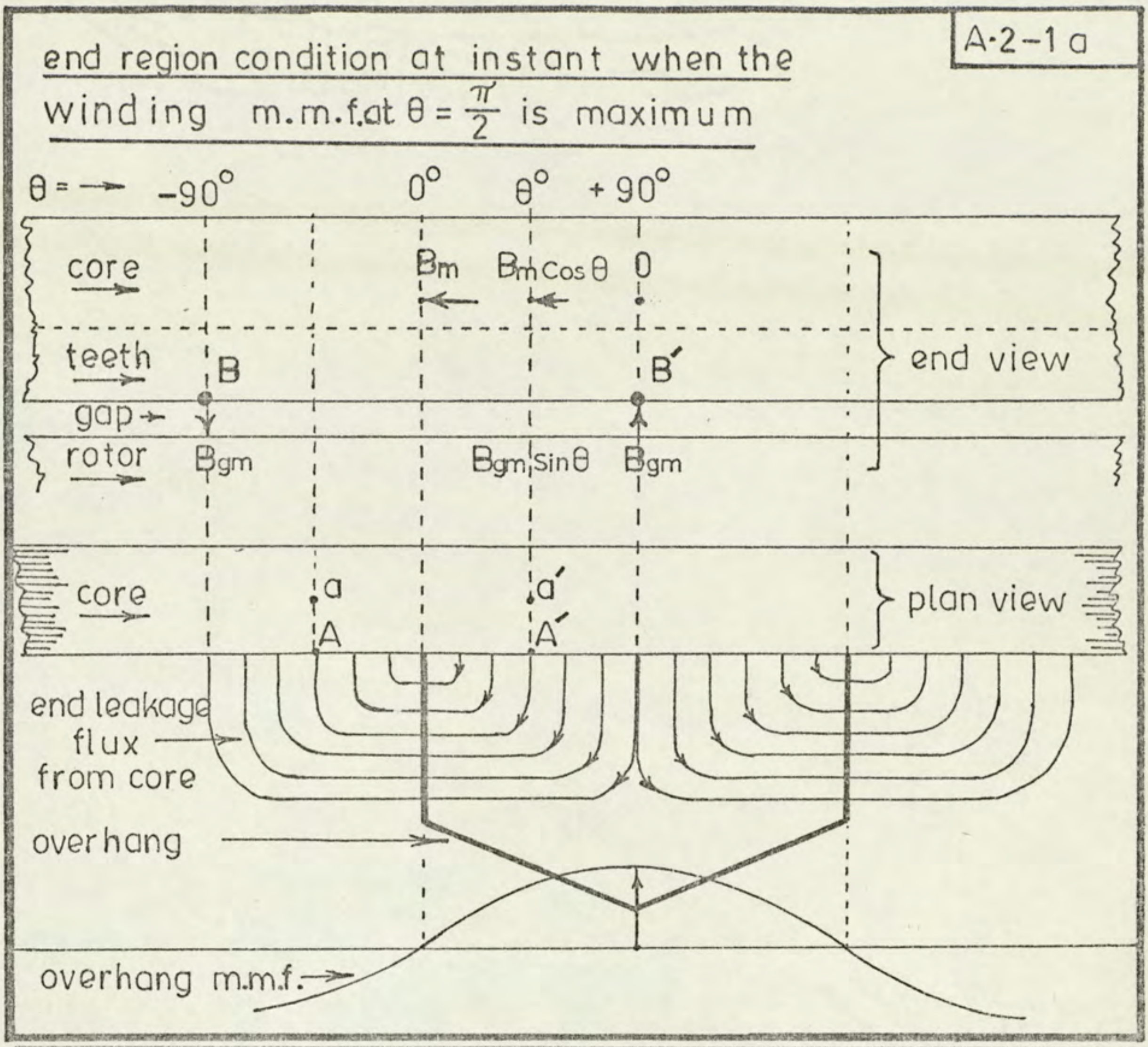
A·2-1 a
end region condition at instant when the winding m.m.f.at θ = π/2 is maximum
θ = → -90° 0° θ° +90°
core
Bm
Bm Cos θ
0
teeth
B
B'
end view
gap
rotor
Bgm
Bgm Sin θ
Bgm
core
a
A
a'
A'
plan view
end leakage flux from core
overhang
overhang m.m.f.

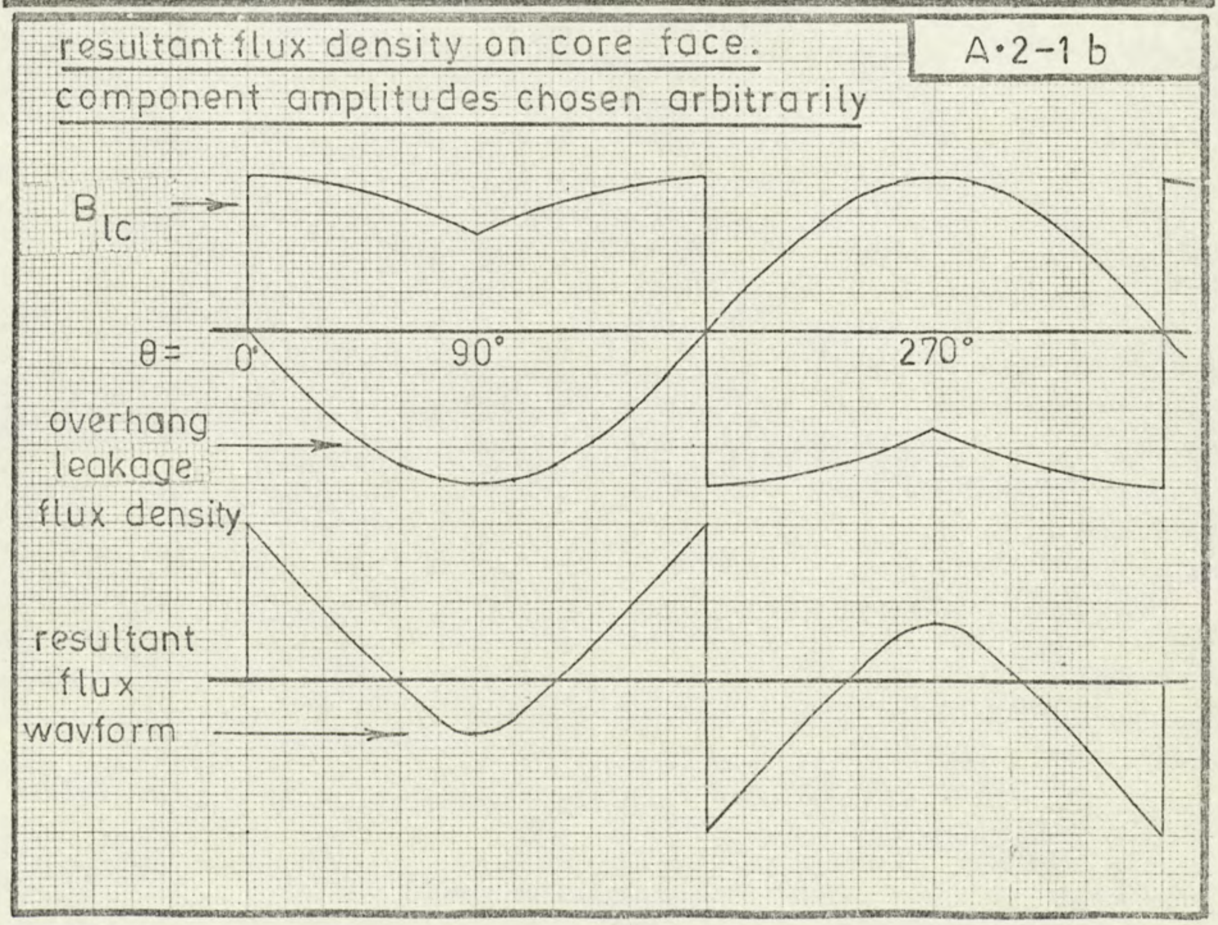
resultant flux density on core face.
component amplitudes chosen arbitrarily
A·2-1 b
Blc
θ= 0° 90° 270°
overhang leakage flux density
resultant flux wavform

where R is the radius at which points a and a' are taken.

Assuming uniform flux density over the core length, this m.m.f. appears at points A and A' on the core-end, and gives rise to a core end leakage flux, shown diagramatically in the bottom half of Fig. A.2 - 1a.

If the effective leakage flux path length from A to A' is L_θ , then the flux density at A(or A') is

$$B_\theta = \frac{2 R \mu_o}{L_\theta} \sum_{n=1}^{n=\alpha} H_{cn} \text{ Sin } n\theta$$

$$\text{for } 0 \leqslant \theta \leqslant 90^\circ$$

This expression can be simplified by making $L_\theta = 2 R \theta$ by which it is assumed that the axial parts of the flux path are negligible compared with the circumferential part, and that the flux density is constant along the whole path. This is a drastic assumption, but it helps to lead to a qualitative solution.

$$\therefore B_\theta = \mu_o \sum_{n=1}^{n=\alpha} H_{cn} \frac{\text{Sin } n\theta}{n\theta}$$

$$\text{for } 0 \leqslant \theta \leqslant 90^\circ \text{ only}$$

This represents the condition with d.c. excitation, or with instantaneous 3 phase a.c. excitation when B_g is maximum at B and B', Fig. A 2 - 1a. By replacing θ with ωt, the variation with time of the core and leakage flux density B_{lc}, at a fixed point on the core end is obtained.

Thus, further simplifying by assuming no distortion due to saturation, so that the fundamental component only is considered,

$$B_{lc} = H_{cl} \left[\frac{\text{Sin } \omega t}{\omega t} \right]_{t=o}^{\frac{\pi}{2\omega}}$$

By symmetry, the function is in fact defined over the whole cycle, and is illustrated by the non-sinusoidal wave in Fig. A.2. - 1b.

The core end is also subjected to the conventional leakage flux which links with the winding overhang. Since the m.m.f. causing this is virtually sinusoidal with respect to time, the associated flux density at the core end surface is also sinusoidal. This waveform is also included in Fig. A.2. - 1b, and is in phase opposition to the flux density resulting from the core magnetisation as can be seen by considering Fig. A.2. - 1a (neglecting hysteresis effects).

Considering variations of these two flux density components along a radial line on the core end surface, it is evident that the magnitude of the core-end component remains reasonably constant, while the overhang component reduces in magnitude as the core outer diameter is approached. The two component waveforms in Fig. A.2. - 1b have been deliberately plotted with equal maximum values, and it is seen that the resultant contains a predominant third harmonic. Qualitatively, this result agrees with the test oscillograms presented in section 7.1. It can be concluded that with 240 A excitation, the fundamental component of the core-end leakage flux density is virtually equal to the overhang leakage flux density at points on the core-end surface near the core outer diameter.

Appendix A.3 Derivation of clamp plate loss from model results.

When considering the design of the model stator it was envisaged that experimental data obtained would be used to evaluate clamp plate losses on actual machines. The machines for which this is possible must bear a certain geometric similarity to the models, this being achieved when the relevant dimensions are limited by the following rules:-

(a) Ratio $\frac{D_i}{D_o} \doteqdot 0.85$ see Fig. A.3 - 1a.

(b) Angle $\gamma \not> 22.5^{\circ}$ see Fig. A.3 - 1b.

These rules were found to apply to an extensive range of salient pole synchronous machines, for which the present work is intended. The range of machines checked extended from 225 MVA at 150 rev/min and 75 MVA at 75 rev/min, to 1 MVA at 1500 rev/min. The few exceptions to the above rules were among the four and six pole machines, in which cases only one of the two rules was followed. The relevant ratios in turbo-type machines differ widely from the values given in both rules.

For a given machine, the clamp plate loss is scaled off the appropriate loss curve in section 6.2, making suitable allowances for the following parameters:-

(1) Supply frequency.

(2) Clamp plate material.

(3) Clamp plate dimensions and position.

(4) Pole pitch (τ).

(5) Effective distance of clamp plate from winding overhang (de).

(6) Effective diameter of clamp plate (D_e)

(7) Ampereturns per pole.

dimensions for geometric similarity. FIG A·3-1

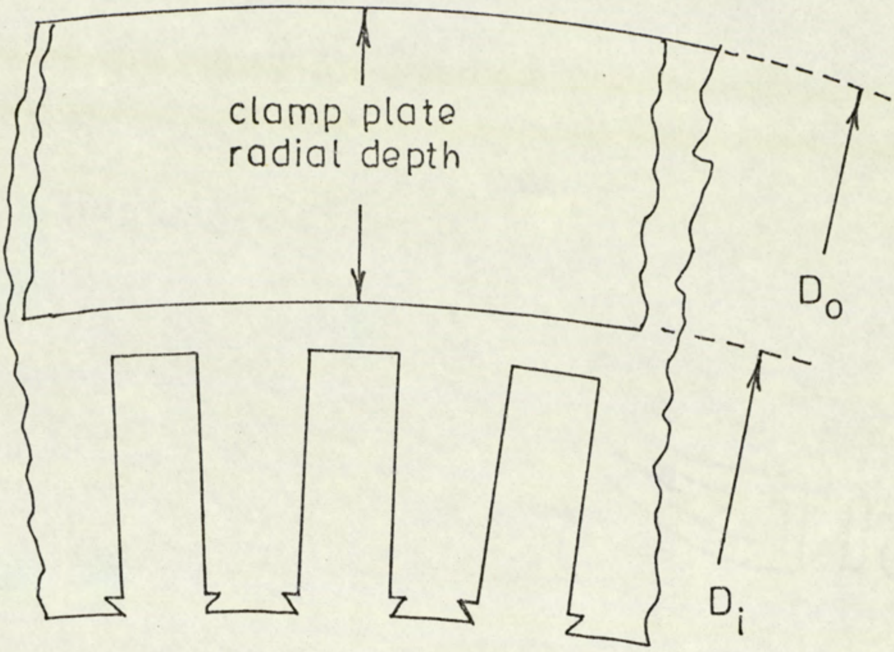

FIG a

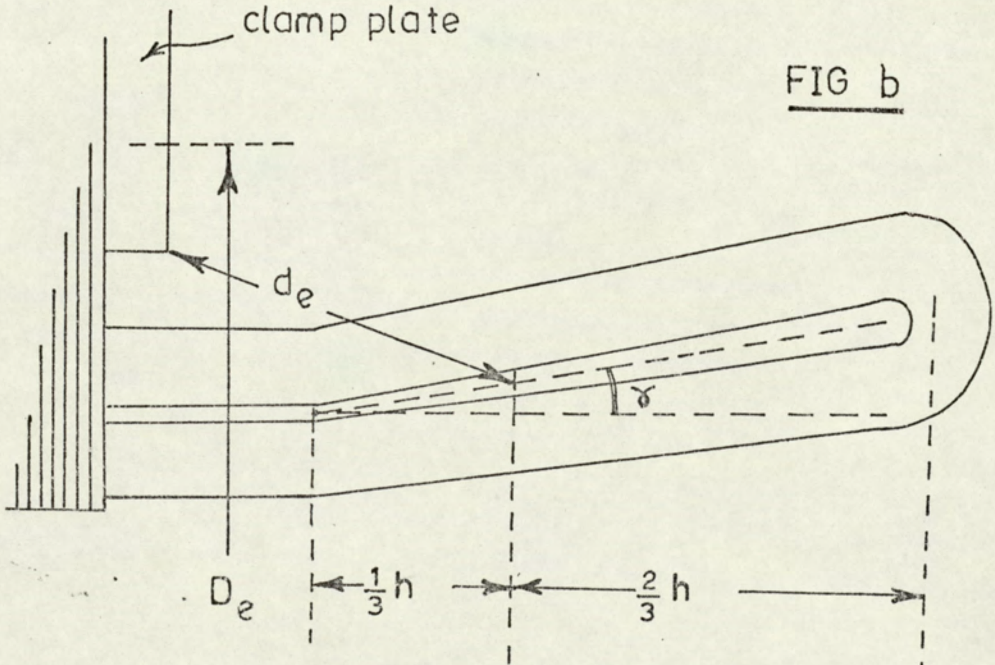

FIG b

d_e = effective overhang distance

D_e = effective clamp plate diameter

Items (1) and (2) are accounted for by selecting the appropriate loss curve from section 6.2.

Item (3) The loss curves of section 6.2 show that differences in clamp plate loss resulting from variations of mild steel clamp plate dimensions and position are too small to be accounted for adequately in any formulation. There is some allowance because the effective distance between clamp plate and winding overhang changes slightly with clamp plate thickness and radial distance from the winding.

Item (4) The pole pitch affects the circumferential part of the end leakage flux path. For ferrous clamp plates, this part is in iron, so that its contribution to the total permeance of the leakage flux path can be neglected. For non-ferrous clamp plates, the circumferential path in the clamp plate cannot be neglected. Thus the pole pitch should appear in the derivation of clamp plate loss for non-ferrous plates only.

Item (5) The inclusion of an effective distance of the clamp plate from the winding overhang as a parameter is intended to account for changes in clamp plate loss resulting from differing overhang axial lengths, all other things being equal. The present investigation has not considered such a parameter, and it is intended to accept the distance d_e, as indicated in Fig. A.3 - 1b, as suggested by Smith (56).

Item (6) Considering clamp plate loss as occurring incrementally in a region bounded by two radial planes of small separation, then all other things being equal, total clamp loss must be proportional to an effective diameter of clamp plate. Because of the concentration of flux density at the inner edge of the ferrous plates, the inner (bore) diameter is taken as being effective. For the non-ferrous plates the effective diameter is taken to be the bore diameter plus two thirds of the clamp plate radial height.

Item (7) In reading off the appropriate loss curve, the stator current is taken such that the resulting ampere turns per pole for the model is equal to the ampere turns per pole in the machine at the load current for which the clamp plate loss is required.

Consequently, the clamp plate loss for a given machine is obtained by reading the loss W_{co} off the appropriate loss curve, corresponding to a stator current $I_o = (T_1/T_e)I_1$ where I_1 is the stator current in the machine, T_1 and T_o being the effective turns per pole in the machine and model respectively. The required loss is then

$$W_{c1} = \frac{D_{e1}}{D_{eo}} \left(\frac{d_{eo}}{d_{e1}}\right)^q W_{co} \quad \text{for ferrous plates}$$

and $$W_{c1} = \frac{D_{e1}}{D_{eo}} \left(\frac{2\, d_{eo} + \tau_o}{2\, d_{e1} + \tau_1}\right)^q W_{co} \quad \text{for non-ferrous plates.}$$

Where τ, d_e and D_e are defined under Items (4), (5) and (6) above, the suffices 1 and 0 referring to the given machine and the model respectively. The exponent q is believied to lie between 1.0 and 2.0, depending on the way in which the clamp plate loss is affected by the effective length of the end leakage flux path. Note that for the ferrous plates, this length is taken as $2\, d_e$, the circumferential parts being neglected. For non-ferrous plates, the effective leakage path length is taken as $(2\, d_e + \tau)$, the circumferential path in the rotor only being neglected.

Bibliography.

B.1 General References

1) On the magnetic field due to current in a wire placed parallel to the axis of a cylinder of iron. - G.F.C. Searle. The Electrician. 1898, Jan Pg. 453 - 456, Feb. Pg. 510 - 511.

2) Eddy-Current Losses in a Semi-Infinite Solid due to a Nearby Alternating Current - H. Poritsky and R.P. Jerrard ... A.I.E.E. Comm. & Electronics - 1954. Pg. 97 - 106.

3) Induced Losses in Steel Plates in the presence of Alternating Currents. W.G. Deuring. A.I.E.E. Trans. 1957. Pg. 166 - 173.

4) Electric and magnetic Images - P. Hammond. Proc. I.E.E. 1960 Pg. 306 - 313.

5) Eddy currents induced in a Solid Slab by a Circular current loop. - P. Hammond. Proc. I.E.E. 1962. Pg. 1 - 8.

6) An experimental and theoretical study of Eddy-Current couplings and brakes. - E.J. Davies, A.I.E.E. Trans. 1963. Pg. 401 - 419.

7) Images of line charges and currents - J.R. Reed and N. Mullineux. Proc. I.E.E. 1964, Pg. 1343 - 1346.

8) General theory of eddy-current couplings and brakes - E.J. Davies Proc. I.E.E. 1966 Pg. 825 - 837.

9) Eddy Current phenomena in Ferro magnetic materials - H.M. McConnell A.I.E.E. Trans. 1954 Vol. 73 Part 1, pg. 226 - 235.

10) Eddy Current in Iron masses. - Rosenberg. The Electrician 1923 Pg. 188 - 191.

11) Eddy current losses in Solid and Laminated Iron - P.D. Agarwal A.I.E.E. Trans. Vol. 78. 1959 Pg. 169 - 181.

12) An Electrical multiplier untilizing the Hall Effect in Indium Arsenide - R. Chasmar & E. Cohen Metropolitan - Vickers Research Series No. 58.

13) The design and performance of a Hall Effect multiplier - R. Chasmar, E. Cohen, D. Holmes Proc. I.E.E. 106 part B Supplement 16, 1959, also A.E.I. research Series No. 76.

14) Magnetic Flux Pattern Instrumentation using Hall Probes - H. Hollitscher A.I.E.E. Trans. Paper 60-835, 1960.

15) Similarity relations in Electrical Engineering. - J.G. Brainerd & J. Neufeld. A.I.E.E. Trans. Vol 54 1935 Pg. 268 - 72.

16) Model laws of Eddy-Current couplings for aircraft alternator drives - E. Erdelyi & E. Kolatorowic A.I.E.E. Trans. Pt. II 1960 Pg. 438 - 42.

17) A.I.E.E. classified Bibliography on rotating Electric machinery.

1) S-32 - 1886 - 1947 published Jan. 1950

2) - - 1948 - 1961 published June 1964

3) - - 1962 - 1965 published March 1968.

18) Nonlinear magnetisation in thin ferro-magnetic plate - V. Subba Rao Proc. I.E.E. Vol. 113 June 1966 Pg. 1125 - 1131.

19) The M.M.F. Wave of Polyphase Windings with special reference to sub-synchronous Harmonics - Q. Graham A.I.E.E. Trans. Vol. 46 Feb. 1927 Pg. 19 - 29.

20) Reactance of End Connections - J.F.H. Douglas A.I.E.E. Trans. Vol. 56 Feb. 1937 Pg. 257-259 disc'n Pg. 1315-1318.

21) Pole-Face losses in alternators - J. Greig and K. Sathirakul. I.E.E. monograph 404S. Pg. 130-138 Oct. 1960

B.2. Text Book References

31) Applied Electrical Measurements - Kinnard - John Wiley 1956.

32) Electrical Measurements and measuring instruments Golding - Pitman's 1950.

33) Diagnosing of troubles in electrical machines. Miles Walker - Longman's 1921.

34) Elektrische Maschinen - R. Richter. Springer Verlag. 1929. Pg. 107 - 110..

35) Die Elektrischen Maschinen. B.111 - M. Liwschitz Verlag and Druck von B.G. Teubner 1934. Pg., 82-83.

36) Berechnung and Bemessung elektrischer maschinen J. Klamt. Springer Verlag 1962. Pg. 224 - 225.

37) The Nature of polyphase Induction Machines - P.L. Alger - John Wiley 1951.

38) Design of electrical apparatus J.H. Kuhlmann - John Wiley 1950 Pg. 335 - 337.

B.3 Rotating Machines references in particular

51) Calculation of Stray load losses - G.H. Rockwood, A.I.E.E. Trans. 1927 pg. 1139 - 1147.

52) Load losses in Salient pole sychronous machines. - E.I. Pollard. A.I.E.E. Trans. 1935, Pg. 1332-1340.

53) Stray losses in sychronous eletrical machinery - P. Richardson J.I.E.E. Vol 92 1945 Pg. 291-304.

54) Stray losses in the Armature End Iron of large turbine generators. - R.L. Winchester A.I.E.E. Trans. 1955 Pg. 381 - 391.

55) Eddy-Currents in the End Portion of Turbine-Generators stator windings - G.W. Staats. A.I.E.E. Trans 1957. Pg. 384 - 392.

56) End Component of Armature Leakage reactance of Round-Rotor Generators - R.T. Smith A.I.E.E. Trans. 1958. Pg. 636 - 647.

57) Stray-load losses in polyphase Induction Machines - Alger, Angst & Davies A.I.E.E. Trans. 1959. Pg. 349-357.

58) Theory of End-Winding Leakage reactance - V.B. Honsinger, A.I.E.E. Trans. 1959. Pg. 417 - 426.

59) The Magnetic field of the End-Windings of Turbo-Generators - P.J. Lawrenson I.E.E. Proc. 1961 Pg. 538 - 549 Dissc. 549 to 553.

60) The field of Turbo-Generator - D. Ashworth and P. Hammond Proc. I.E.E. 1961 Pg. 527 - 538, disscn. Pg. 549 - 553.

61) Current Sheets Equivalent to End-Winding currents of Turbine-Generator Stator and rotors - J.A. Tegopoulos A.I.E.E. Trans. 1962 Pg. 695 - 700.

62) Flux Impinging on the End plate of turbine generators - J.A. Tegopoulos, A.I.E.E. Trans. 1962 Pg. 700 - 707.

63) Leakage Fields, Eddy current losses. Heating, Forces and Iron burning in the End region of Turbo-Generators - K. Oberrettl. U. and M. - 1963 Pg. 539 - 550.

64) Determination of the Magnetic Field in the End Zone of Turbine Generators - J.A. Tegopoulos. A.I.E.E. Trans. 1963 Pg. 562 - 572.

65) Calculation of the magnetic field in the coil-ends of turbo-generators - P. Althammer. Brown Boveri Review. 1964. Pg. 281 - 292.

66) Approximate determination of the field and the losses associated with eddy currents in conducting surfaces - R. Stoll and P. Hammond Proc. I.E.E. 1965 Pg. 2083 - 2094.

67) Forces on the End Winding of Turbine-Generators Pt. 1. - Determination of Flux Densities - J.A. Tegopoulos. A.I.E.E. Trans. 1966, Pg. 105 - 113.

68) Field in the end region of turbo generators and the eddy-current loss in the end plates of stator cores R. Stoll and P. Hammond. Proc. I.E.E. 1966 Pg. 1793 - 1804.

69) Calculation of the end-region field of a.c. machines - A.B. Reece and A. Pramanik Proc. I.E.E. Vol. 112 July 1965 Pg. 1355 - 1366.

70) Turbo generator end-region magnetic fields Qualitative prediction by flux plotting - Hawley, Stoll, Edwards and Heaton, Proc. I.E.E. Vol. 114 Aug. 1967. Pg. 1107 - 1114.

71) Determination et tracé des champs à trois dimensions Application aux têtes de bobines, notamment des turbo-alternateurs. - G. Darrieus. Review Genéral de L̀ Électricite. March 1967 Pg. 333 - 354.

72) 115,000 K.W. Turbo Alternator - R.B. Williamson A.I.E.E. Trans. Sept. 1932 Pg. 652 - 658.

73) Additional Losses of Synchronous Machines - C.M. Laffoon, J.F. Calvert A.I.E.E. Trans. Vol. 46 Feb 1927 Pg. 84 - 100.